Modeling of Water-containing Reservoir Oil for Steam Injection Simulation

by

Arun Venkat Venkatramani

A thesis submitted in partial fulfillment of the requirements for the degree of

Master of Science

in

Petroleum Engineering

Department of Civil and Environmental Engineering
University of Alberta

Abstract

Experimental results in the literature show that the water solubility in the oleic (L) phase can be high at reservoir conditions in thermal oil recovery processes; e.g., 24 mol% in the water/n-eicosane binary system at 41 bars and 523 K. It becomes even more significant as the L phase becomes more aromatic, which is the case with heavy oil and bitumen. Efficient and accurate representation of multiphase behavior, which consists of the L, vapor (V), and aqueous (W) phases, is crucial in reliable numerical simulation of steam injection processes. This research presents a new framework to model the multiphase behavior of water-containing reservoir oil by use of the Peng-Robinson equation of state (PR EOS) with the van der Waals mixing rules.

The development of this framework involves two stages. In the first stage, a new characterization framework for the accurate representation of the multiphase compositional behavior of mixtures of water and reservoir oil is developed (Approach 1). The resulting product is a new set of correlations for the binary interaction parameter (BIP) between water and hydrocarbons (n-alkanes and pseudo-components). These correlations are functions of the molecular weight (MW) of the hydrocarbon.

In the second stage, the shortcoming of Approach 1 with regard to the predicted volumetric behavior is addressed by first optimizing component-specific critical constants (T_C, P_C) and acentric factor (ω) of n-alkanes and water. The optimized T_C, P_C and ω are then employed to develop a new set of correlations for the BIP between water and hydrocarbons (Approach 2).

Results show that both Approach 1 and Approach 2 can accurately represent the multiphase compositional behavior of binary and multicomponent, water-containing mixtures of n-alkanes and reservoir oil. In terms of density predictions, Approach 2 offers improved accuracy over Approach 1. The distinct advantage of employing the characterization framework developed in this research over prior thermodynamic models is the simultaneous obtainment of improved accuracy in phase behavior predictions and computational efficiency. The results of the numerical reservoir simulation performed for the expanding-solvent steam assisted gravity drainage using n-C_5 as the solvent indicate that the dissolution of water in the L phase can significantly enhance the local displacement efficiency. Case studies show that the resulting improvement in oil drainage rate can be greater than 10%, signifying the importance of the accurate representation of phase behavior.

Acknowledgements

I express my deepest gratitude to my advisor, Dr. Ryosuke Okuno, for his guidance, patience and support without which I could not have completed this thesis. I am indebted to Dr. Subhash Mahajan (University of California, Davis), Dr. Patrick Phelan (Arizona State University), Dr. Kaushal Rege (Arizona State University), Dr. David Nielsen (Arizona State University), and Dr. Madhusree Kundu (National Institute Technology, Rourkela) for their encouragement and support towards my pursuit of higher education. I also thank my thesis committee members, Dr. Japan Trivedi and Dr. Huazhou Li, for their feedback on this work.

I gratefully acknowledge the financial support received from the Society of Petroleum Engineers (Junior Faculty Research Initiation Fellowship awarded to Dr. Ryosuke Okuno, 2012-13), Natural Sciences and Engineering Research Council of Canada (RGPIN 418266), and Japan Petroleum Exploration Co., Ltd. (JAPEX) towards conducting this research.

I would like to thank my colleague, Ashutosh Kumar, for providing crucial data for this study, and useful suggestions over the course of this research. I am also thankful to my colleagues Di Zhu, and Bo Zhang for their participation in technical discussions and willingness to help me in every stage of this research. Finally, I would like to thank my family for their encouragement and support through all these years.

Table of Contents

List of tables

List of figures

Nomenclature

Roman Symbols

a	attraction parameter for the PR EOS
A	constant used in equations 2 and 3
B	constant used in equations 2 and 3
C	constant used in equation 3
D	constant used in equation 3
f	weight fraction
f_j	fractional flow of phase j
$\hat{f}_{ij}$	fugacity of component i in phase j
g	gravitational acceleration
$\Delta_m\underline{G}$	molar Gibbs free energy change on mixing
H	reservoir thickness
Io	term used in equation 1.5
k_{rj}	relative permeability of phase j
L	oleic phase
m	term used in equation equation A-4
N_C	number of components
N_C	number of phases
P	pressure, bar
P^{sat}	saturation pressure, bar
R	gas constant
S_j	saturation of phase j

T temperature, K

T_r non-dimensionalized temperature

U velocity

V vapor phase

$\underline{V}$ molar volume

W aqueous phase

x_{ij} concentration of component i in phase j

z overall composition

Z compressibility factor

Greek Symbols

α temperature dependence term of the attraction parameter

β_j phase fraction

δ distance in composition space

Δ difference operator

λ scaling factor for BIP correlation

μ viscosity

∇ gradient operator

φ porosity

$\hat{\varphi}_{ij}$ fugacity coefficient of component in phase j

ρ density of phase

ω acentric factor

Ω PR EOS constant

Subscripts

C	critical point
hc	hydrocarbon component
i	component index
j	phase index {L, V, W}
L	oleic phase
T	temperature
R	reservoir
UCEP	upper critical endpoint
P	pressure or phase
V	vapor phase
w	water component
W	aqueous phase
3φ	three phases

Superscripts

Data	values from measured data
EOS	values calculated from an EOS

Abbreviations

AAD	absolute average deviation
AD	absolute deviation
BIP	binary interaction parameter

CN	carbon number
EOS	equation of state
MW	molecular weight
UCEP	upper critical endpoint
PR	Peng and Robinson
PVT	pressure-volume-temperature

Chapter 1. Introduction

1.1 Problem statement

Steam-injection is widely employed in the recovery of heavy oils and bitumens (Prats, 1982). In addition to sensible heat, the latent heat released when the injected steam condenses into hot water at thermal fronts effectively reduces the viscosity of heavy oil, thereby making it more mobile. Recovery factors in steam-injection processes are typically on the order of 50-60% oil-in-place (Thomas, 2008). The enhancement of their economic viability requires an elaborate understanding of recovery mechanisms, which currently remains elusive.

Numerical reservoir simulation serves as a useful tool to discern mechanisms for oil recovery, in addition to experimental measurements (Keshavarz et al., 2013). Reliable simulation of steam injection processes requires accurate representation of the multiphase behavior of water-containing mixtures of reservoir oils. Broadly, its importance can be understood from the fact that a minimum of three phases- vapor (V), oleic (L), and aqueous (W) can coexist within the confines of the reservoir, and their propagation within the reservoir is governed by their transport, volumetric and interfacial properties. However, the mechanism by which phase properties impact oil recovery estimates requires a closer examination of how transport phenomena are modeled in the reservoir.

In reservoir simulation, the reservoir is fragmented in to grid blocks, with each grid block treated as a zone of local thermodynamic equilibrium. As seen in

equations 1.1 through 1.4, the fractional flow of a phase across the boundaries of the grid block is affected by its density, viscosity and interfacial tension.

$$f_j = \frac{q_j}{q} \tag{1.1}$$

where f_j and q_j represent the fractional flow and volumetric flow rate of phase j, respectively, and q represents the total volumetric flow rate.

$$q_j = \frac{-kk_{rj}A}{\mu_j}(\nabla P_j + \rho_j \vec{g}) \tag{1.2}$$

where ∇P_j, ρ_j and k_{rj} represent the pressure gradient, mass density and relative permeability of phase j, respectively. $\vec{g}$ stands for the acceleration due to gravity, while k stands for the absolute permeability.

$$k_{rj} = k_{rj}(S_1, S_2, \dots, S_j, \dots S_{N_p-1}) \tag{1.3}$$

where S_j represents the saturation of phase j. N_p represents the number of phases.

$$S_j = \beta_j Z_j / \sum_{i=1}^{N_p} \beta_i Z_i \tag{1.4}$$

where βj and Zj, represent the phase fraction and compressibility factor of phase j, respectively.

In steam-assisted-gravity-drainage (SAGD), steam and bitumen condense at the edge of the steam chamber and drain into the producer well, from which they are recovered. The drainage occurs due to the effect of gravity. Based on the work of Reis et al. (2006), Keshavarz et al. (2014) derived an expression for the volumetric drainage rate of the L phase (equation 1.5).

$$q_o = \sqrt{0.5 k k_{rL} g \phi \Delta S_o H (U_m . I_o)} \quad (1.5)$$

where q_o is the volumetric drainage rate of the bitumen component per unit length of the horizontal section along one side of the chamber edge, k is the absolute permeability, k_{rL} is the average relative permeability to the L phase beyond the chamber edge, g is the gravitational acceleration, φ is the porosity, H is the reservoir thickness above the producer and ΔS_o is the reduction in the local bitumen saturation. The expression for Io is presented in equation 1.6.

$$I_o = -(\alpha/\varepsilon U_m) \int_{T_{edge}}^{T_R} \{[(MW_L \rho_L)/\mu_L]/(T - T_R)\} \, dT \quad (1.6)$$

where ρ_L, μ_L and MW_L are the molar density, viscosity, and molecular weight of the L phase, respectively. As with equations 1.1 through 1.4, equations 1.5 and 1.6 indicate that phase properties can play a pivotal role in the estimation of oil recovery. These equations accentuate the importance of the development of a fluid model capable of accurate representation of multiphase behavior of water/hydrocarbon mixtures.

Besides accurate representation, the efficient representation of multiphase behavior is an essential attribute for a fluid model employed in reservoir simulation. This requirement stems from the fact that phase equilibrium computations alone can consume more than 50% of total reservoir simulation time (Okuno et al., 2009). The obtainment of computational efficiency through a simple mathematical formulation along with their capability of continuous description of both vapor and liquid states renders cubic equations of state (EOSs) as potential candidates for phase behavior modeling in reservoir simulation.

Experimental investigations conducted on the phase behavior of water-containing mixtures indicate that the dissolution of water in the L phase (x_{wL}) can be significantly high at elevated temperatures (Griswold and Kasch, 1942; Skripka et al., 1979; Glandt and Chapman, 1995; Amani et al., 2013). The significance is enhanced if the L phase comprises aromatic compounds. In contrast, the dissolution of the hydrocarbon in the W phase (x_{hcW}) is lower than 1 mol% (Tsonopoulos and Wilson, 1983; Heidman et al., 1985). From a modeling standpoint, cubic EOSs with the van der Waals (classical) mixing rules have been found to be capable of representing x_{wL} at least qualitatively (Heidemann 1974; Daridon et al. 1993; Eubank et al. 1994; Nasrifar and Moshfeghian 2002). However, a single cubic EOS with the classical mixing rules cannot model x_{wL} and x_{hcW} simultaneously over a wide temperature range (Heidemann 1974; Daridon et al. 1993; Nasrifar and Moshfeghian 2002; Satyro et al. 2013). Peng and Robinson (1980) observed that the Peng-Robinson (PR) EOS with the classical mixing rules under-predicted x_{hcW} by a few orders of magnitude. For reservoir engineering applications (sub-surface processes), the significance of x_{hcW} is likely minimal. Thus, the accurate representation of x_{wL} takes precedence, justifying the use of the simplistic classical mixing rules.

Over the last few decades a number of thermal reservoir simulation studies have been performed using cubic EOSs. Brantferger et al. (1991) developed a PR EOS-based thermal simulator in which the mutual solubilities of water and hydrocarbons were not considered. That is, both x_{wL} and x_{hcW} were considered to be negligible. A similar approach to fluid modeling was adopted in the simulation

studies of Iranshahr et al. (2010), and Keshavarz et al. (2009). Luo and Barrufet (2005) and Varavei and Sepehrnoori (2009) developed simulators in which the dissolution of water in the oleic phase was considered. Both studies employed the PR EOS with the classical mixing rules. As for the binary interaction parameter (BIP) between water and hydrocarbon components, while Varavei and Sepehrnoori (2009) employed the values by Shinta and Firoozabadi (1997), those employed by Luo and Barrufet (2005) are unclear. It is to be noted that the BIP values recommended by Shinta and Firoozabadi (1997) are for interactions between water and n-alkanes for use with the association EOS, which is distinct from the PR EOS. As with Luo and Barrufet (2005), Liu et al. (2009) have not furnished specifics of the PR EOS model parameters in their simulation study.

The investigations by Luo and Barrufet (2005) and Keshavarz et al. (2013) are of most significance to this research. The significance of these works is attributed to two factors:

- These investigations are on the mechanisms by which oil is recovered in steam-injection processes,
- The scope of these works included the study of phase behavior, the crux of this research.

Luo and Barrufet (2005) concluded that the dissolution of water in the oleic phase considerably reduces the oil viscosity and the gross effect of this phenomenon is an improvement in oil recovery by up to 7%. In their work, the authors assumed that the aqueous phase (W) comprised 100% water. This

assumption was justified based on experimental observations that the dissolution of hydrocarbons in the W phase is only on the order of 0.01 mol% or lower (Tsonopoulos and Wilson, 1983, Heidman et al., 1985).

Keshavarz et al. (2013) investigated oil recovery mechanisms in expanding-solvent steam assisted gravity drainage (ES-SAGD) processes. They concluded that there are three major factors governing oil recovery: propagation of component and thermal fronts, accumulation of the solvent at the chamber edge, and the transition from three-phase coexistence to two-phase coexistence at the chamber edge. As stated before, a simplifying assumption made by Keshavarz et al. (2013) is that the mutual solubilities of water and hydrocarbon are negligible.

The studies performed by Luo and Barrufet (2005) and Keshavarz et al. (2013), albeit insightful, do not clearly answer an important question: how does the dissolution of water in the L phase affect oil displacement through propagation of heat and components in porous media? An important step towards understanding this is the development of an appropriate characterization framework for water-containing reservoir oils. For application in thermal reservoir simulation, it is preferable for a fluid characterization framework to have the following attributes:

- The capability to adequately represent the multiphase behavior of water-containing mixtures of hydrocarbons over a wide range of temperature and pressure.

- The capability to represent mixtures wherein the constituent hydrocarbons can be both heavy (in terms of the carbon number), and their chemical identity may be uncertain (pseudo-components, as with oils).

- A simple mathematical formulation for the EOS and the mixing rules.

Over the last several decades, numerous studies on the modeling of phase behavior water/hydrocarbon mixtures using cubic EOSs have been performed (Heidemann 1974; Daridon et al. 1993; Heidman et al., 1985; Eubank et al. 1994; Nasrifar and Moshfeghian 2002). Yet, a single characterization framework with all of the aforementioned attributes does not exist, to the best of our knowledge.

1.2 Research Objective

The objective of this research is to develop a framework for the characterization of water-containing reservoir oils using the PR EOS employing the classical mixing rules, capable of adequately representing multiphase behavior.

1.3 Structure of thesis

This thesis has been structured into 4 chapters. In Chapter 1, the introduction, the motivation for this research is presented. In Chapter 2, a new framework for the characterization of water-containing reservoir oils, capable of accurate representation of multiphase compositional behavior is proposed. In Chapter 3, a critical evaluation of the performance of the framework presented in Chapter 2 in terms of the predicted volumetric behavior is performed. A demonstration of its

shortcomings is first presented. Following this, a new framework capable of adequately representing both multiphase compositional and volumetric behavior is proposed. Subsequently, the compositional behavior predicted using this framework is employed to simulate the ES-SAGD process with n-C_5 as the solvent, the objective being to obtain quantitative understanding of the potential importance of the dissolution of water in the L phase.

A common feature observed in both Chapters 2 and 3 is the optimization of the BIP between water and n-alkanes against the corresponding experimentally measured binary three-phase curves. This is followed by the correlation of the optimized BIPs as a function of the molecular weight of the hydrocarbon, and its subsequent extension to water-containing reservoir oils. Its significance is elucidated in both Chapters 2 and 3. This thesis culminates with Chapter 4 in which the findings of this research are summarized and recommendations for future work are presented.

This thesis also comprises an appendix that is further divided into 3 sub-sections labeled A through C. In Appendix A, the Peng-Robinson EOS and the classical mixing rules are shown. Robust computational methods for three-phase curves including upper critical endpoints (UCEPs), at which the three-phase curves terminate, are a prerequisite for the optimization of the BIP. The computational algorithms employed in this work along with the justification for their robustness are explained in Appendix B. The development of the framework proposed in Chapter 2 requires the compilation of critical constants and acentric

factors of n-alkanes spanning from methane (C_1) to n-C_{100}. The compiled values for the aforementioned properties are presented in Appendix C.

Chapter 2. Characterization of multiphase compositional behavior for water-containing reservoir oils in steam injection processes

In this chapter, a new framework for the multiphase compositional behavior of water-containing mixtures of reservoir oils is proposed. The framework is first developed for water-containing mixtures of n-alkanes, specifically, water/n-alkane binaries, and subsequently extended to reservoir oils. Briefly, the critical constants (T_C, P_C) and acentric factor (ω) of n-alkanes with carbon number (CN) up to 100 are first compiled, following which, the BIPs between water and n-alkanes are optimized against the corresponding binary three-phase curves measured by Brunner (1990), and then correlated as a function of the n-alkane molecular weight (MW). The developed BIP correlation is validated against phase composition data (in the two and three-phase regions) published for both binary and multi-component mixtures of water and hydrocarbons, and then tuned to represent the L-phase compositional data of water-containing reservoir oils measured in the neighborhood of the three-phase region.

The basis for this methodology stems from the following:

i. Reservoir oils can be characterized using the paraffinic-naphthenic-aromatic (PNA) scheme (Kumar and Okuno, 2013). Mixtures of n-alkanes represent the paraffinic end of the PNA spectrum.
ii. N-alkanes are a well-defined homologous series for which systematic experimental measurements are available.

iii. Experimental measurements, solubility and calorimetric, indicate that the affinity of n-alkanes towards water is lowest in comparison with those of naphthenes and aromatics (Tsonopoulos and Wilson, 1983, Heidman et al., 1985, Tsonopouolos, 1999). Thus, a framework developed for water and n-alkanes can be harnessed as a limiting bound for extension to water-containing reservoir oils, which can comprise aromatics and naphthenes.

iv. The accurate representation of the multiphase behavior of binary mixtures is of considerable importance as multiphase behavior in higher dimensional composition space is influenced by that in lower dimensions. In the subsequent section, the fact that the two-phase equilibria of water/n-alkane binaries are originated with three-phase behavior will be elucidated.

In the sections to follow, an overview of the phase behavior of water/n-alkane binaries is first presented (section 2.1). Following this, the methodology for optimization and correlation for the optimized BIPs between water and n-alkanes is explained (section 2.2). The results for the validation of the developed BIP correlation and its extension to water-containing Peace River and Athabasca bitumens are presented in section 2.3. The significance of the BIP correlation is elucidated in section 2.4 through a detailed analysis of the short comings of the current practice in phase behavior modeling of water/hydrocarbon mixtures. This chapter culminates with a summary presented in section 2.5.

2.1 Multiphase behavior of water/n-alkane binaries

This section gives an overview for multiphase behavior of water/n-alkane binaries. Three-phase curves and x_{wL} for water/n-alkane binaries are of particular importance as they are used for our development of a new BIP correlation.

2.1.1 Overview

Brunner (1990) presented three-phase pressure-temperature (P-T) conditions measured for 21 binary mixtures of water and n-alkanes, ranging from C_3 through n-C_{36}. The phases considered were the V, L, and W phases. The three-phase curve for each of the measured binaries was present on the higher pressure side of the pure-component vapor pressure curves. The three-phase curve of each binary culminated at an UCEP, where the less dense of the two liquid phases (L and W) became critical with the V phase in the presence of the denser liquid phase.

The multiphase behavior of water/n-alkane binaries was classified into types IIIa and IIIb, according to the classification scheme of van Konynenburg and Scott (1980). P-T projections of representative binaries for types IIIa and IIIb are schematically shown in Figures 2.1 and 2.2, respectively.

Results of Brunner (1990) showed that type IIIa occurs for water with n-alkanes with CNs up to 25. The relative volatility of n-alkane to water changes at CN six. For water/n-alkane binaries with CNs lower than six, the vapor pressure curve of the n-alkane component lies on the higher pressure side of the water vapor pressure (Figure 2.1a). For binaries with CNs higher than six, the relative volatilities are the other way around (Figure 2.1b). The UCEP for a type IIIa

system is where the L and V phases merge in the presence of the W phase. That is, the L phase is less dense than the W phase along the three-phase curve in this case.

Brunner (1990) observed the barotropic reversal between the L and W phases along the three-phase curve for water with n-alkanes with the CN of 28 and higher. Thus, the W phase was less dense than the L phase at the UCEP for these binaries. This is a key characteristic of types IIIb, where the W and V phases merge in the presence of the L phase at the UCEP (Figure 2.2). According to Brunner (1990), the temperature at which the barotropic reversal of the two liquid phases takes place along the three-phase curve decreases with increasing CN of n-alkane. The classification of phase behavior for water/n-alkane binaries with CNs 26 and 27 is not entirely clear.

Scheffer (1913, 1914), Tsonopoulos and Wilson (1983), Heidman et al. (1985), and Economou et al. (1997) presented that the three-phase pressures ($P_{3\varphi}$) of water/n-alkane binaries were approximately the sum of the vapor pressures of the pure components. That is,

$$P_{3\varphi}(T) \approx P_{hc}^{sat}(T) + P_{w}^{sat}(T), \qquad (2.1)$$

where P_{hc}^{sat} and P_{w}^{sat} are the saturation vapor pressures of the hydrocarbon and water components, respectively. Heidman et al. (1985) observed that equation equation 2.1 was accurate for water/n-C_8 at temperatures below 423 K, which corresponds to $T_r = T/T_{UCEP} = 0.78$. No explanation was given as to why equation 2.1 gave reasonable accuracy for $P_{3\varphi}$.

Equation 2.1 can be obtained through the following assumptions regarding the three-phase equilibrium of a water/n-alkane binary: (i) complete immiscibility between the W and L phases, and (ii) Raoult's law for phase equilibrium relations (V-L for the hydrocarbon component and V-W for the water component). **Table 2.1** compares $P_{3\varphi}$ estimated using equation 2.1 with experimental $P_{3\varphi}$ data for the water/n-C_6, water/n-C_8, and water/n-C_{10} binaries (Tsonopoulos and Wilson 1983; Heidman et al. 1985; Economou et al. 1997). For the water/n-C_8 binary, x_{wV} are also compared, where x_{wV} is the water concentration in the V phase. The uncertainties were ±0.6 K, ±0.4 bars, and ±0.02 in terms of temperature, pressure, and concentration, respectively, in these measured data. Based on the two assumptions (i and ii), x_{wV} can be calculated as P_w^{sat}/P at a given T. Equation 2.1 yields reasonably accurate estimations of $P_{3\varphi}$ and x_{wV} even at temperatures higher than 423 K in these cases. Equation 2.1, however, can be inaccurate near the UCEPs.

Figure 2.3 shows that $P_{3\varphi}$ from equation 2.1 deviates from measured $P_{3\varphi}$ near the UCEPs for the water/n-C_8 and water/n-C_{10} binaries. Our analysis of Brunner's three-phase data has indicated that equation 2.1 may give satisfactory $P_{3\varphi}$ estimations up to about $T_r = 0.80$. For water/n-C_{36}, for example, $P_{3\varphi}$ at $T_r = 0.855$ (549.25 K) is 60.48 bars from equation 2.1, which is reasonably close to the measured value, 60.86 bars.

The systematic investigation made by Brunner (1990) showed that the three-phase curve becomes closer to the water vapor pressure curve as n-alkane becomes heavier. Figure 2.4 presents the deviation of the three-phase pressure

from the water vapor pressure at T_r = 0.86 and 0.90 based on the data given in Brunner (1990). The fluctuations observed for CNs from 20 through 36 are owing to experimental uncertainties. For example, temperatures in these measurements were over 600 K, where thermal decomposition of hydrocarbons could occur. Brunner (1990) mentioned that for temperatures above 600 K, the experimental uncertainties were about ±1 K and ±0.005P bars, where P is the operating pressure. For measurements at temperatures below 600 K, the experimental uncertainties were ±0.2 K and ±0.004P bars. The proximity of the three-phase curve to the water vapor pressure curve presented in Figure 2.4 for CN 20 and higher is not always within, but at the level of the experimental uncertainties mentioned by Brunner (1990).

Figure 2.4 indicates that the three-phase curve approaches a certain asymptotic limit near the water vapor pressure curve in P-T space as the n-alkane CN becomes larger. This can be qualitatively reproduced by equation 2.1 for temperatures that are sufficiently lower than T_{UCEP} (e.g., $T_r < 0.80$). Figure 2.4 shows P_{hc}^{sat}, which is $(P_{3\varphi} - P_w^{sat})$ from equation 2.1, for different CNs. The three-phase curves for water with n-alkanes heavier than approximately n-C_{20} may be nearly invariant with CN when temperatures are sufficiently lower than T_{UCEP}.

Figures 2.5 and 2.6 schematically illustrate pressure-concentration (P-x) diagrams at $T \leq T_{UCEP}$ for types IIIa and IIIb. Note that these figures are not drawn to scale. The V phase is the intermediate phase between the L and W phases in composition space for water/n-alkane binaries. For type IIIa, the V and

L phases merge in the presence of the W phase at UCEP as shown in Figure 2.5. For type IIIb, the V and W phases merge in the presence of the L phase at UCEP as shown in Figure 2.6. The two-liquid-phase tie lines at pressures above $P_{3\varphi}$ are relatively insensitive to pressure (Tsonopoulos and Wilson 1983; Heidman et al. 1985; Economou et al. 1997). These figures show that two-phase equilibria (i.e., V-W, V-L, and L-W) are originated with three-phase behavior (L-V-W). Also, the UCEP is the limiting three-phase behavior. Therefore, it is of fundamental importance that the thermodynamic model used in reservoir flow simulation can reasonably represent three-phase curves, including the UCEPs, for water/n-alkane binaries.

2.1.2 Solubility of water in the oleic phase

Due to the apparent validity in terms of $P_{3\varphi}$ and x_{wV} at temperatures sufficiently lower than $T_{UCEP,}$ the assumptions (i) and (ii) may be used as simplified phase behavior in simulation of thermal reservoir processes (Keshavarz et al. 2013). However, the water solubility in the L phase can be significant at operating conditions in thermal oil recovery. For example, the water solubility in the L phase was measured to be 23.68 mol% for the water/n-C_{20} binary at 523.15 K (the corresponding $P_{3\varphi}$ measured by Skripka, 1979 is 41.38 bars).

The L and V phase compositions along the three-phase curve were reported for the water/C_3 binary by Kobayashi and Katz (1953) and for the water/n-C_8 binary by Heidman et al. (1985), which are reproduced in **Figures 2.7 and 2.8** in P-x space. The V-L envelopes in these figures correspond to the ones

schematically shown in Figures 2.5 and 2.6. The water concentration of the critical phase at the UCEP is much higher for the water/n-C_8 binary than for the water/C_3 binary. Consequently, the V and L phases at the subcritical conditions are richer in water for the water/n-C_8 binary than for the water/C_3 binary at a given pressure. The water concentration in the V phase (x_{wV}) exhibits a maximum for these binaries. The water concentration (or solubility) in the L phase (x_{wL}) monotonically increases with pressure along the three-phase curve for these binaries.

Figures 2.9 and 2.10 show the x_{wL} values measured along three-phase curves for water with n-alkanes with CNs 3, 4, 6, 7, 8, 9, 10, 12, 16, and 20 (Reamer et al. 1944; Kobayashi and Katz 1953; Skripka 1979; Tsonopoulos and Wilson 1983; Heidman et al 1985; Economou et al. 1997; Maczynski et al. 2005; Shaw et al. 2005; Shaw et al. 2006a, b). Based on Maczynski et al. (2005) and Shaw et al. (2005, 2006a, b), the experimental uncertainties in the measurements were approximately ±30% relatively to the reported values. To our knowledge, experimental data for x_{wL} along the three-phase curves have not been presented for CNs higher than 20. Figures 2.9 and 2.10 indicate that x_{wL} along the three-phase curve increases with temperature for a given binary, as also shown indirectly in Figures 2.7 and 2.8 for C_3 and n-C_8. The dependency of x_{wL} on the n-alkane CN for a given temperature is apparently weak in Figures 2.9 and 2.10.

Tsonopoulos (1999) explained that the heat of solution (approximately 35 kJ/mol) in calorimetric measurements was insensitive to temperature and the n-alkane CN. Since the value was on the order of a normal hydrogen-bond energy

(20 – 40 kJ/mol), he considered that the dissolution of n water molecules led to the breaking of n hydrogen bonds. He then presented a simple correlation for x_{wL}

$$\ln(x_{wL}) = A + B/T \qquad (2.2)$$

where A and B are constants to be adjusted for a given binary and T is temperature in Kelvin. Tsonopoulos (1999) observed that equation 2.2 was accurate for water/n-C_8 at temperatures below (T_{UCEP} – 30) K, which corresponds to $T_r = 0.94$. Equation 2.2 can be derived by use of the following assumptions: (a) an ideal mixture is formed, and (b) partial molar excess enthalpy of water in the L phase is independent of temperature and the n-alkane CN. Our analysis of the x_{wL} data reported for water/n-alkanes (C_3, n-C_4, n-C_6, n-C_7, n-C_8, n-C_9, n-C_{10}, n-C_{12}, n-C_{16}, and n-C_{20}) has indicated that equation 2.2 may give satisfactory x_{wL} estimations for T_r below at least 0.90.

Although the accuracy is limited near T_{UCEP}, the simple correlation of Tsonopoulos (1999) is remarkable considering that $P_{3\varphi}$ values at a given temperature are considerably different from one another for n-alkanes lighter than n-C_{20} (Figure 2.4). However, the dependency of x_{wL} on pressure was weak in the L-W two-phase region (Tsonopoulos and Wilson 1983; Heidman et al. 1985; Economou et al. 1997; Tsonopoulos 1999). The correlation of Tsonopoulos at $T_r < 0.90$ may be also applicable for CNs higher than 20 since their three-phase curves are almost invariant in P-T space near the water vapor pressure curve (see Figure 2.4). Thus, the pressure dependency of x_{wL} does not affect the $x_{wL}(T)$ trends for different binaries for such cases. The x_{wL} data available up to n-C_{20}, along with the research by Tsonopoulos (1999), indicate that the x_{wL} trend in

temperature may be nearly invariant for heavier n-alkanes as long as T_r is not close to unity (e.g., $T_r < 0.90$). This is in line with the correlation of Eubank et al. (1994), in which x_{wL} is a function of only temperature for CNs above five.

The x_{wL} values deviate from the trend described by equation 2.2 as the UCEP is approached (Figures 2.9 and 2.10). This can be interpreted as a deviation from the assumptions a and b that were used for equation 2.2. Heidman et al. (1985) and Economou et al. (1997) presented a more flexible correlation for x_{wL} as follows:

$$\ln(x_{wL}) = A + B(1/T_r - 1) + C(1 - T_r)^{1/3} + D(1 - T_r), \qquad (2.3)$$

where $T_r = T/T_{UCEP}$, and A, B, C, and D are constants. They showed that equation 2.3 was applicable to higher temperatures near T_{UCEP}. Since temperature is scaled with respect to T_{UCEP}, equation 2.3 accommodates the x_{wL} behavior near T_{UCEP}, which is dependent on the n-alkane CN.

2.2 Optimization of Binary Interaction Parameters

As presented in the preceding section, phase equilibria of water/n-alkane binaries are originated with L-V-W three-phase behavior. This section presents a new correlation for the interaction parameters of water/n-alkane binaries that enables the PR EOS to accurately represent the three-phase P-T curves including UCEPs.

The optimization of BIPs uses the three-phase P-T data points, including those for UCEPs, reported in Brunner (1990) for water/n-alkanes binaries from C_3 through C_{36}. He presented such data for 21 binaries, but data for the water/n-C_{26}

binary are not used in our optimization. This is because the UCEP for this binary was reported to be identical to that for the water/n-C_{28} binary, which caused a deviation from the overall trend. No explanation was given regarding this deviation. There are 213 data points on three-phase curves, out of which 20 data points are for UCEPs for 20 different binaries, all of which are used in the optimization. Three types of deviations are considered in the BIP optimization as follows:

$$\Delta T_{3\varphi} = \left| T_{3\varphi}^{EOS}(P) - T_{3\varphi}^{Data}(P) \right| \tag{2.4}$$

$$\Delta T_{UCEP} = \left| T_{UCEP}^{EOS} - T_{UCEP}^{Data} \right| \tag{2.5}$$

$$\Delta P_{UCEP} = \left| P_{UCEP}^{EOS} - P_{UCEP}^{Data} \right|, \tag{2.6}$$

where superscripts "EOS" and "Data" indicate prediction from EOS and measured data, respectively. Subscripts "3φ" and "UCEP" indicate values for three-phase equilibrium and UCEP. In addition to equations 2.4 through 2.6, the values for the optimized BIP are determined based on the type of transition that occurs in the near-critical region (type IIIa or type IIIb). For systems exhibiting type IIIb phase behavior, an additional criterion has been employed to determine the optimized BIP. It is the obtainment of asymptotic behavior of x_{wL} along the three-phase curves with respect to CN. The importance of this criterion is discussed at length in section 2.4. The PR EOS with classical mixing rules, and the computational algorithms employed for the prediction of binary three-phase curves are presented in Appendix A and B, respectively.

The only adjustment parameter in the optimization for each binary is the BIP. The critical temperature (T_C) and critical pressure (P_C) of water are 647.096 K and 220.64 bars, respectively (Wagner and Pruß, 2002). The acentric factor (ω) of water estimated using the vapor pressure correlation of Wagner and Pruß (2002) is 0.3433. The API technical data book (Daubert and Danner, 1997) presents recommended values for T_C, P_C, and ω for n-alkanes up to n-C_{30}. Constantinou and Gani (1994) and Constantinou et al. (1995) used a group-contribution method to estimate T_C, P_C, and ω for a homologous series of n-alkanes. Kontogeorgis and Tassios (1997) gave a critical review of various correlations for T_C, P_C, and ω, and concluded that the group-contribution method of Constantinou and Gani (1994) and Constantinou et al. (1995) is reliable for extrapolation to extended CNs. In this research, therefore, the values from the API technical data book (1997) and those from the group-contribution method are integrated with smooth trends. The accuracy level is kept within the experimental uncertainties for the n-alkanes for which measured values are available. **Table C-1** (Appendix C) tabulates the resulting values for T_C, P_C, and ω for n-alkanes from C_1 through n-C_{100} that are used in this research. Equations C4 through C6 are correlations based on the tabulated values, but not used in the BIP optimization.

For type IIIa binaries, the UCEP predicted by the PR EOS shifts upward along the extension of the three-phase curve in P-T space as the BIP value is increased. This trend is reversed for type IIIb binaries. Because of this type-wise monotonic behavior of three-phase predictions, it is not difficult to find optimum BIP values. The values of $\Delta T_{3\varphi}$, ΔT_{UCEP}, and ΔP_{UCEP} tend to increase with increasing

temperature (and pressure) along a three-phase curve. This is difficult to improve since the adjustment of a single BIP gives little control over the curvature of the three-phase curve for each binary on the basis of the PR EOS. Therefore, not all values of $\Delta T_{3\varphi}$, ΔT_{UCEP}, and ΔP_{UCEP} can be retained within the experimental uncertainties mentioned in Brunner (1990).

Table 2.2 presents the optimized BIPs along with the absolute average deviations (AADs) in $T_{3\varphi}$ and the absolute deviations (ADs) in T_{UCEP} and P_{UCEP} for the 20 binaries considered. For water with n-C_{25} and lighter, the largest AAD in $T_{3\varphi}$ is 2.99 K that occurs for the water/n-C_{11} binary. The largest AD in T_{UCEP} is 4.65 K for the water/n-C_{20} binary. These deviations of temperature predictions correspond to relative errors of lower than 1%. The AD in P_{UCEP} (i.e., ΔP_{UCEP}) is 1.34 bars for the water/n-C_{25} binary, which gives the largest ΔP_{UCEP} among the water/n-alkanes binaries with n-C_{25} and lighter. For water with n-C_{26} and heavier, the UCEP data reported are somewhat dispersed around the overall trend. When these raw data are used in equation 6, the highest ΔP_{UCEP} of 12.70 bars occurs for the water/n-C_{28} binary.

The optimized BIP values for water with n-alkanes CNs from 28 through 36 are constant at 0.242. This is related to the experimental fact that the three-phase curve and x_{wL} approach their asymptotic limits as the n-alkane component becomes heavier as will be presented in section 2.4.

The optimized BIPs for water with n-alkanes are correlated with n-alkane MW by use of the following equation:

$$\text{BIP} = c_1[1 + \exp(c_2 - c_3 \text{MW})]^{-1/c_4}, \qquad (2.7)$$

where c_1 = 0.24200, c_2 = 65.90912, c_3 = 0.18959, and c_4 = -56.81257. The correlation gives the R^2 value of 0.9967 and the standard deviation of 0.0068 against the optimized BIPs. The maximum deviation of 0.021 occurs for 100.20 g/mol (i.e., n-C_7). The correlated values for the BIP for the 20 binaries considered in this work are shown in Table 2.2. The correlation can result in reasonably accurate three-phase predictions when used with the PR EOS.

The PR EOS also exhibits reasonable accuracy for x_{wL} predictions when BIPs from equation 2.7 are used. **Table 2.3** summarizes the AADs in predictions of x_{wL} for the water/n-alkane binaries for which experimentally measured x_{wL} are available.

Figure 2.11 presents x_{wL} predictions along the three-phase curve for the water/n-C_{20} binary, which gives the highest AAD in Table 2.3. The x_{wL} data were taken from Skripka (1979). The UCEP in Skripka (1979) deviates from that in Brunner (1990), based on which the BIP correlation was developed. This is why a measured x_{wL} value exists at a temperature higher than T_{UCEP} from the PR EOS in Figure 2.11. The AAD for x_{wL} is 4.2 mol% with the maximum AD of 7.0 mol% for the water/n-C_{20} binary. The reasonable accuracy in the x_{wL} predictions (Table 2.3) is remarkable considering the simplicity of the PR EOS and the van der Waals mixing rules and that the x_{wL} data have not been considered in the BIP optimization.

To see the sensitivity of phase behavior predictions through the PR EOS with equation 2.7, the water/n-C_8 and water/n-C_{16} binaries are considered. The MW of n-C_8 and n-C_{16} are 114.23 and 226.44 g/mol, respectively. Equation 7 gives a BIP

of 0.527 for water/n-C_8 and 0.363 for water/n-C_{16}. The perturbation of MW by –10% yields a BIP of 0.548 for water/n-C_8 and 0.391 for water/n-C_{16}. The perturbation of MW by +10% yields a BIP of 0.508 for water/n-C_8 and 0.336 for water/n-C_{16}. The UCEP predicted for the water/n-C_8 binary, 535.43 K and 73.42 bars, is shifted by +1.54 K and +1.58 bars through the –10% perturbation, and by –1.33 K and –1.37 bars through the +10% perturbation. The UCEP predicted for the water/n-C_{16} binary, 605.57 K and 150.01 bars is shifted by +12.31 K and +23.71 bars through the –10% perturbation, and by –7.34 K and –13.43 bars through the +10% perturbation.

Figure 2.12 shows three-phase P-T data for water/n-C_{16} (Brunner, 1990) and three predicted curves; one with the BIP from equation 7, and the others with ±10% perturbations in MW with equation 2.7. It is observed that the UCEP is shifted upward as the BIP value becomes larger. **Figure 2.13** presents the V and L phase compositions along the three-phase curves presented in Figure 2.6. These compositional predictions can be compared with the x_{wL} data measured along the three-phase curve for water/n-C_{16} (Skripka, 1979, Shaw et al., 2006b). This figure shows that the x_{wL} at a given T below T_{UCEP} is predicted to be larger as the BIP becomes smaller. Matching the UCEP is necessary to give reasonable predictions of phase compositions along the three-phase curve.

2.3 Validation and application of the BIP correlation

This section presents validation and application of the PR EOS with the BIP correlation developed in the preceding section. Predictions are compared with experimental data for two ternary n-alkane and four quaternary n-alkane systems,

for which limited experimental data are available in the literature. Also, the BIP correlation is applied to represent water solubilities in reservoir oils reported in the literature, such as the Coalinga, Huntington Beach, Cat Canyon, Peace River, and Athabasca oils. This serves as qualitative validation of the correlation when it is extrapolated to higher MW. In this section, equation 7 is applied to calculate BIPs for water with n-alkanes from C_1 through n-C_{100}. BIPs between hydrocarbons are assumed to be zero for simplicity.

2.3.1. Ternary systems

McKetta and Katz (1948) gave tie triangles measured for the water/C_1/n-C_4 ternary at different P-T conditions. **Figure 2.14** compares the prediction with the data at 377.6 K for three different pressures: 44.88, 58.95, and 85.56 bars. In terms of the C_1 concentration, the V phase composition exhibits a deviation of only 6.73 mol%, 6.03 mol%, and 3.47 mol%, respectively. The L phase exhibits a deviation of 0.78 mol%, 1.51 mol%, and 4.55 mol%, respectively.

Peng and Robinson (1976) recommended a BIP of 0.500 for water with C_1 and 0.480 for water with n-C_4 on the basis of two-phase predictions. The tie triangles predicted with BIPs of Peng and Robinson (1976) are nearly the same as that with BIPs from equation 2.7, and are presented in **Figure 2.15**. BIPs recommended by various researchers, including Peng and Robinson (1976), are further discussed in section 2.4.

The tie triangle for the water/n-C_{10}/n-C_{15} ternary was predicted at four different P-T conditions: 394.26 K and 2.12 bars, 422.04 K and 4.89 bars, 505.37 K and

32.50 bars, and 533.15 K and 52.44 bars. The predictions are visualized in **Figure 2.16**. Chawla et al. (1995) reported experimental data for the V phase composition for this system. The measured V-phase composition at the specified conditions is close to the prediction. The distance in composition space between the measured and predicted compositions is calculated as $\delta_j = \left\| \underline{x}_j^{EOS} - \underline{x}_j^{Data} \right\|_2$ for phase j, where $\underline{x}_j$ is the vector consisting concentrations of the three components. For this system, the composition distance (δ_V) computed for the V phase, for the four P-T conditions are 0.0349, 0.0214, 0.0035 and 0.0363, respectively. At 533.15 K and 52.44 bars, the L phase contains 29.27 mol% of water, indicating the potential importance of considering x_{wL} in reservoir studies.

2.3.2. Quaternary systems

Barrufet et al. (1996) presented measured compositions of the V, L, and W phases for a quaternary mixture of 75.97% water, 12.92% C_3, 5.44% n-C_5, and 5.67% n-C_8 at six different P-T conditions. **Table 2.4** summarizes the comparison between the data and predictions from the PR EOS with BIPs from equation 2.7. The deviations from the data are expressed using the composition distance $\delta_j = \left\| \underline{x}_j^{EOS} - \underline{x}_j^{Data} \right\|_2$ for phase j, where $\underline{x}_j$ is the vector consisting concentrations of the four components. The values for δ_L for all cases are lower than 0.1 indicating that the predicted values for the L-phase are reasonably close to the data. The largest deviations from the data were observed at 448 K and 51.50 bars. The corresponding values for δ_L and δ_V at this condition are 0.0916 and 0.1278, respectively.

Chawla et al. (1995) presented the V-phase compositions of three-phase equilibria measured for three different quaternary systems at different P-T conditions. Their approximate compositions were 69% water, 10% n-C_6, 10% n-C_7, and 11% n-C_8; 76% water, 12% n-C_7, 7% n-C_9, and 5% n-C_{12}; and 98% water, 0.2% n-C_{10}, 0.8% n-C_{15}, and 1% n-C_{20}. **Table 2.5** gives comparisons between the data and predictions for these cases. In table 2.5, the aforementioned systems have been labelled as systems 1, 2 and 3, respectively. Water has been assigned an index of 1. The n-alkanes have been assigned indices 2, 3 and 4 in the order of increasing CN. The largest value for δ_V (0.2436) occurs for water/n-C_6/n-C_7/n-C_8 system at 438.71 K and 12.94 bars. The values for δ_V presented in table 2.5 indicate that equation 2.7 can yield reasonably accurate predictions for the V-phase composition for multicomponent systems over a wide range of temperatures, pressures, and CNs.

The highest x_{wL} value calculated in these cases is 0.3285 for the water/n-C_{10}/n-C_{15}/n-C_{20} system at 533.15 K and 49.00 bars. Although there are no experimental data to compare, this value is plausible considering that even higher x_{wL} values have been reported for water-containing oil mixtures at similar temperatures as discussed in the next subsection.

2.3.3. Water-containing reservoir oils

Quantitative validation of the extrapolation of the BIP correlation (equation 2.7) to higher MWs requires experimental data for water with heavy n-alkanes. However, the heaviest n-alkane for which phase behavior data measured with water are available is n-C_{20} (See Table 2.3 for the water/n-C_{20} binary and Table

2.5 for the quaternary containing n-C_{20}). This subsection, therefore, presents qualitative validation of the BIP correlation by use of x_{wL} data reported for water-containing reservoir oils.

Results presented in Griswold and Kasch (1942), Tsonopoulos and Wilson (1983), and Heidman et al. (1985) show that x_{wL} becomes higher with increasing level of aromaticity in the L phase. This is consistent with the discussion of Tsonopoulos and Wilson (1983) that the affinity towards water is lowest for n-alkanes and highest for aromatics. Since reservoir oils contain a variety of hydrocarbon compounds, such as paraffins, naphthenes, and aromatics, the PR EOS with the BIP correlation developed for n-alkanes is expected to yield systematic under-predictions of x_{wL} for water-containing reservoir oils.

The Athabasca bitumen has been characterized by use of the method of Kumar and Okuno (2013) along with experimental data presented in Badamchi-Zadeh et al. (2009). Properties used in the PR EOS model for the water/Athabasca-bitumen mixture are presented in **Table 2.6**. Flash calculations have been performed at the experimental P-T conditions given in Amani et al. (2013). **Table 2.7** shows that the predicted x_{wL} values are systematically lower than the measured values at the conditions considered in Amani et al. (2013). This is expected since the BIP correlation has been developed for water with n-alkanes. The predicted x_{wL} monotonically increases with increasing temperature, which is in line with the reported data.

A similar case study is presented for the Peace River bitumen. The experimental data presented in Mehrotra and Svrcek (1985) are used in the

characterization method of Kumar and Okuno (2013). **Table 2.8** shows properties used in the fluid model for the water/Peace-River-bitumen mixture. In **Table 2.9**, predictions are compared with the x_{wL} data presented in Glandt and Chapman (1995). Glandt and Chapman (1995) presented temperatures for the x_{wL} data points reported, but not the corresponding pressures. It is reasonable to assume that their measurements were made at pressures on the boundary between two and three phases so that the W phase could exist (Chapman 2014[1]). The predicted results given in Table 2.9 are based on this assumption. As expected, the x_{wL} predictions are systematically lower than the measured values.

As presented in section 2.2, the x_{wL} predicted by the PR EOS tends to increase with decreasing BIP at a given three-phase temperature for a given binary. This indicates a possibility that more accurate representation of x_{wL} for water-containing reservoir oils requires a systematic reduction of water/hydrocarbon BIPs from the values given by equation 2.7. The BIPs presented in Tables 2.6 and 2.8 are systematically reduced by the λ factor, which is 0.415 for the water/Athabasca-bitumen system and 0.780 for the water/Peace-River-bitumen system. Tables 2.7 and 2.9 present that the resulting x_{wL} predictions are closer to the measured values than those based on the water/n-alkane BIPs.

The x_{wL} data were also presented in Glandt and Chapman (1995) for three more systems, the Coalinga, Huntington Beach, and Cat Canyon oils. However, it is difficult to use them due to the lack of PVT data required to characterize the oils. Therefore, the MW distributions given in Glandt and Chapman (1995) are used with the assumption that the oils consist of 100% n-alkanes. Table C-1 is

[1] Personal communication with Professor W.G. Chapman, Rice University, Houston, Texas.

used to assign T_C, P_C, and ω for the hydrocarbon components, which are assumed to be n-alkanes. BIPs for water/n-alkanes are taken from Equation 2.7, and the other BIPs are set to zero. Tables 2.10 through 2.12 compare the predicted x_{wL} with experimental data. In spite of the simplistic assumptions made for these three systems, the predicted values are lower than the data, except for four data points for the Coalinga case and a single data point for the Huntington Beach oil.

2.4 Discussion

This section presents various thermodynamic predictions from the PR EOS with BIPs from equation 2.7. They are also compared to predictions with a BIP value 0.500, which is a representative value from the literature.

2.4.1. P-x diagrams

The PR EOS with the BIP values from equation 2.7 is used to construct P-x diagrams for a few water/n-alkane binaries. **Figures 2.17 and 2.18** compare P-x diagrams at 450.00 K for water with n-C_6 and with n-C_8. T_{UCEP} is predicted to be 494.87 K for water/n-C_6 and 536.25 K for water/n-C_8 using equation 2.7. That is, 450.00 K corresponds to T_r of 0.91 for water/n-C_6 and T_r of 0.84 for water/n-C_8. In these figures, the vapor pressure of pure n-alkane is shown as the merging point of the V and L phases at the n-alkane concentration of 1.0. The vapor pressure of pure water is the merging point of the V and W phases at the n-alkane concentration of 0.0. Water is less volatile than n-C_6 at this temperature and more volatile than n-C_8. This results in the V phase at $P_{3\varphi}$ that is richer in water for the water/n-C_8 binary than for the water/n-C_6 binary. However, the x_{wL} at $P_{3\varphi}$ is nearly the same for the two binaries at the temperature (note that $x_{wL} = 1.0 - x_{hcL}$).

The sensitivity of x_{wL} to pressure above $P_{3\varphi}$ is predicted to be very low since the temperature 450 K is sufficiently lower than T_{UCEP}.

Figures 2.19 and 2.20 show P-x diagrams at a higher temperature of 503.00 K for water with n-C_8 and with n-C_{12}. This temperature corresponds to T_r of 0.94 for water/n-C_8 and 0.87 for water/n-C_{12}. Comparison between Figures 2.19 and 2.20 indicates that x_{wL} at $P_{3\varphi}$ is increased at the higher temperature. However, figures 18 and 19 present that x_{wL} at $P_{3\varphi}$ is only weakly sensitive to the n-alkane CN at this temperature. The V phase becomes richer in water as n-alkane becomes less volatile as shown in figures 2.17 through 2.20.

Figure 2.21 shows the P-x diagram for water with n-C_8 at T_r of 0.99 (533.00 K). The x_{wL} at $P_{3\varphi}$ is predicted to be 0.3834 at this temperature. The V-phase composition is close to the L-phase composition, since the V and L phases are merging at the UCEP (i.e., type IIIa). The x_{wL} above $P_{3\varphi}$ becomes sensitive to pressure as T_r is close to unity.

P-x diagrams are also constructed for water with n-C_{30} at two different temperatures; 560.00 K (T_r = 0.87) for **Figure 2.22** and 637 K (T_r = 0.98) for **Figure 2.23.** Due to the proximity of the $P_{3\varphi}$ to the water vapor pressure, the V-W region is nearly invisible in these figures. Thus, the V phase consists of nearly 100% water due to the low volatility of n-C_{30}. However, it is calculated that the V phase at $P_{3\varphi}$ is richer in n-C_{30} at T_r of 0.98 than at T_r of 0.87. The V phase is merging with the W phase at the UCEP (i.e., type IIIb). The x_{wL} at $P_{3\varphi}$ is predicted to be 0.5229 at T_r of 0.87 and 0.8208 at T_r of 0.98. The x_{wL} above $P_{3\varphi}$ is more sensitive to pressure as the UCEP is approached.

2.4.2. Significance of the new BIP correlation

Peng and Robinson (1976) applied their EOS to represent the phase behavior of water/hydrocarbon mixtures using the van der Waals mixing rules. They presented optimized BIPs for water with n-alkanes (C_1 through n-C_6, and n-C_8) in terms of phase compositions in two-phase regions. A constant BIP value of 0.500 was used for water with C_1 and C_2. For the other binary systems considered, a constant value of 0.480 was deemed to be optimum.

The same approach was adopted by Heidman et al. (1985), and Tsonopoulos and Heidman (1986). A BIP value of 0.467 was recommended for water with n-C_8 in Heidman et al. (1985). Tsonopoulos and Heidman (1986) furnished optimum values for BIPs as follows: 0.496 for water with n-C_6, 0.456 for water with n-C_8, and 0.454 for water with n-C_{10}. The optimum BIP value suggested by Nasrifar and Moshfeghian (2002) is 0.508 for water with n-C_6, 0.456 for water with n-C_8, and 0.451 for water with n-C_{10}. They are similar to those of Tsonopoulos and Heidman (1986).

In accordance with Peng and Robinson (1976), Eubank et al. (1994) performed phase equilibrium calculations for water/n-alkane mixtures using a constant BIP value of 0.48 for water with n-alkanes lighter than n-C_{10}. A constant value of 0.46 was used for water with n-C_{10} and heavier. The reason for the suggested BIP value of 0.46 was unclear in their paper. Mohebbinia et al. (2013) employed the van der Waals mixing rules with phase-specific BIPs. For the W phase, the correlation of Søreide and Whitson (1992) was used to obtain the BIPs. For the

non-W phases, BIP values of 0.485 and 0.500 were used for water with C_1 and for water with all other hydrocarbons, respectively. Equation 2.7 gives similar values for water with n-C_6, n-C_8, n-C_9 and n-C_{10} (see Table 2), but a much lower value of 0.242 for water with n-alkanes heavier than n-C_{25}.

We compare thermodynamic predictions by use of a constant BIP of 0.500 and those with equation 2.7 for water binaries with n-C_{12}, n-C_{25}, and n-C_{30}. **Figure 2.24** shows the dimensionless molar Gibbs free energy change on mixing ($\Delta_m\underline{G}/RT$) at 100.00 bars and 571.88 K ($T_r = 0.98$) for water with n-C_{12}. The BIP value 0.437 from equation 2.7 is used in Figure 2.24a, and 0.500 is used in Figure 2.24b. In Figure 2.24a, the three equilibrium phases are shown as tangent points on the Gibbs free energy. The x_{wL} and x_{wV} are 0.5469 and 0.8259, respectively. The W phase consists of nearly 100% water. As the BIP is increased from 0.437 to 0.500 at the same pressure and temperature, the Gibbs free energy systematically shifts upward, resulting in the W-L equilibrium. The right lobe of the Gibbs free energy associated with the L phase keeps the level of convexity as it is displaced upward. Then, the x_{wL} (= 1.0 – x_{hcW}) becomes lower as the BIP is increased since the tangent slope from the W phase onto the L-phase lobe becomes greater. With the BIP of 0.500, temperature must be increased to 573.08 K to predict the three-phase equilibrium at 100.00 bars. The resulting x_{wL} and x_{wV} are 0.4602 and 0.8567, respectively.

The effect of the BIP value on prediction of the three-phase curve is shown in **Figure 2.25** for the water/n-C_{12} binary. As the BIP is increased, the UCEP is extended to higher pressure and temperature. The PR EOS with the BIP value of

0.500 erroneously predicts the UCEP for water with n-C_{12} at 137.48 bars and 594.59 K. Accurate prediction of the UCEP is important since it is the limiting three-phase behavior. **Figure 2.26** compares the x_{wL} and x_{wV} along the three-phase curves by use of the BIP value 0.437 from equation 7 and 0.500. The W phase consists of nearly 100% water, and is not shown in Figure 18. It clearly shows how the over-prediction of the UCEP results in under-prediction of x_{wL} and over-prediction of x_{wV}.

The effect of BIP on the three-phase curve becomes less as the n-alkane component becomes heavier. This is especially true for binaries exhibiting type IIIb as shown in **Figure 2.27** for water with n-C_{30}. The less sensitivity is likely because the W and V phases merge at the UCEP very close to 100% water in composition space. The BIP little affects phase behavior predictions there. However, x_{wL} is still affected significantly by the BIP value used. **Figure 2.28** compares phase compositions along the three-phase curve for water with n-C_{30} with two BIP values; 0.242 from equation 2.7 and 0.5. Although the UCEP temperatures are nearly the same, the x_{wL} predictions are substantially different from each other.

The PR EOS with BIPs for water with n-alkanes from equation 2.7 predicts type IIIa up to n-C_{25} and type IIIb for n-C_{26} and heavier. In Brunner (1990), type IIIa was observed for water/n-alkane binaries up to n-C_{25}, and type IIIb for water/n-C_{28} and heavier. **Figure 2.29** shows that type IIIa is predicted for the water/n-C_{25} binary with the BIP value 0.243 from equation 2.7, but type IIIb is erroneously predicted with the BIP value of 0.500. Since the critical point

between the V and L phases in Figure 2.29a occurs near the coexisting W phase, the V phase merges with the W phase at the UCEP for water with the next n-alkane n-C_{26}. The BIP of 0.500 results in significantly lower x_{wL} than the value from equation 2.7, indicating the importance of accurate representation of three-phase behavior.

Normal eicosane (n-C_{20}) is the heaviest n-alkane for which measured x_{wL} data were reported in the literature. Normal hexatriacontane (n-C_{36}) is the heaviest n-alkane measured in Brunner (1990). **Figure 2.30** presents the asymptotic behavior of x_{wL} predictions for water with four n-alkanes, n-C_8, n-C_{20}, n-C_{32}, and n-C_{100}. The sensitivity of x_{wL} at a fixed temperature (e.g., 450 K, or $1/T = 2.2 \times 10^{-3}$) to the n-alkane CN tends to diminish as the n-alkane component becomes heavier as long as temperature is not close to T_{UCEP}'s. The behavior of x_{wL} near T_{UCEP} for type IIIa is different from that for type IIIb. The former exhibits a somewhat convex shape in Figure 2.30 since the L phase should merge with the V phase, not with the W phase, at the UCEP. This is not the case for type IIIb. Use of equation 2.7 yields a constant BIP of 0.242 for water with n-alkanes heavier than n-C_{25}. If the BIP values are not kept constant for water with heavier n-alkanes, the asymptotic behavior of x_{wL} cannot be predicted due to the effect of BIP on x_{wL} as discussed previously with Figure 2.28.

Figure 2.14 indicated that equation 2.7 may be extrapolated for BIPs for water with C_1 and C_2. Further investigation is made into the application of equation 2.7 for these two binaries. Equation 2.7 gives 0.732 for water with C_1 and 0.698 for water with C_2, while Peng and Robinson (1976) recommended 0.500 for both

binaries. They obtained these values using the experimental measurements of Olds et al. (1942) and Reamer et al. (1943) for the two binaries.

Olds et al. (1942) and Reamer et al. (1943) measured the V-phase composition in equilibrium with the W phase for the water/C_1 and water/C_2 binaries, respectively. Measurements were made for pressures up to 689.48 bars at seven different temperatures 310.93 K, 344.26 K, 377.59 K, 410.93 K, 444.26 K, 477.59 K, and 510.93 K. Only pressures lower than the critical point of water (220.64 bars) are considered for the evaluation because the intended application of equation 2.7 is in the simulation of thermal recovery processes. Thus, the highest pertinent value for the system pressure used in this assessment is 206.84 bars. The evaluation for the water/C_1 and water/C_2 binaries considers 65 and 66 data points, respectively.

The AADs for the predicted x_{wV} with equation 2.7 are 0.0064 for water/C_1 and 0.0086 for water/C_2. For both binaries, the maximum deviation in x_{wV} (0.0306 for water/C_1, 0.0451 for water/C_2) occurs at 510.93 K and 206.84 bars. Olds et al. (1942) stated that the uncertainty associated with their composition measurements is about 2%. Over the considered set of 65 points, the average uncertainty in x_{wV} measurements is approximately 0.0023. Reamer et al. (1943) did not specify uncertainty values for their composition measurements. The BIP values recommended by Peng and Robinson (1976) result in similar AADs for the same set of data; 0.0013 for water/C_1 and 0.0032 for water/C_2. Given these results, it is reasonable to conclude that equation 2.7 can be extrapolated for BIPs for water with C_1 and C_2.

2.4.3. Hydrocarbon solubilities in the aqueous phase

The BIP correlation given in equation 2.7 was developed for reliable predictions of three-phase behavior and x_{wL} for water with n-alkanes. This subsection shows x_{hcW} predicted by the PR EOS with the BIP values from equation 2.7.

Figure 2.31 compares the predictions and data for x_{hcW} for the water/n-C_3 and water/n-C_8 binaries. Although the predicted trends agree qualitatively with the data, the predicted values are orders of magnitude lower than the data. Equation 2.7 is not recommended for applications in which quantitative predictions of x_{hcW} are important. Considering the small values predicted for x_{hcW}, Henry's law would be appropriate for reservoir engineering applications (Li and Nghiem, 1986; Luo and Barrufet, 2005).

2.5 Summary and conclusions

This chapter presented a new characterization framework for water/reservoir oil mixtures by use of the Peng-Robinson equation of state (PR EOS) with the van der Waals mixing rules. The proposed framework is capable of reasonably accurate representation of multiphase compositional behavior of water-containing reservoir oils. A new correlation was developed for binary interaction parameters (BIPs) for water with n-alkanes. The development used the three-phase curves, including upper critical endpoints (UCEPs), measured in pressure-temperature (P-T) space for water with n-alkanes by Brunner (1990). Phase behavior predictions from the PR EOS with the new BIP correlation were compared with experimental

data available in the literature, such as the solubilities of water in the oleic (L) phase (x_{wL}). The conclusions of this chapter are as follows:

1. The PR EOS with the BIP values from the new correlation can accurately represent three-phase curves measured by Brunner (1990) for water with n-alkanes up to n-C_{36}. Type IIIa is predicted for water with n-alkanes up to n-C_{25}, and type IIIb for water with n-C_{26} and heavier. This transition between types IIIa and IIIb is plausible. Although the phase behavior classification was not clear for water with n-C_{26} and n-C_{27} in Brunner's experiments, he observed type IIIa for water with n-alkanes up to n-C_{25} and type IIIb for water with n-C_{28} and heavier.

2. The PR EOS with the new BIP correlation yields reasonable predictions of x_{wL} for water with n-alkanes up to n-C_{20}, for which limited experimental data are available in the literature. The BIP correlation was also applied to represent x_{wL} measured for water-containing reservoir oils. Reservoir oil consists of various types of hydrocarbons, such as paraffins, naphthenes, and aromatics. Also, the affinity towards water is lowest for n-alkanes and highest for aromatics. That is, application of the BIP correlation gives a systematic underprediction of x_{wL} when applied to water-containing reservoir oils. This was confirmed by use of EOS fluid models developed for the Athabasca and Peace River bitumens with the detailed PVT data available in the literature. Accurate x_{wL} predictions for these bitumens were then obtained by systematically reducing the BIP values from the correlation. This indicates that the correlation may serve as the upper limit of BIPs for water with pseudo

components that are required for characterizing water-containing reservoir fluids.

3. The PR EOS with the new BIP correlation reproduces the asymptotic behavior experimentally observed for three-phase curves and x_{wL} for water with heavy n-alkanes. As n-alkane becomes heavier, the three-phase curve approaches a certain asymptotic limit near the water vapor pressure curve. The x_{wL} exhibits a limiting trend line in temperature that is nearly independent of the n-alkane CN as long as temperature is not close to the UCEP temperature. A constant BIP of 0.242 is required for water with n-C_{26} and heavier when used with the PR EOS.

4. The solubilities of n-alkanes in the aqueous phase (x_{hcW}) are predicted to be orders of magnitude lower than experimental data reported in the literature. The proposed framework is not recommended for applications in which the quantitative accuracy of x_{hcW} is important.

Table 2.1. Comparison of three-phase pressures estimated from equation 2.1 with those from experimental studies

CN	T, K	P, bar (Data)	P, bar (Eq. 1)	x_{wV} (Data)	x_{wV} (Eq.1)
6	423.15	12.55	12.27	—	—
6	473.15	35.16	33.54	—	—
8	423.40	6.74	6.71	0.7360	0.7146
8	479.50	25.10	23.93	0.7040	0.7408
10	424.65	5.31	5.51	—	—
10	475.15	17.79	18.17	—	—

Table 2.2. Optimized and resulting deviations of three-phase curve predictions, and correlated BIP values

CN	MW	BIP	Number of	AAD in $T_{3\phi}$	UCEP (Optimized BIP)		AD in UCEP		BIP
	g/mol	(Optimized)	data points	K	T_{UCEP}, K	P_{UCEP}, bar	T_{UCEP}, K	P_{UCEP}, bar	(Correlation)
3	44.10	0.666	4	0.32	369.39	43.26	0.31	0.66	0.666
4	58.12	0.636	9	0.86	422.65	42.36	1.45	0.24	0.636
5	72.15	0.630	7	0.86	463.11	45.91	0.69	0.14	0.607
6	86.18	0.555	6	1.93	492.71	52.52	3.69	0.30	0.579
7	100.20	0.548	8	1.12	516.87	62.64	3.13	0.56	0.553
8	114.23	0.530	7	2.49	535.64	73.63	4.36	0.47	0.527
9	128.26	0.509	11	1.53	550.98	85.26	3.02	0.14	0.503
10	142.28	0.487	5	2.50	563.21	96.31	4.39	0.24	0.480
11	156.31	0.466	13	2.99	573.68	107.28	4.12	0.22	0.458
12	170.34	0.442	12	2.51	581.53	116.31	3.27	0.29	0.437
14	198.39	0.400	13	2.51	594.95	133.74	3.75	0.36	0.398
16	226.44	0.362	11	2.43	605.23	149.38	3.07	0.68	0.363
18	254.50	0.329	12	2.64	612.31	160.51	4.19	0.19	0.330
20	282.55	0.300	11	2.66	618.05	169.86	4.65	0.94	0.301
24	338.66	0.253	8	1.66	630.84	193.21	1.86	0.79	0.250
25	352.68	0.243	15	2.47	636.29	203.54	0.11	1.34	0.243
28	394.76	0.242	10	1.14	649.59	227.10	8.39	12.70	0.242
30	422.82	0.242	13	0.64	647.49	221.80	5.89	8.30	0.242
32	450.87	0.242	10	0.95	647.07	220.68	4.97	8.68	0.242
36	506.98	0.242	8	0.92	647.06	220.60	4.66	5.70	0.242

Table 2.3. Deviations of predicted water solubilities in the L phase (x_{wL}) for a few different water/n-alkane binaries

CN	Number of data points	AAD in x_{wL}	Data sources	Average uncertainty in x_{wL} data
3	9	0.003	Kobayashi and Katz (1953)	0.001
4	7	0.003	Reamer et al. (1944)	0.005
6	6	0.022	Skripka (1979), Tsonopoulos and Wilson (1983), Maczynski et al. (2005)	0.027
7	4	0.008	Skripka (1979)	0.055
8	5	0.018	Skripka (1979), Heidman et al. (1985), Shaw et al. (2005)	0.066
9	5	0.026	Skripka (1979)	0.098
10	6	0.009	Skripka (1979), Shaw et al. (2006a)	0.101
12	3	0.022	Skripka (1979)	0.139
16	5	0.022	Skripka (1979), Shaw et al. (2006b)	0.113
20	6	0.042	Skripka (1979)	0.170

Table 2.4. Deviations of predicted three-phase compositions for a mixture of 75.97% water, 12.92% C_3, 5.44% n-C_5, and 5.67% n-C_8. The deviations are expressed as distances (δ) in composition space.

Case	T, K	P, bar	δ_V	δ_L	δ_W
1	313.00	7.00	0.01140	0.02102	0.00087
2	338.00	11.76	0.01768	0.03595	0.00003
3	373.00	20.34	0.08276	0.03395	0.00027
4	393.00	26.33	0.09204	0.03330	0.00032
5	423.00	39.30	0.07134	0.05695	0.00130
6	448.00	51.50	0.12779	0.09156	0.00318

Table 2.5. Deviations of predicted V-phase compositions for quaternary mixtures presented in Chawla et al. (1995). Systems 1 through 3 have been specified above.

System	T	P	x_{iV} (EOS)				x_{iV} (Data)				δ_V
number	K	bar	i = 1	i = 2	i = 3	i = 4	i = 1	i = 2	i = 3	i = 4	
1	399.82	4.53	0.5178	0.1987	0.1618	0.1217	0.4800	0.2700	0.1500	0.1000	0.0844
1	416.48	6.87	0.5589	0.1484	0.1475	0.1452	0.4900	0.2500	0.1700	0.0900	0.1365
1	438.71	12.94	0.5280	0.2184	0.1504	0.1032	0.3200	0.3000	0.2400	0.1400	0.2436
1	455.37	19.00	0.5300	0.2181	0.1484	0.1035	0.5700	0.1800	0.1400	0.1100	0.0562
1	472.04	26.80	0.5346	0.2001	0.1504	0.1149	0.4500	0.2300	0.1700	0.1500	0.0983
1	488.71	36.59	0.5380	0.1682	0.1534	0.1404	0.6500	0.1300	0.1000	0.1200	0.1314
1	510.93	52.86	0.5566	0.1406	0.1465	0.1563	0.6000	0.1300	0.1300	0.1400	0.0503
2	404.82	3.50	0.7939	0.1349	0.0587	0.0125	0.8000	0.1500	0.0480	0.0020	0.0221
2	416.48	5.70	0.6821	0.2610	0.0504	0.0065	0.7500	0.1750	0.0600	0.0150	0.1103
2	438.71	10.00	0.7026	0.2337	0.0549	0.0089	0.7800	0.1500	0.0650	0.0050	0.1145
2	455.37	14.90	0.7020	0.2311	0.0563	0.0105	0.7300	0.1800	0.0700	0.0200	0.0606
2	472.04	21.30	0.7085	0.2172	0.0608	0.0135	0.7700	0.1400	0.0600	0.0300	0.1001
2	488.71	29.90	0.7058	0.2115	0.0655	0.0172	0.7500	0.1500	0.0800	0.0200	0.0772
2	510.93	42.93	0.7473	0.1453	0.0735	0.0339	0.7000	0.1700	0.1200	0.0100	0.0747
2	527.59	56.24	0.7565	0.1188	0.0735	0.0511	0.7700	0.1100	0.0800	0.0400	0.0206
3	394.26	2.00	0.9971	0.0014	0.0014	0.0001	0.9600	0.0300	0.0009	0.0091	0.0477
3	422.04	4.50	0.9962	0.0015	0.0022	0.0002	0.9450	0.0500	0.0010	0.0040	0.0706
3	449.82	9.40	0.9872	0.0086	0.0037	0.0004	0.9450	0.0540	0.0009	0.0001	0.0621
3	477.59	17.40	0.9872	0.0063	0.0055	0.0010	0.9400	0.0580	0.0019	0.0001	0.0701
3	505.37	30.00	0.9840	0.0058	0.0080	0.0022	0.9350	0.0590	0.0030	0.0030	0.0725
3	533.15	49.00	0.9755	0.0079	0.0120	0.0046	0.9350	0.0590	0.0030	0.0030	0.0658

Table 2.6. Properties of the Athabasca bitumen containing water. BIPs with water are based on equation 2.7. Data given in Badamchi-Zadeh et al. (2009) were used to characterize PC1, PC2, PC3, and PC4.

Component	z_i	MW, g/mol	T_C, K	P_C, bar	ω	BIP with water
Water	0.8115	18.01	647.10	220.64	0.3433	0.000
PC1	0.0754	345.52	1024.88	17.54	0.8503	0.246
PC2	0.0493	528.46	1137.29	13.35	1.0564	0.242
PC3	0.0376	692.98	1207.42	11.20	1.1782	0.242
PC4	0.0262	996.26	1292.51	8.78	1.3301	0.242

Table 2.7. Water solubilities predicted near the V-L-W/L-W boundary for the water/Athabasca-bitumen mixture given in Table 2.7. Experimental data were taken from Amani et al. (2013). The water concentrations for the V and W phases were predicted to be greater than 0.999. A stable single phase is indicated by "–".

P, bar	T, K	x_{wL} (Data)	x_{wL} (EOS, λ = 1)	x_{wL} (EOS, λ = 0.415)
60.42	548.20	0.5412	0.3402	0.5446
87.18	573.10	0.6321	0.4116	0.6386
100.25	583.20	0.6699	0.4406	0.6770
114.50	593.10	0.7192	0.4687	0.7157
131.00	603.50	0.7477	0.4969	0.7546
148.30	613.40	0.7964	0.5222	0.7924
167.20	623.20	0.8274	0.5451	—
189.90	633.80	0.8462	0.5670	—
216.47	644.00	0.8620	0.5854	—

Table 2.8. Properties of the Peace River bitumen containing water. BIPs with water are based on equation 2.7. Data given in Mehrotra and Svrcek (1985) were used to characterize PC1, PC2, PC3, and PC4.

Component	z_i	MW, g/mol	T_C, K	P_C, bar	ω	BIP with water
Water	0.7300	18.01	647.10	220.64	0.3433	0.000
PC1	0.0961	330.22	773.64	15.08	0.7907	0.257
PC2	0.0650	505.04	836.99	11.48	0.9932	0.242
PC3	0.0485	662.27	870.20	9.57	1.1151	0.242
PC4	0.0604	952.11	902.17	7.41	1.2654	0.242

Table 2.9. Water solubilities predicted near the V-L-W/L-W boundary for the water/Peace-River-bitumen mixture given in Table 2.8. Experimental data were taken from Glandt and Chapman (1995). The water concentrations for the V and W phases were predicted to be greater than 0.99.

P, bar	T, K	x_{wL} (Data)	x_{wL} (EOS, λ = 1)	x_{wL} (EOS, λ = 0.78)
9.94	452.65	0.1800	0.1235	0.1497
15.35	472.15	0.2800	0.1670	0.1993
24.41	495.15	0.3200	0.2302	0.2703
33.43	512.15	0.3600	0.2854	0.3315
46.74	531.65	0.3700	0.3577	0.4110
69.94	557.15	0.5300	0.4663	0.5299

Table 2.10. Water solubilities predicted near the V-L-W/L-W boundary for the mixture of 77 mol% water and 23 mol% Coalinga oil. The oil has been assumed to be n-alkanes due to the lack of pertinent PVT data. Experimental data were taken from Glandt and Chapman (1995).

P, bar	T, K	x_{wL} (EOS)	x_{wV} (EOS)	x_{wW} (EOS)	x_{wL} (Data)
10.09	453.15	0.1252	0.9966	> 0.9999	0.0900
15.74	473.15	0.1739	0.9957	> 0.9999	0.1800
23.59	493.15	0.2341	0.9948	> 0.9999	0.2300
34.18	513.15	0.3053	0.9936	> 0.9999	0.2800
48.11	533.15	0.3866	0.9920	> 0.9999	0.3500
71.25	558.15	0.4984	0.9887	> 0.9999	0.5300

Table 2.11. Water solubilities predicted near the V-L-W/L-W boundary for the mixture of 74 mol% water and 26 mol% Huntington Beach oil. The oil has been assumed to be n-alkanes due to the lack of pertinent PVT data. Experimental data were taken from Glandt and Chapman (1995).

P, bar	T, K	x_{wL} (EOS)	x_{wV} (EOS)	x_{wW} (EOS)	x_{wL} (Data)
10.39	453.15	0.1202	0.9687	> 0.9999	0.1800
16.32	473.55	0.1689	0.9696	> 0.9999	0.1950
24.59	493.85	0.2287	0.9696	> 0.9999	0.2700
35.14	513.15	0.2961	0.9693	> 0.9999	0.3100
48.90	532.45	0.3729	0.9689	> 0.9999	0.3700
77.20	561.65	0.5007	0.9673	> 0.9999	0.5300

Table 2.12. Water solubilities predicted near the V-L-W/L-W boundary for the mixture of 71 mol% water and 29 mol% Cat Canyon oil. The oil has been assumed to be n-alkanes due to the lack of pertinent PVT data. Experimental data were taken from Glandt and Chapman (1995).

P, bar	T, K	x_{wL} (EOS)	x_{wV} (EOS)	x_{wW} (EOS)	x_{wL} (Data)
6.34	434.15	0.9955	0.0895	> 0.9999	0.1700
10.59	455.15	0.9946	0.1312	> 0.9999	0.1900
15.61	472.65	0.9936	0.1747	> 0.9999	0.2800
24.02	493.95	0.9922	0.2385	> 0.9999	0.3200
36.11	512.75	0.9912	0.3191	> 0.9999	0.4500
52.13	532.65	0.9893	0.4057	> 0.9999	0.5400
78.06	562.65	0.9846	0.5059	> 0.9999	0.6100

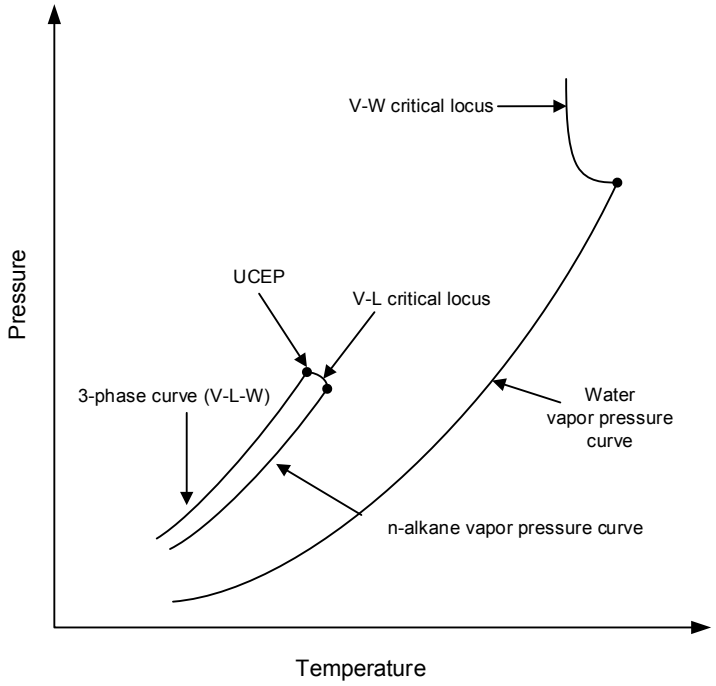

Figure 2.1a. Schematic for the P-T projection for type IIIa in which the n-alkane component is more volatile than water (e.g., water/n-C_4).

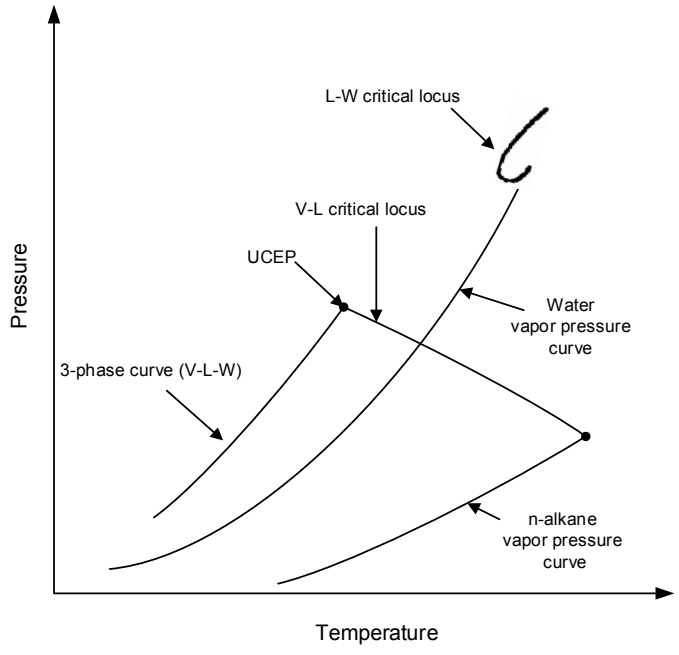

Figure 2.1b. Schematic for the P-T projection for type IIIa in which the n-alkane component is less volatile than water (e.g., water/n-C_{12}).

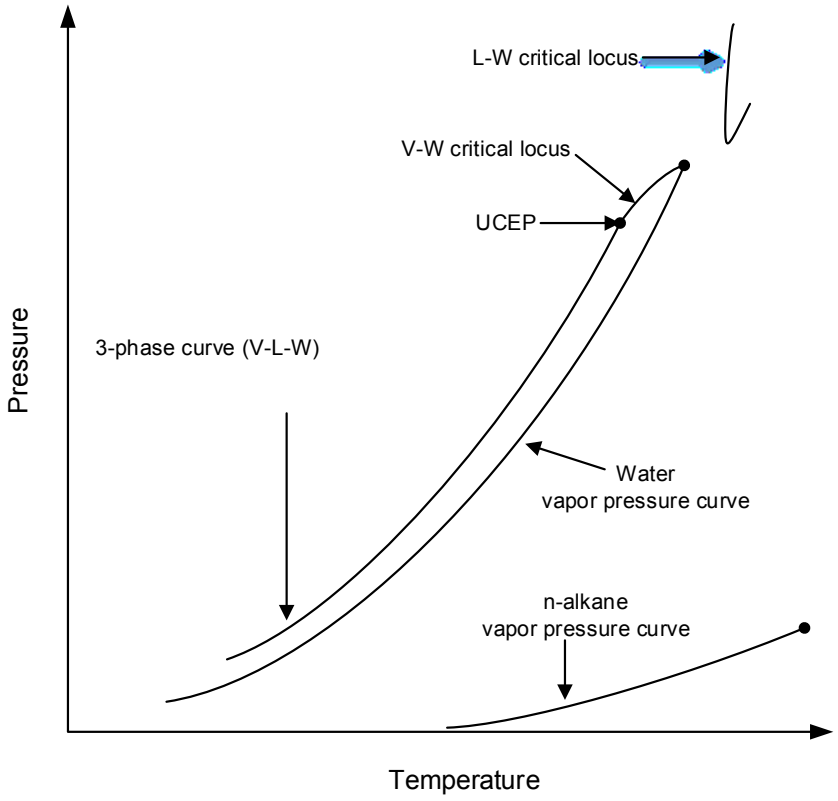

Figure 2.2. Schematic for the P-T projection for type IIIb (e.g., water/n-C_{28}).

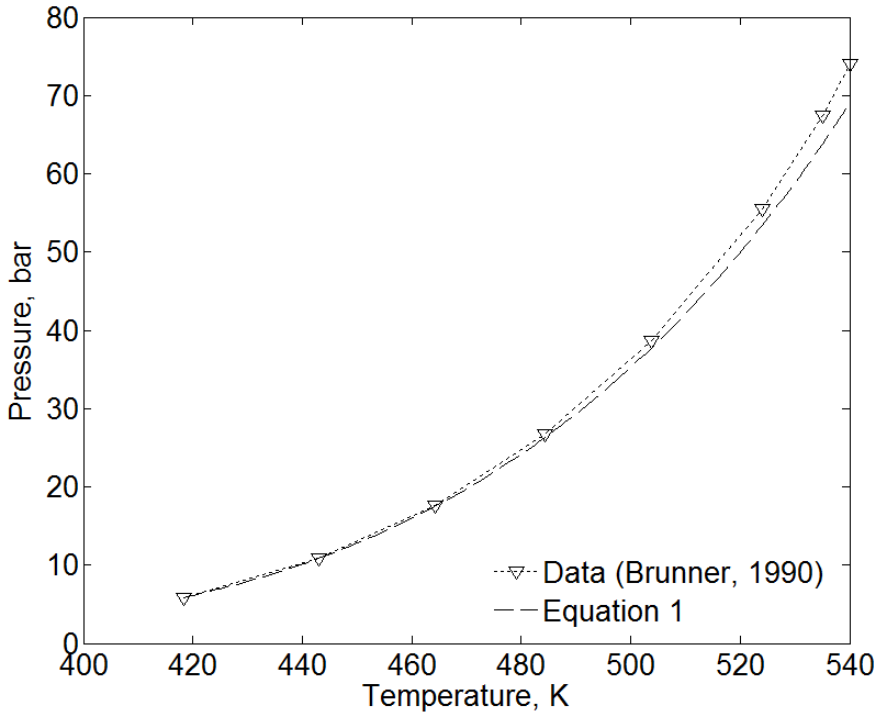

Figure 2.3a. Comparison of three-phase pressures calculated by equation 2.1 with experimental data (Brunner 1990) for the water/n-C_8 binary. The vapor pressure of the n-alkane component was calculated using the Wagner correlation with coefficients computed by McGarry (1983). The vapor pressure of water was calculated using the correlation of Wagner and Pruß (2002).

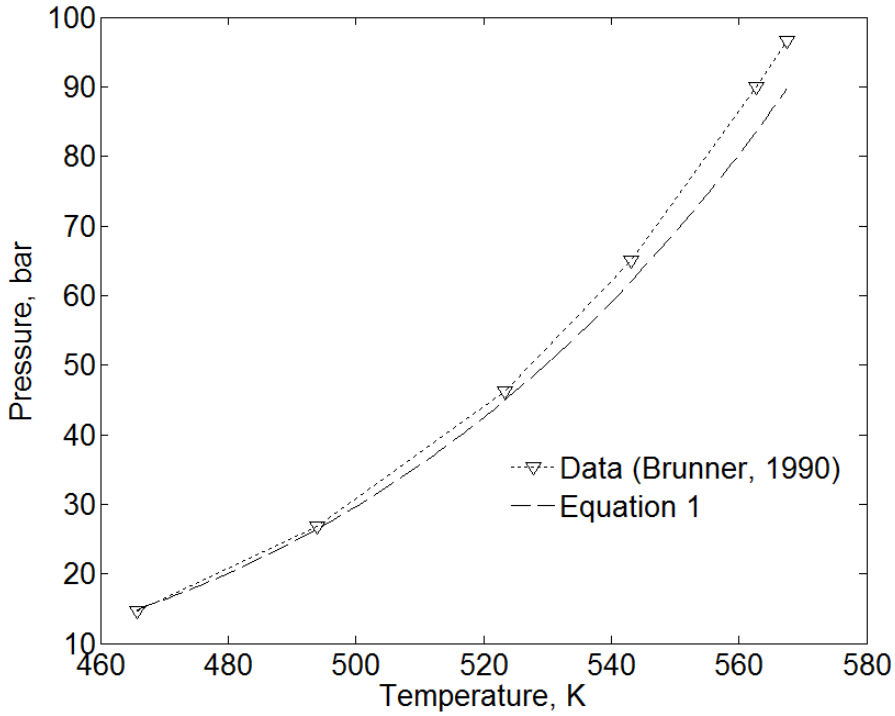

Figure 2.3b. Comparison of three-phase pressures calculated by equation 2.1 and experimental data (Brunner 1990) for the water/n-C_{10} binary. The vapor pressure of the n-alkane component was calculated using the Wagner correlation with coefficients computed by McGarry (1983). The vapor pressure of water was calculated using the correlation of Wagner and Pruß (2002).

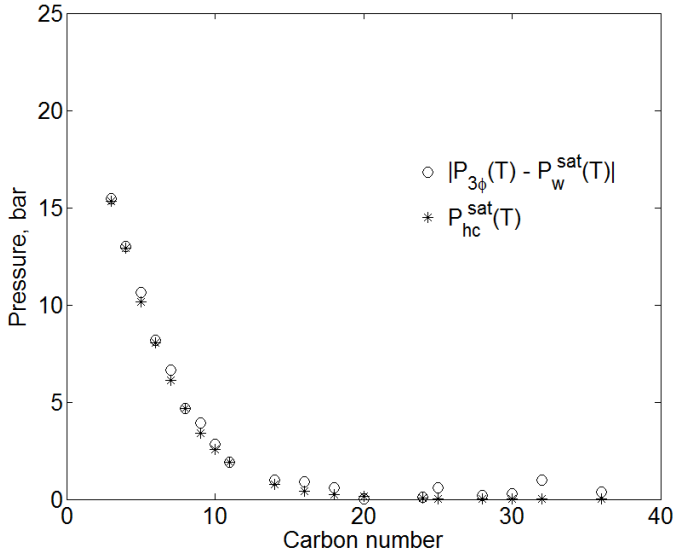

Figure 2.4a. Asymptotic approach of binary three-phase curves to the vapor pressure curve of water. The normalized temperature (T_r) value of 0.86 was used for each binary.

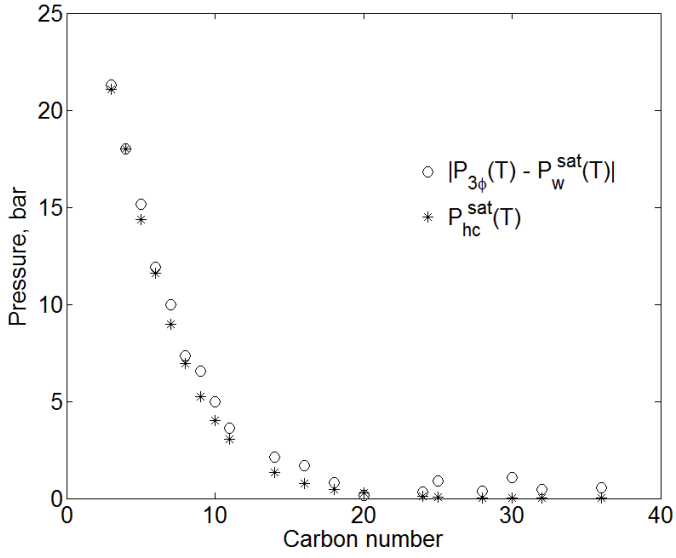

Figure 2.4b. Asymptotic approach of binary three-phase curves to the vapor pressure curve of water. The normalized temperature (T_r) value of 0.90 was used for each binary.

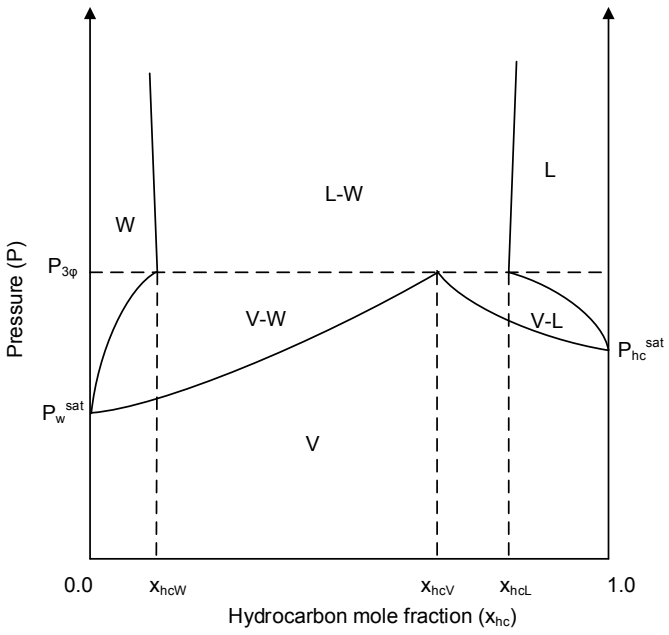

Figure 2.5a. Schematic for the P-x cross-section at T below T_{UCEP} for a type IIIa binary in which water is less volatile than the n-alkane component (e.g., water/n-C_4).

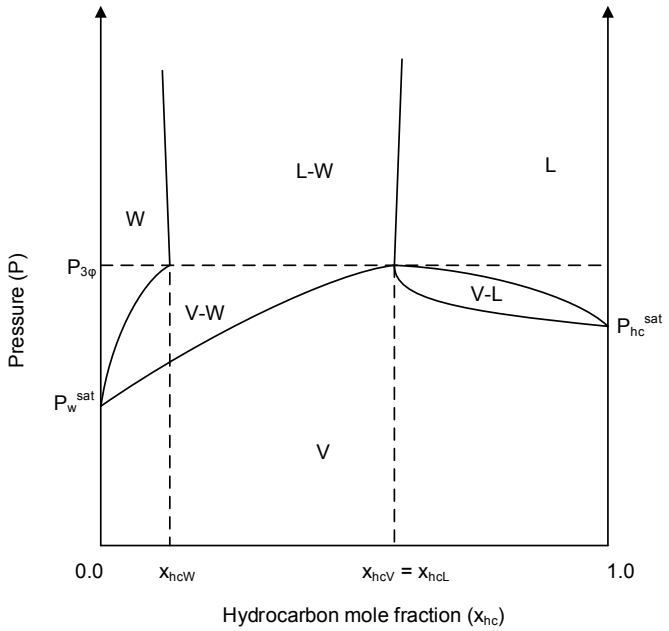

Figure 2.5b. Schematic for the P-x cross-section at T_{UCEP} for a type IIIa binary in which water is less volatile than the n-alkane component (e.g., water/n-C_4).

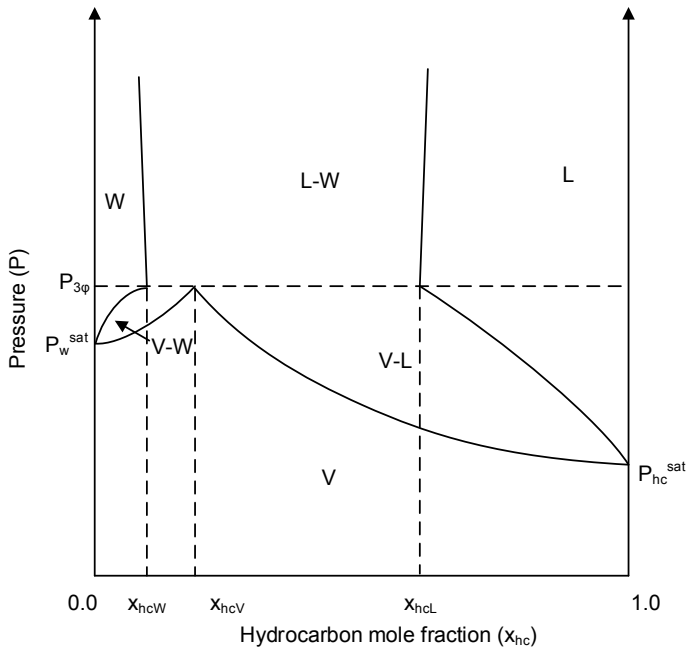

Figure 2.6a. Schematic for the P-x cross-section at T below T_{UCEP} for a type IIIb binary (e.g., water/n-C_{28}).

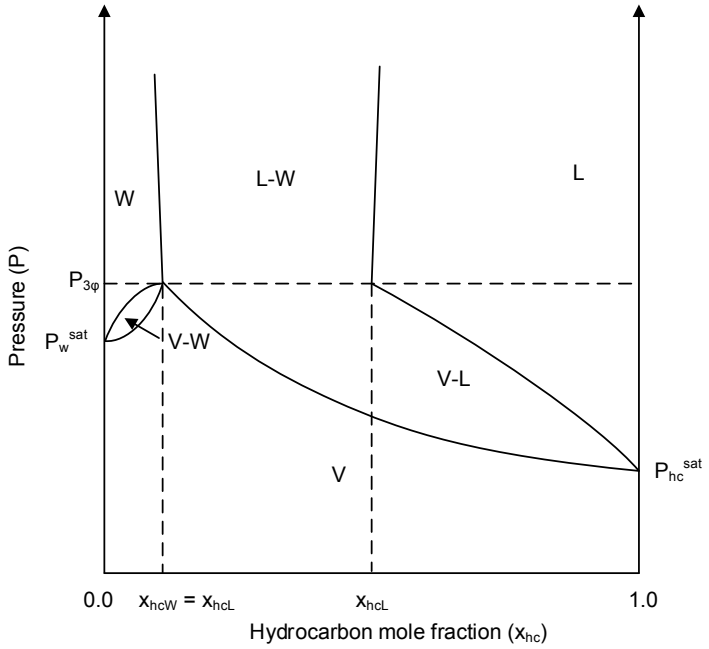

Figure 2.6b. Schematic for the P-x cross-section at T_{UCEP} for a type IIIb binary (e.g., water/n-C_{28}).

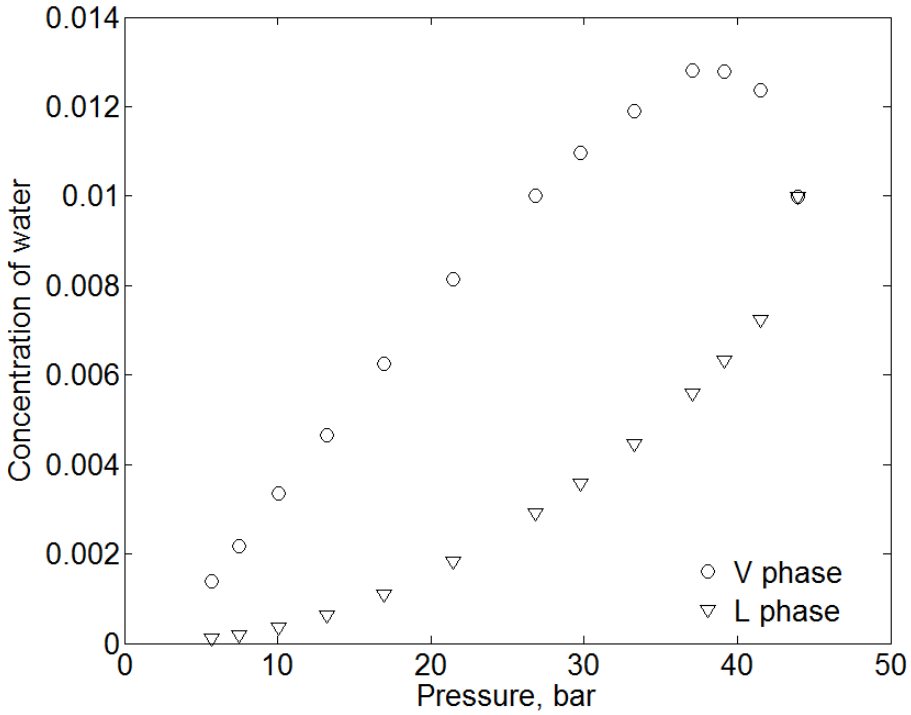

Figure 2.7. Compositions of the V and L phases along the three-phase curve for water/C_3 system (Kobayashi and Katz, 1953).

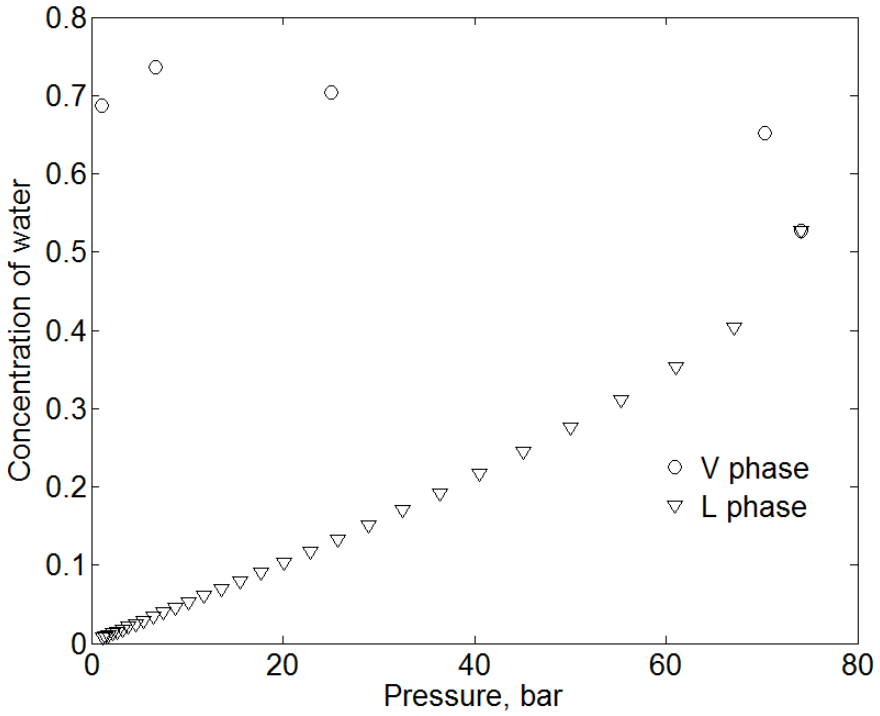

Figure 2.8. Compositions of the for V and L phases along three-phase line for water/nC_8 system (Heidman et al., 1985). The solubility values in the L phase (x_{wL}) were generated using the solubility correlation in conjunction with the three-phase pressure correlation developed by the authors from regression of the experimental data. For the V phase, no correlation was developed.

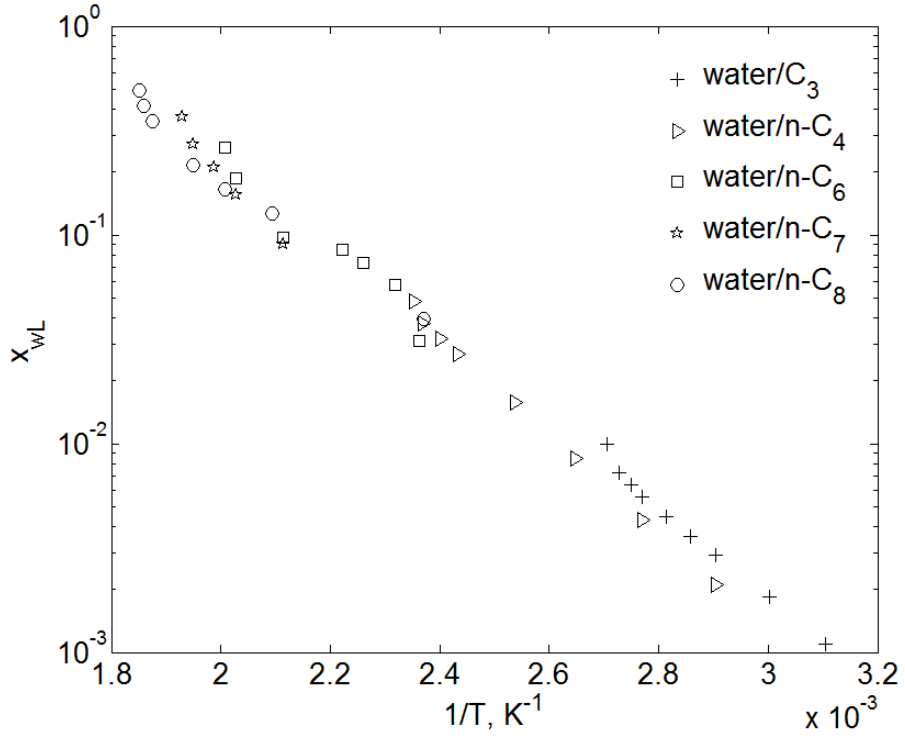

Figure 2.9. L-phase compositions measured along the three-phase curves for different binaries. Data sources are as follows: Kobayashi and Katz (1953) for water/C_3; Reamer et al. (1944) for water/n-C_4; Skripka (1979), Tsonopoulos and Wilson (1983), and Maczynski et al. (2005) for water/n-C_6; Skripka (1979) for water/n-C_7, and Skripka (1979), Heidman et al. (1985), and Shaw et al. (2005) for water/n-C_8.

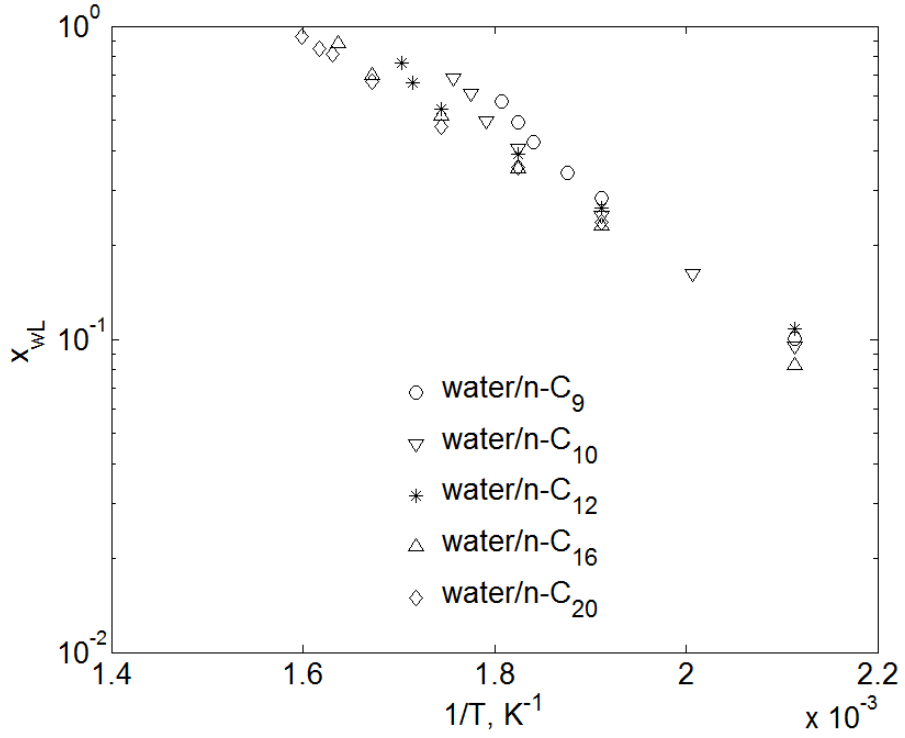

Figure 2.10. L-phase compositions measured along the three-phase curves for different binaries. Data sources are as follows: Skripka (1979) for water/n-C_9, water/n-C_{12}, and water/n-C_{20}; Skripka (1979) and Shaw et al. (2006a) for water/n-C_{10}, and Skripka (1979) and Shaw et al. (2006b) for water/n-C_{16}.

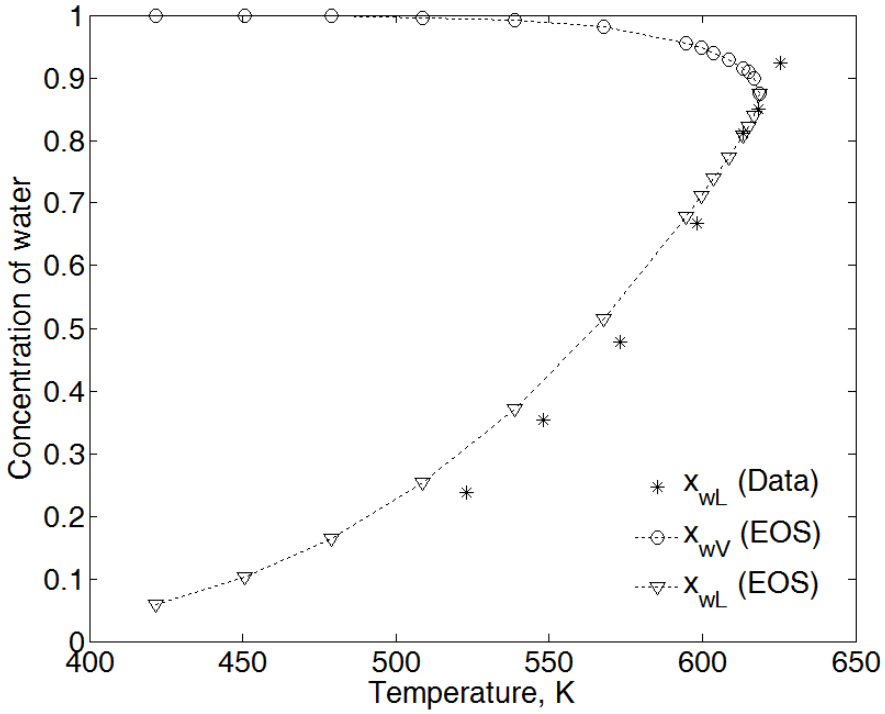

Figure 2.11. Non-aqueous phase compositions predicted by the PR EOS with the BIP correlation (equation 2.7), and solubilities of water in the L phase (x_{wL}) measured along the three-phase curve of water/n-C_{20} system (Skripka, 1979).

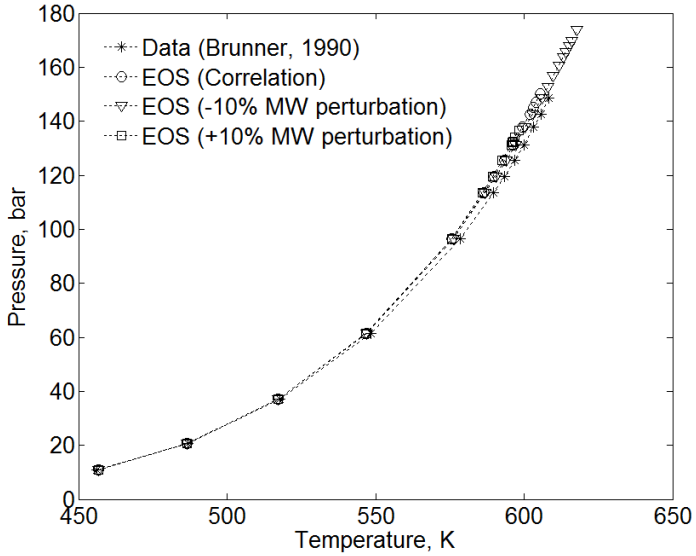

Figure 2.12. Effect of molecular-weight (MW) perturbation in equation 2.7 on the three-phase curve predicted for the water/n-C_{16} binary.

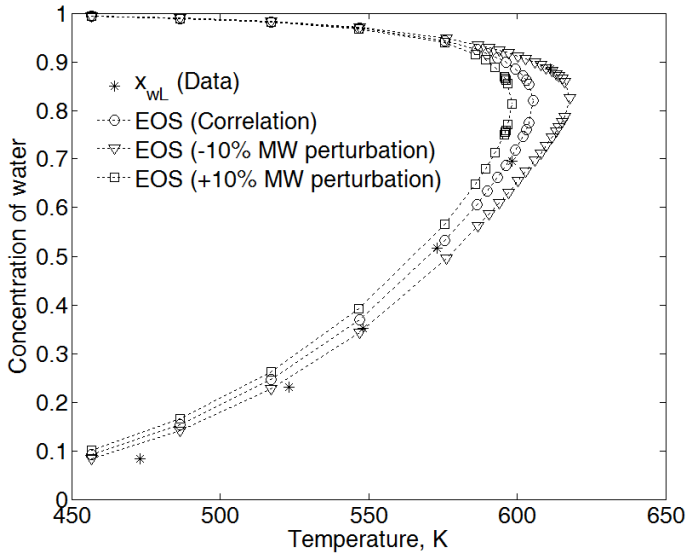

Figure 2.13. Effect of MW perturbation in equation 2.7 on the V- and L-phase compositions predicted along the three-phase curve for the water/n-C_{16} binary. The L-phase composition data were taken from Skripka (1979) and Shaw et al. (2006b).

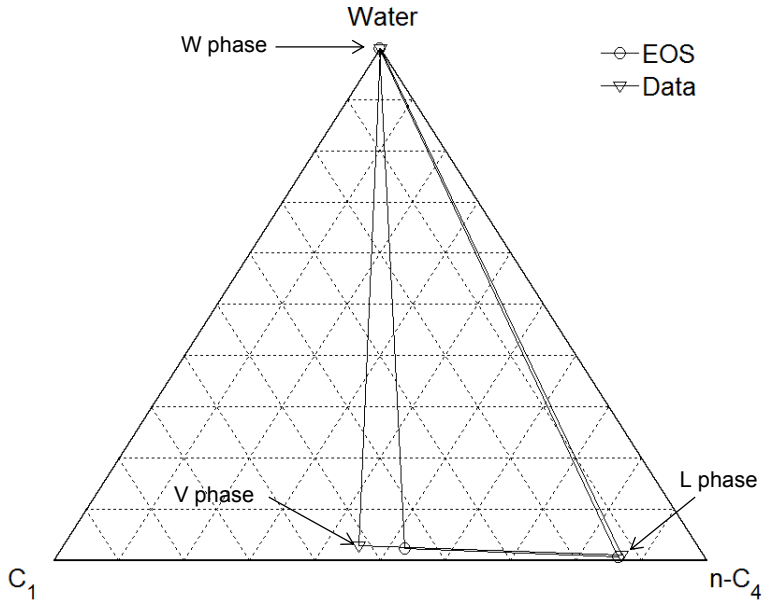

Figure 2.14a. Tie triangle predicted by the PR EOS with the BIP correlation (equation 2.7) for the water/C_1/n-C_4 system at 377.60 K and 44.88 bar. The phase compositions measured by McKetta and Katz (1948) are also shown.

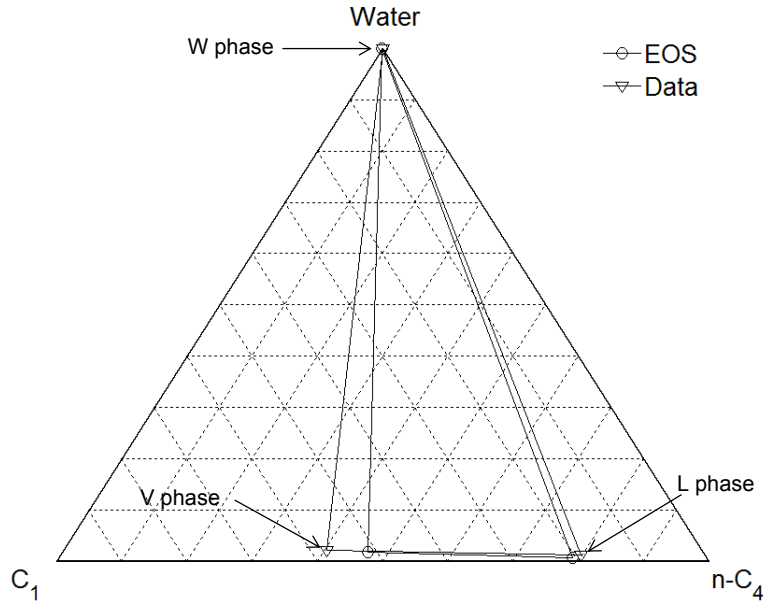

Figure 2.14b. Tie triangle predicted by the PR EOS with the BIP correlation (equation 2.7) for the water/C_1/n-C_4 system at 377.60 K and 58.95 bar.

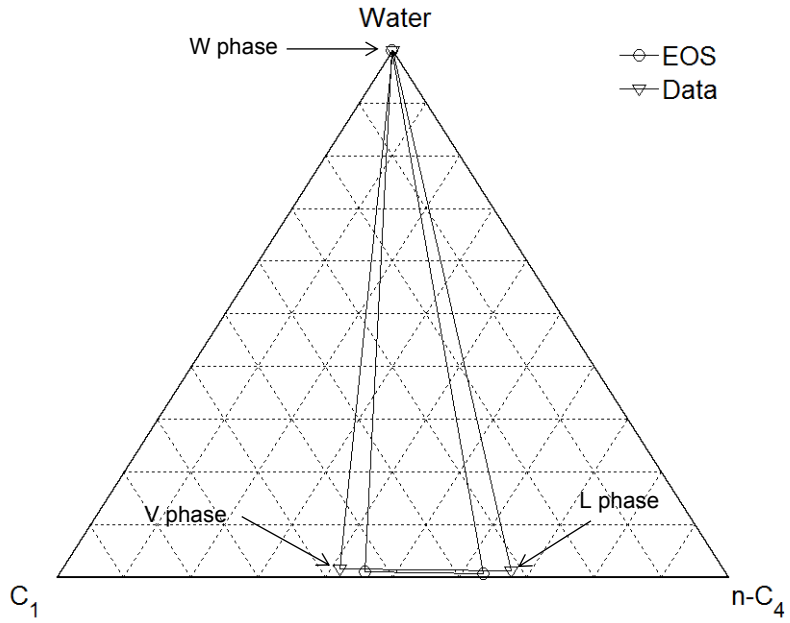

Figure 2.14c. Tie triangle predicted by the PR EOS with the BIP correlation (equation 2.7) for the water/C_1/n-C_4 system at 377.60 K and 85.56 bar.

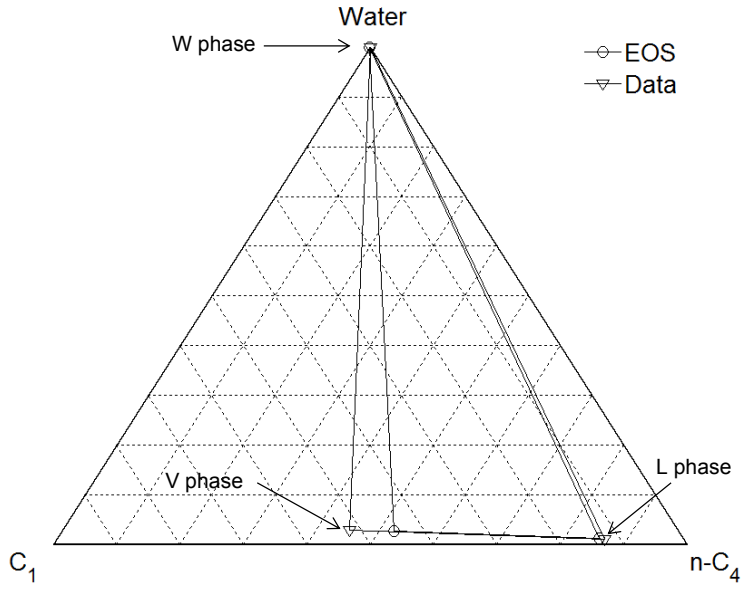

Figure 2.15a. Tie triangle predicted by the PR EOS with BIPs recommended by Peng and Robinson (1976) for the water/C_1/n-C_4 system at 377.60 K and 44.88 bar.

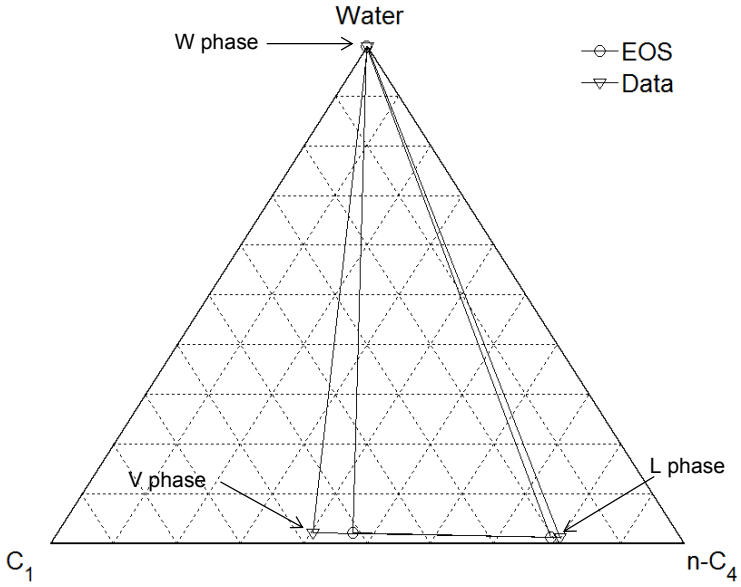

Figure 2.15b. Tie triangle predicted by the PR EOS with the BIPs of Peng and Robinson (1976) for the water/C_1/n-C_4 system at 377.60 K and 58.95 bar.

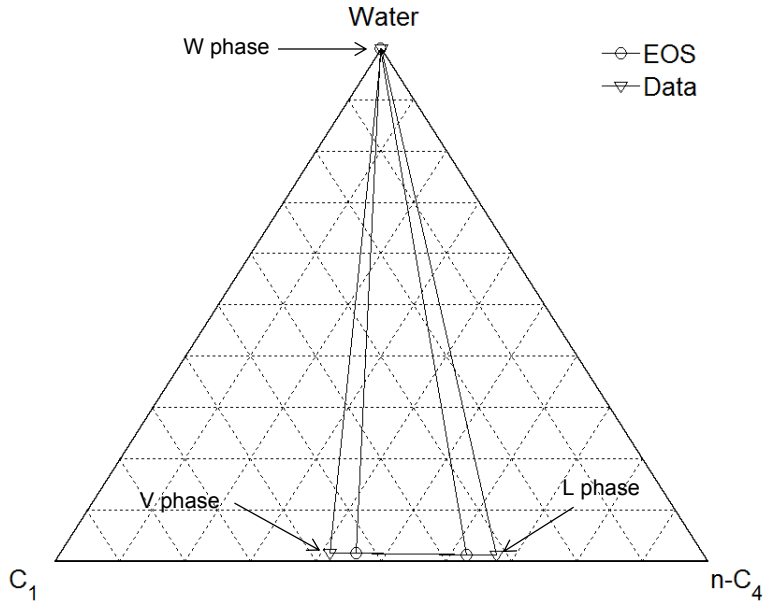

Figure 2.15c. Tie triangle predicted by the PR EOS with the BIPs of Peng and Robinson (1976) for the water/C_1/n-C_4 system at 377.60 K and 85.56 bar.

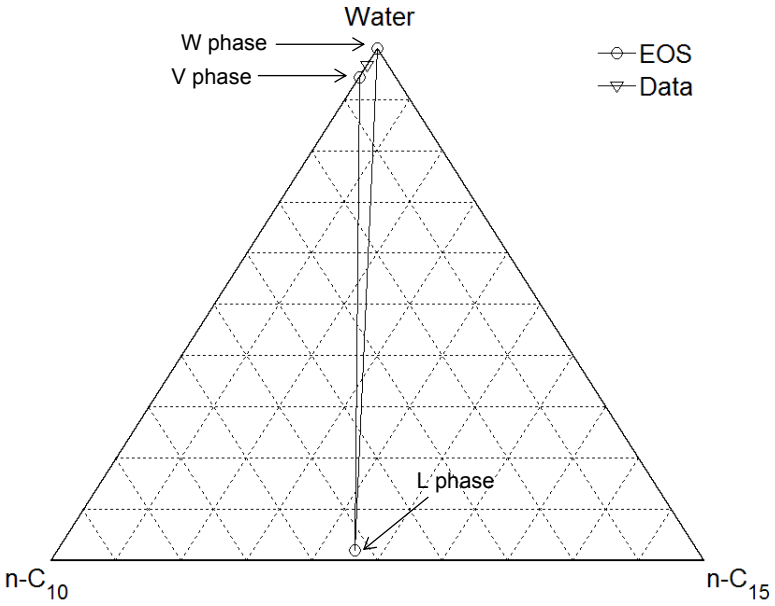

Figure 2.16a. Tie triangle predicted by the PR EOS with the BIP correlation (equation 2.7) for the water/n-C_{10}/n-C_{15} system at 394.26 K and 2.12 bars. The phase compositions measured by Chawla et al. (1995) are also shown.

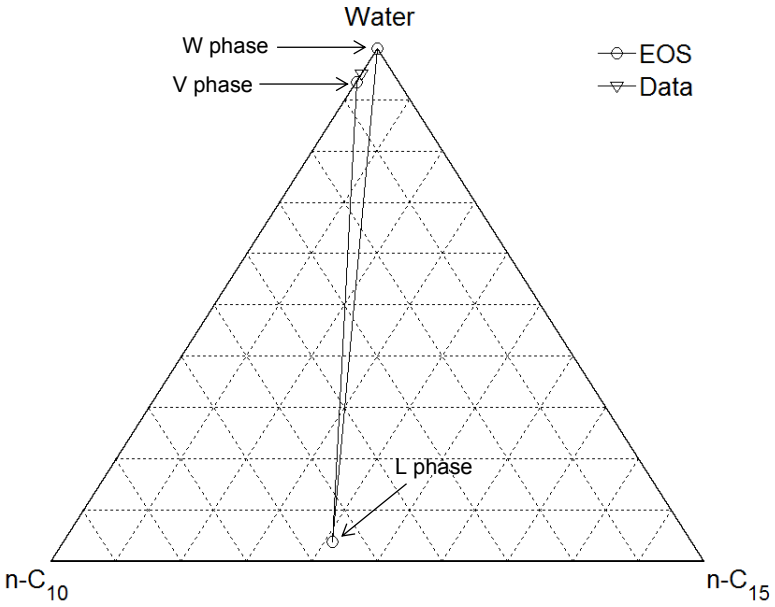

Figure 2.16b. Tie triangle predicted by the PR EOS with the BIP correlation (equation 2.7) for the water/n-C_{10}/n-C_{15} system at 422.04 K and 4.89 bars.

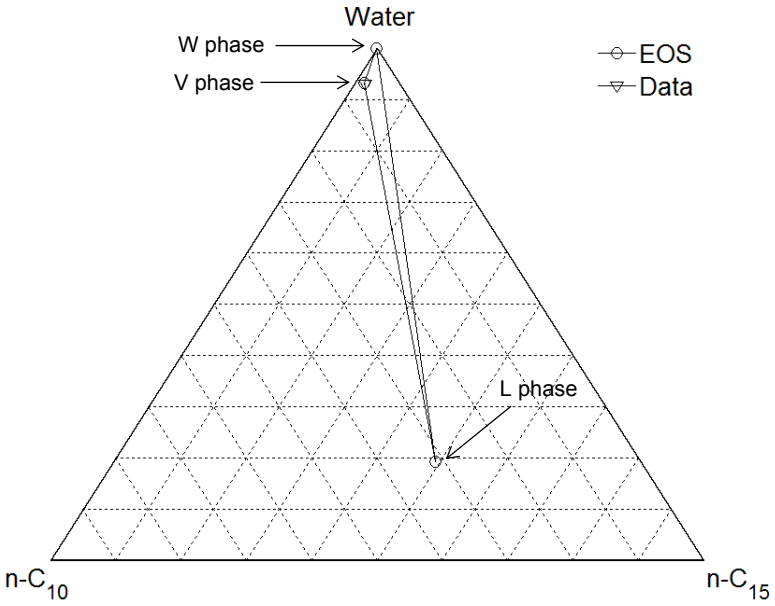

Figure 2.16c. Tie triangle predicted by the PR EOS with the BIP correlation (equation 2.7) for the water/n-C_{10}/n-C_{15} system at 505.37 K and 32.50 bars.

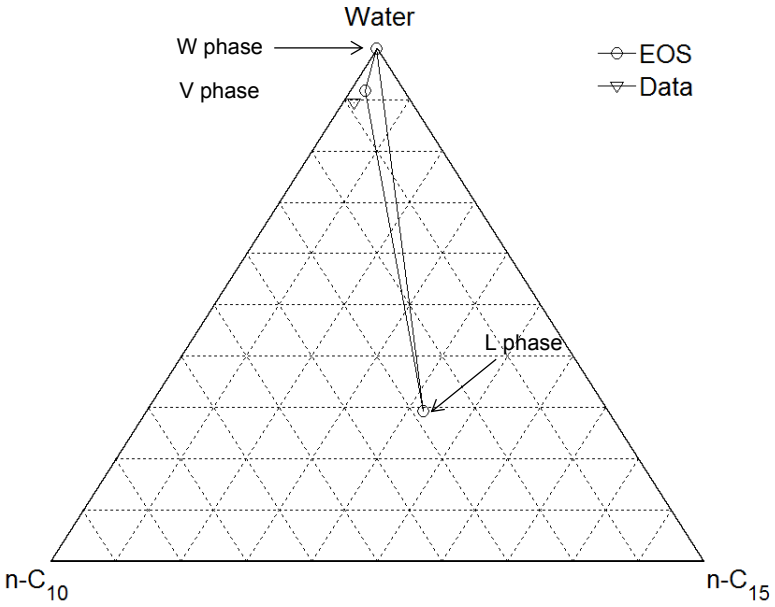

Figure 2.16d. Tie triangle predicted by the PR EOS with the BIP correlation (equation 2.7) for the water/n-C_{10}/n-C_{15} system at 533.15 K and 52.44 bars.

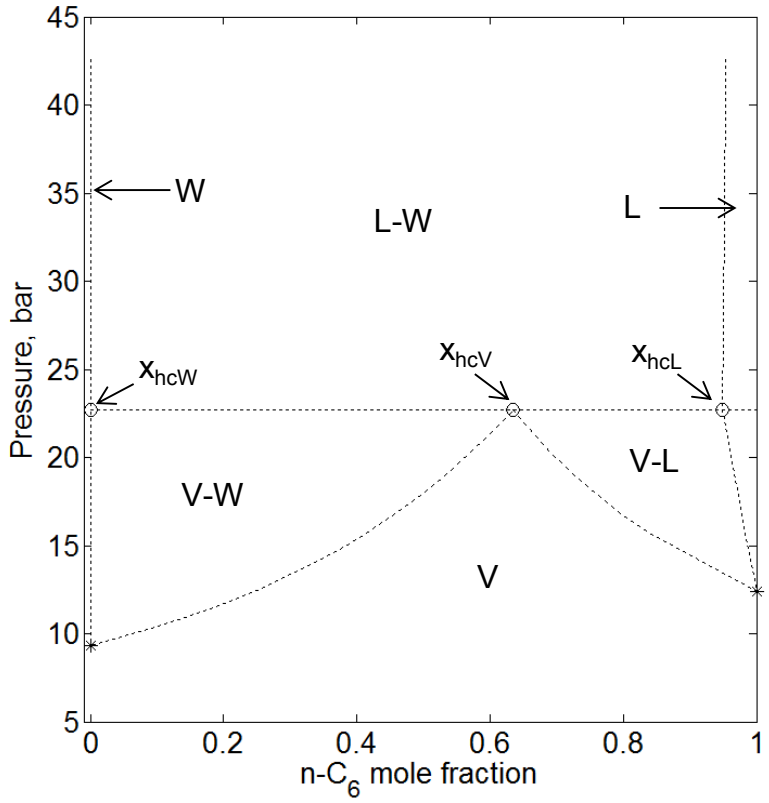

Figure 2.17. P-x cross-section predicted by the PR EOS at 450 K for the water/n-C_6 binary (T_r = 0.91). The BIP (0.579) used was obtained from equation 2.7.

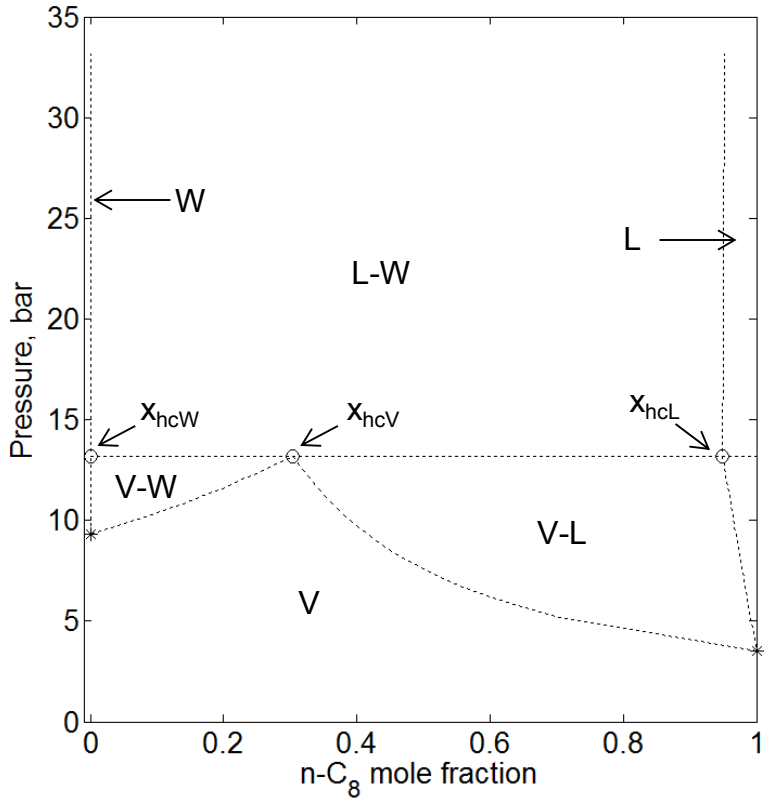

Figure 2.18. P-x cross-section predicted by the PR EOS at 450 K for the water/n-C_8 binary (T_r = 0.84). The BIP (0.527) used was obtained from equation 2.7. The L-phase composition at the three-phase pressure is similar to that of the water/n-C_6 binary given in figure 2.17.

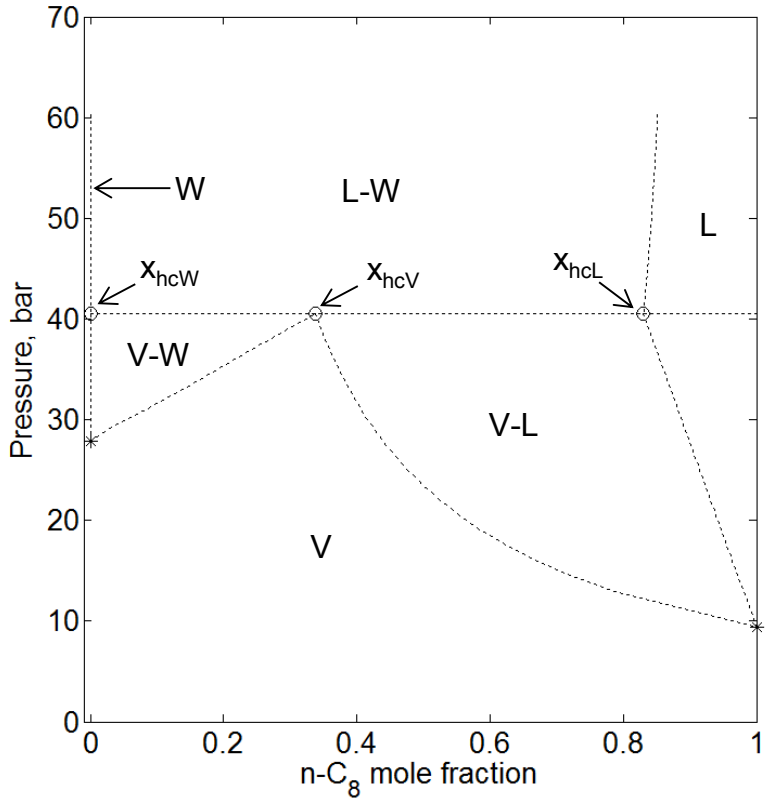

Figure 2.19. P-x cross-section predicted by the PR EOS at 503 K for the water/n-C_8 binary (T_r = 0.94). The compositions of the V and L phases are closer to each other than in figure 2.18 at a lower temperature.

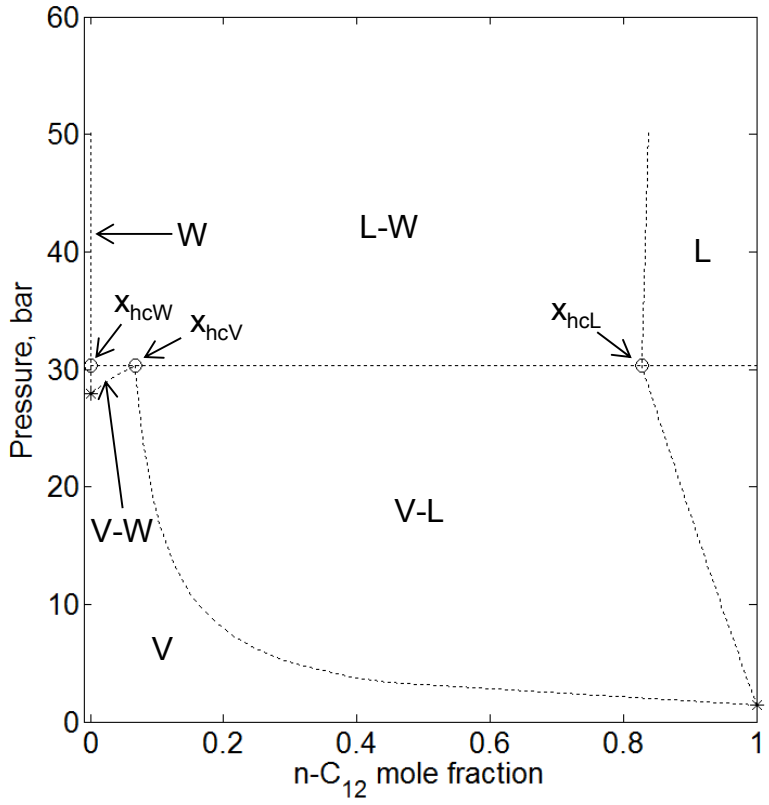

Figure 2.20. P-x cross-section predicted by the PR EOS at 503 K for the water/n-C_{12} binary (T_r = 0.87). The BIP (0.437) used was obtained from equation 2.7. The L-phase composition at the three-phase pressure is similar to that of the water/n-C_8 binary presented in figure 2.19.

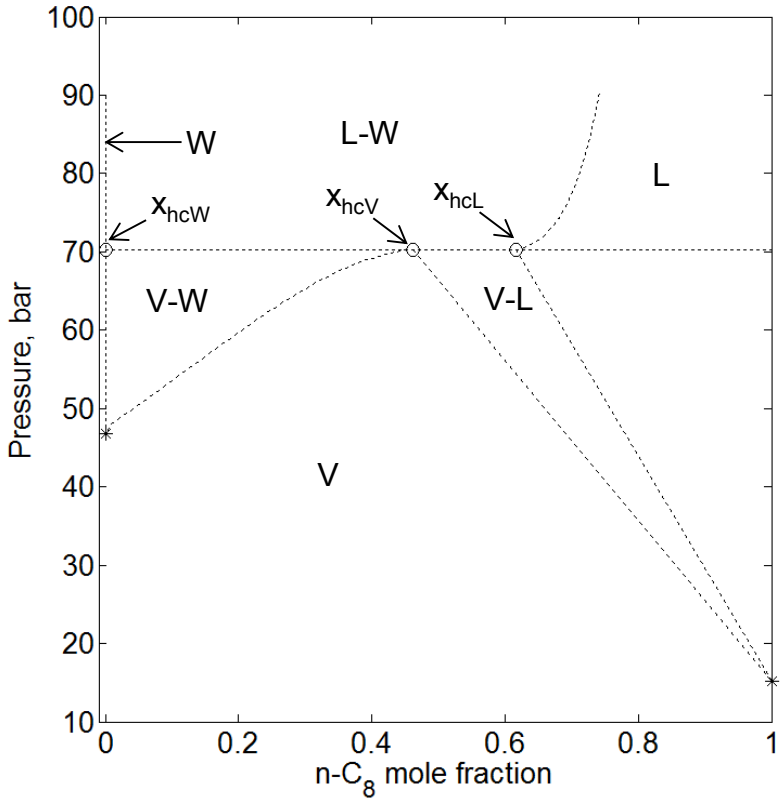

Figure 2.21. P-x cross-section predicted by the PR EOS for the water/n-C_8 binary at 533.00 K in the vicinity of the UCEP (T_r = 0.99). The UCEP for this system is predicted to be 535.43 K and 73.42 bars. Note the change in the curvature of the V- and L-phase arms of the V-W and L-W regions, respectively, when compared to those in figures 2.18 and 2.19. The boundaries for the V-L region are approximated to be linear due to computational difficulties.

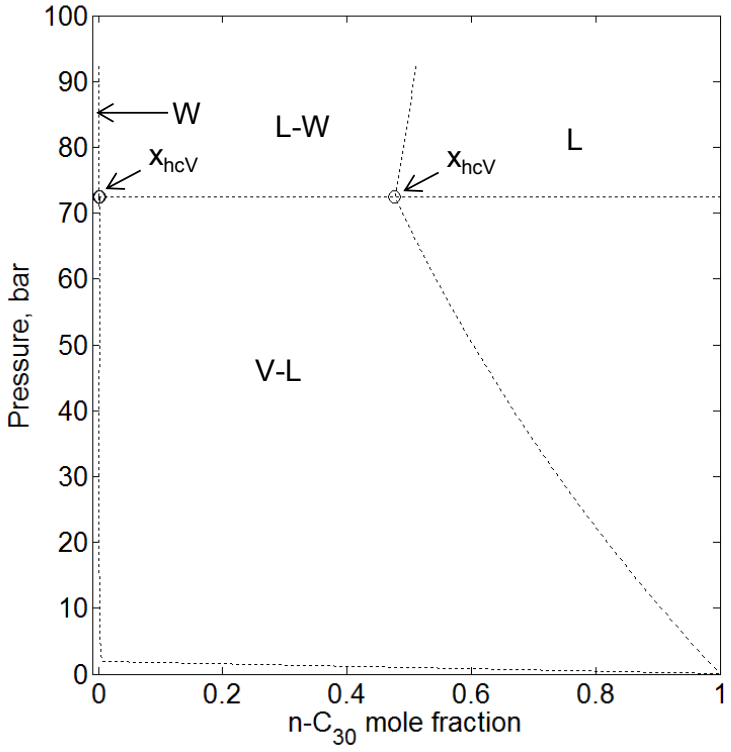

Figure 2.22. P-x cross-section predicted by the PR EOS at 560 K for the water/n-C_{30} binary (T_r = 0.87). The BIP (0.242) used was obtained from equation 2.7. The predicted phase behavior is of type IIIb. The dissolution of water in the L phase ($x_{wL} = 1 - x_{hcL}$) is substantially high.

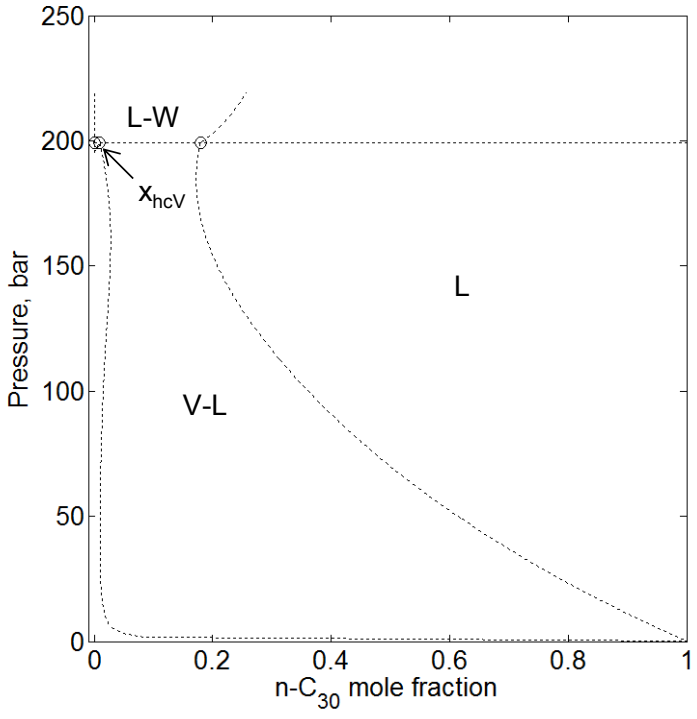

Figure 2.23. P-x cross-section predicted by the PR EOS for the water/n-C_{30} binary at 637 K in the neighborhood of the UCEP (T_r = 0.98). The UCEP is predicted to be approximately 647.49 K and 221.8 bars. Note the change in the curvature of the V- and L-phase arms of the V-L and L-W regions, respectively, in comparison with figure 21 (T_r = 0.87). x_{wL} at this condition is even higher than the one at T_r = 0.87.

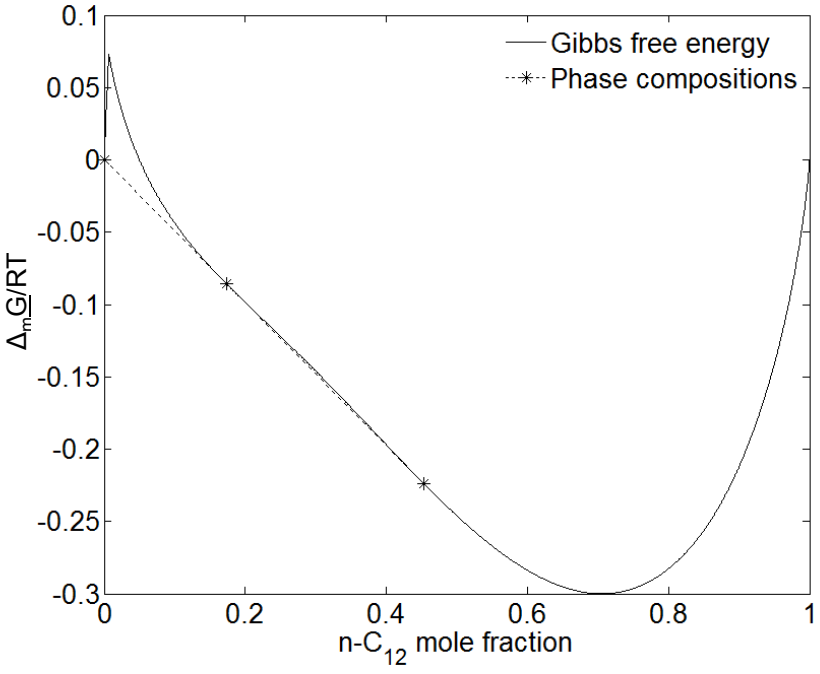

Figure 2.24a Dimensionless molar Gibbs free energy change on mixing predicted by the PR EOS for the water/n-C_{12} binary at 100.00 bars and 571.88 K. The BIP (0.437) used was obtained from equation 2.7. The three equilibrium phases are presented by the tangent points

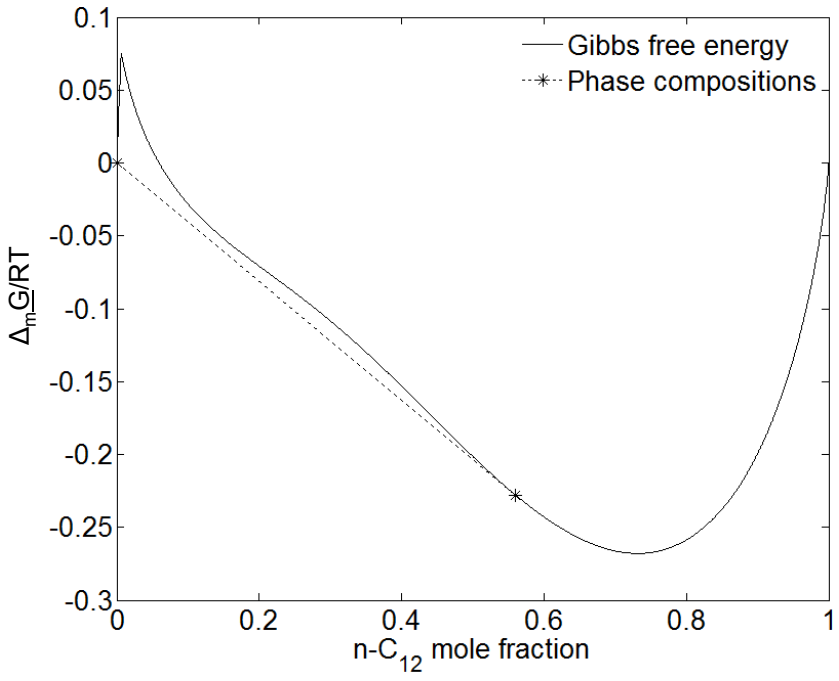

Figure 2.24b. Dimensionless molar Gibbs free energy change on mixing predicted by the PR EOS for the water/n-C_{12} binary at 100.00 bars and 571.88 K. The BIP used is 0.500. The two equilibrium phases are presented by the tangent points. As the BIP is increased from 0.437 to 0.500 at the same pressure and temperature, the Gibbs free energy systematically shifts upward, resulting in the W-L equilibrium. The right lobe of the Gibbs free energy associated with the L phase keeps the level of convexity as it is displaced upward. Then, the x_{wL} (= 1.0 – x_{hcW}) becomes lower as the BIP is increased since the tangent slope from the W phase onto the L phase lobe becomes greater. With the BIP of 0.500, temperature must be increased to 573.08 K to predict the three-phase equilibrium at 100.00 bars.

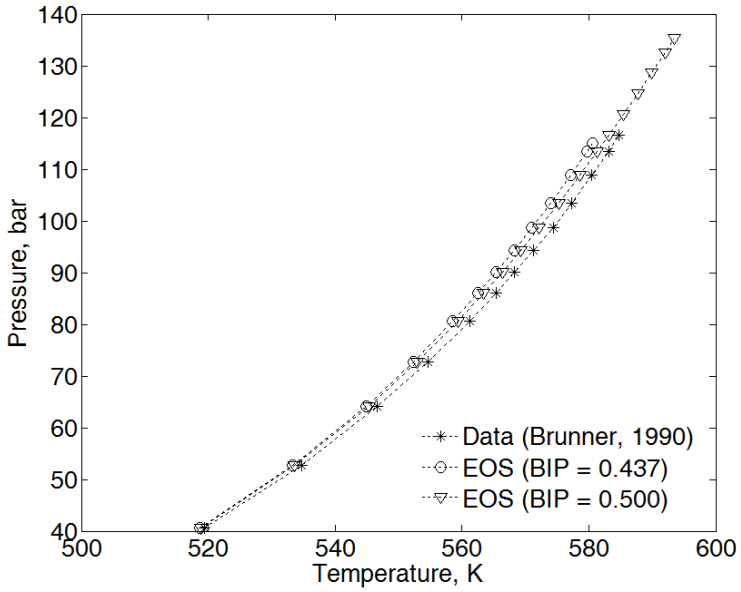

Figure 2.25. Impact of BIP on the three-phase predictions for the water/n-C_{12} binary.

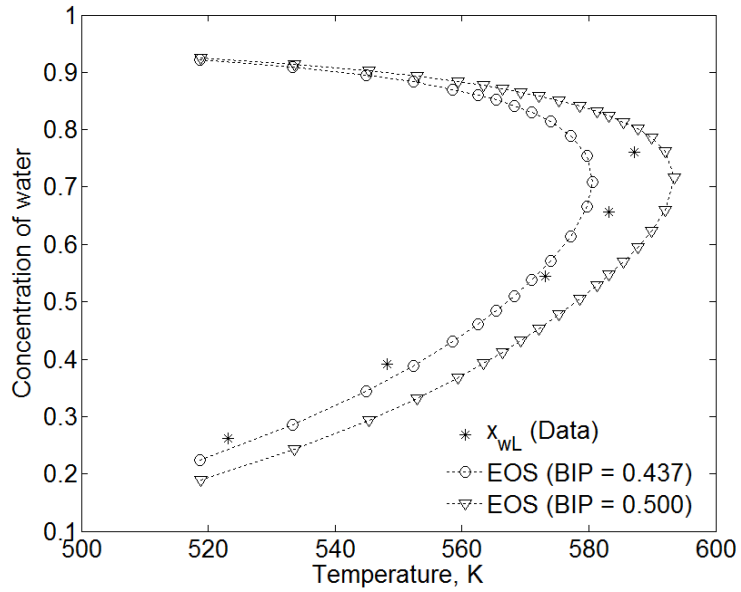

Figure 2.26. Impact of BIP on the compositions of the V and L phases along the three-phase curve for the water/n-C_{12} binary. The data for the L-phase composition was taken from Skripka (1979).

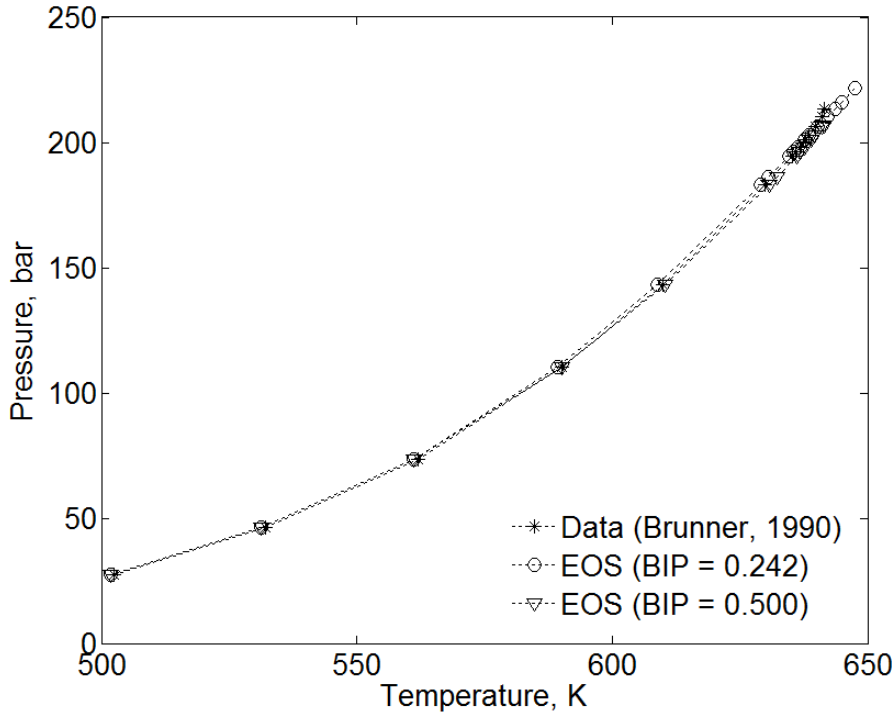

Figure 2.27. Impact of BIP on the three-phase predictions for the water/n-C_{30} binary. Equation 2.7 yields a value of 0.242 for the BIP for this binary.

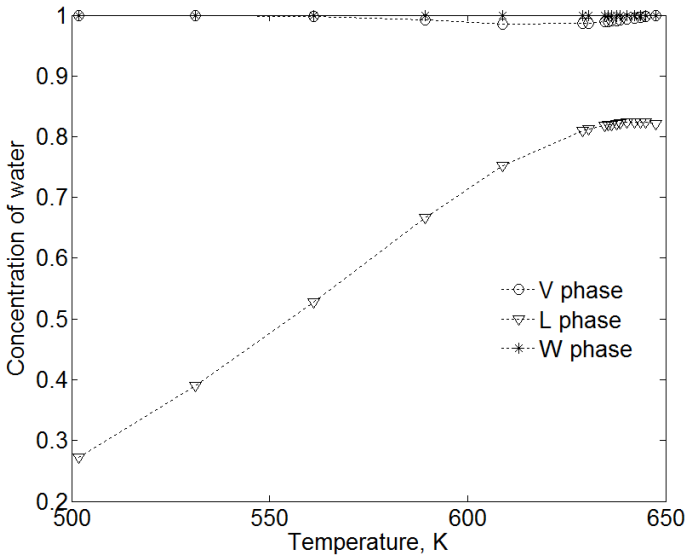

Figure 2.28a

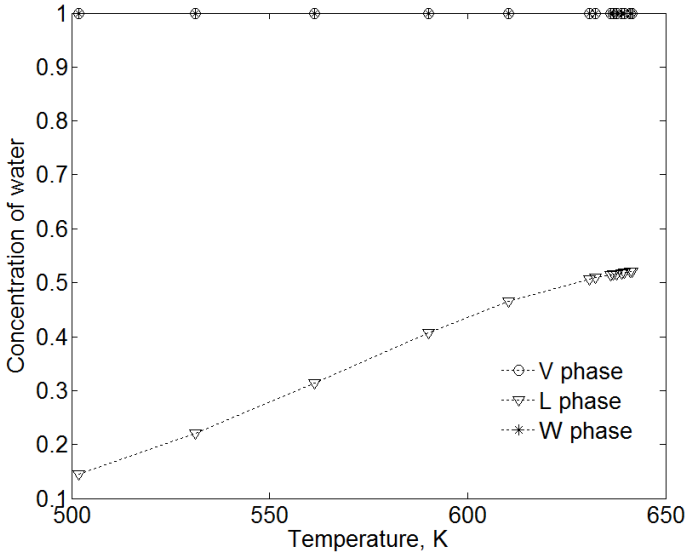

Figure 2.28b

Figure 2.28. Phase compositions predicted by the PR EOS along the three-phase curve of the water/n-C_{30} binary; (a) BIP = 0.242 (on the basis of equation 2.7) and (b) BIP = 0.500. Note the change in the predicted compositions of the V and L phases in (b) in comparison with (a). The predicted solubilities of water in the L phase are substantially lower than when the BIP from equation 2.7, 0.242, is used.

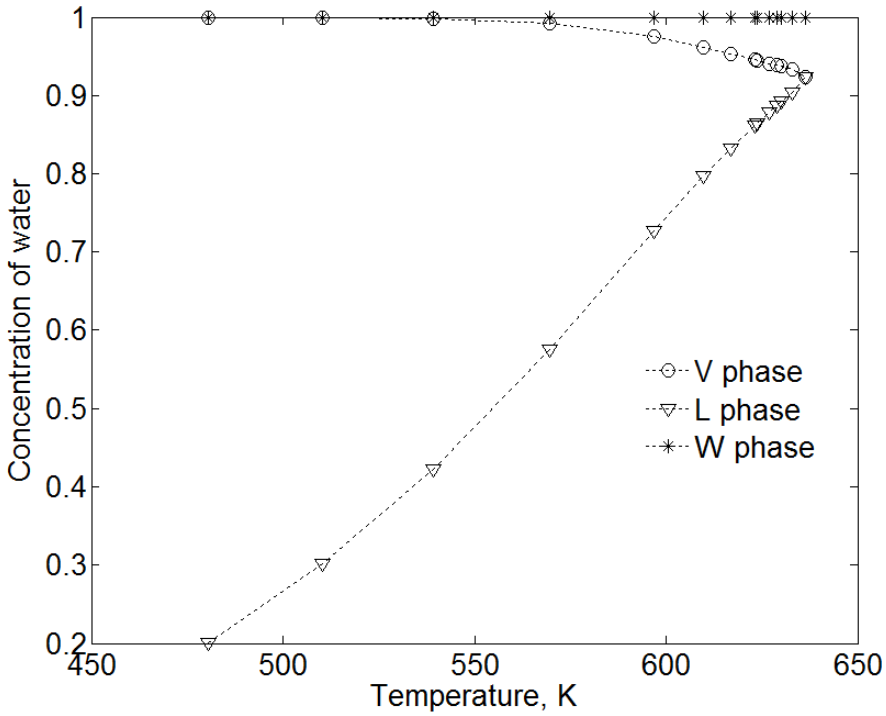

Figure 2.29a. Phase compositions predicted by the PR EOS along the three-phase curve of the water/n-C_{25} binary. The value of 0.243 is used for the BIP. The specified BIP value, 0.243, obtained using equation 2.7, yields type IIIa phase behavior, wherein the V and L phases merge at the UCEP. This is consistent with the experimental results of Brunner (1990).

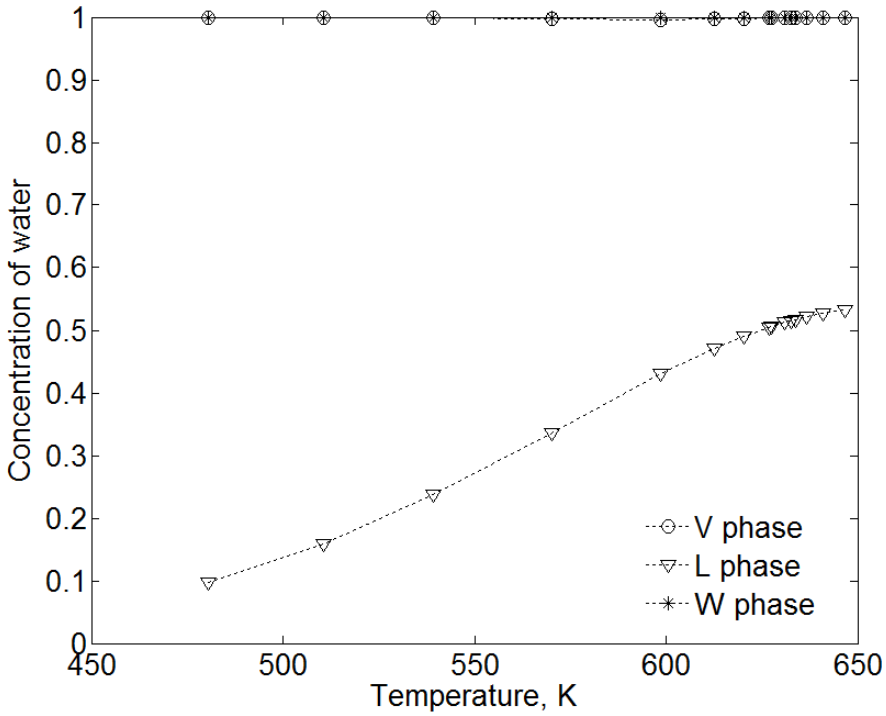

Figure 2.29b. Phase compositions predicted by the PR EOS along the three-phase curve of the water/n-C_{25} binary. The value of 0.5 is used for the BIP. In contrast with Figure 2.29a, the BIP value of 0.500 results in type IIIb phase behavior, wherein the V and W phases merge at the UCEP. This is inconsistent with the experimental results of Brunner (1990).

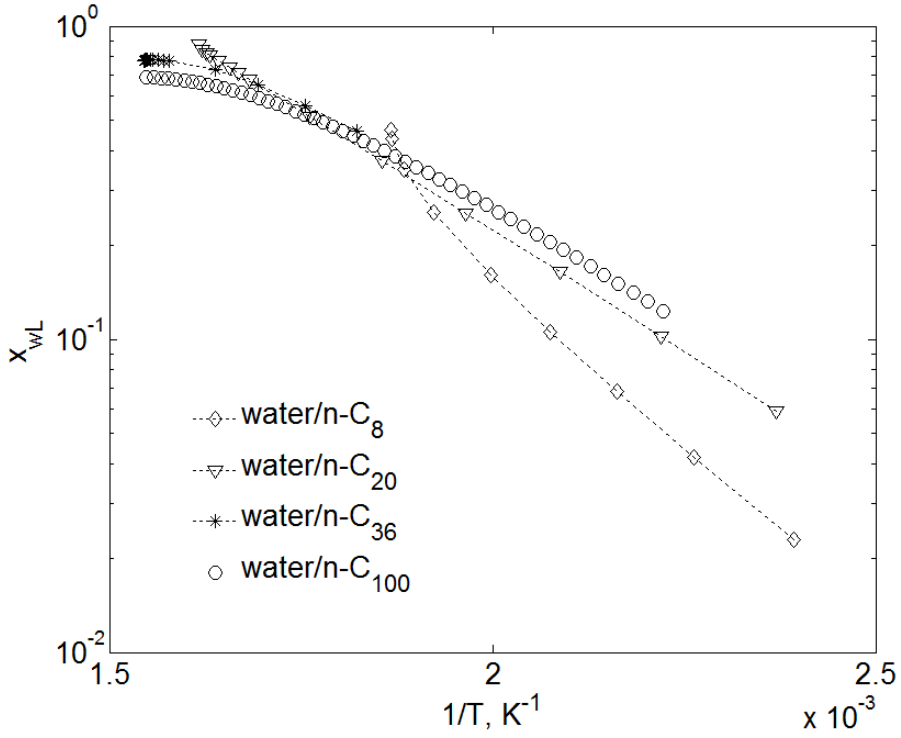

Figure 2.30. Trends in x_{wL} predicted along the three-phase curves for the water binaries with n-C_8, n-C_{20}, n-C_{32}, and n-C_{100}. .

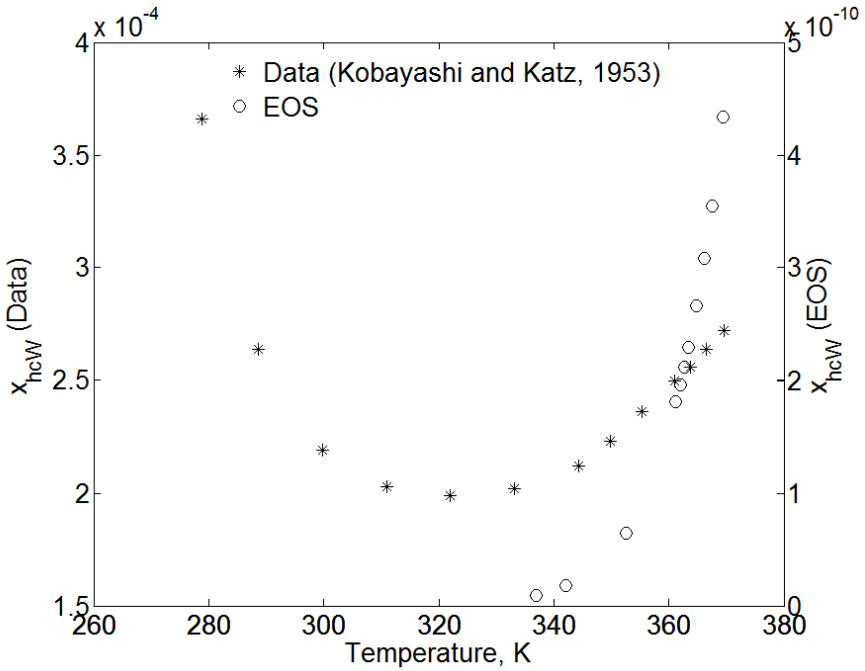

Figure 2.31a. Comparison between predicted and experimentally measured/ascertained compositions of the aqueous (W) phase along the three-phase curve of water/C_3 binary. The data for the W phase was obtained from Kobayashi and Katz (1953). The EOS under-predicts the dissolution of C_3 in the W phase by a few orders of magnitude.

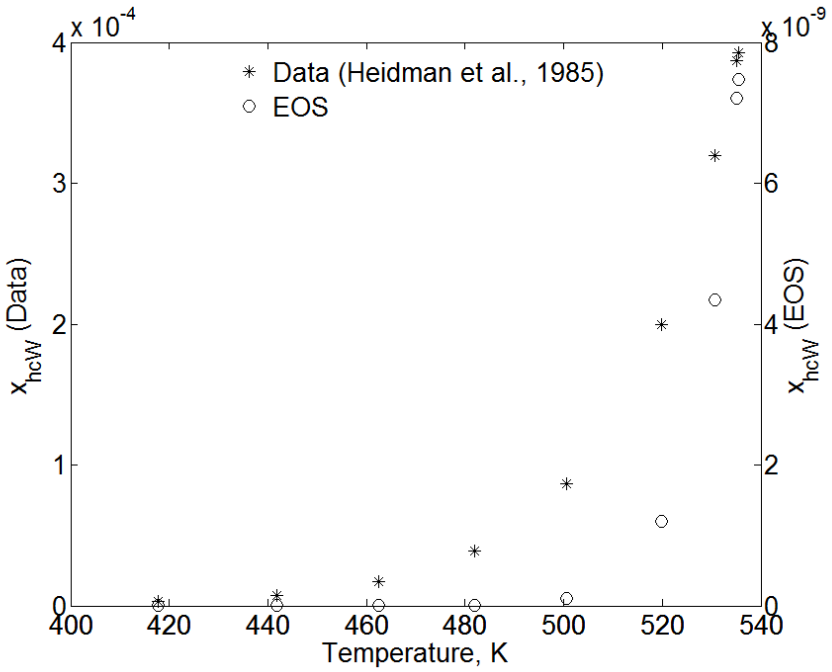

Figure 2.31b. Comparison between predicted and experimentally measured/ascertained compositions of the aqueous (W) phase along the three-phase curve of water/n-C_8 binary. The data points were obtained from the correlation developed by Heidman et al. (1985) for the W phase based on experimental measurements. The EOS under-predicts the dissolution of n-C_8 in the W phase by a few orders of magnitude.

Chapter 3. Improved predictions of the volumetric behavior of water-containing reservoir oils using the Peng-Robinson equation of state

In Chapter 2, the focus was solely on the development of a reliable characterization framework for water-containing reservoir oils in terms compositional behavior. The accurate prediction of volumetric behavior (phase densities) has not been explicitly considered for the development. Also, a critical evaluation of the framework's capability to render accurate predictions for phase densities has not been performed. Prior studies indicate that two-constant cubic EOSs such as that of PR can yield erroneous predictions for phase densities (Peneloux and Rauzi, 1982, Søreide, 1989, Kumar and Okuno, 2012, 2014). For the binary mixture of C_1/n-C_9, Peneloux and Rauzi (1982) demonstrated that the predicted density of the L phase is more erroneous than that of the V phase. For this case study, the average relative deviations (with respect to measurements) in the predicted L- and V-phase densities are 4.02% and 3.84%, respectively. The investigated range for temperature and pressure are 223-423 K, and 10-317 bars, respectively. Valderrama (2003) presented a critical review of cubic EOSs in terms of volumetric behavior predictions. This review presents the implication that between vapor and liquid states, the predicted density of the L phase is generally more erroneous. In reservoir engineering applications, the accurate prediction of phase densities can be potentially important. Inaccurate predictions for phase densities can affect oil recovery estimates through the incorrect

prediction of phase saturations. This mechanism has been mathematically elucidated in equations 1.1 through 1.6 (Chapter 1).

In current simulation practice, the shortcoming of cubic EOSs with respect to density predictions is often addressed using volume translation, first proposed by Peneloux and Rauzi (1982). The use of volume shift alters the form of the cubic EOS, but not the fugacity equations (Peneloux and Rauzi, 1982). Thus, phase equilibrium calculations are not affected by the use of volume shift. Numerical values for the translation parameters are obtained through regression against measured phase densities.

Reservoir oils are characterized as pseudo-components whose exact chemical identity is unknown. When a cubic EOS with the classical mixing rules is employed to characterize oils, the accurate specification of the component-specific (including pseudo-components) attraction and co-volume parameters is of importance. This is because attraction and co-volume parameters for the mixture are dependent on those of individual components (equations A-7 and A-8). Often, the specification of component-specific attraction and co-volume parameters is performed by optimization of T_C, P_C and ω against phase equilibrium (vapor pressure) data. The shortcoming of cubic EOSs with regard to density predictions is addressed subsequently using volume shift.

An alternative way to model the component-specific attraction and co-volume parameters of is to treat component-specific T_C, P_C and ω as decision variables for optimization against both vapor pressure and density data (Kumar and Okuno, 2012). For hydrocarbon mixtures, Kumar and Okuno (2012, 2013)

demonstrated that the resulting values for the optimum T_C, P_C and ω are considerably different than when volume shift is not used. This in turn results in discrepancies in the predicted topology of the free energy surface in P-T-x space. Kumar and Okuno, (2013) showed that the topology of the free energy surface when volume shift is erroneous. Qualitatively, this result can be attributed a fundamental deficiency of volume shift- that it ignores a key principle that volumetric behavior is a consequence of compositional behavior. Another significant drawback of volume translation is that it cannot be used when the effect of capillarity is considered in phase equilibrium calculations. The effects of capillarity are not necessarily negligible in sub-surface oil recovery processes.

The focus of this chapter is to develop a framework to characterize water-containing mixtures of reservoir oils that is capable of simultaneously yielding accurate predictions for compositional and volumetric multiphase behavior. The intended application of this framework is in the simulation of steam-injection processes, wherein the operating temperature is typically lower than 550 K. Towards this end, in section 3.1 we first demonstrate the shortcomings of the framework proposed in Chapter 2, which from here on will be referred to as Approach 1, in terms of density predictions using case studies. In section 3.2, we attempt to fix the issues with Approach 1 concerning phase-density predictions by first extending the method of Kumar and Okuno (2012) to water/n-alkane mixtures. This method will be addressed as Approach 2 from here on. As with Approach 1, a new BIP correlation between water and n-alkanes is developed for Approach 2 by optimization against the binary three-phase curves measured by

Brunner (1990). In section 3.3, the developed BIP correlation is first validated against measured phase composition (x_{wL}) and density data, and then extended to represent the multiphase behavior of water-containing reservoir oils. In section 3.4, the mechanistic explanations for the behavior of Approach 2 are presented. In section 3.5, the compositional behavior predicted using Approach 2 is utilized to perform K-value-based reservoir simulation of the ES-SAGD process with n-C_5 as the injected solvent. The purpose of this is to investigate the potential impact of the dissolution of water in the L phase on the bitumen drainage rate. As with Chapter 2, this chapter also culminates with a section (3.6) comprising a summary along with a list of key conclusions. The significance and the novelty of the modeling framework proposed in this chapter stems from the obtainment of accurate estimates for both the L-phase composition and phase densities (L and W phases). This is obtained through the extension of the method of Kumar and Okuno (2012) to water-containing mixtures of hydrocarbons.

3.1.Evaluation of Approach 1 in terms of predicted phase densities

In this section, a critical evaluation of the performance of Approach 1 in terms of predicted phase densities (L and W) is presented. As explained in Chapter 2, for Approach 1, a correlation developed for the BIP between water and n-alkanes (equation 2.7) was extended to water-containing Peace River bitumen and water-containing Athabasca bitumen by systematic reduction of the BIPs through scaling using a factor (λ) less than unity. The optimum values for the scaling factors are 0.780 and 0.415 for water/Peace River bitumen and water/Athabasca bitumen, respectively (Tables 2.7 and 2.9). The characterized

pseudo-components and their corresponding BIPs with water computed from equation 2.7 are shown in Tables 2.6 and 2.8. The experimental data presented in Mehrotra and Svrcek (1985), and Badamchi-Zadeh et al. (2009a, b) were used to characterize the Peace River and Athabasca bitumens, respectively. The bitumens were characterized by the method of Kumar and Okuno (2013). As seen in tables 2.6 and 2.8, the critical constants of water used in these calculations is 640.096 K and 220.640 bars, as recommended by Wagner and Pruß (2002). The value 0.3433 for the acentric factor (ω) of water was estimated using the vapor pressure correlation developed by Wagner and Pruß (2002).

In **Figures 3.1 and 3.2**, x_{wL} and W-phase density (ρ_W) predicted using the adapted BIP correlation for Approach 1 are presented for water/Peace River and water/Athabasca bitumens, respectively. The dissolution of the bitumens in the W phase is very small (Amani et al., 2013). Further, the pressures corresponding to the temperatures shown in Figures 3.1 and 3.2 are in the neighborhood of the three-phase region, which in turn is in the neighborhood of the corresponding saturation pressures of water. Hence, the accuracy of the predicted W-phase density has been evaluated using the liquid phase density of pure water along the vapor pressure curve. For water/Athabasca bitumen, Amani et al. (2013b) measured both the density of the L phase and solubility of water in the L phase at various pressures and temperatures. The solubility of water in the L phase has been expressed as a weight fraction (f_w). For Approach 1, a comparison between the predicted and measured values for these properties is presented in **Table 3.1**. The average absolute deviation (AAD) in prediction of the L-phase density is

0.0340 g/cc, while the AAD in the predicted solubility of water in the L phase in terms of weight fraction (f_w) is 0.0108.

From Figures 3.1 and 3.2, it is evident that Approach 1, which employs physical values for critical constants to model the attraction and co-volume parameters for water, systematically under-predicts the density of the W phase. The compositional behavior of the W phase for these systems, under the investigated conditions, has not been published. However, it is likely that the PR EOS using the developed correlation under-estimates the dissolution the hydrocarbon in the W phase. In contrast, from Table 3.1, the predicted compositional and volumetric behavior of the L phase using Approach 1 seems reasonably accurate.

The under-estimation of the W-phase density must be addressed as it could potentially result in erroneous estimates of oil recovery when used in reservoir simulation. To address this, in the subsequent section, a new scheme (Approach 2) is proposed.

3.2.Development of Approach 2

The appropriate definition of the topology of the free energy surface in thermodynamic space (P-T-x) is a priority in the modeling of phase equilibrium. As stated previously, besides P and T, the topology of the free energy surface in composition space is affected by the choice of model parameters which includes the attraction and co-volume parameters of pure components. This section presents optimum values for T_C, P_C and ω for water and n-alkanes, and the BIP for their mutual interaction.

3.2.1. Optimization of critical constants (T_C, P_C) and acentric factor (ω) of n-alkanes and water

In their investigation of the phase behavior of mixtures of n-alkanes using the PR EOS, Kumar and Okuno (2012) modeled the pure component attraction and co-volume parameters by optimization of T_C, P_C and ω against both vapor pressure and liquid phase density data. The approach of Kumar and Okuno (2012) is distinct from prior attempts such as that of Stryjek and Vera (1986) and Mathias and Copeman (1983). Two attributes render the latter method distinct from the former. First, the functional form of the α-term (presented in equation A-3) is modified in an attempt to improve pure component vapor pressure predictions. And second, physical values for T_C, P_C and ω, when available, are employed. The achievement of accurate predictions for phase densities is not a priority in the development of the new functional form for the α-term. Based on case studies, Stryjek and Vera (1986) have concluded that the aforementioned modification can result in reasonably accurate predictions of phase densities for both pure components and mixtures at conditions away from the near-critical region. For reservoir engineering applications, the preservation of the original functional form for the α-term, as recommended by Peng and Robinson (1986), facilitates application in commercial simulators. From this standpoint, the method of Kumar and Okuno (2012) seems preferable.

As stated earlier, the PR EOS being a two-constant EOS has the inherent weakness of yielding inaccurate predictions for phase densities. For hydrocarbon systems (pure component and mixtures), Kumar and Okuno (2012) demonstrated

that the consideration of component-specific T_C, P_C and ω as decision variables for optimization against both vapor pressure and density data can address this shortcoming. Also, the accuracy of the predicted compositional behavior (for mixtures) was improved through a more accurate prediction of the free energy surface. It is to be noted that this improvement in the predicted phase compositions was observed despite the use of a value of zero for all BIPs.

The mechanism by which the improvement occurs is through the definition of another component-specific constant, Ω, for the attraction and co-volume parameters. We now mathematically elucidate the origin of the component-specific constant Ω. The expressions for the attraction and co-volume parameters can rewritten in the manner shown in equations 3.2 and 3.3.

$$a_i = 0.45724 \frac{R^2 {T_{c,i}}^2}{P_{c,i}} \alpha_i(T) = \Omega_a \frac{R^2 {T_{c,i}}^2}{P_{c,i}} \alpha_i(T) \tag{3.2}$$

where Ω_a = 0.45724, and $T_{C,i}$, $P_{C,i}$ and α_i have their respective meaning in the classical sense.

$$b_i = 0.0778 \frac{RT_{c,i}}{P_{c,i}} = \Omega_b \frac{RT_{c,i}}{P_{c,i}} \tag{3.3}$$

where Ω_b = 0.0778

The optimization of T_C, P_C and ω against both vapor pressure and density data results in values that are distinct from the physical values (Kumar and Okuno, 2012). Correspondingly, the calculated values for the component-specific attraction and co-volume parameters will be different. Component-specific values for Ω are obtained can be expressing the attraction and co-volume parameters in

terms of those computed using the physical values for T_C, P_C and ω. These are shown in equations 3.4 and 3.5, respectively.

$$a_i' = 0.45724 \frac{R^2 {T'_{c,i}}^2}{P'_{c,i}} \alpha'_i(T) = \Omega'_a \left(\frac{R^2 {T_{c,i}}^2}{P_{c,i}} \alpha_i(T) \right) \quad (3.4)$$

where $\Omega'_a = 0.45724 \left(\frac{{T'_{c,i}}^2}{{T_{c,i}}^2} \right) \left(\frac{P_{c,i}}{P'_{c,i}} \right) \left(\frac{\alpha'_i(T)}{\alpha_i(T)} \right)$

And $T_{C,i}$', $P_{C,i}$' and α_i' represent the optimized critical constants, and attraction parameter computed using the optimized critical temperature and acentric factor.

$$b_i = 0.0778 \frac{RT'_{c,i}}{P'_{c,i}} = \Omega'_b \left(\frac{RT_{c,i}}{P_{c,i}} \right) \quad (3.5)$$

where $\Omega'_b = 0.0778 \left(\frac{T'_{c,i}}{T_{c,i}} \right) \left(\frac{P_{c,i}}{P'_{c,i}} \right)$

For n-alkanes, Søreide (1989) observed that the PR EOS over-predicts the liquid phase density for CNs lower than seven, while the reverse is true for CNs seven and higher. For water, we observed that the predicted density of the liquid phase both along the saturation vapor pressure curve and in the compressed liquid region were systematically lower than the experimental data. Kumar and Okuno (2012) presented optimized values for T_C, P_C and ω for n-alkanes with CN from 7 up to 100. The optimized values for the critical constants are systematically greater than the experimental values presented in Appendix C (Table C-1). In contrast, the optimum values for ω are systematically lower than the physical values (Kumar and Okuno, 2012).

In this Chapter, the work of Kumar and Okuno (2012) is extended to mixtures containing water. Towards this end, the critical constants and acentric factor of n-alkanes with CN from 1 up to 6, and that of water were first optimized using the two-step, exhaustive search-based optimization routine developed by Kumar and Okuno (2012). The optimized values for T_C, P_C and ω, for the aforementioned components are tabulated in **Table 3.2**. Note that the optimized values for the critical constants for the n-alkanes are lower than the experimentally ascertained values presented in Appendix C (also shown in table 3.2). Also, the corresponding optimized values for the acentric factor are systematically lower than those employed in Approach 1. This is necessary to address the under-prediction of liquid phase densities resulting from the use of physical values for T_C, P_C and ω. In contrast, the optimized critical constants (672.48 K, 277.15 bars) for water are considerably larger than the measured values (647.096 K, 220.64 bars) presented in Wagner and Pruß (2002), and the optimized ω (0.2699) is smaller than that used in Approach 1 (0.3433). The performance of the component-specific critical constants and acentric factor used in Approaches 1 and 2, in terms of the predicted vapor pressure and liquid phase density is presented in **Tables 3.3** and **3.4**, respectively.

3.2.2. Development of BIPs between water and n-alkanes

In his review of cubic EOSs, Valderrama (2003) implied that interaction parameters (e.g., BIPs) serve as empirical means to adequately capture the interaction between unlike molecules in a mixture. The complexity of these

interactions may stem from size-asymmetry and asymmetry in polarity between the interacting molecules. For water/hydrocarbon mixtures, we have observed that the accurate prediction of multiphase behavior requires the use of non-zero values for BIPs. This requirement arises even with the employment of the optimized values for T_C, P_C and ω.

Analogous to equation 2.7, a correlation for the BIP between water and n-alkanes has been developed by optimization against the three-phase curves of type IIIa binaries measured by Brunner (1990). As with Approach 1, this correlation is set to have a limiting value for the BIP equivalent to the optimum BIP for water/n-C_{25} binary (0.239), occurring at CN = 26. The purpose of this is to reproduce the asymptotic behavior of temperature trend lines for x_{wL} with respect to the n-alkane CN. The objective functions for the BIP optimization for Approach 2 are identical to those employed in Approach 1 (equations 2.4 to 2.6). The developed BIP correlation is presented in equation 3.5.

$$\text{BIP} = c_1[1 + \exp(c_2 - c_3 \text{MW})]^{-1/c_4}, \quad (3.5)$$

where c_1 = 0.23899, c_2 = 51.92767, c_3 = 0.15202, and c_4 = -50.60828

The correlation gives the R^2 value of 0.8612 and a standard deviation of 0.0423 against the optimized BIPs. The maximum deviation of 0.113 occurs for 72.15 g/mol (i.e., n-C_5).

The experimentally measured three-phase curves of Brunner (1990) for water/n-alkanes binaries with CN in the range [3, 25] were used to developed equation 3.5. A total of 169 data points, including UCEPs, spanning 16 binary

systems were utilized. The optimized BIPs and their performance in terms of the three-phase curve predictions are shown in **Table 3.5.** This table also shows the correlated BIPs calculated using equation 3.5. The largest AAD in the predicted $T_{3\varphi}$ is 2.73 K, and occurs for the water/n-C_{11} binary. In terms of the AD in P_{UCEP} and T_{UCEP}, the largest values occur for water/n-C_{18} (2.56 bars) and water/ C_3 (3.97 K), respectively.

As seen in table 3.5, the optimized BIP for water/n-C_{11} binary is an outlier with regard to the trend in the BIP with respect to the n-alkane CN. The optimized BIP for water/n-C_{11} is 0.480. In comparison, the optimized BIPs for water/n-C_{10} and water/n-C_{12} are 0.444 and 0.410, respectively. The reason for this aberration may likely be due to the larger error associated with the optimization of the T_C, P_C and ω of n-C_{11} against the liquid phase density data in comparison with n-C_{10} and n-C_{12}. The optimized T_C, P_C, and ω for n-C_{10}, n-C_{11} and n-C_{12} are (618.54 K, 22.35 bars, and 1.0888), (628.90 K, 21.03 bars, and 1.1436), and (657.99 K, 19.81 bars, and 1.2205), respectively. Specifically, in terms of the predicted density of the liquid n-alkane, Kumar and Okuno (2012) reported that the optimized T_C, P_C, and ω for n-C_{11} yielded a deviation of 2.9% in comparison with n-C_{10} and n-C_{12} which yielded deviations of 1.5% each. For optimized BIP between water and n-C_{11} to lie within the BIP trend, the T_C, P_C, and ω of the n-C_{11} must be closer to that of n-C_{12}. However, this results in more erroneous for phase equilibrium and liquid phase density for pure n-C_{11}.

For water/n-alkane binaries with CN in the interval [3, 6], although the trend in the optimized BIP with respect to the n-alkane CN is preserved, the optimized

values are considerably greater than those yielded by equation 3.5. The two aforementioned factors result in a lower value for the R^2 for Approach 2 in comparison with Approach 1. Despite the seemingly large value for the maximum deviation and a smaller value for R^2 in comparison with Approach 1, this correlation can result in reasonably accurate three-phase predictions when used with the PR EOS. This is because the sensitivity of the three-phase curves of type IIIa binaries to the BIP diminishes with decreasing CN, and the CN interval in which the largest deviations between correlated and optimized values for the BIP occur is [3, 11], which entirely comprises light n-alkanes.

3.3.1. Validation and application of the BIP correlation

3.3.2. Water/n-alkane binaries

As with Approach 1, the BIP correlation developed for Approach 2 was validated against compositional data measured for both binary and multi-component mixtures. For water/n-alkane binaries, the AAD in the predicted x_{wL} along the three-phase curve with respect to the experimental data is presented in **Table 3.6**. The resulting deviations lie within the experimental uncertainty bounds. The largest AAD (3.90 mol%) in x_{wL} is observed for water/n-C_{20} binary with a maximum deviation of 7.39 mol%.

3.3.3. Ternary water/n-alkane mixtures

For a ternary mixture of water/C_1/n-C_4, the predicted tie-triangles at 377.59 K for two different pressures: 44.88 bars, 58.95 bars, using the BIPs calculated from equation 3.5 are shown along with the experimental measurements of

Mcketta and Katz (1948) in **Figure 3.3**. The predicted phase compositions match reasonably well with the data. The deviations in the V-phase composition in terms C_1 mole fraction are 8.00 mol% and 7.84 mol% at 44.98 bars and 58.95 bars, respectively. With respect to the mole fraction of C_1, the deviations in the L-phase composition are 1.30 mol% and 2.50 mol% at 44.98 bars and 58.95 bars, respectively.

For water/n-C_{10}/n-C_{15} system the predicted tie-triangles at four different P-T conditions are shown in **Figure 3.4**. Also shown in Figure 3.4 is the V-phase composition measured by Chawla et al. (1995) at each of the aforementioned conditions. The corresponding V-phase composition distance (δ_V) between the predictions and the data are 0.0059, 0.0059, 0.0542, and 0.0058.

3.3.4. Quaternary water/n-alkane mixtures

Table 3.7 summarizes the comparison between the data and predictions from the PR EOS with BIPs from equation 3.5. The deviations from the data are expressed using the composition distance δ_j for phase j, with composition x_j, comprising the four components. The predicted values for the L-phase composition are reasonably close to the data values as indicated by the values δ_L which are lower than 0.1 for all cases. The largest deviations from the data were observed at 448 K and 51.50 bars. The corresponding values for δ_L and δ_V at this condition are 0.08192 and 0.1364, respectively.

As with Approach 1, for Approach 2, the predicted V-phase compositions for four quaternary systems at different P-T conditions corresponding to three-phase coexistence has been compared against the measurements of Chawla et al. (1995).

As mentioned earlier, their approximate compositions were 69% water, 10% n-C_6, 10% n-C_7, and 11% n-C_8; 76% water, 12% n-C_7, 7% n-C_9, and 5% n-C_{12}; and 98% water, 0.2% n-C_{10}, 0.8% n-C_{15}, and 1% n-C_{20}. Table 3.8 gives comparisons between the data and predictions for these cases. In table 3.8, the aforementioned systems have been labelled as systems 1, 2 and 3, respectively. Water has been assigned an index of 1. The n-alkanes have been assigned indices 2, 3 and 4 in the order of increasing CN. The largest value for δ_V (0.2509) occurs for water/n-C_6/n-C_7/n-C_8 system at 438.71 K and 12.94 bars. The values for δ_V presented in table 3.8 indicate that equation 3.5 can yield reasonably accurate predictions for the V-phase composition for multicomponent systems over a wide range of temperatures, pressures, and CNs.

3.3.5. Water-containing bitumens

Due to the lack of experimental data for phase compositions for water/n-alkane mixtures with n-alkane CNs greater than 20, an alternative method for the validation of equation 3.5 is necessary for application to systems comprising heavy hydrocarbons. Water exhibiting the lowest affinity towards n-alkanes in comparison with naphthenes and aromatics. So, equation 3.5 developed for water- is expected to systematically under-predict the dissolution of water in the L phase for water-containing reservoir oils relative to the measured values for x_{wL} data. This is indeed observed to be true. For two water-containing bitumens, Peace River and Athabasca, the results of the validation study are shown in **Figures 3.12** and **3.13**, respectively. The values for the BIPs between the characterized pseudo-

components and water computed using equation 3.2 for the Peace River and Athabasca bitumens are presented is **Tables 3.9** and **3.10**, respectively.

As with Approach 1, equation 3.2 was extended to match the measured x_{wL} data by scaling using a factor (λ) less than unity. For Approach 2, the optimum values for λ for Peace River and Athabasca bitumens are 0.570 and 0.270, respectively (**Figure 3.7**). In contrast, the optimum values for the scaling factors using Approach 1 are 0.780 and 0.415 for Athabasca and Peace River bitumens, respectively. The use of an extended vapor pressure curve for water (Approach 2) results in a systematic under-prediction of x_{wL} in comparison with Approach 1. This in turn necessitates the use of smaller values for λ to obtain a close match with the measured data. For both systems (water/Peace River bitumen and water/Athabasca bitumen), the predicted W-phase density using Approach 2 has been compared against the liquid phase density of pure water along the vapor pressure curve. As seen in **Figure 3.8**, the predicted W-phase density matches using Approach 2 reasonably well the data, which is in contrast with Approach 1 (Figures 3.1b and 3.2b).

For water-containing Athabasca bitumen, the predicted L-phase density (ρ_L) and solubility of water in the L-phase (expressed as a weight fraction, f_w) have been compared against measurements of Amani et al. (2013) for Approach 2. The results are presented in **Table 3.11**. The average deviation in ρ_L is 0.0271 g/cc, which is slightly lower than that from Approach 1 (0.0340 g/cc). In terms of f_w, the average deviation is 0.0133, which is slightly higher than that from Approach

1 (0.0108). This deviation in f_w is within the experimental uncertainty bounds of up to 2.2 wt%.

3.4.Discussion

For water/n-alkanes binaries with CN in the interval [7, 25], the optimized BIPs between water and n-alkanes for Approach 2 are systematically lower than those from Approach 1. Approach 2 employs an extended vapor pressure curve for both the n-alkane and water. The consequence of this is an elongated three-phase curve. The mechanism by which this occurs is through a systematic under-prediction of the dissolution of water in the L phase, and a systematic over-prediction of the concentration of water in the V phase.

Figure 3.9 presents the $\Delta_m\underline{G}/RT$ in composition space for the water/n-C_{20} binary at 167.00 bars and 616.73 K. The specified temperature represents the three-phase equilibrium temperature at 167.00 bars and the specified P-T condition is in the vicinity of the UCEP (see table 2.2). The T_C, P_C and ω employed in this calculation correspond to that for Approach 1 (table C-1). The value of 0.3 is used for the BIP. This represents the optimized BIP for this binary for Approach 1. **Figure 3.10** presents the $\Delta_m\underline{G}/RT$ in composition space for this binary using Approach 2 at the three-phase temperature corresponding to 167 bars. The value for the BIP used in this computation is 0.300 (identical to Figure 3.10). The employment of Approach 2 shifts the three-phase temperature to 620.29 K. In terms of the V- and L-phase compositions, the concentration of water in the V phase is over-predicted, while its dissolution in the L phase is under-predicted. As a result, this BIP (0.300) yields a UCEP considerably higher

than the measured value of 622.70 K and 170.80 bars (Brunner, 1990). To obtain a close match with the experimental data, a lower value of 0.281 is required for the BIP (see table 3.5), for this binary. For Approach 2, the $\Delta_m\underline{G}/RT$ in composition space for this binary at the three-phase temperature corresponding to 167 bars (619.74 K) using the optimized BIP (0.281) is shown in **Figure 3.11**. The phase compositions of the V, L and W phases in Figures 3.17 and 3.18 are quite similar to each other.

In contrast with CNs in the interval [7, 25], the optimized BIPs for Approach 2 are systematically higher than those for Approach 1 for water/n-alkane binaries with CNs in the interval [3, 6]. As shown previously (table 3.2), the optimized critical constants are systematically lower than those for Approach 1 in this CN interval. This is to address the shortcomings of the under-prediction of liquid phase densities of the n-alkanes (Soreide, 1989). Despite the employment of a considerably higher T_C and P_C for water, the optimized BIPs are higher than those for Approach 1. For instance, for the water/n-C_5 binary, the optimized BIP for Approaches 1 and 2 are 0.630 and 0.650, respectively (tables 2.2 and 3.5). This is indicative that for CN ϵ [3, 6], at fixed BIP, the span of the three-phase curve is dictated by the T_C, P_C and ω of the n-alkane to a greater extent than that of water.
For water/n-alkane binaries, the employment of the optimized T_C, P_C and ω for pure components yields a slight improvement in the curvature of the predicted three-phase curve (Tables 2.4 and 3.5). **Figure 3.12** presents the predicted three-phase curve for water/n-C_{25} binary using approaches 1 and 2 along with the experimental measurements of Brunner (1990). The improved accuracy in the

predicted curvature becomes apparent in the near-critical region. In terms of x_{wL}, the aforementioned observation has little impact as the deviations between the predicted x_{wL} and the measured data using both approaches lie within the experimental bounds of uncertainty (tables 2.5 and 3.6).

For ternary and quaternary systems, the predicted x_{wV} and x_{wL} using Approaches 1 and 2 are very similar to each other. For both x_{wL} and x_{wV}, the resulting difference between predictions made using the two approaches is small enough to lie within the experimental uncertainty limits. As seen in tables 2.4, 2.5, 3.7 and 3.8, the resulting values for the composition distance (δ_j) between the predicted V and L-phase compositions and the measured data are similar for both approaches.

As for the dissolution of the hydrocarbon in the W phase, just like Approach 1, Approach 2 systematically under-predicts x_{hcW} by a few orders of magnitude. **Figure 3.13** presents the predicted x_{hcW} for water/n-C_8 binary along the three-phase curve using Approach 2. From Figure 3.13, it is apparent that the improved accuracy in the predicted density of the W phase obtained using Approach 2 (Figure 3.8) is not due to an improvement in the predicted compositional behavior of the W-phase. The underlying mechanism is explained at length later on in this section.

For water-containing Peace River bitumen and water-containing Athabasca bitumen, the distinction between Approaches 1 and 2 in terms of the predicted x_{wL} mainly stems from the choice of T_C, P_C and ω for water. This is evident from the limiting BIP yielded by equation 3.5 is 0.239, which is very close to that yielded

by equation 2.7 for Approach 1 (0.242), and from tables 2.7, 2.9, 3.9 and 3.10, wherein the BIP of the hydrocarbon pseudo-components with water for the two approaches are very similar. For each of the two mixtures, the employment of the optimized critical constants of water, which are substantially greater than the physical values leads to a suppression of the dissolution of water in the L phase. This is apparent by comparing **Figure 3.5** and table 2.9 for Peace River bitumen, and **Figure 3.6** and table 2.7 for Athabasca bitumen. Hence to match the predictions using Approach 2 to the x_{wL} data, the required reduction in the BIP values for Approach 2 is greater than that for Approach 1. This in turn results in lower values for the optimum scaling factor (λ). For water/Peace River bitumen the optimum values for λ for Approaches 1 and 2 are 0.780 and 0.570, respectively. For water/Athabasca bitumen the optimum values for Approaches 1, and 2 are 0.415 and 0.270, respectively.

We now explain the mechanism behind the advantage of Approach 2 over Approach 1 with regard to the prediction of phase densities. The predicted densities of the L phase using Approaches 1 and Approaches 2 for both water-containing Peace River and Athabasca bitumens are quite similar to each other. For water-containing Athabasca bitumen, in addition to tables 3.1 and 3.9, this is evident in **Figure 3.14** in which the predicted densities of the L phase are presented for the conditions shown in Figures 3.13 and 3.14b. For water-containing Peace River bitumen, this is observed in **Figure 3.15** in which the predicted L-phase densities at conditions shown in Figures 3.12 and 3.14a are presented. In contrast, as seen in Figures 3.1b, 3.2b, and 3.5, the predicted W-

phase density using Approach 2 is considerably different than that predicted using Approach 1. The predicted W-phase densities using Approach 2 match more closely with experimental measurements.

For a phase with specified composition, Approaches 1 and 2 would yield similar values for its density if both the attraction parameter (a) and co-volume parameter (equations A-7 and A-8) for the mixture are very similar to each other. As seen in equation A-7, the BIP impacts compositional behavior through the attraction parameter. The tuning of the BIP for each approach to compositional data yields similar values for the attraction parameter for each approach. For the L phase, this point is visualized in **Figure 3.16** for water-containing Peace River bitumen (Figure 3.16a) and water-containing Athabasca bitumen (Figure 3.16b). As for the co-volume parameter of the mixture (equation A-8) can be rewritten in the form shown in equation 3.6,

$$b = x_w b_w + \sum_{i=2}^{N_c} x_i b_i = x_w b_w + \sum x_{hc} b_{hc} \quad (3.6)$$

The critical constants and acentric factors for the hydrocarbon-based pseudo-components are identical for both approaches. So the predicted phase density at specified T and P yielded by both approaches would be very similar to each other if the co-volume parameter of the mixture is dominated by the second term in equation 3.6. For the L phase, the left hand side (LHS) of equation 3.6 is dominated by term the second term of the RHS for both water-containing Peace Rive bitumen and water-containing Athabasca bitumen. This is demonstrated in **Figures 3.17 and 3.18**. Figure 3.17a and Figure 3.18a represent the case for

water-containing Peace River bitumen, while Figure 3.17b and 3.18b represent the case for water-containing Athabasca bitumen.

For the W phase, as the predicted dissolution of hydrocarbon is practically zero (< 10^{-5} in terms of mole fraction), the co-volume parameter of the mixture is dominated by term the first term in equation 3.6. As the infinite dilution limit is approached, the value for the first term in equation 3.6 is governed by the co-volume parameter of water. Specifically, it is governed by the ratio of its critical pressure to its critical temperature ($T_{C,w}/P_{C,w}$). This ratio is equivalent to 2.9328 and 2.4264 for Approaches 1 and 2, respectively. The difference between the two values albeit small, the resulting impact on the predicted density of the W phase is significant.

3.5 Application of Approach 2 in steam-solvent coinjection

3.5.1. Overview

In this section, we perform a simplistic simulation of the steam-solvent SAGD process for the recovery of the Athabasca bitumen. The software used for this purpose is the commercial thermal reservoir simulator, STARS (Computer Modelling Group Limited). The focus of this simulation study is to provide a quantitative perspective of the importance of the consideration of the dissolution of water in the L phase on the drainage of bitumen in steam-solvent co-injection processes. The solvent employed in this simulation is n-pentane (n-C_5). It is of importance to note that STARS is not an EOS-based simulator. The thermodynamic behavior of water/bitumen/solvent mixtures is reflected through

component K-values, defined as the ratio of component-specific concentrations across phases, tabulated as functions of temperature and pressure. The demonstration of the significance of x_{wL} on oil drainage rates involves the definition of two cases:

- Base case, wherein the dissolution of water in the L phase, and the dissolution of the hydrocarbon components in W phase are neglected. The bitumen is characterized as a single pseudo-component, C_D. The K-values for n-C_5 and C_D are generated using P-T flash calculations with the PR EOS for pertinent overall compositions lying on the n-C_5/C_D edge of the ternary composition space (i.e., the n-C_5/C_D binary limit in composition space). The K-values of water are generated based on Raoult's law. The base case is representative of a thermodynamic modeling method that is commonly employed in current, non-EOS thermal reservoir simulation practice.
- Modified case, wherein the dissolution of water in the L phase is considered while the dissolution of the hydrocarbon components in W phase is neglected. The PR EOS employing Approach 2 is used to generate component K-values for the V and L phases. Again, the bitumen is characterized as single pseudo-component.

The T_C, P_C and ω of the hydrocarbon components used in this study are: (469.70 K, 33.70 bars and 0.2511) for n-C_5, (469.70 K, 33.70 bars and 0.2511) for C_D (Mehrotra and Svercek, 1987). For water, the values for T_C, P_C and ω are 672.48 K, 277.15 bars, and 0.2699, respectively. The BIPs between water and n-

C_5, water and C_D, and n-C_5 and C_D are 0.5370, 0.0445, and 0.0650, respectively. The molecular weights of the hydrocarbon components are 72.15 g/mole for n-C_5 and 594.60 g/mole for C_D.

The molar density and viscosity of the system phases are calculated by the simulator using mixing rules. Equation 3.7 presents the mixing rule employed for the molar density of phase j (ρ_j).

$$\frac{1}{\rho_j} = \sum_{i=1}^{N_c} \frac{x_{ij}}{\rho_{ij}} \tag{3.7}$$

where x_{ij} is the mole fraction of component i in phase j, and ρ_{ij} represents the molar density of component i in phase j. The expression for the mixing rule for the L-phase viscosity is furnished in equation 3.8.

$$\mu_j = \sum_{i=1}^{N_c} x_{ij} \ln \mu_{ij} \tag{3.8}$$

where μ_{ij} represents the viscosity of component i in phase j.

3.5.2. Reservoir model

In this study, one half of the ES-SAGD chamber is simulated over a span of 10 years in two-dimensional space. The specifications of this reservoir model are identical to that of Keshavarz et al. (2013). The dimensions of this 2-d reservoir model are 70 m, 37.5 m and 20 m, in the x, y and z directions respectively. The reservoir is fragmented into 70, 1 and 20 grid blocks in the x, y, and z directions, respectively. The grid blocks are of uniform size with dimensions 1 x 37.5 x 1 m^3. The production well is located 3m above the bottom of the reservoir model, with the injection located 4m above the production well.

The initial temperature and pressure (at 15 m depth) of the reservoir are 286.15 K, and 15 bars, respectively. The porosity of the reservoir is 0.30. The vertical and horizontal permeabilities are 3000 md and 4000 md, respectively. The relative permeability model employed in this work is that of Stone (model II, CMG 2011).

Prior to the commencement of the process, the reservoir is considered to comprise of only two components, bitumen with a saturation of 0.75, and water with a saturation of 0.25. Steam of quality 0.9 is injected into the reservoir at 27.30 bars. The concentration of the injected solvent is 2 mol%. The maximum values for the bottom-hole pressure for the injector and producer wells are 27.30 bars and 15 bars, respectively. At 27.30 bars, the saturation temperature of water is approximately 502.00 K. The saturation temperature of water at the injection pressure represents the upper bound for the reservoir temperature. The reservoir is subjected to an initial heating period of 6 months during which bitumen is not produced.

3.5.3. Specification of component K-values

Prior to the generation of K-value tables, it is essential to understand how the phase behavior in the ES-SAGD process is modeled in STARS. A maximum of 3 phases is considered to exist. Three phases, V, L and W exist within the confines of the ES-SAGD chamber. The V phase disappears at the chamber edge and only two phases, L and W, exist beyond it. STARS accommodates the input of up to two sets of K-values. One represents the vapor-liquid equilibrium (for the V and L phases, and V and W phases), while the other represents the liquid-liquid

equilibrium (for the L and W phases). For both cases (base and modified), the dissolution of the hydrocarbon components is assumed to be negligible, obviating the use of liquid-liquid K-value tables for the hydrocarbon components. For the base case, as x_{wL} is considered to be zero, the input of liquid-liquid K value tables for water is unnecessary. In contrast, it is necessary for the modified case owing to the consideration of x_{wL}.

As outlined above, the number of system phases and their respective identities are fixed a priori by the simulator. A potentially detrimental consequence of this assumption is that the existence of a solvent-rich phase L′ is neglected. The PR EOS predicts the occurrence of L′ for both the base and modified cases. In **Figure 3.19**, the predicted T-x cross-section at 27 bars, representative of the operating pressure of this simulation, for the n-C_5/C_D binary mixture is presented. This T-x cross-section (Figure 3.19) is of significance with regard to the base case. This is because the K-values for n-C_5 and C_D for the ES-SAGD process are computed from flash calculations performed at the n-C_5/C_D binary limit in ternary composition space. As seen in Figure 3.19, at 27 bars, for temperatures lower than the three-phase temperature (≈ 455.30 K), the two-phase region comprises of the oleic (L) and the solvent-rich (L′) phases. **Figure 3.20** presents the predicted three-phase region for the water/n-C_5/C_D system at 432.15 K and 27 bars using Approach 2. The three-phase temperature of the water/n-C_5 binary at 27 bars is 434.79 K. So, at temperatures lower than 434.79 K, it is the phase L′ phase that is in equilibrium with the L and W phases.

The inclusion of component K-values based on the L-L′ edge of the tie-triangle as part of the vapor-liquid K-value tables leads to failure of convergence of the simulation. To circumvent this, for P-T conditions at which L′ occurs, the fictitious V phase is defined, and the K-values computed based on the fictitious V-L-W equilibrium are employed to perform the simulation. The rationale behind this adjustment is now explained. The focus of this simulation study is to investigate the potential significance of proper representation of the compositional behavior of the L phase. The definition of a fictitious V phase in lieu of the L′ does not affect the L-W edge of the tie-triangle. For both the base and modified cases, this is demonstrated for 27 bars and 423.15 K in **Figure 3.21**. The compositional behavior of the fictitious V phase is determined by first setting the mole fraction of C_D to be 10^{-7}, which is a reasonable estimate given its low volatility. The relative amounts of n-C_5 and water in this fictitious V phase are then estimated using Raoult's law for water.

3.5.4. Results

The daily production rate and cumulative production of bitumen for the base and modified cases are presented in **Figure 3.22**. The gas saturation profiles for the two cases at 1 year from the commencement of operation are presented in **Figure 3.23**. For the same time period, **Figures 3.24 and 3.25** present the temperature and V-phase saturation profiles for the base and modified cases, respectively. The L-phase saturation profiles are presented in **Figure 3.26**. The L-phase viscosity and mobility profiles are presented in **Figures 3.27 and 3.28**, respectively. The molar density profiles are presented in **Figure 3.29**. The

concentration profiles of the components in the L phase are presented in **Figure 3.30**. **Figure 3.31** presents the global concentration profiles for the two cases.

3.5.5. Analysis of simulation results

At the end of 1 year of operation, the daily production rate for the base and modified cases are 13.97 m^3/day and 15.90 m^3/day, respectively (Figure 3.22). The modified case yields an increased estimate of 13.82% relative to the base case. Figure 3.23 indicates that the propagation of the ES-SAGD chamber is enhanced when the dissolution of water in the L phase is considered. We now examine the mechanisms that result in this observation. Keshavarz et al. (2014) derived the following expression (equation 1.5, shown below) for the oil drainage rate for the SAGD operation.

$$q_o = \sqrt{0.5 k k_{rL} g \phi \Delta S_o H (U_m . I_o)} \tag{1.5}$$

For the ES-SAGD process, the integral term in equation 1.5 is formulated as shown in equation 3.9.

$$I_o = -(\alpha/\varepsilon U_m) \int_{T_{edge}}^{T_R} \left\{ \left[\left(MW_L \rho_L C_{C_D} \right) / \mu_L \right] / (T - T_R) \right\} dT \tag{3.9}$$

where C_{CD} represents the volume fraction of the bitumen component in the L phase. The impact of the consideration of x_{wL} on oil drainage rate can be analytically quantified from the ratio $\frac{{q_o}^{modified}}{{q_o}^{base}}$. The computation of this ratio can be facilitated from the following simplifying assumption:

$$\frac{{I_o}^{modified}}{{I_o}^{base}} \sim \frac{\left(\frac{MW_L \rho_L C_{C_D}}{\mu_L} \right)^{modified}}{\left(\frac{MW_L \rho_L C_{C_D}}{\mu_L} \right)^{base}} \tag{3.10}$$

This leads to:

$$\frac{{q_o}^{\text{modified}}}{{q_o}^{\text{base}}} \sim \left(\frac{\left(\sqrt{\lambda_L MW_L \rho_L C_{C_D}}\right)^{\text{modified}}}{\left(\sqrt{\lambda_L MW_L \rho_L C_{C_D}}\right)^{\text{base}}} \right) \left(\frac{\left(\sqrt{0.75 - {S_L}^{\text{edge}}}\right)^{\text{modified}}}{\left(\sqrt{0.75 - {S_L}^{\text{edge}}}\right)^{\text{base}}} \right) \tag{3.11}$$

Based on equation 3.11, at 365 days, the ratio, $\frac{{q_o}^{\text{modified}}}{{q_o}^{\text{base}}}$, is equal to 1.1467. For the two cases, the values for the physical properties correspond to that at the chamber edge (refer to Figures 3.24 through Figure 3.31). So from equation 3.11, the modified case presents an increase of 14.67% relative to the base case, in terms of the production rate at 365 days. This matches reasonably well with the result observed from the simulation (13.82%). The individual contributions of the property-specific ratios to $\frac{{q_o}^{\text{modified}}}{{q_o}^{\text{base}}}$ are presented in equations 3.12 through 3.16.

$$\frac{\left(\sqrt{\lambda_L}\right)^{\text{modified}}}{\left(\sqrt{\lambda_L}\right)^{\text{base}}} = 1.1801 \tag{3.12}$$

$$\frac{\left(\sqrt{MW_L}\right)^{\text{modified}}}{\left(\sqrt{MW_L}\right)^{\text{base}}} = 0.9295 \tag{3.13}$$

$$\frac{\left(\sqrt{\rho_L}\right)^{\text{modified}}}{\left(\sqrt{\rho_L}\right)^{\text{base}}} = 1.0630 \tag{3.14}$$

$$\frac{\left(\sqrt{C_{C_D}}\right)^{\text{modified}}}{\left(\sqrt{C_{C_D}}\right)^{\text{base}}} = 0.9670 \tag{3.15}$$

$$\frac{\left(\sqrt{0.75 - {S_L}^{\text{edge}}}\right)^{\text{modified}}}{\left(\sqrt{0.75 - {S_L}^{\text{edge}}}\right)^{\text{base}}} = 1.0169 \tag{3.16}$$

From equations 3.12 through 3.16, we see that the governing physical properties in equation 3.11 are the L-phase mobility, followed by the L-phase molar density. These results presented above indicate that the accounting of x_{wL} can be of importance in the recovery of oil using solvent-steam coinjection processes. The dissolution of water in the L phase enhances the local displacement efficiency through the enhancement of the mobility and molar density of the L phase.

We now elucidate the shortcomings of this simplistic simulation case study. The first shortcoming of this simulation case study is that the K-values of the components are tabulated solely as a function of temperature and pressure. The dependence of the K-values on overall composition is neglected contrary to physical behavior.

Second, the reliability of this simulation study is confined to early times of the operation (1 year or less). The reason for this is related to the employment of K-values based on fictitious V-L-W tie-triangles. The consequence of such a specification method to perform the simulation is that the chamber edge temperature can be multivalued. To understand this, we first take a closer examination of the trend in the predicted tie-triangles for the water/n-C_5/C_D ternary at 27 bars for various temperatures using Approach 2 (**Figure 3.32**). As seen in Figure 3.32, the V-L-W region disappears as the temperature falls towards the three-phase temperature of the water/n-C_5 binary (434.79 K at 27 bars). As the temperature falls below the three-phase temperature of the water/n-C_5 binary and drops further, towards the initial reservoir temperature, we observe the emergence

and growth of the L′-L-W region in composition space. These phase diagrams clearly indicate that a specified global composition that is rich in water (> 50 mol%) can lie on both the L-W edge of V-L-W region, and the L′-W edge of the L′-L-W region. This observation holds for the base case as well (See Figure 3.19). As mentioned earlier, a fictitious V phase is defined in place of the L′ phase to avoid the failure of convergence. We now describe the effect of this in flow simulation. As the ES-SAGD operation proceeds in time, the retention of n-C_5 in the reservoir increases, leading to an increase in the global concentration of n-C_5 in the grid blocks into which the reservoir is fragmented. This in turn results in an increase of the likelihood of the global composition of the mixture to lie on the L-W edge of both the physical and fictitious V-L-W tie-triangles. When this occurs, the simulator considers the temperature corresponding to the fictitious tie-triangle as the representative temperature for the chamber edge. So, the observed implications of the employment fictitious tie-triangles are: first, the simulated chamber edge temperature can be multivalued, which is in violation in regard to our physical understanding of the ES-SAGD process, and second, the chamber temperature can be significantly lower than the three-phase temperature of the water/n-C_5 binary at the operating pressure, which is in violation with our understanding of the thermodynamic behavior of the water/n-C_5/C_D ternary. These implications restrict the reliability of the simulation to only early times of the operation (for instance, 1 year) when the accumulation of n-C_5 is not nearly as significant as at later times. Other potential shortcomings of this simulation case study include the employment of simplistic mixing rules for phase densities and

viscosities, lack of consideration of the dependence of relative permeabilities on temperature, and characterization of the Athabasca bitumen as a single pseudo-component.

3.6 Summary and conclusions

This chapter presented a new framework (Approach 2) to characterize water-containing reservoir oils. The advantage of this framework over Approach 1 stems from its capability to represent both the multiphase compositional and volumetric behavior of mixtures of water/reservoir oils with reasonable accuracy. As with Approach 1, a new correlation was developed for binary interaction parameters (BIPs) for water with n-alkanes, which was subsequently extended to represent the phase behavior of water-containing bitumens. Prior to developing the new BIP correlation, the critical constants (T_C, P_C) and acentric factors for n-alkanes with CNs < 7, and water were first optimized against the experimentally measured vapor pressure and liquid phase density data using the method of Kumar and Okuno (2012). The development of the BIP correlation between water and n-alkanes with the optimized T_C, P_C, and ω for both the n-alkanes and water used the measured three-phase curves (including UCEPs) of water/n-alkane binaries presented by Brunner (1990). For n-alkanes heavier than n-C_6, the optimized T_C, P_C, and ω were obtained from the prior work of Kumar and Okuno (2012). The developed BIP correlation between water and n-alkanes was validated against the published phase composition data for both water/n-alkane and water/reservoir oil mixtures. A simplistic simulation of the ES-SAGD process was performed with n-C_5 as the solvent, injected at a rate of 2 mol%. The

purpose of the simulation study is to investigate the potential importance of the dissolution of water in the L phase on the oil drainage rate. The compositional behavior predicted using Approach 2 was used for the simulation study. The conclusions of this chapter are as follows:

1. The PR EOS with classical mixing rules employing Approach 1 is capable of predicting the density of the L phase with reasonably accuracy. But it yields erroneous estimates for the density of the W phase through systematic under-prediction. This can potentially affect oil recovery predictions in reservoir simulation through the inaccurate prediction of fluid saturations in the reservoir.

2. For n-alkanes with CN $\leq$ 6, the optimized values for the critical constants are lower than the physical values while those for ω are higher than the physical values. This trend is required to correct the over-prediction of L phase densities by the PR EOS for these n-alkanes. For water, the optimized T_C and P_C are considerably higher than the physical values, while the opposite true for the optimized value of ω. This is necessary to correct for the systematic under-prediction of the liquid phase density by the PR EOS.

3. The consequence of the difference in the trend in the optimized T_C, P_C, and ω for CNs in the interval [1, 6], and those in the interval [7, 100] relative to the physical values (which are similar to Approach 1) is that the optimized BIPs between water and n-alkanes for Approach 2 in the CN interval [7, 25] are systematically lower than those for Approach 1. The reverse is true in the CN interval [3, 6].

4. The predicted three-phase curves for water/n-alkane binaries using Approach 2 exhibit a curvature that is slightly more consistent with the measured three-phase curves of Brunner (1990). However, in terms of the predicted phase compositions (V, L and W) for both binary and multicomponent systems, both approaches yield very similar values, with the apparent difference in predictions lying within the experimental uncertainty bounds.

5. For water/bitumen mixtures, the employment of Approach 2 results in a slight improvement in accuracy of the predicted density of the L phase and a significant improvement in the predicted density of the W phase. The co-volume parameter has a significant impact on density predictions, and is crucial for understanding the mechanism behind the aforementioned observation.

6. As with Approach 1, the solubilities of n-alkanes in the aqueous phase (x_{hcW}) predicted using Approach 2 are orders of magnitude lower than experimental data. Hence, the framework proposed in this chapter is not recommended for applications in which the quantitative accuracy of x_{hcW} is important.

7. Numerical simulation of the ES-SAGD process indicates that the dissolution of water in the L phase can have considerable impact on the drainage of bitumen. The main mechanisms for the observed increase in the local displacement efficiency of the process are that the dissolution of water in the L phase enhances the mobility and the molar density of the L phase.

Table 3.1. Accuracy of predicted concentration of water in the L phase (expressed as weight fraction, f_w), and density of L phase (ρ_L) for water/Athabasca bitumen (z_w = 0.8115), using Approach 1. The overall composition of the mixture used in the volumetric behavior measurements has not been explicitly stated by Amani et al. (2013). The average absolute deviations (AADs) for the predicted f_w and ρ_L, computed relative to the data, are 0.0108 and 0.0340 g/cc, respectively.

T, K	P, bar	f_w (EOS)	f_w (Data)	ρ_L (EOS), g/cc	ρ_L (Data)	AD in f_w	AD in ρ_L, g/cc
593.10	54	0.0207	0.0400	0.8493	0.8240	0.0193	0.0253
593.10	122	0.0738	0.0810	0.7590	0.7610	0.0072	0.0020
593.30	118	0.0753	0.0810	0.7552	0.7689	0.0057	0.0137
593.30	122	0.0741	0.0810	0.7583	0.7883	0.0069	0.0300
593.20	120	0.0745	0.0810	0.7571	0.7653	0.0065	0.0082
593.00	122	0.0736	0.0810	0.7594	0.7875	0.0074	0.0281
593.00	119	0.0745	0.0810	0.7571	0.7625	0.0065	0.0054
603.70	55	0.0197	0.0400	0.8470	0.8164	0.0203	0.0306
603.40	133	0.0910	0.0940	0.7245	0.7588	0.0030	0.0343
603.70	140	0.0885	0.0940	0.7306	0.7603	0.0055	0.0297
603.90	148	0.0857	0.0950	0.7376	0.7648	0.0093	0.0272
603.40	144	0.0862	0.0940	0.7360	0.7660	0.0078	0.0300
602.90	141	0.0863	0.0930	0.7353	0.7684	0.0067	0.0331
603.60	138	0.0892	0.0940	0.7290	0.7603	0.0048	0.0313
613.50	144	0.1011	0.1020	0.7020	0.7523	0.0009	0.0503
613.60	161	0.1047	0.1080	0.7021	0.7418	0.0033	0.0397
613.50	179	0.0946	0.1080	0.7242	0.7669	0.0134	0.0427
613.50	178	0.0950	0.1080	0.7232	0.7411	0.0130	0.0179
613.30	171	0.0980	0.1080	0.7165	0.7657	0.0100	0.0492
613.20	165	0.1010	0.1080	0.7098	0.7574	0.0070	0.0476
623.40	60	0.0197	0.0400	0.8392	0.8088	0.0203	0.0304
623.10	149	0.0957	0.1020	0.7041	0.7501	0.0063	0.0460
623.00	195	0.1132	0.1230	0.6919	0.7592	0.0098	0.0673
623.10	207	0.1058	0.1240	0.7071	0.7626	0.0182	0.0555
623.30	210	0.1047	0.1240	0.7096	0.7484	0.0193	0.0388
623.30	228	0.0962	0.1240	0.7279	0.7414	0.0278	0.0135
633.60	162	0.1037	0.1020	0.6850	0.7456	0.0017	0.0606
633.90	260	0.1071	0.1430	0.7120	0.7558	0.0359	0.0438
642.80	68	0.0210	0.0400	0.8283	0.7847	0.0190	0.0436
644.10	170	0.1032	0.1020	0.6790	0.7220	0.0012	0.0430

Table 3.2 Optimum values for T_C, P_C and ω for water and n-alkanes (C_1 to n-C_6) for Approach 2

Component	Approach 2			Approach 1		
	T_C, K	P_C, bar	ω	T_C, K	P_C, bar	ω
C_1	187.41	41.55	0.0258	190.56	45.99	0.0157
C_2	299.54	43.33	0.1218	305.32	48.72	0.0906
C_3	366.07	40.00	0.1708	369.83	42.48	0.1543
n-C_4	421.56	36.01	0.2127	425.12	37.96	0.2014
n-C5	466.98	32.14	0.2524	469.70	33.70	0.2511
n-C_6	505.89	29.49	0.3027	507.60	30.25	0.3010
Water	672.48	277.15	0.2699	647.10	220.64	0.3433

Table 3.3. AAD% for liquid density prediction from PR EOS using values for physical and optimized T_C, P_C, and ω

Component	Data sources	Number of data points	Temperature range (T_r)	Pressure range (T_r)	%AAD (Physical)	%AAD (Optimized)
C_1	Klimeck et al. (2001), Perry and Green (2008)	176	1.26-2.72	0.00-6.54	8.89	4.42
C_2	Philips and Thodos (1962), Claus et al. (2003)	111	0.70-2.00	1.00-14.00	5.67	3.00
C_3	Glos et al. (2004), Kayukaw a et al. (2005)	97	0.26-1.03	0.03-2.80	5.02	2.80
n-C_4	Glos et al.(2004), Kayukaw a et al. (2005), Miyamoto and Uematsu (2007)	222	0.33-0.89	0.01-3.20	4.19	1.54
n-C5	Lee and Ellington (1965)	164	0.66-0.91	0.20-16.40	4.24	1.55
n-C_6	Kelso and Felsing (1940)	42	0.75-1.30	0.18-7.30	2.97	1.84
Water	Cengel and Bole (2001)	2505	0.42-0.99	0.00-0.99	16.68	1.52

Table 3.4 AAD% for vapor pressure prediction from PR EOS using values for physical and optimized T_C, P_C, and ω

Component	Data sources	Number of data points	%AAD (Physical)	%AAD (Optimized)
C_1	Perry and Green (2008)	18	0.61	0.12
C_2	Funke et al. (2002)	20	0.72	0.49
C_3	Perry and Green (2008)	18	1.41	0.92
n-C_4	Miyamoto and Uematsu (2007), Perry and Green (2008)	20	0.59	0.54
n-C_5	Ewing and Ochoa (2006a), Beattie et al. (1951), Sage and Lacey (1942)	53	0.49	0.12
n-C_6	Ewing and Ochoa (2006b), Perry and Green (2008)	67	0.41	0.22
Water	Cengel and Bole (2001)	75	3.85	0.88

Table 3.5. Optimized and resulting deviations of three-phase curve predictions, and correlated BIP values for Approach 2

CN	MW	BIP	Number of	AAD in $T_{3\phi}$	UCEP (Optimized BIP)		AD in UCEP		BIP
	g/mol	(Optimized)	data points	K	T_{UCEP}, K	P_{UCEP}, bar	T_{UCEP}, K	P_{UCEP}, bar	(Correlation)
3	44.10	0.690	5	0.27	365.73	40.74	3.97	1.86	0.584
4	58.12	0.670	9	0.81	419.68	40.24	4.42	2.36	0.560
5	72.15	0.650	7	0.63	461.53	44.06	2.27	1.71	0.537
6	86.18	0.580	6	1.56	493.35	52.15	3.05	0.67	0.515
7	100.20	0.483	8	0.64	517.77	62.29	2.23	0.91	0.493
8	114.23	0.472	7	2.21	536.42	73.22	3.58	0.88	0.473
9	128.26	0.453	11	1.03	551.36	84.11	2.64	1.29	0.454
10	142.28	0.444	5	1.76	564.27	95.59	3.33	0.96	0.435
11	156.31	0.480	13	2.73	574.48	106.93	3.32	0.57	0.417
12	170.34	0.410	12	0.88	583.46	116.09	1.34	0.51	0.400
14	198.39	0.372	13	0.84	597.33	133.63	1.37	0.47	0.367
16	226.44	0.337	11	0.58	606.68	146.88	1.62	1.82	0.338
18	254.50	0.303	12	1.29	614.00	158.14	2.50	2.56	0.310
20	282.55	0.281	11	1.31	621.57	171.22	1.13	0.42	0.285
24	338.66	0.244	8	0.89	633.29	193.54	0.59	0.46	0.243
25	352.68	0.239	15	0.80	636.83	200.99	0.43	1.21	0.240

Table 3.6. Deviations of predicted water solubilities in the L phase (x_{wL}) for a few different water/n-alkane binaries using Approach 2

CN	Number of data points	AAD in x_{wL}	Data sources	Average uncertainty in x_{wL} data
3	9	0.007	Kobayashi and Katz (1953)	0.001
4	7	0.003	Reamer et al. (1944)	0.005
6	6	0.025	Skripka (1979), Tsonopoulos and Wilson (1983), Maczynski et al. (2005)	0.027
7	4	0.005	Skripka (1979)	0.055
8	5	0.014	Skripka (1979), Heidman et al. (1985), Shaw et al. (2005)	0.066
9	5	0.029	Skripka (1979)	0.098
10	6	0.011	Skripka (1979), Shaw et al. (2006a)	0.101
12	3	0.026	Skripka (1979)	0.139
16	5	0.025	Skripka (1979), Shaw et al. (2006b)	0.113
20	6	0.039	Skripka (1979)	0.170

Table 3.7. Deviations of predicted three-phase compositions for a mixture of 75.97% water, 12.92% C_3, 5.44% n-C_5, and 5.67% n-C_8. The deviations are expressed as distances (δ) in composition space.

Case	T, K	P, bar	δ_V	δ_L	δ_W
1	313.00	7.00	0.01404	0.01569	0.00087
2	338.00	11.76	0.02113	0.02899	0.00003
3	373.00	20.34	0.08854	0.02552	0.00027
4	393.00	26.33	0.08888	0.02814	0.00032
5	423.00	39.30	0.07034	0.04747	0.00130
6	448.00	51.50	0.13638	0.08192	0.00318

Table 3.8. Deviations of predicted V-phase compositions for quaternary mixtures presented in Chawla et al. (1995). Systems 1 through 3 have been specified above.

System	T	P	x_{iV} (EOS)				x_{iV} (Data)				δ_V
number	K	bar	i = 1	i = 2	i = 3	i = 4	i = 1	i = 2	i = 3	i = 4	
1	399.82	4.53	0.5351	0.1840	0.1529	0.1279	0.4800	0.2700	0.1500	0.1000	0.1059
1	416.48	6.87	0.5717	0.1393	0.1384	0.1506	0.4900	0.2500	0.1700	0.0900	0.1536
1	438.71	12.94	0.5337	0.2156	0.1452	0.1056	0.3200	0.3000	0.2400	0.1400	0.2509
1	455.37	19.00	0.5315	0.2211	0.1432	0.1042	0.5700	0.1800	0.1400	0.1100	0.0567
1	472.04	26.80	0.5320	0.2091	0.1454	0.1135	0.4500	0.2300	0.1700	0.1500	0.0954
1	488.71	36.59	0.5314	0.1829	0.1503	0.1355	0.6500	0.1300	0.1000	0.1200	0.1401
1	510.93	52.86	0.5377	0.1491	0.1491	0.1640	0.6000	0.1300	0.1300	0.1400	0.0721
2	404.82	3.50	0.8172	0.1168	0.0529	0.0132	0.8000	0.1500	0.0480	0.0020	0.0393
2	416.48	5.70	0.6974	0.2443	0.0517	0.0065	0.7500	0.1750	0.0600	0.0150	0.0878
2	438.71	10.00	0.7099	0.2259	0.0553	0.0089	0.7800	0.1500	0.0650	0.0050	0.1039
2	455.37	14.90	0.7039	0.2295	0.0563	0.0103	0.7300	0.1800	0.0700	0.0200	0.0584
2	472.04	21.30	0.7052	0.2215	0.0602	0.0131	0.7700	0.1400	0.0600	0.0300	0.1055
2	488.71	29.90	0.6975	0.2217	0.0645	0.0163	0.7500	0.1500	0.0800	0.0200	0.0903
2	510.93	42.93	0.7322	0.1616	0.0741	0.0320	0.7000	0.1700	0.1200	0.0100	0.0608
2	527.59	56.24	0.7359	0.1392	0.0768	0.0481	0.7700	0.1100	0.0800	0.0400	0.0457
3	394.26	2.00	0.9966	0.0017	0.0015	0.0001	0.9600	0.0300	0.0009	0.0091	0.0472
3	422.04	4.50	0.9956	0.0018	0.0024	0.0002	0.9450	0.0500	0.0010	0.0040	0.0700
3	449.82	9.40	0.9930	0.0028	0.0038	0.0004	0.9450	0.0540	0.0009	0.0001	0.0703
3	477.59	17.40	0.9835	0.0093	0.0063	0.0008	0.9400	0.0580	0.0019	0.0001	0.0655
3	505.37	30.00	0.9821	0.0069	0.0091	0.0020	0.9350	0.0590	0.0030	0.0030	0.0705
3	533.15	49.00	0.9711	0.0108	0.0139	0.0043	0.9350	0.0590	0.0030	0.0030	0.0612

Table 3.9. Properties of the Peace River bitumen containing water. BIPs with water are based on equation 3.2. Data given in Mehrotra and Svrcek (1985) were used to characterize PC1, PC2, PC3, and PC4.

Component	z_i	MW, g/mol	T_C, K	P_C, bar	ω	BIP with water
Water	0.7300	18.01	672.48	277.15	0.2699	0.000
PC1	0.0961	330.22	773.64	15.08	0.7907	0.248
PC2	0.0650	505.04	836.99	11.48	0.9932	0.239
PC3	0.0485	662.27	870.20	9.57	1.1151	0.239
PC4	0.0604	952.11	902.17	7.41	1.2654	0.239

Table 3.10. Properties of the Athabasca bitumen containing water. BIPs with water are based on equation 3.2. Data given in Badamchi-Zadeh et al. (2009) were used to characterize PC1, PC2, PC3, and PC4.

Component	z_i	MW, g/mol	T_C, K	P_C, bar	ω	BIP with water
Water	0.8115	18.01	672.48	277.15	0.2699	0.000
PC1	0.0754	345.52	1024.88	17.54	0.8503	0.241
PC2	0.0493	528.46	1137.29	13.35	1.0564	0.239
PC3	0.0376	692.98	1207.42	11.20	1.1782	0.239
PC4	0.0262	996.26	1292.51	8.78	1.3301	0.239

Table 3.11. Accuracy of predicted concentration of water in the L phase (expressed as weight fraction, f_w), and density of L phase (ρ_L) for water/Athabasca bitumen ($z_w = 0.8115$), using Approach 2. The average absolute deviations (AADs) for the predicted f_w and ρ_L, computed relative to the data, are 0.0133 and 0.0271 g/cc, respectively.

T, K	P, bar	f_w (EOS)	f_w (Data)	ρ_L (EOS), g/cc	ρ_L (Data)	AD in f_w	AD in ρ_L, g/cc
593.10	54	0.0213	0.0400	0.8512	0.8240	0.0187	0.0272
593.10	122	0.0721	0.0810	0.7716	0.7610	0.0089	0.0106
593.30	118	0.0735	0.0810	0.7681	0.7689	0.0075	0.0008
593.30	122	0.0724	0.0810	0.7709	0.7883	0.0086	0.0174
593.20	120	0.0728	0.0810	0.7699	0.7653	0.0082	0.0046
593.00	122	0.0719	0.0810	0.7719	0.7875	0.0091	0.0156
593.00	119	0.0727	0.0810	0.7699	0.7625	0.0083	0.0074
603.70	55	0.0204	0.0400	0.8487	0.8164	0.0196	0.0323
603.40	133	0.0885	0.0940	0.7399	0.7588	0.0055	0.0189
603.70	140	0.0864	0.0940	0.7452	0.7603	0.0076	0.0151
603.90	148	0.0839	0.0950	0.7513	0.7648	0.0111	0.0135
603.40	144	0.0843	0.0940	0.7500	0.7660	0.0097	0.0160
602.90	141	0.0843	0.0930	0.7495	0.7684	0.0087	0.0189
603.60	138	0.0870	0.0940	0.7438	0.7603	0.0070	0.0165
613.50	144	0.1130	0.1020	0.6958	0.7523	0.0110	0.0565
613.60	161	0.1021	0.1080	0.7186	0.7418	0.0059	0.0232
613.50	179	0.0933	0.1080	0.7381	0.7669	0.0147	0.0288
613.50	178	0.0937	0.1080	0.7371	0.7411	0.0143	0.0040
613.30	171	0.0963	0.1080	0.7312	0.7657	0.0117	0.0345
613.20	165	0.0989	0.1080	0.7253	0.7574	0.0091	0.0321
623.40	60	0.0204	0.0400	0.8405	0.8088	0.0196	0.0317
623.10	149	0.1083	0.1020	0.6951	0.7501	0.0063	0.0550
623.00	195	0.1117	0.1230	0.7074	0.7592	0.0113	0.0518
623.10	207	0.1051	0.1240	0.7209	0.7626	0.0189	0.0417
623.30	210	0.1041	0.1240	0.7231	0.7484	0.0199	0.0253
623.30	228	0.0961	0.1240	0.7400	0.7414	0.0279	0.0014
633.60	162	0.1203	0.1020	0.6704	0.7456	0.0183	0.0752
633.90	260	0.1082	0.1430	0.7234	0.7558	0.0348	0.0324
642.80	68	0.0219	0.0400	0.8293	0.7847	0.0181	0.0446
644.10	170	0.1205	0.1020	0.6622	0.7220	0.0185	0.0598

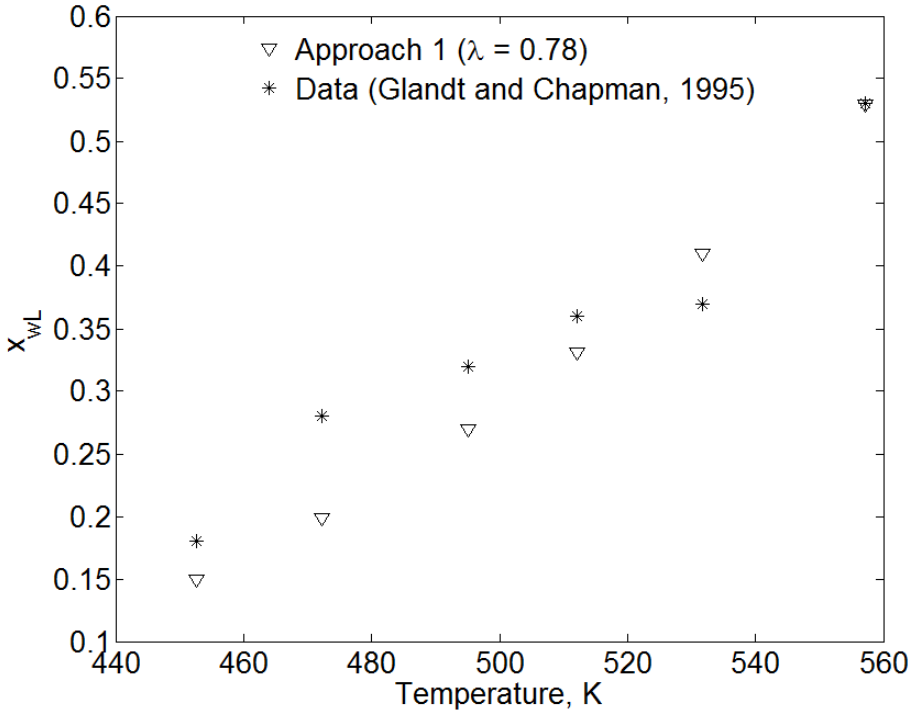

Figure 3.1a. Water solubilities predicted near the V-L-W/L-W boundary for the water/Peace-River-bitumen mixture (Table 2.8) for Approach 1. The BIPs in table 2.8 were scaled by a factor (λ) of 0.78. Experimental data were taken from Glandt and Chapman (1995). The water concentrations for the V and W phases were predicted to be greater than 0.99.

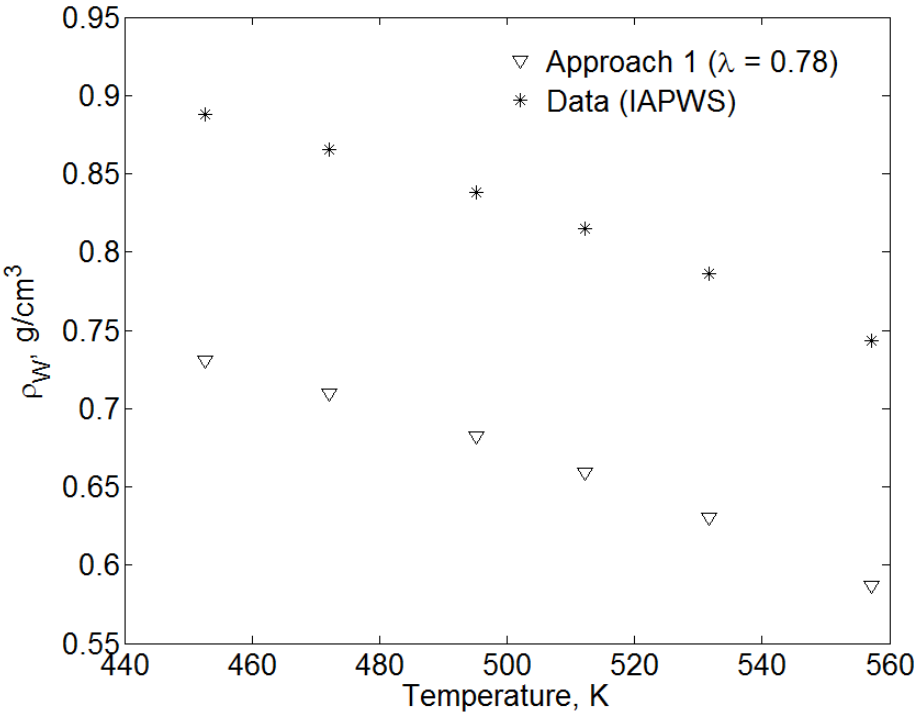

Figure 3.1b. Predicted density of the W phase near the V-L-W/L-W boundary for the water/Peace-River-bitumen mixture given in table 2.8. The density data for the W phase correspond to the density of liquid water along the saturation pressure curve.

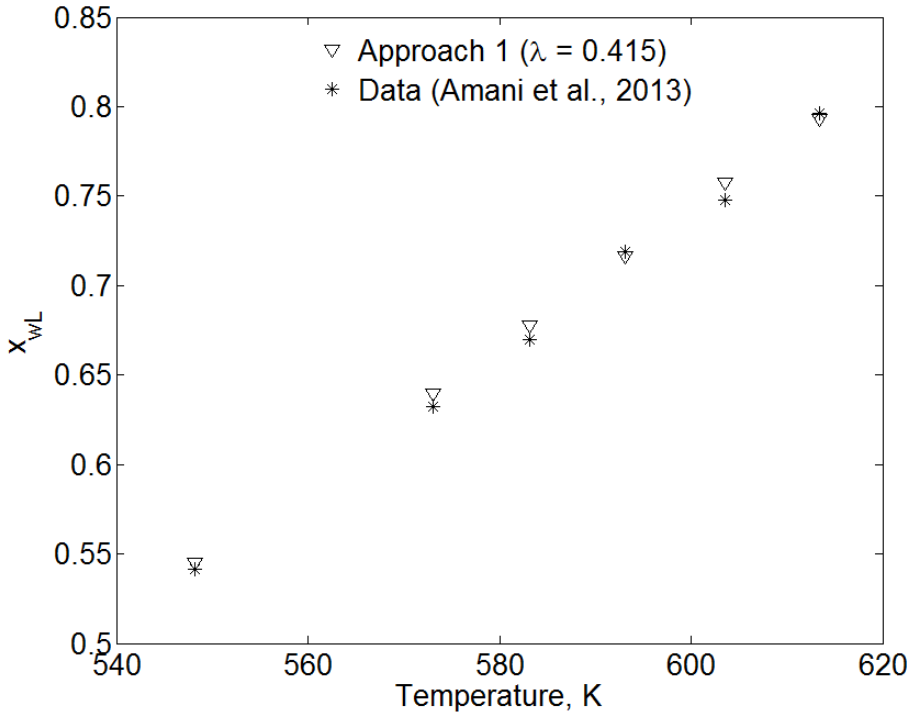

Figure 3.2a. Water solubilities predicted near the V-L-W/L-W boundary for the water/Athabasca bitumen mixture given in table 2. The BIPs in table 2 were scaled by a factor (λ) of 0.415. Experimental data were taken from Amani et al. (2013b). The water concentrations for the V and W phases were predicted to be greater than 0.99.

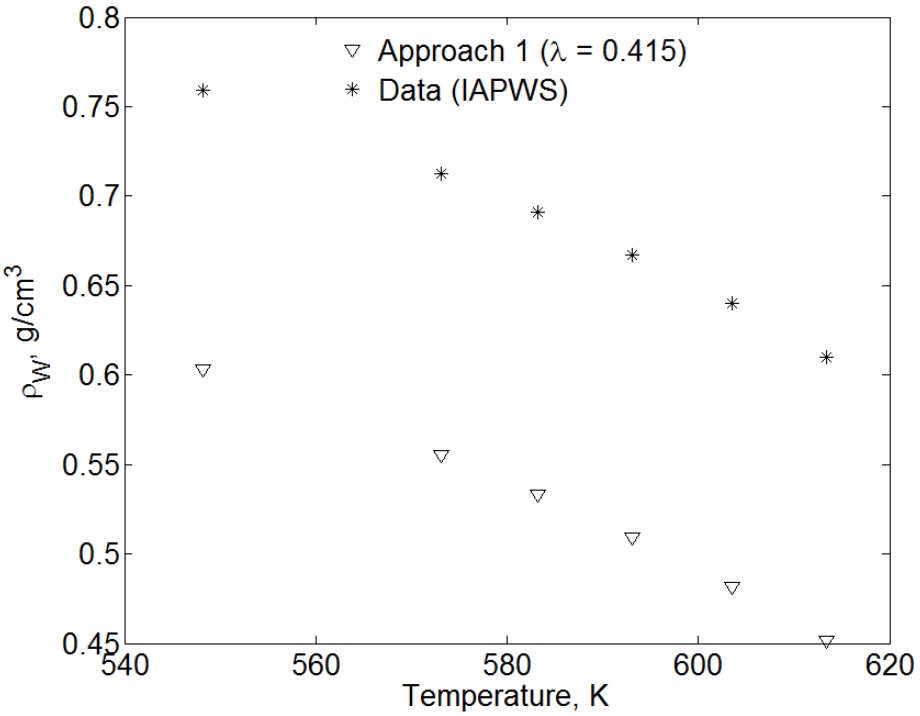

Figure 3.2b. Predicted density of the W phase near the V-L-W/L-W boundary for the water/Athabasca bitumen mixture given in table 2. The density data for the W phase correspond to the density of liquid water along the saturation pressure curve.

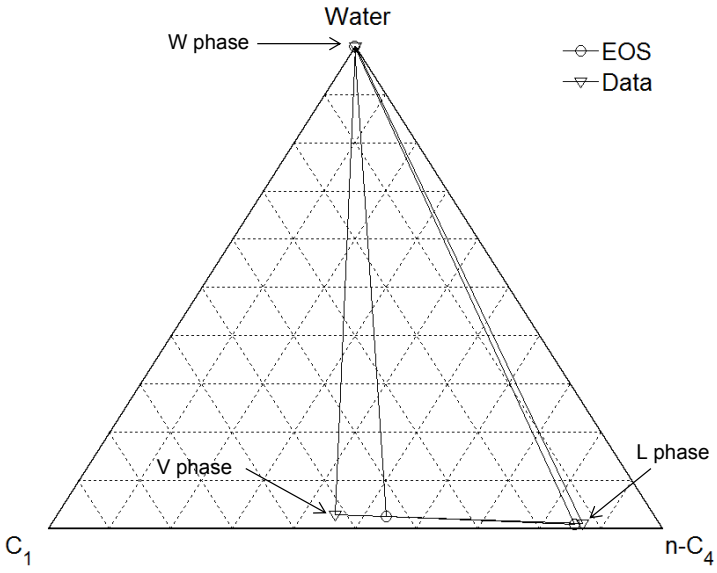

Figure 3.3a. Tie triangle predicted by the PR EOS with the BIP correlation (equation 3.2) for the water/C_1/n-C_4 system at 377.60 K and 44.88 bar. The phase compositions measured by McKetta and Katz (1948) are also shown.

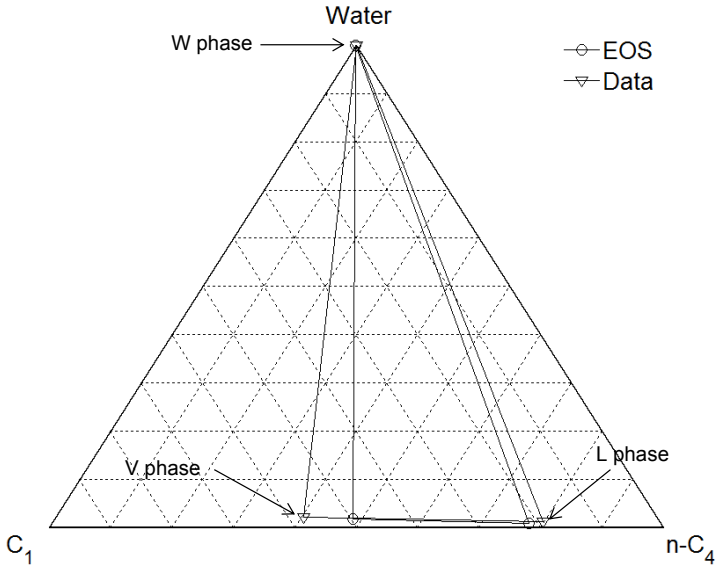

Figure 3.3b. Tie triangle predicted by the PR EOS with the BIP correlation (equation 3.2) for the water/C_1/n-C_4 system at 377.60 K and 58.95 bar.

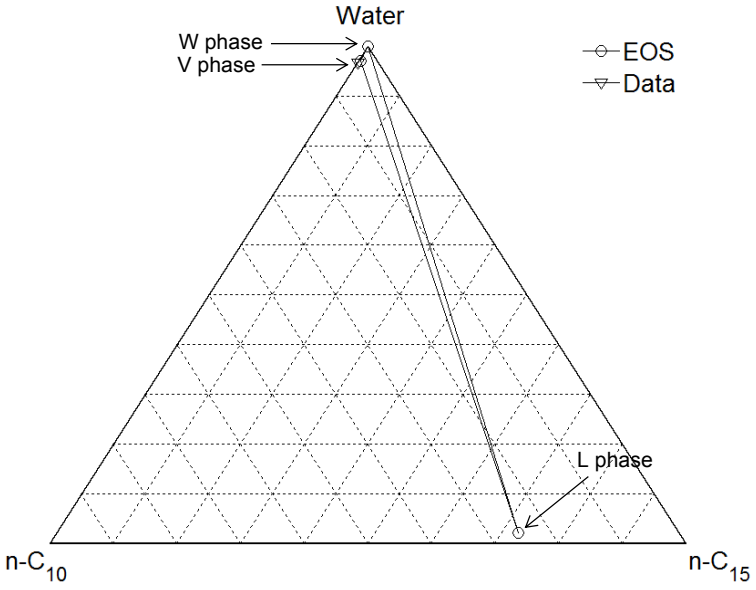

Figure 3.4a. Tie triangle predicted by the PR EOS with the BIP correlation (equation 3.2) for the water/n-C_{10}/n-C_{15} system at 394.26 K and 2.12 bars. The phase compositions measured by Chawla et al. (1995) are also shown.

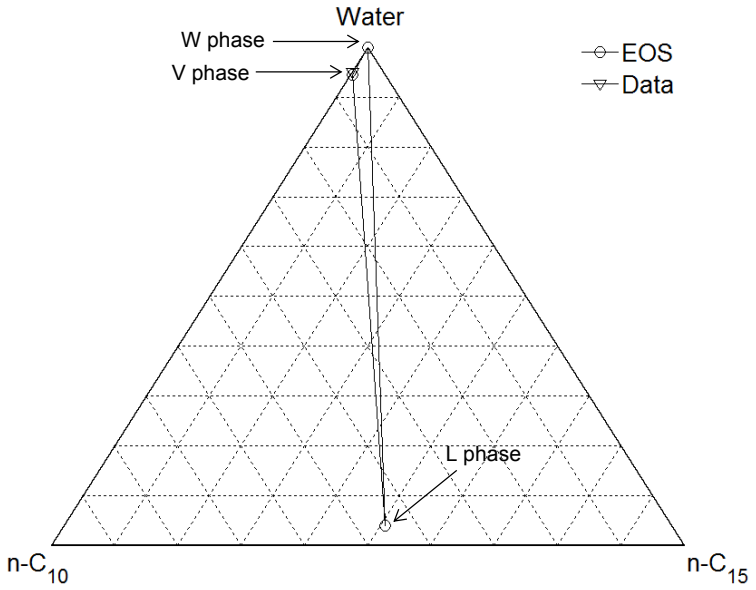

Figure 3.4b. Tie triangle predicted by the PR EOS with the BIP correlation (equation 3.2) for the water/n-C_{10}/n-C_{15} system at 422.04 K and 4.93 bars.

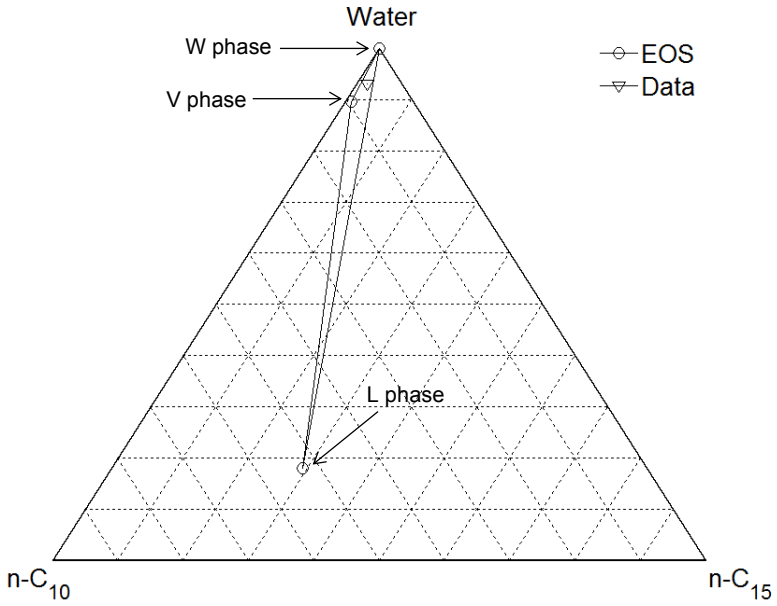

Figure 3.4c. Tie triangle predicted by the PR EOS with the BIP correlation (equation 2.7) for the water/n-C_{10}/n-C_{15} system at 505.37 K and 32.58 bars.

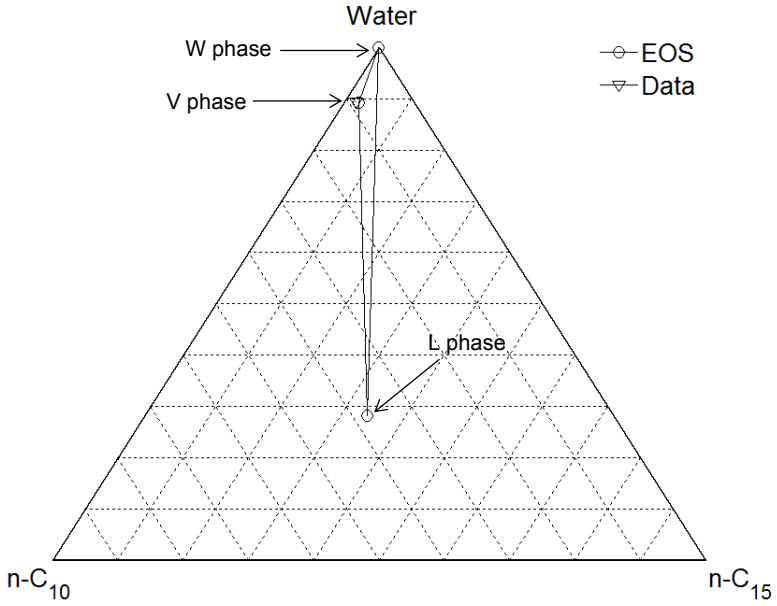

Figure 3.4d. Tie triangle predicted by the PR EOS with the BIP correlation (equation 3.2) for the water/n-C_{10}/n-C_{15} system at 533.15 K and 52.44 bars.

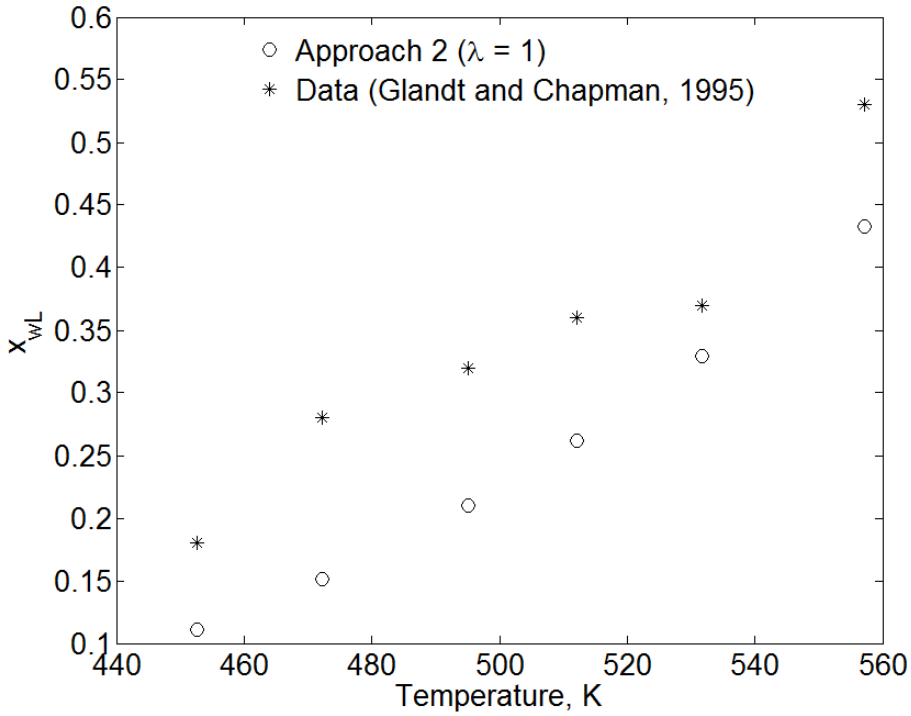

Figure 3.5. Validation of BIP correlation developed for Approach 2 (equation 3.2) against L-phase compositional data for water-containing Peace-River Bitumen measured in the near the V-L-W/L-W boundary (properties shown in table 3.7).

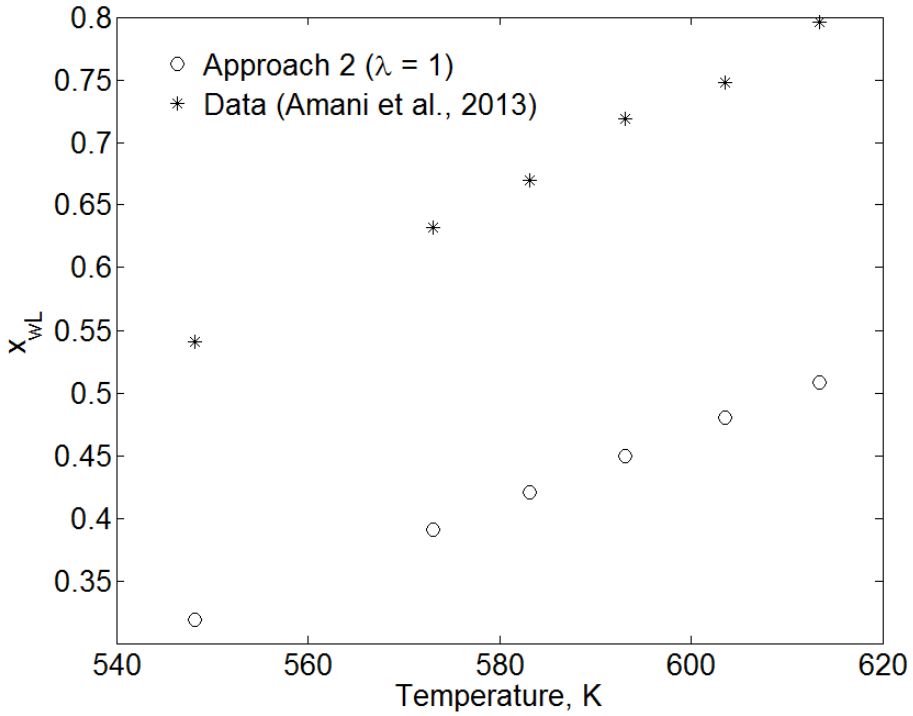

Figure 3.6. Validation of BIP correlation developed for Approach 2 (equation 3.2) against L-phase compositional data for water-containing Athabasca Bitumen measured in the near the V-L-W/L-W boundary (properties shown in table 3.8)

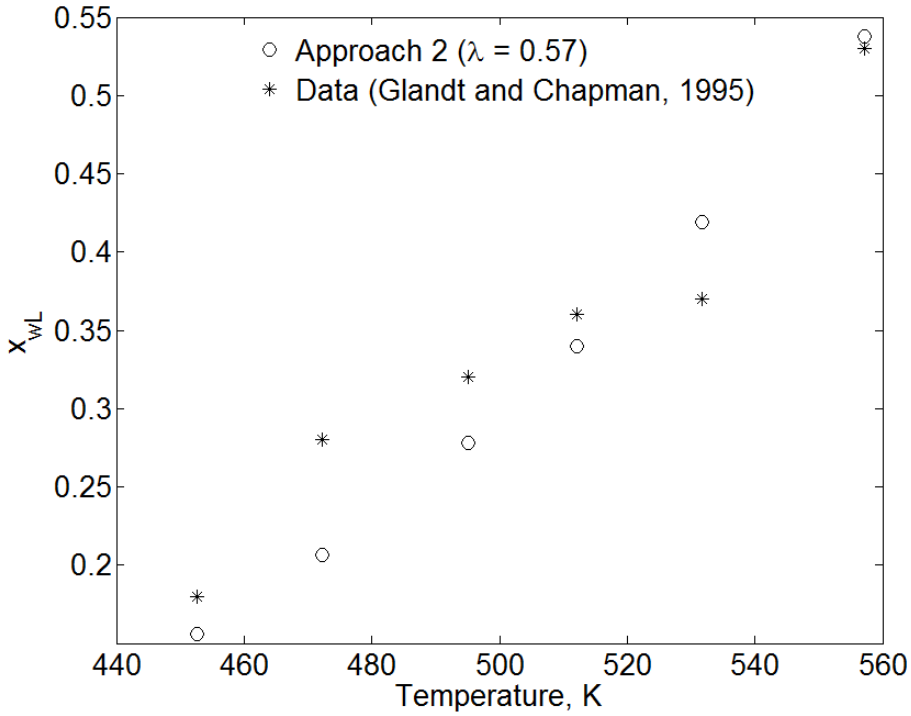

Figure 3.7a. Extension of BIP correlation developed for Approach 2 (equation 3.2) to water-containing Peace-River Bitumen. The BIPs calculated from equation 3.2 are systematically reduced by scaling with a factor λ = 0.570.

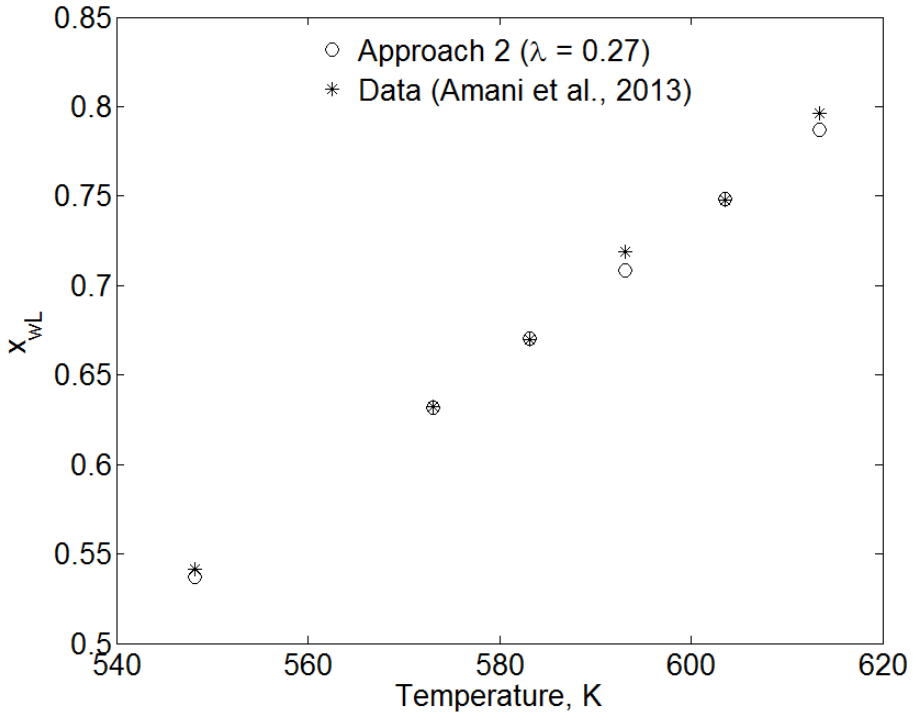

Figure 3.7b. Extension of BIP correlation developed for Approach 2 (equation 3.2) to water-containing Athabasca Bitumen. The BIPs calculated from equation 3.2 are systematically reduced by scaling with a factor λ = 0.270.

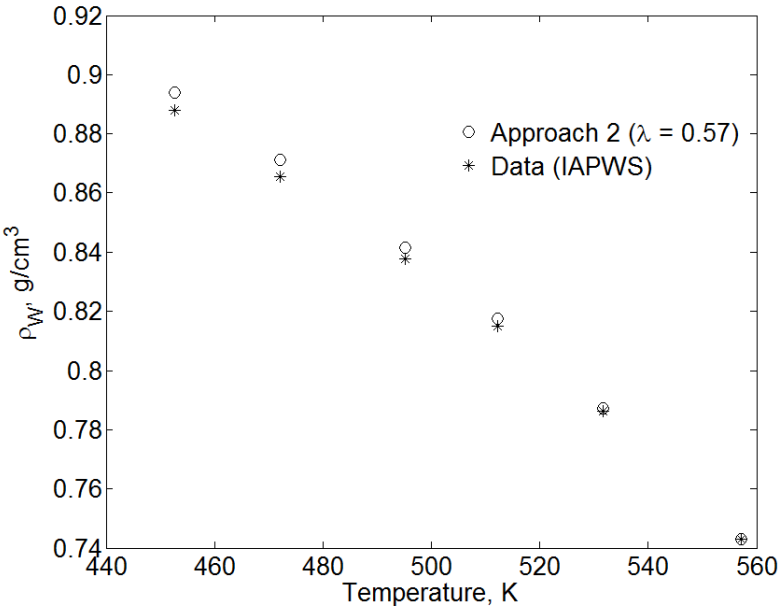

Figure 3.8a. Predicted W-phase density using equation 3.2 extended to water-containing Peace River bitumen.

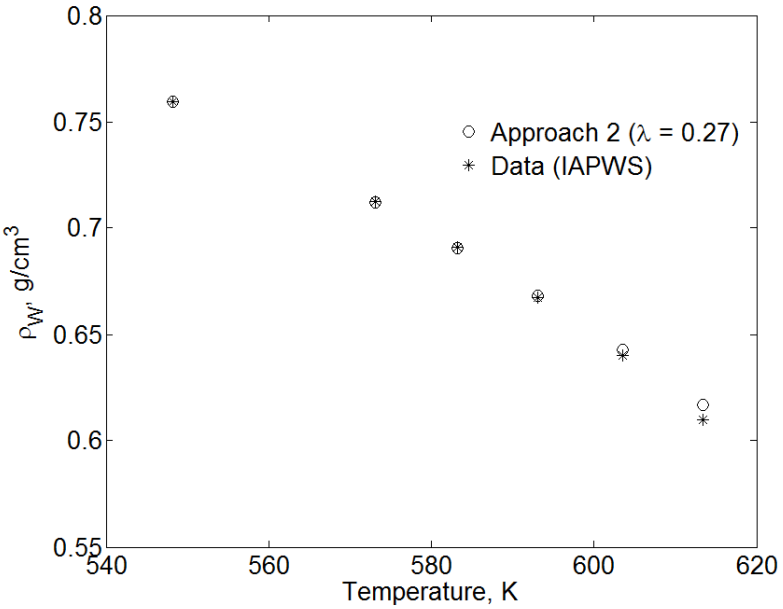

Figure 3.8b. Predicted W-phase density using equation 3.2 extended to water-containing Athabasca bitumen.

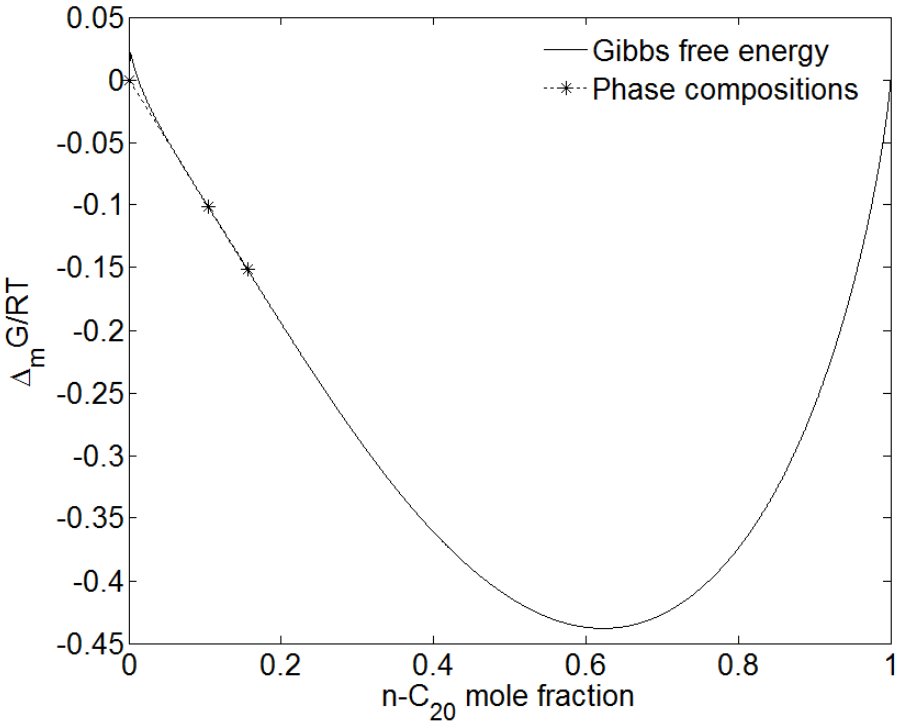

Figure 3.9. Molar Gibbs free energy change of mixing for water/n-C_{20} binary at 167 bars and 616.73 K using Approach 1. For Approach 1, the optimized BIP for this system is 0.3. At the specified temperature and pressure, three phases coexist at equilibrium (V, L, and W). In terms of the mole fraction of n-C_{20}, the concentration of the V, L and W phases are 0.1042, 0.1557, 1.7099E-09, respectively.

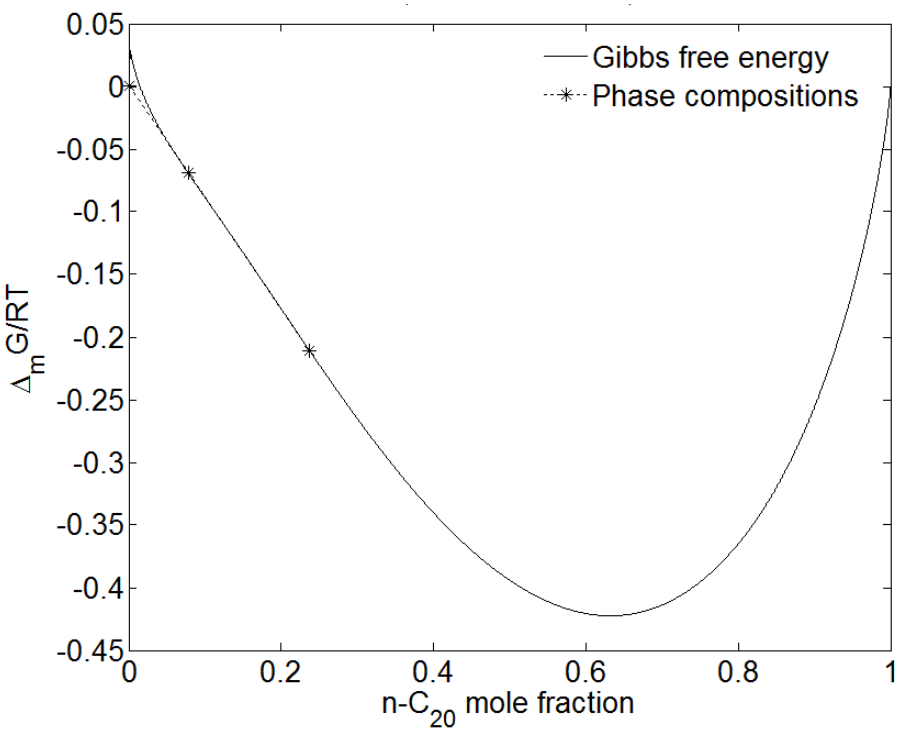

Figure 3.10. Molar Gibbs free energy change of mixing for water/n-C_{20} binary at 167 bars and 620.29 K using Approach 2. The BIP employed 0.3, the optimized BIP for Approach 2. At the specified temperature and pressure, three phases coexist at equilibrium (V, L, and W). In terms of the mole fraction of n-C_{20}, the concentration of the V, L and W phases are 0.0779, 0.2376, 1.7129E-11, respectively. In comparison with Figure 3.9, we observe that the use of Approach 2 results in an over-prediction of x_{wV} and under-prediction of x_{wL}. This in turn leads to an elongated three-phase curve which is erroneous. The correction of this result requires the use of a lower value for the BIP (see Figure 3.11).

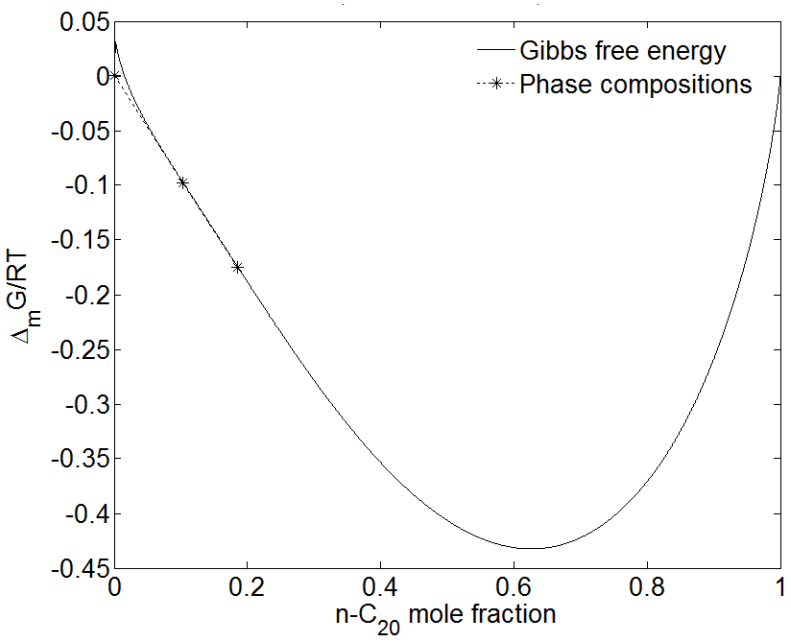

Figure 3.11. Molar Gibbs free energy change of mixing for water/n-C_{20} binary at 167 bars and 619.74 K using Approach 2. For Approach 2, the optimized BIP for this system is 0.281. At the specified temperature and pressure, three phases coexist at equilibrium (V, L, and W). In terms of the mole fraction of n-C_{20}, the concentration of the V, L and W phases are 0.1035, 0.1854, 2.4433E-11, respectively. Note the closeness of the phase compositions presented here with those for Figure 3.9. The optimized BIP value of 0.281 results in a UCEP of 621.57 K and 171.22 bars. This is matches reasonably well the measured UCEP of 170.80 bars and 622.70 K by Brunner (1990)

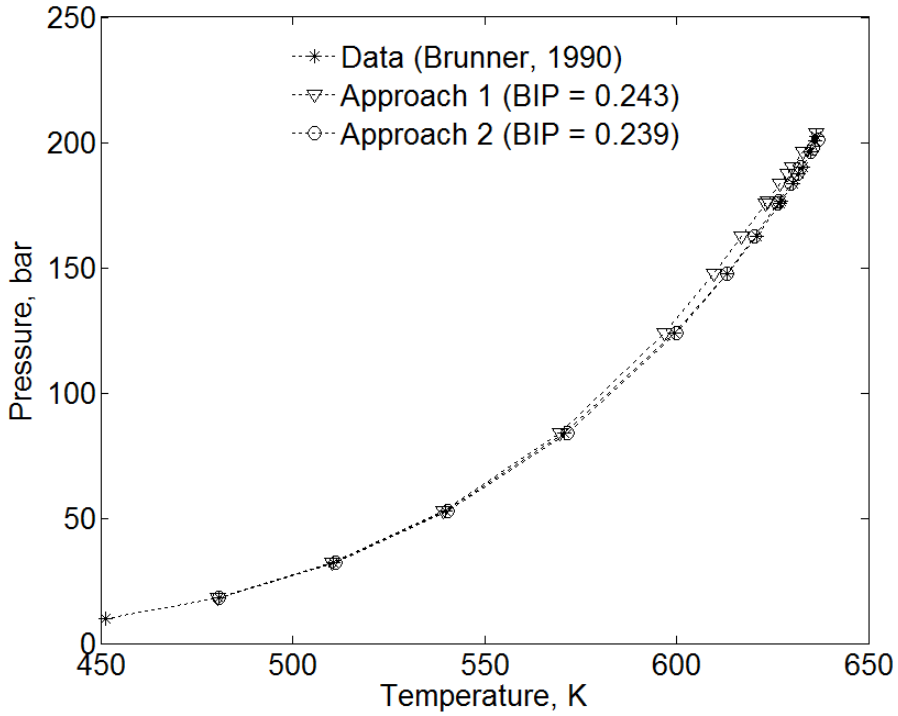

Figure 3.12. Comparison between predicted and experimentally measured three-phase curve for water/n-C_{25} binary using Approaches 1 and 2. The measurements of Brunner (1990) have been used for this comparison.

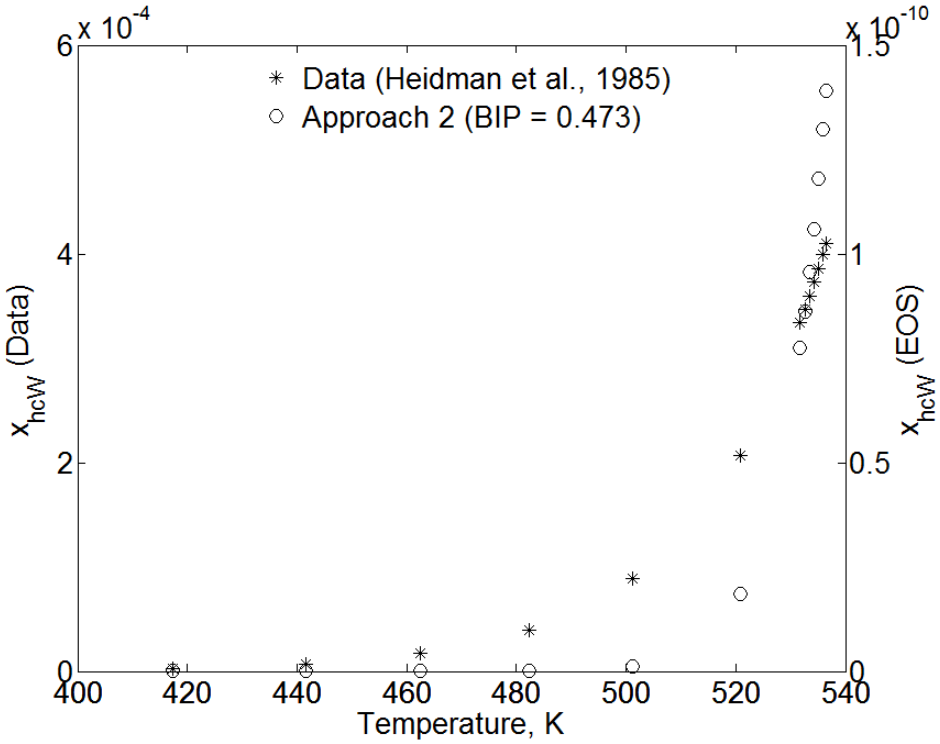

Figure 3.13. Comparison between predicted (Approach 2) and experimentally ascertained compositions of the aqueous (W) phase along the three-phase curve. The data points were obtained from the correlation developed by Heidman et al. (1985) for the W phase based on experimental measurements. Like Approach 1, Approach 2 also under-predicts the dissolution of n-C_8 in the W phase by a few orders of magnitude.

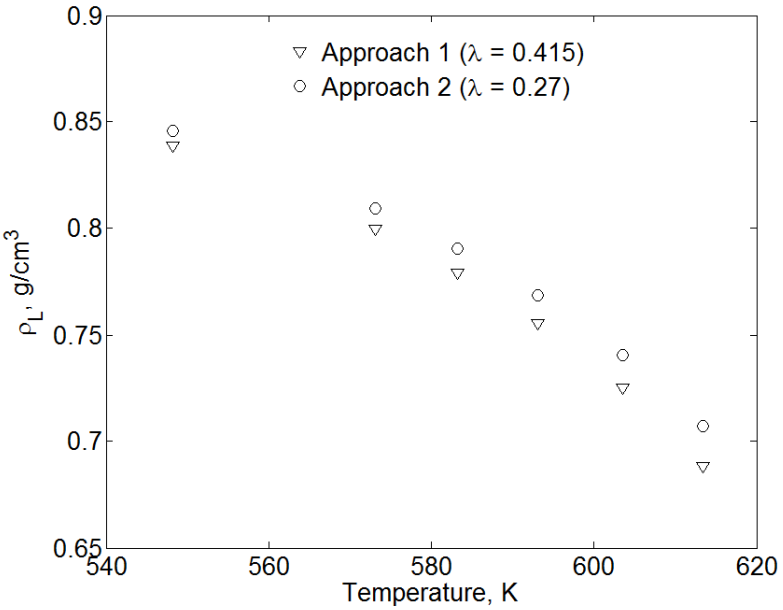

Figure 3.14. Predicted L-phase density using equation 3.2 extended to water-containing Athabasca bitumen.

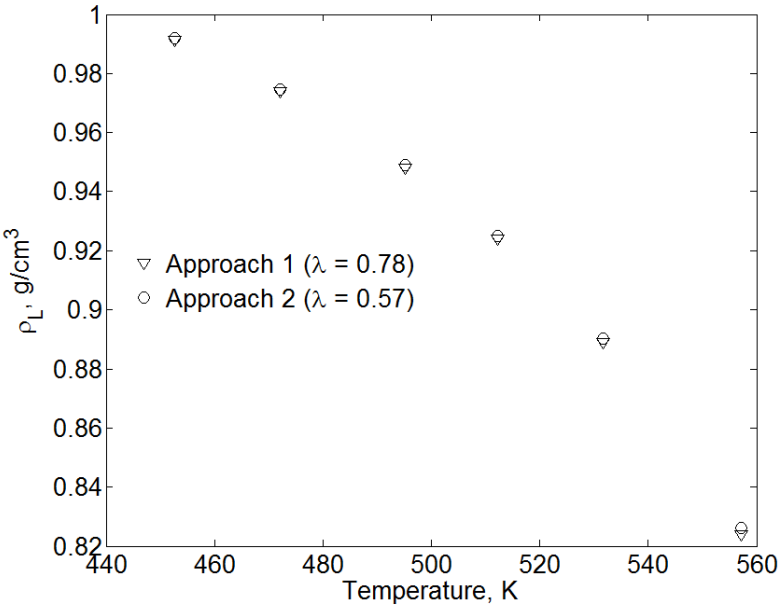

Figure 3.15. Predicted L-phase density using equation 3.2 extended to water-containing Peace River bitumen.

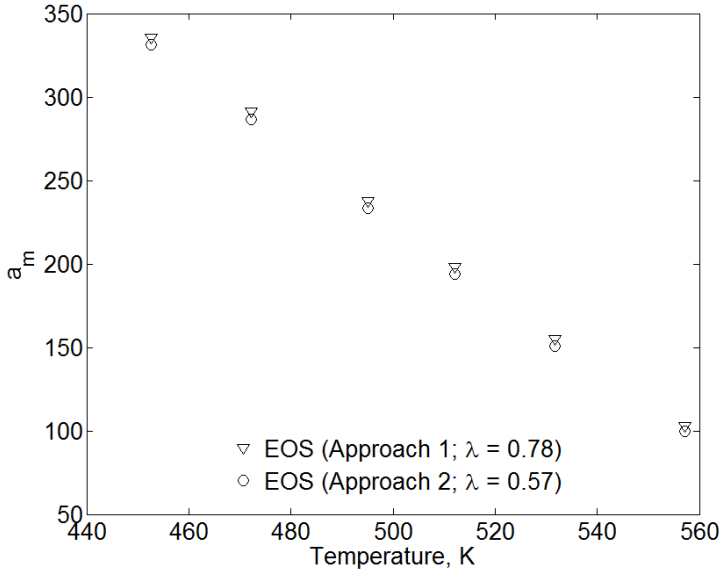

Figure 3.16a. Predicted attraction parameter of the mixture (a_m) of the L phase using for water-containing Peace River bitumen using Approaches 1 and 2.

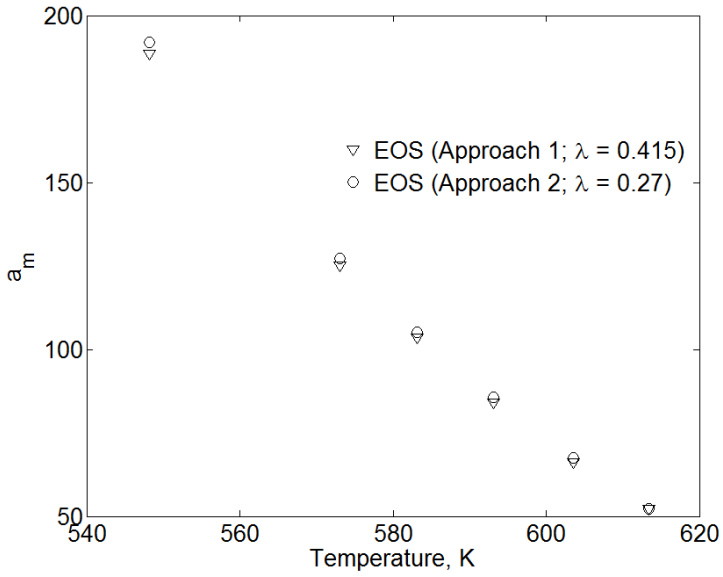

Figure 3.16b. Predicted attraction parameter of the mixture (a_m) of the L phase using for water-containing Athabasca bitumen using Approaches 1 and 2.

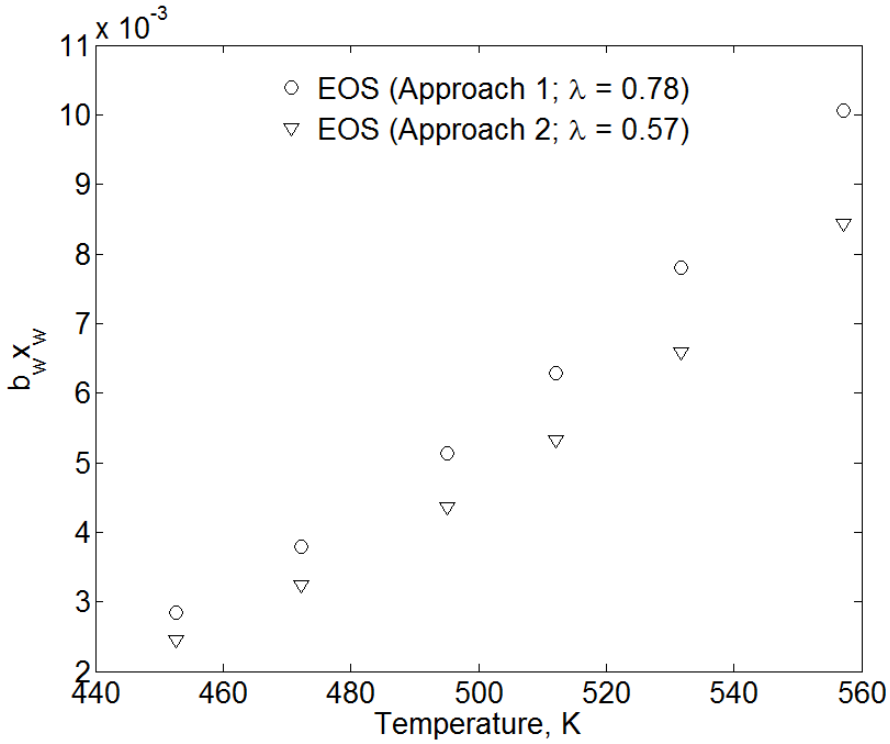

Figure 3.17a. Term I of equation 3.3 computed for the L phase of water-containing Peace River bitumen using Approaches 1 and 2. Although the dissolution of water in the L phase is significantly high, the co-volume parameter computed for pure water, for both approaches is an order of magnitude lower than that for the hydrocarbon-based pseudo-components. The value of the term $b_w x_w$ seems diminished because of this, and it is small enough to be offset by term II ($\Sigma b_{hc} x_{hc}$) for the L phase (shown in Figure 3.15).

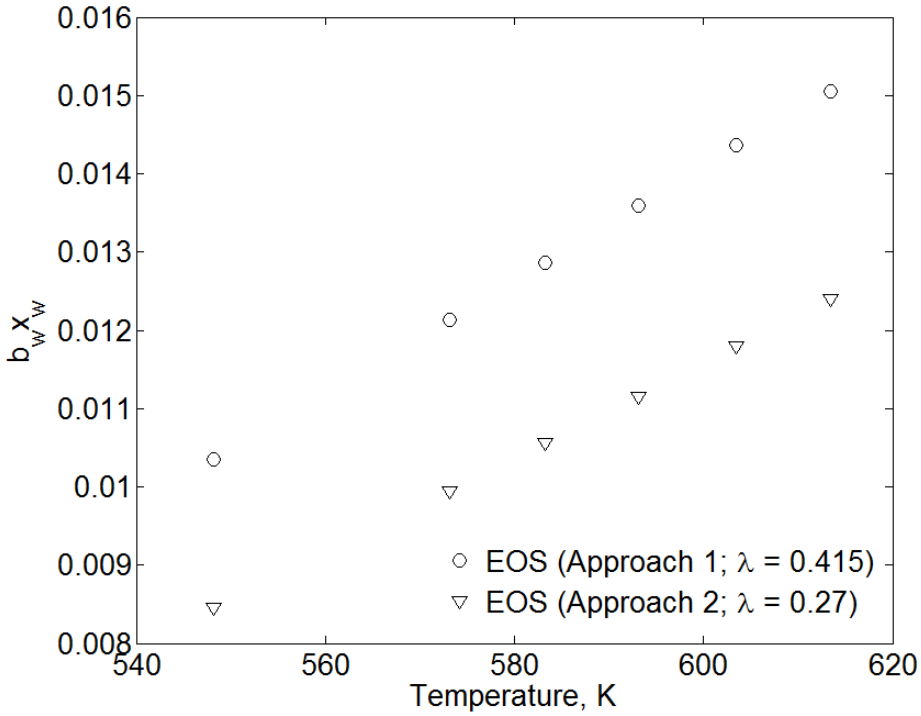

Figure 3.17b. Term I of equation 3.3 computed for the L phase of water-containing Athabasca bitumen (z_w = 0.8115) using Approaches 1 and 2.

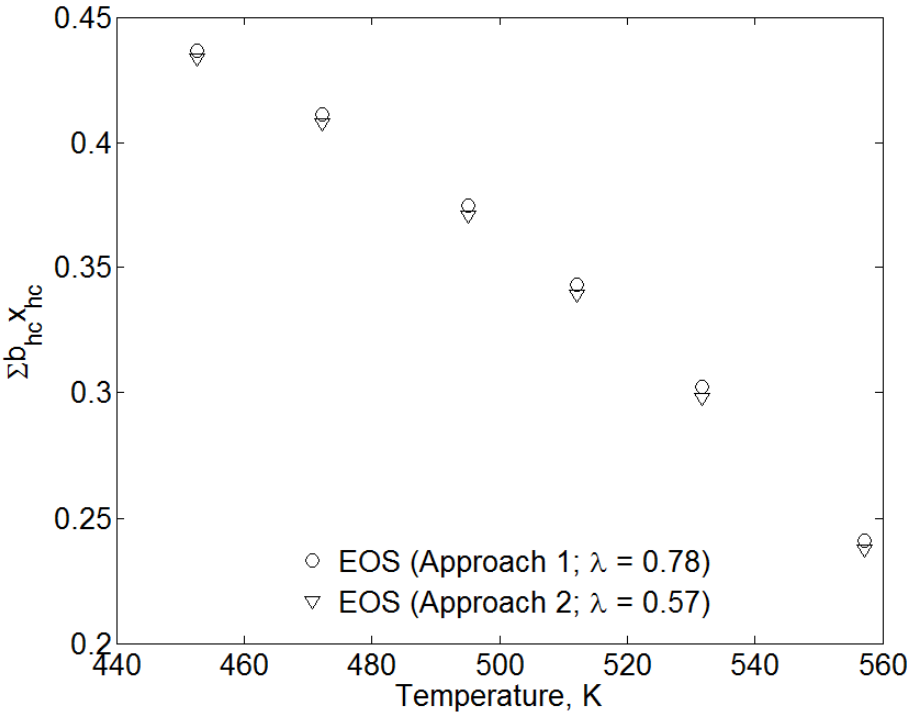

Figure 3.18a. Term II of equation 3.3 computed for the L phase of water-containing Peace River bitumen (z_w = 0.73) using approaches 1 and 2. Note that term II for this system is more than 2 orders of magnitude greater than term I (figure 3.17a). Thus the co-volume parameter of the mixture for this system is dominated by term II which in turn, results in very similar L-phase density predictions for the two approaches.

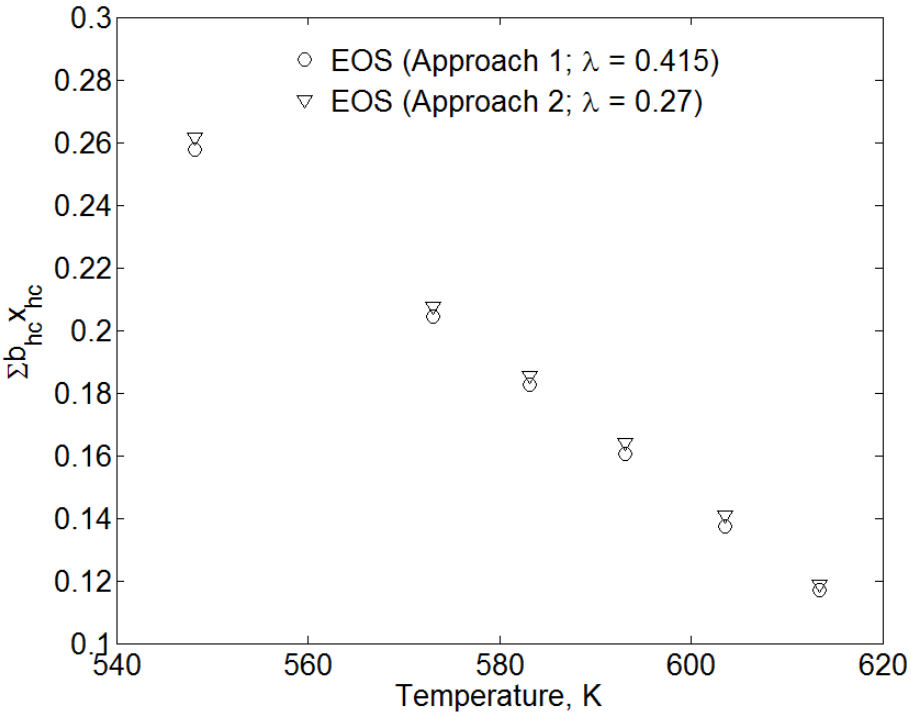

Figure 3.18b. Term II of equation 3.3 computed for the for the L phase of water-containing Athabasca bitumen (z_w = 0.8115) using approaches 1 and 2. Note that term II for this system is more than an order of magnitude greater than term I (figure 3.17b). Thus the co-volume parameter of the mixture for this system is dominated by term II which in turn, results in very similar L-phase density predictions for the two approaches.

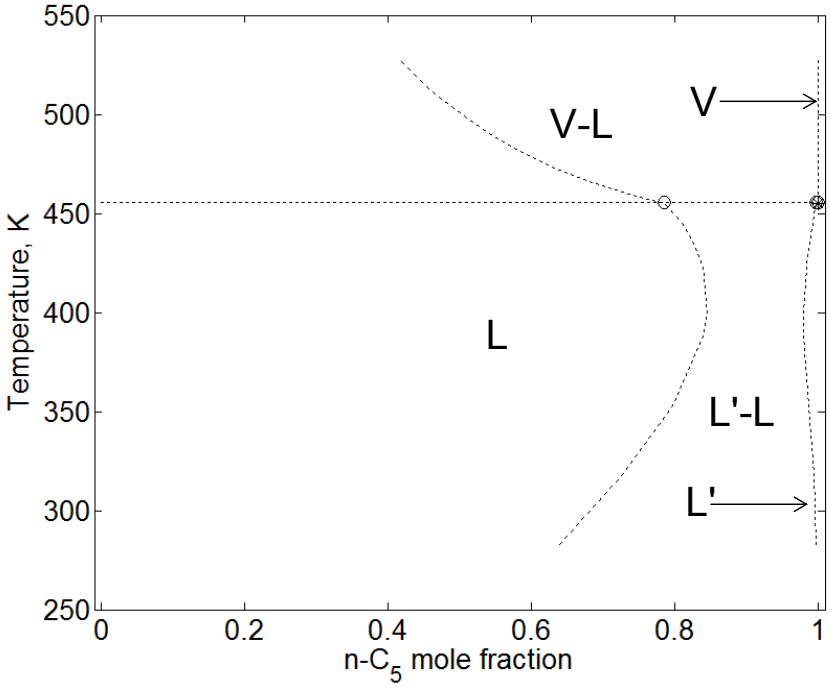

Figure 3.19. Predicted T-x cross section for n-C_5/C_D binary at P = 27 bars. Asterisk marker represents the saturation pressure temperature of n-C_5 at 27 bars. Circle markers represent three-phase compositions. The solvent-rich phase is denoted as L′. The predicted three-phase temperature at this pressure is approximately 455.30 K. The low volatility of C_D renders the V-phase concentration of n-C_5 to be greater than 99 mol%. The three-phase P-T projection of this system is in close proximity to the vapor pressure curve of n-C_5. The critical point of n-C_5 is 469.70 K and 33.70 bars. The P-T conditions presented here are in the near-critical region. Hence, the compositions of the V and L′ phases at three-phase coexistence are similar.

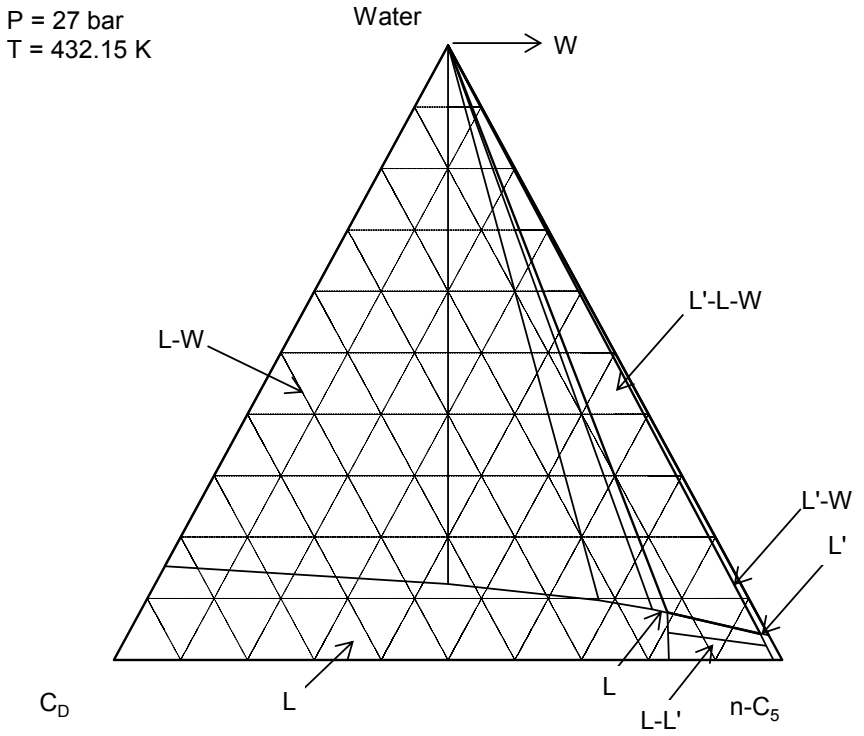

Figure 3.20a Predicted tie-triangle for water/n-C_5/C_D ternary at 432.15 K and 27 bars. This tie-triangle has been predicted using Approach 2. At 27 bars, the three-phase temperature of the water/n-C_5 binary is 434.79 K (see Figures 3.20b and 3.20c).

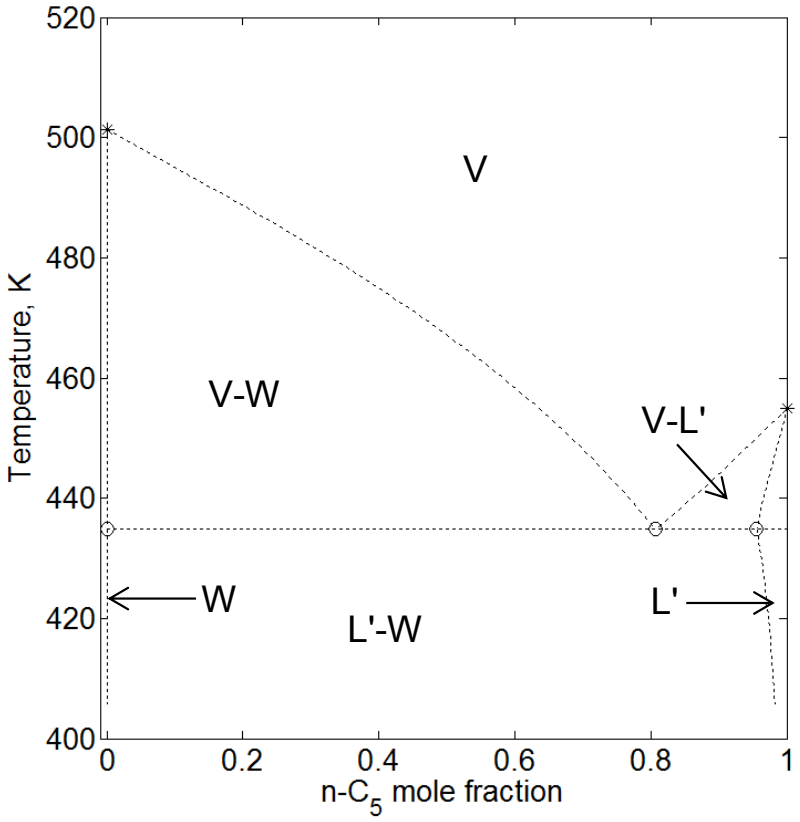

Figure 3.20b. Predicted T-x cross-section of water/n-C_5 binary at 27 bars. The asterisk markers represent the pure component saturation temperatures. The circular markers represent the phase compositions at three-phase coexistence. The three-phase temperature of this binary at 27 bars is approximately 434.79 K (see Figure 3.20c).

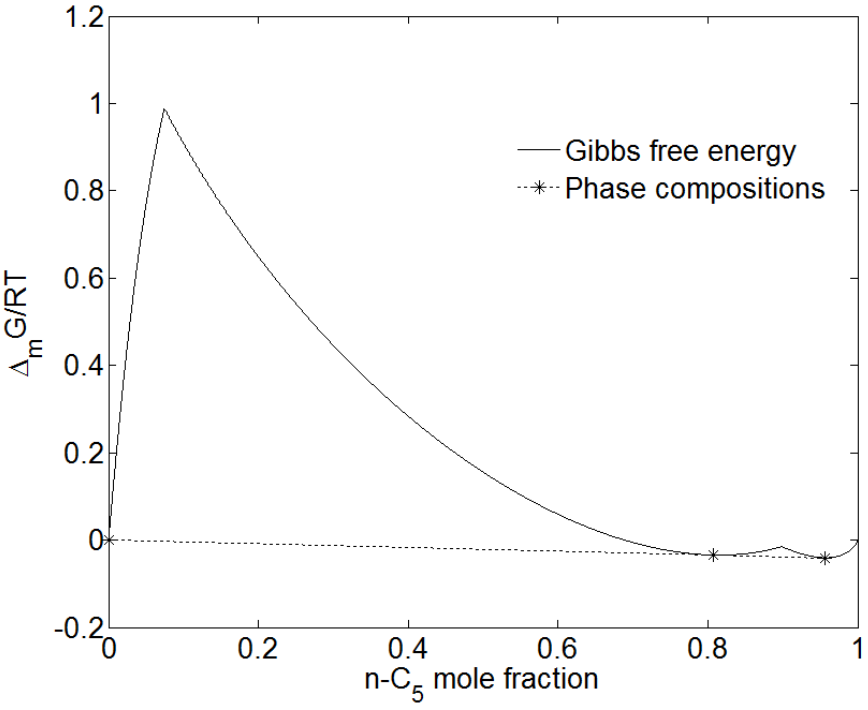

Figure 3.20c. Molar Gibbs free energy change of mixing at the three-phase coexistence temperature (434.79 K) for the water/n-C_5 binary at 27 bars predicted using Approach 2.

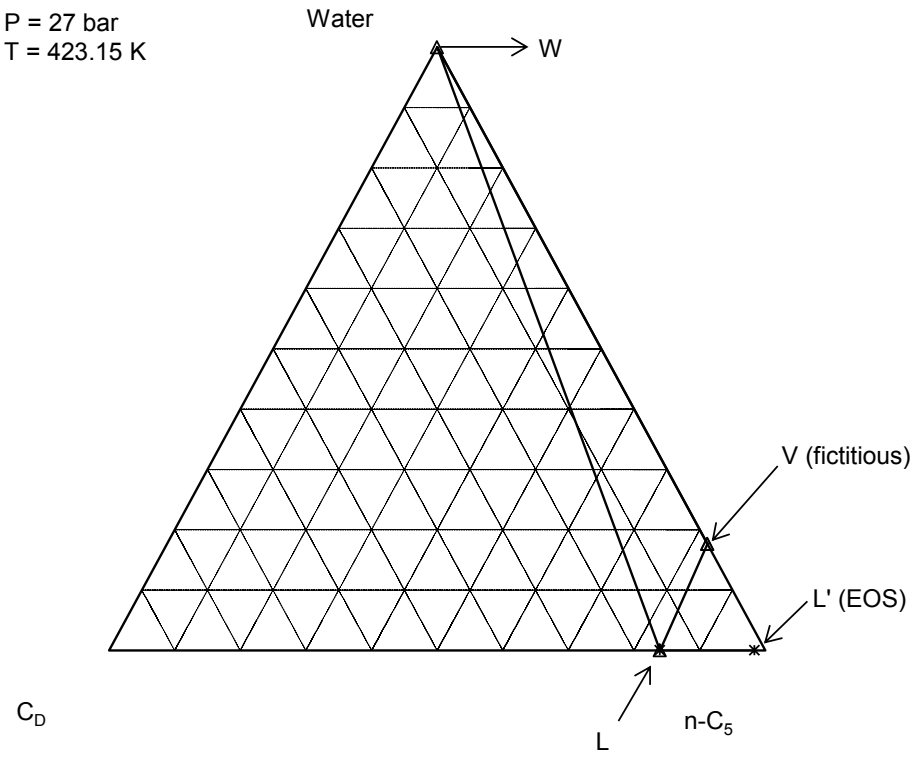

Figure 3.21a. Physical tie-line and fictitious tie-triangle for the base case. Asterisk markers represent the end points of the predicted tie-line in the n-C_5/C_D binary limit (L-L′). The vertices of the fictitious tie-triangle (V-L-W) are shown using triangular markers and connected by solid lines. Note that the composition of the L phase is unaltered after the definition of the fictitious tie-triangle.

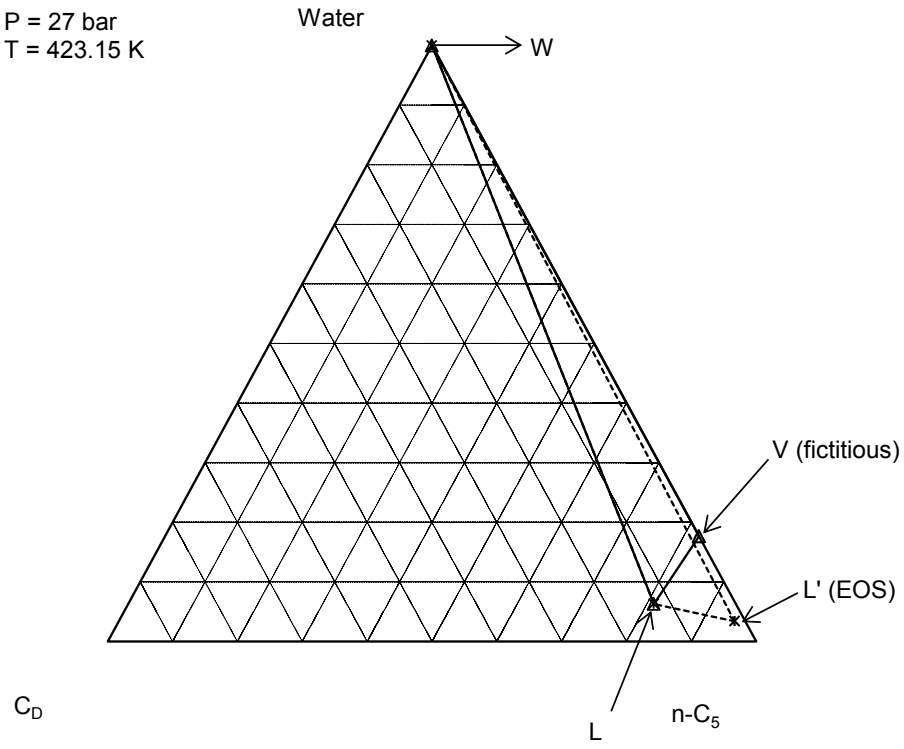

Figure 3.21b. Physical and fictitious tie-triangles for the modified case. Asterisk markers connected by dashed lines represent the tie-triangle predicted using the EOS (L-L′-W). The vertices of the fictitious tie-triangle (V-L-W) are shown using triangular markers and connected by solid lines. Note that the composition of the L phase is unaltered after the definition of the fictitious tie-triangle. The composition of the V phase is identical for both the base and modified cases as the concentration of C_D has been to 10^{-7}, and the concentration of water depends only on temperature and pressure of the system.

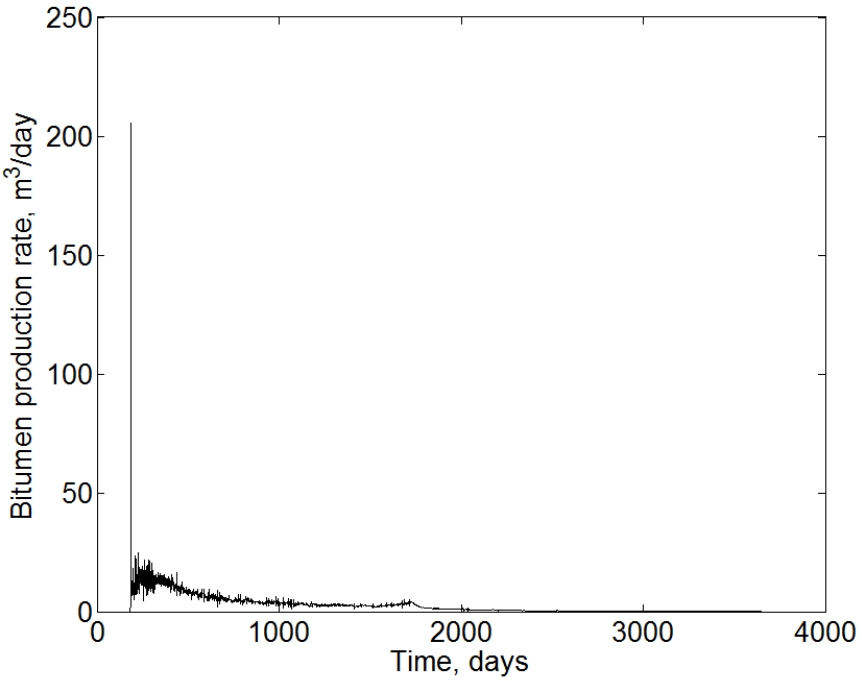

Figure 3.22a Daily production rate of bitumen for the base case. At 1 year, production rate is 13.97 m^3/day. The reservoir is subjected to an initial heating period of 6 months.

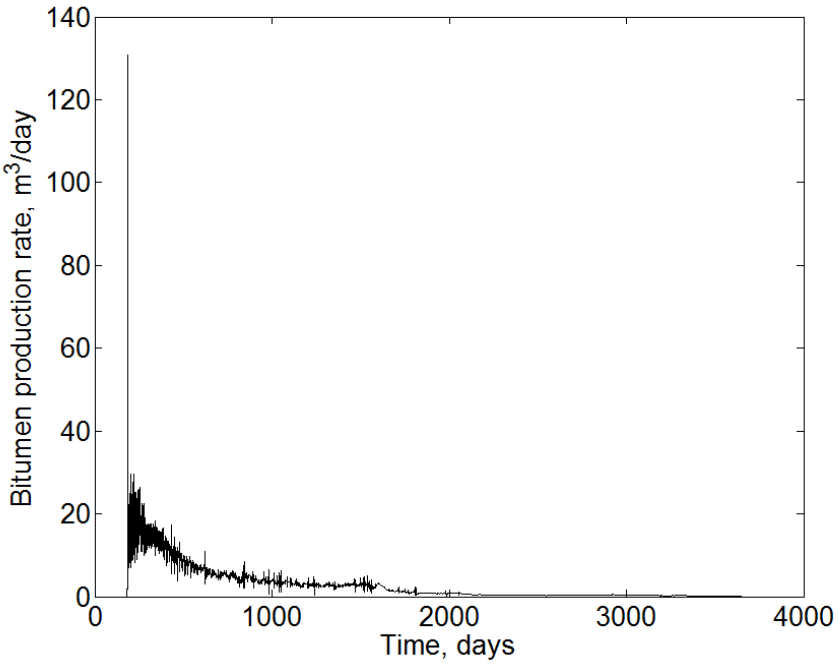

Figure 3.22b Daily production rate of bitumen for the modified case. At 1 year, production rate is 15.90 m^3/day.

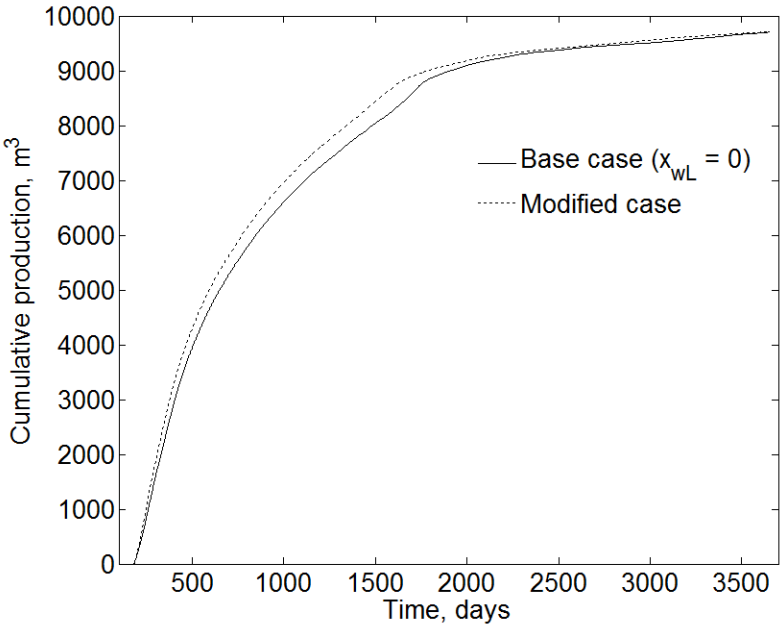

Figure 3.22c. Cumulative bitumen produced for the base and modified cases.

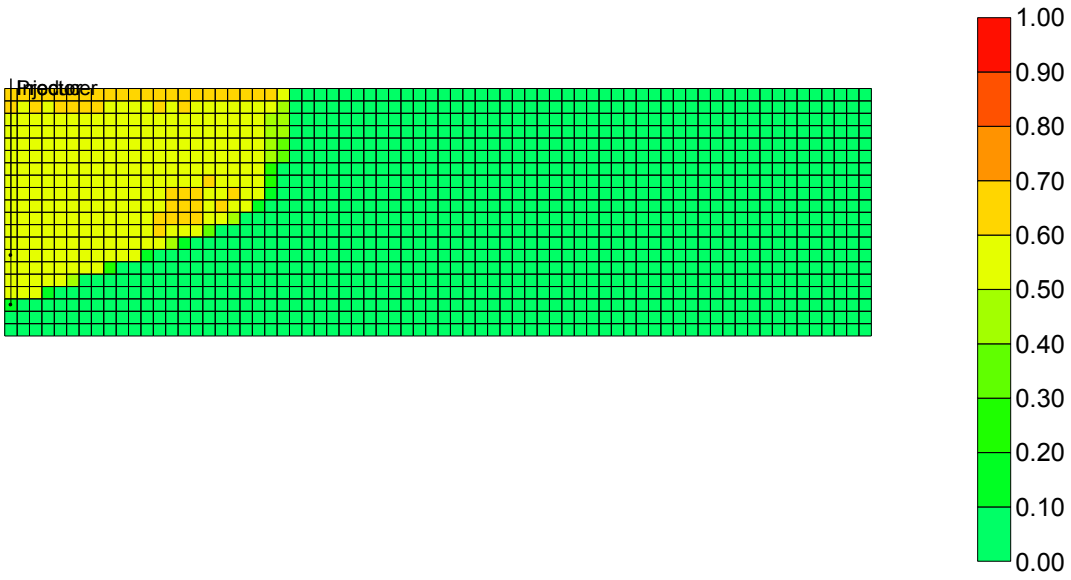

Figure 3.23a V-phase saturation profile for the base case at 1 year

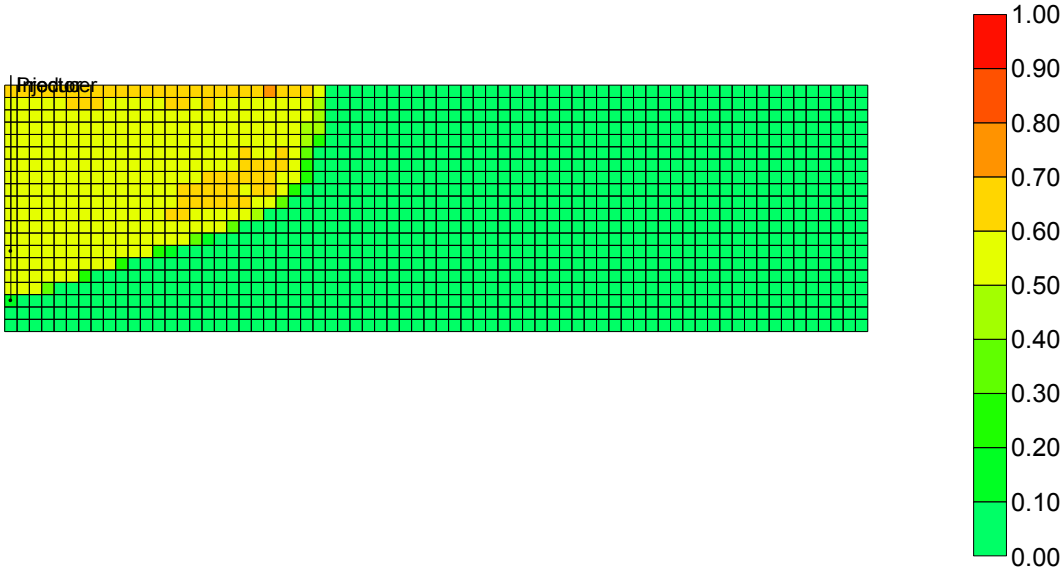

Figure 3.23b V-phase saturation profile for the modified case at 1 year. These maps indicate that the consideration of x_{wL} enhances the propagation of the ES-SAGD chamber.

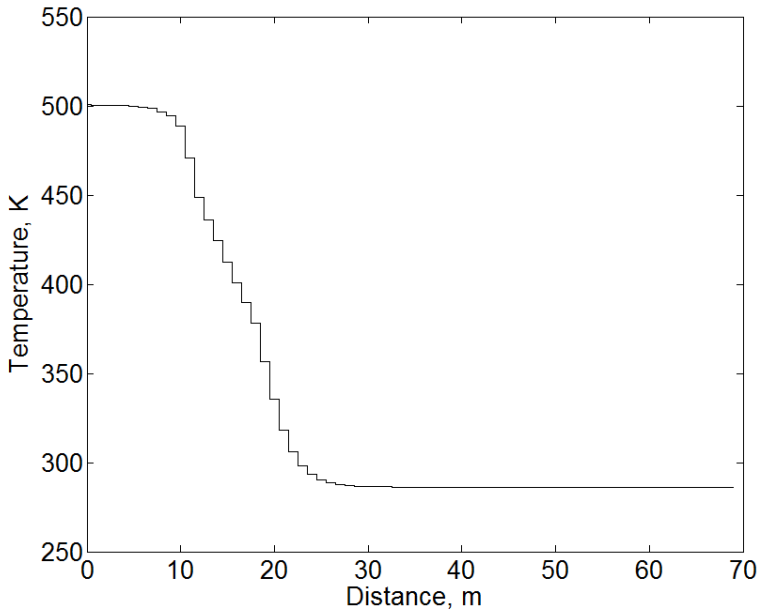

Figure 3.24a. Temperature profile for the base case for the 14th row at 1 year.

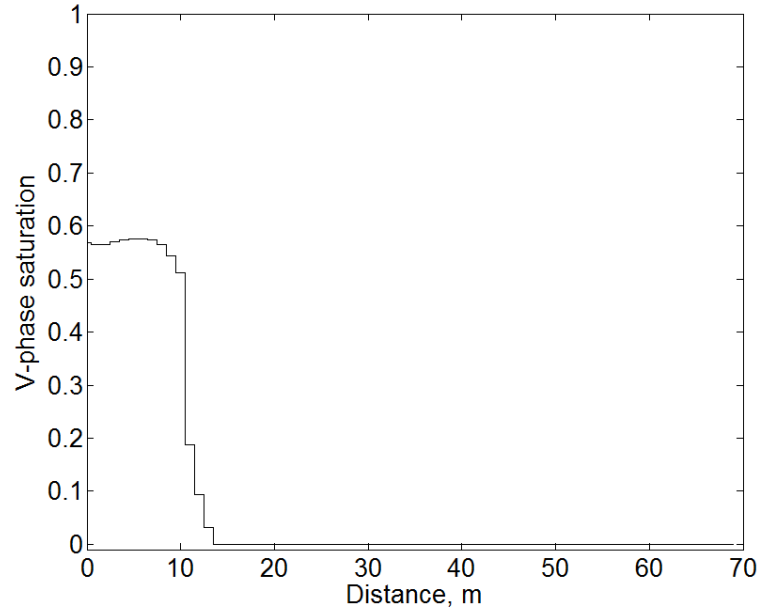

Figure 3.24b. V-phase saturation profile for the base case for the 14th row at 1 year. The chamber edge is located at 13.5m. The chamber edge temperature is 435.83 K.

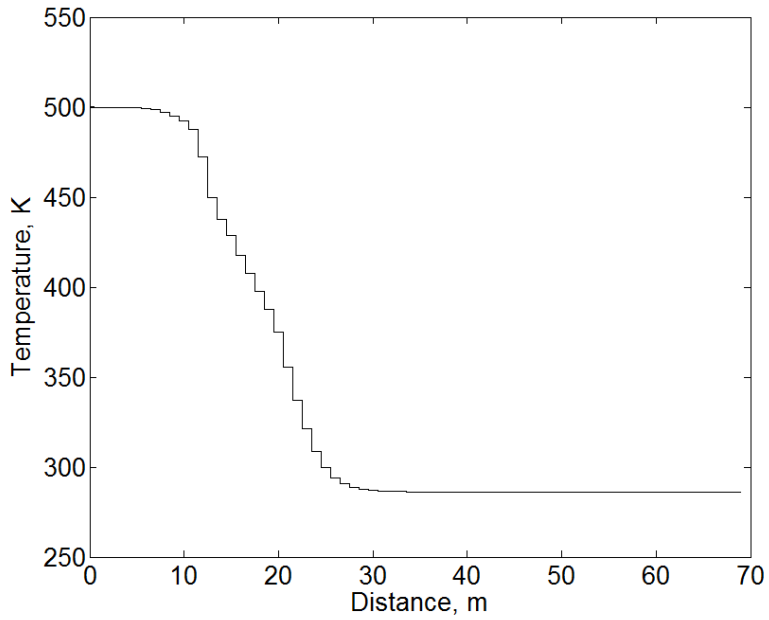

Figure 3.25a. Temperature profile for the modified case for the 14th row at 1 year.

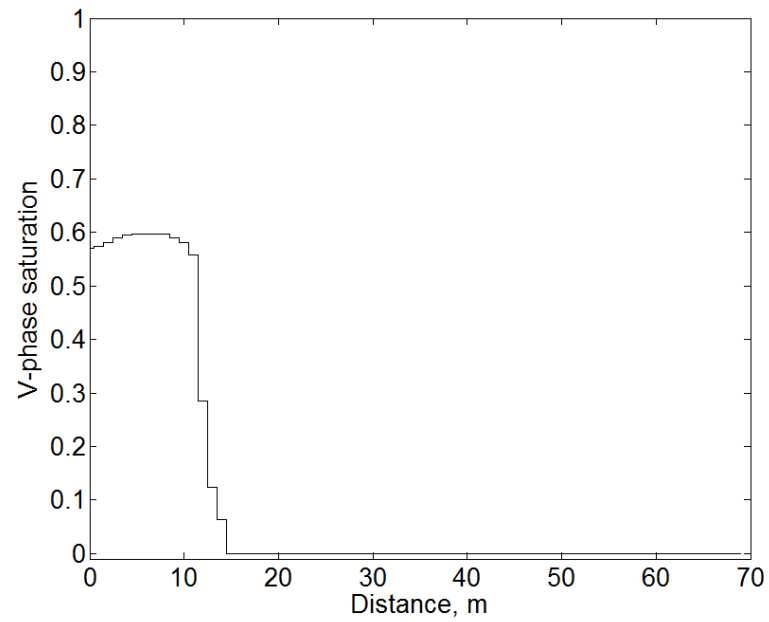

Figure 3.25b. V-phase saturation profile for the modified case for the 14th row at 1 year. The chamber edge is located at 14.5 m. The chamber edge temperature is 437.73 K.

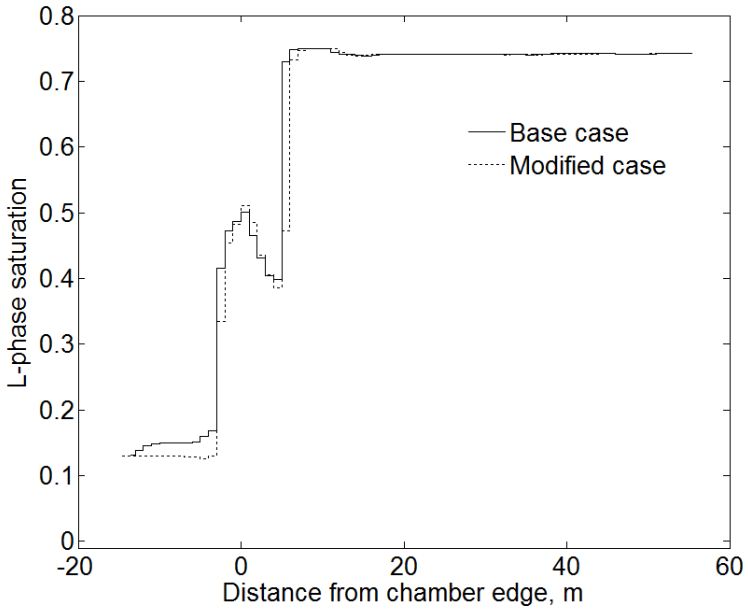

Figure 3.26. L-phase saturation profile for the 14th row at 1 year. At the chamber edge, the values for the base and modified cases are 0.5015, and 0.5114, respectively.

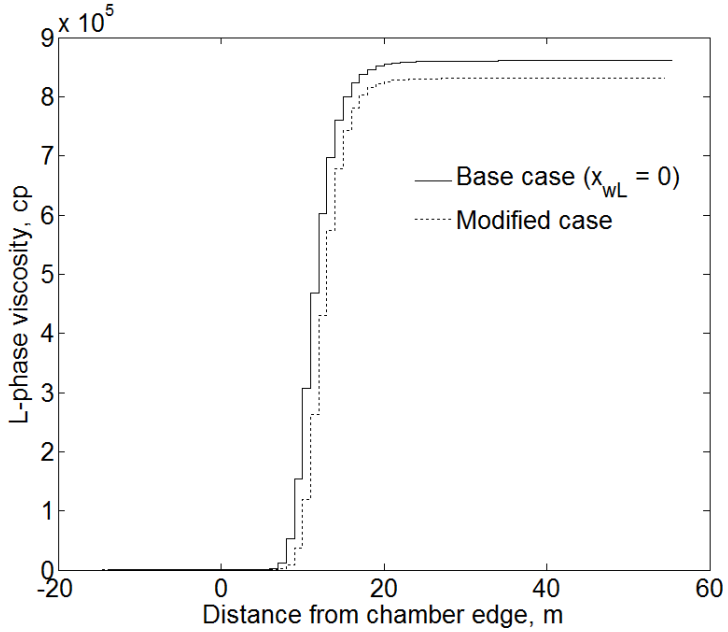

Figure 3.27. L-phase viscosity profile for the 14th row at 1 year.

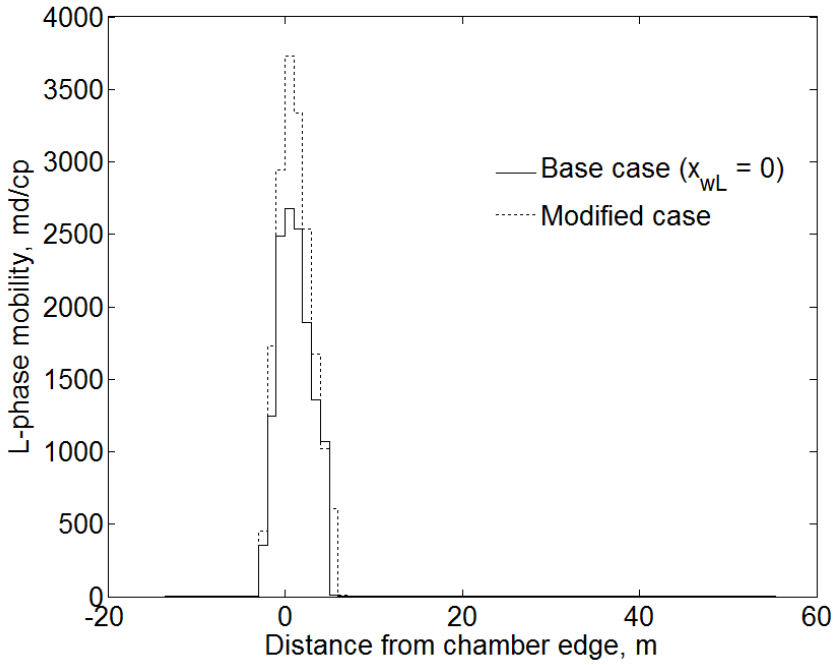

Figure 3.28. L-phase mobility profile for the 14th row at 1 year.

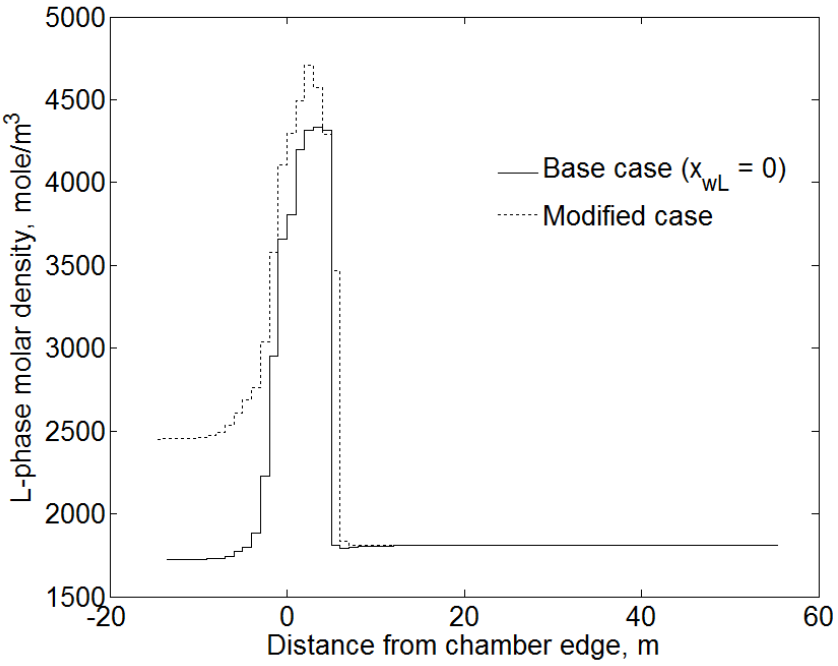

Figure 3.29. L-phase molar density profile for the 14th row at 1 year.

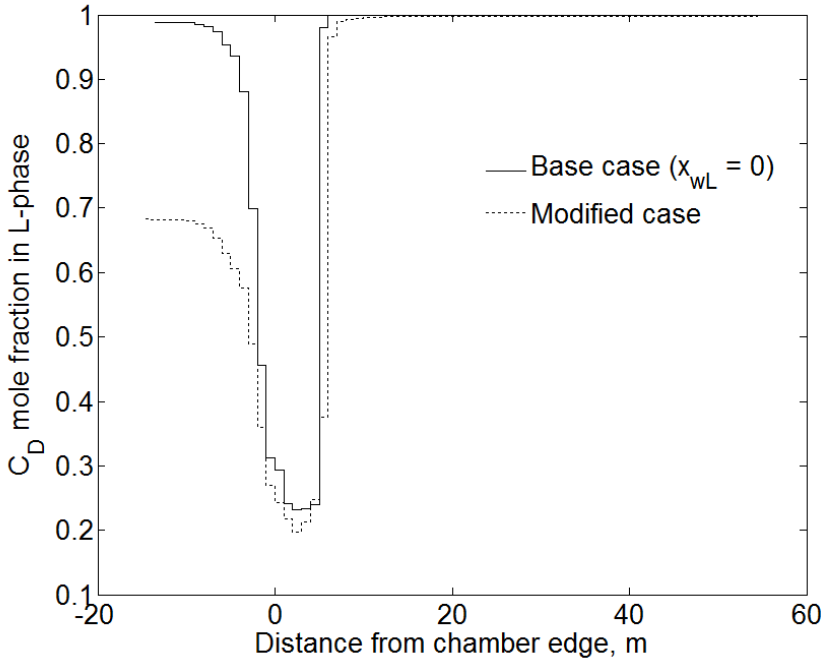

Figure 3.30a. Concentration profile of C_D in the L phase for the 14th row at 1 year.

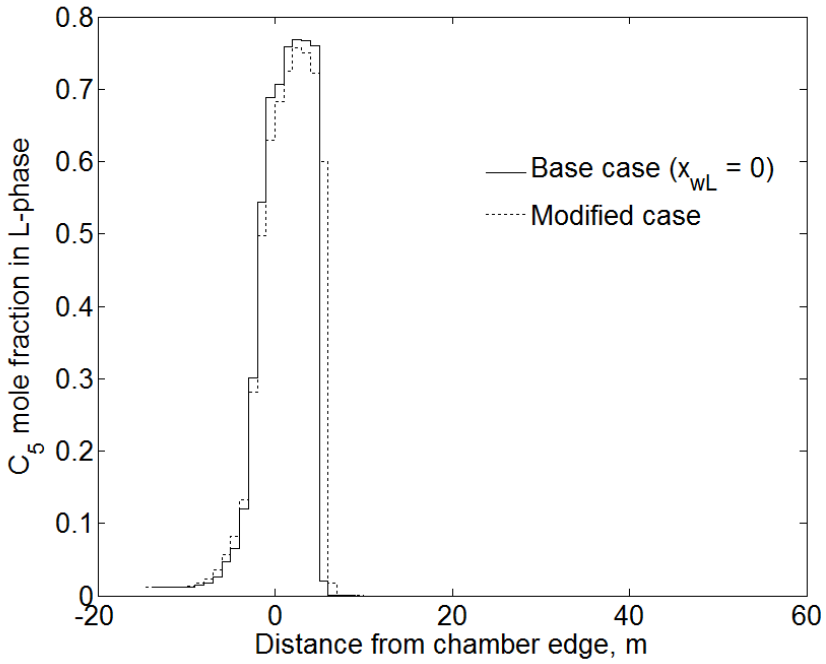

Figure 3.30b. Concentration profile of C_5 in the L phase for the 14th row at 1 year.

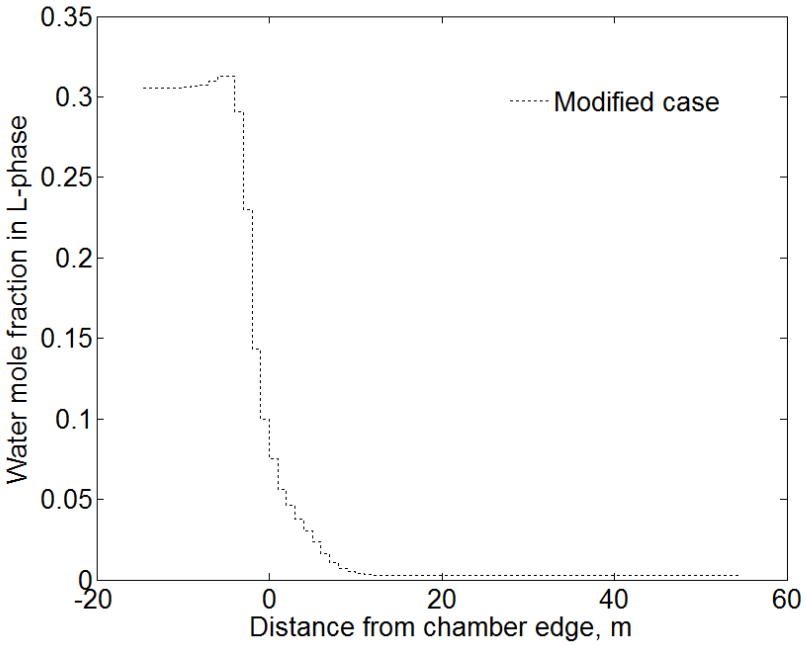

Figure 3.30c. Concentration profile of water in the L phase for the 14th row at 1 year.

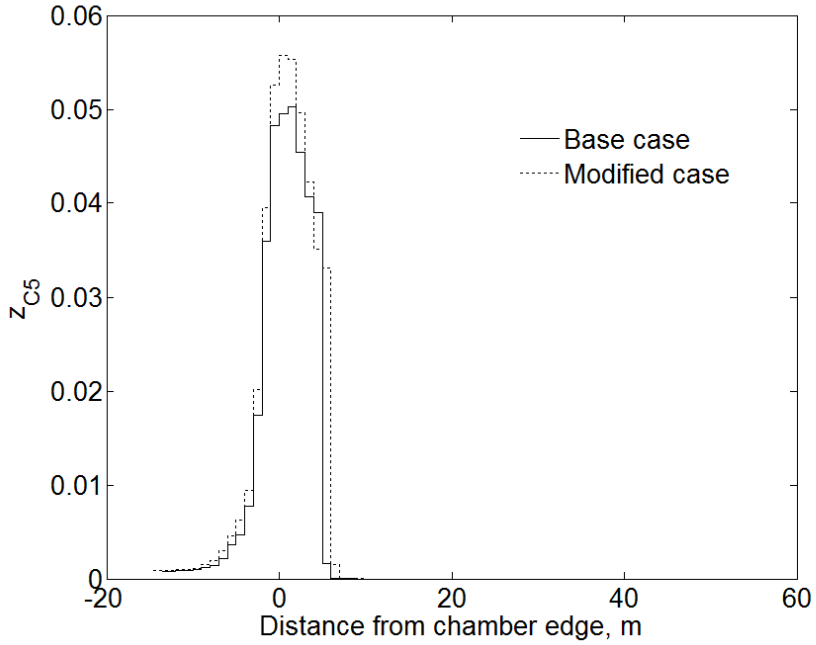

Figure 3.31a. Global concentration profile for n-C_5 for the 14th row at 1 year.

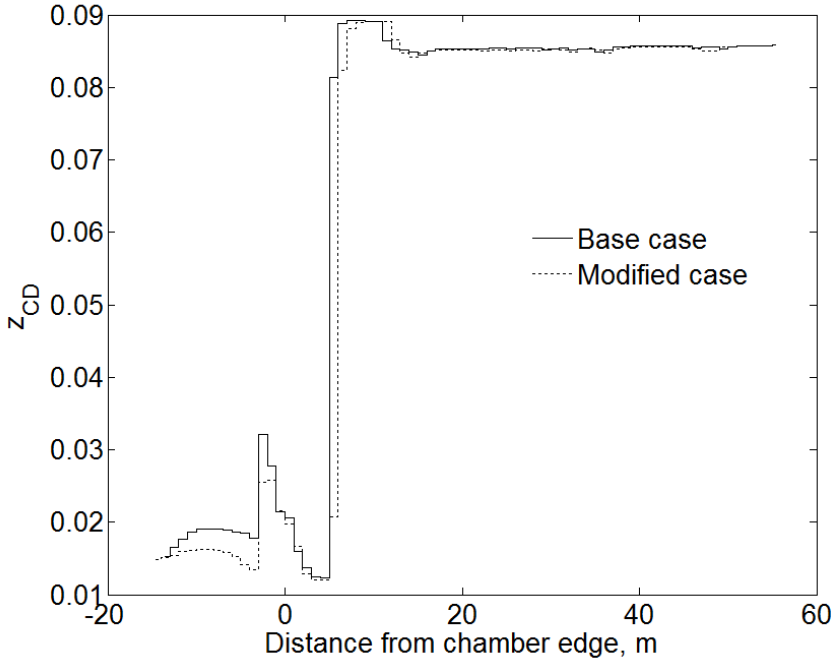

Figure 3.31b. Global concentration profile for C_D for the 14th row at 1 year.

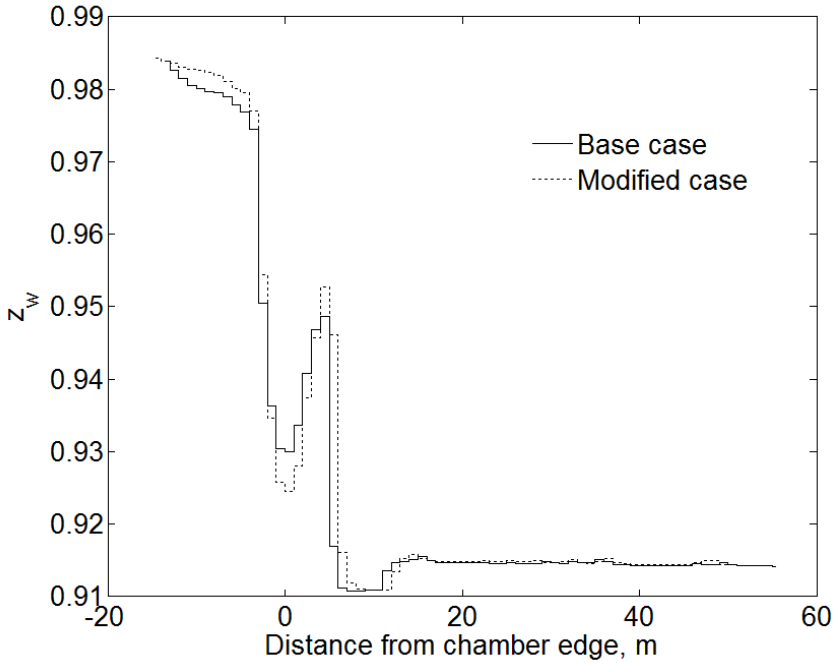

Figure 3.31c. Global concentration profile for water for the 14th row at 1 year.

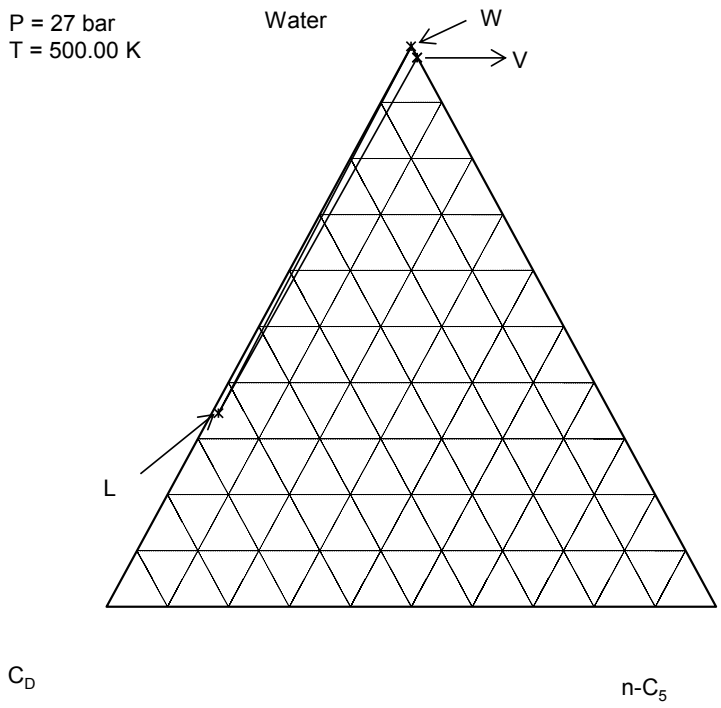

Figure 3.32a. Tie-triangle predicted using Approach 2 at 27 bars and 500.00 K.

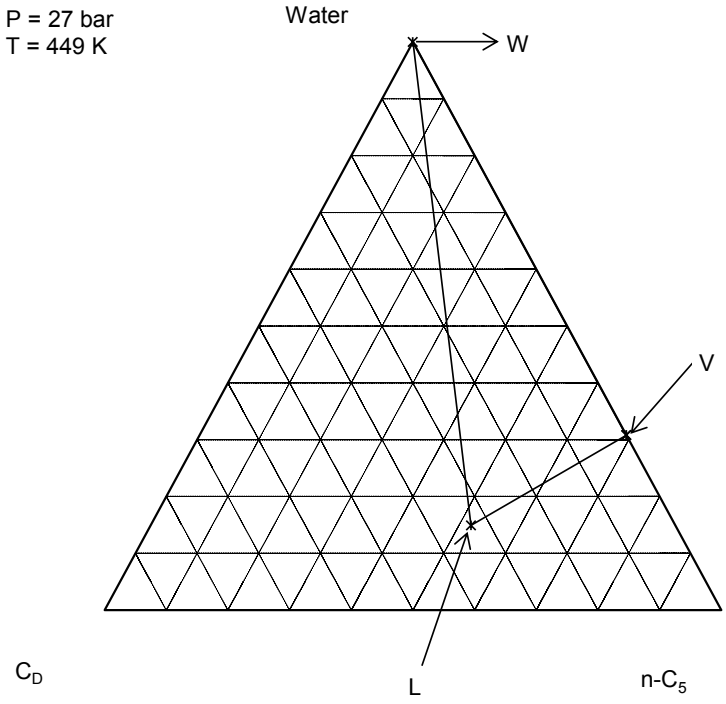

Figure 3.32b. Tie-triangle predicted using Approach 2 at 27 bars and 449.00 K.

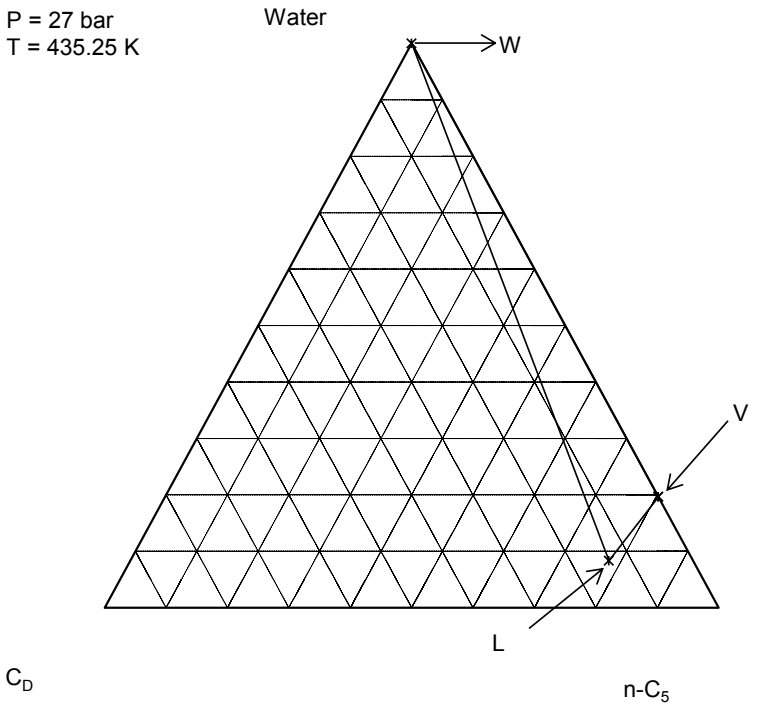

Figure 3.32c. Tie-triangle predicted using Approach 2 at 27 bars and 435.25 K.

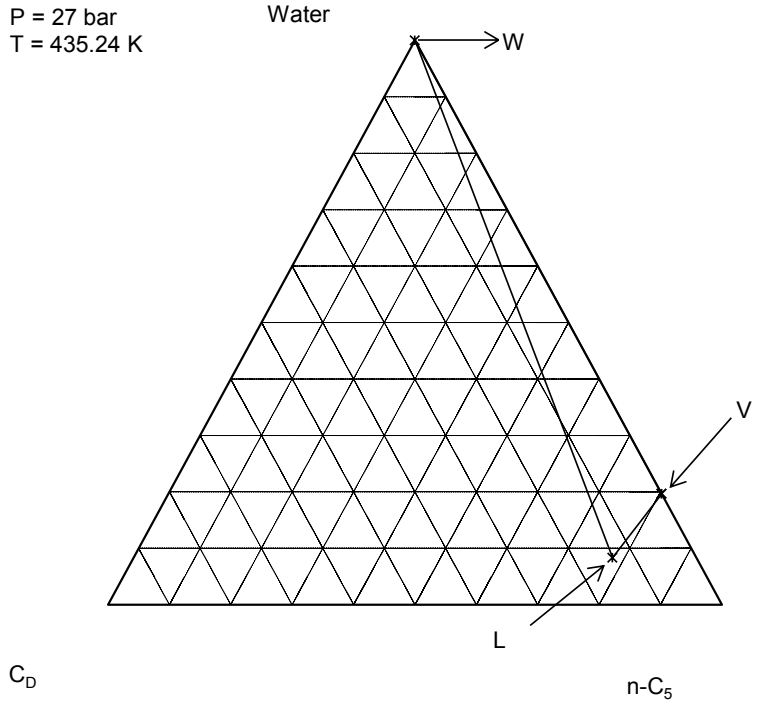

Figure 3.32d. Tie-triangle predicted using Approach 2 at 27 bars and 435.24 K.

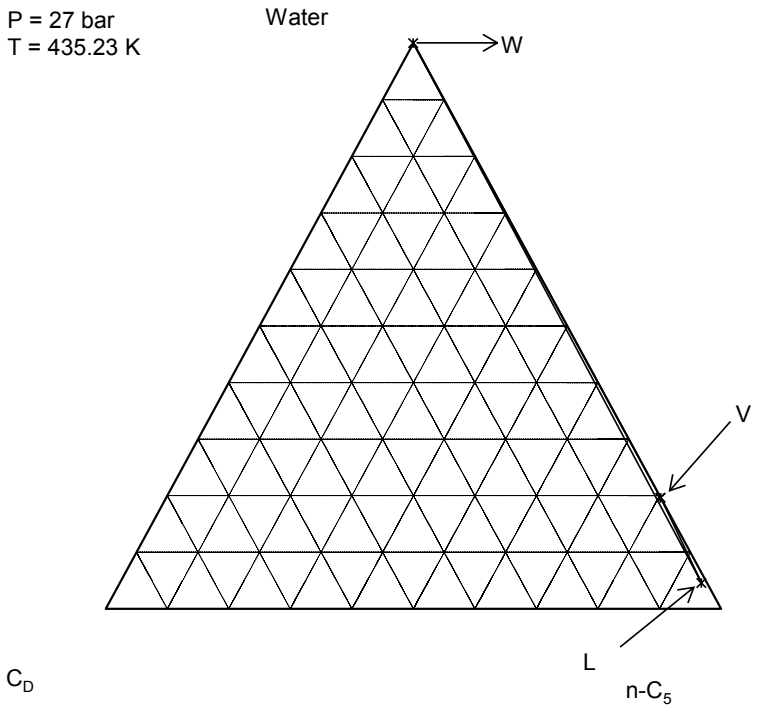

Figure 3.32e. Tie-triangle predicted using Approach 2 at 27 bars and 435.23 K. In the vicinity of the three-phase temperature of the water/n-C_5 binary, for global compositions in the vicinity of the n-C_5-water edge of composition space, the predicted composition of the L phase changes drastically, mimicking the composition of the L phase of the water/n-C_5 binary at three-phase coexistence (also see Figure 3.20c).

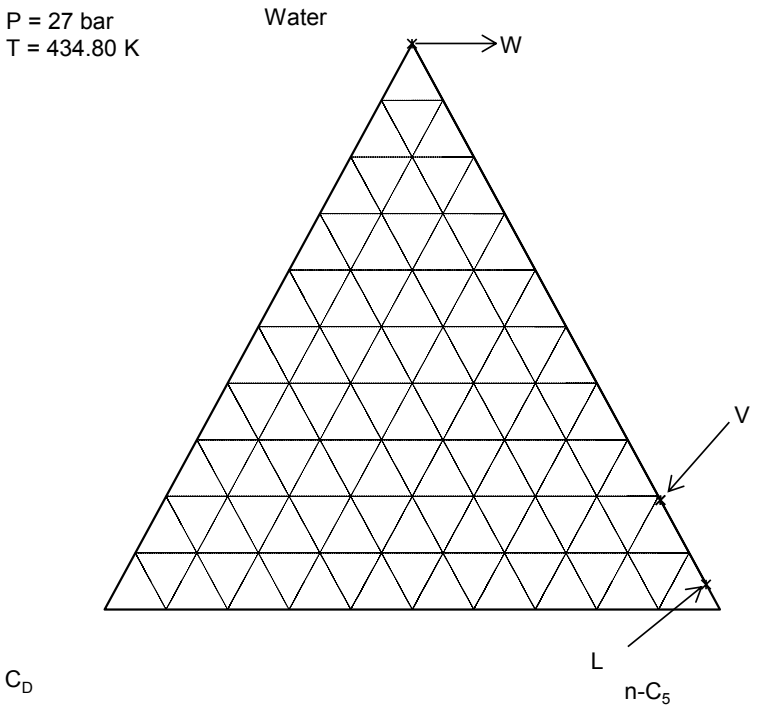

Figure 3.32f. Tie-triangle predicted using Approach 2 at 27 bars and 434.80 K. This represents the lowest temperature at which a tie-triangle comprising the V phase could be estimated. The resolution in temperature space employed is 0.01 K.

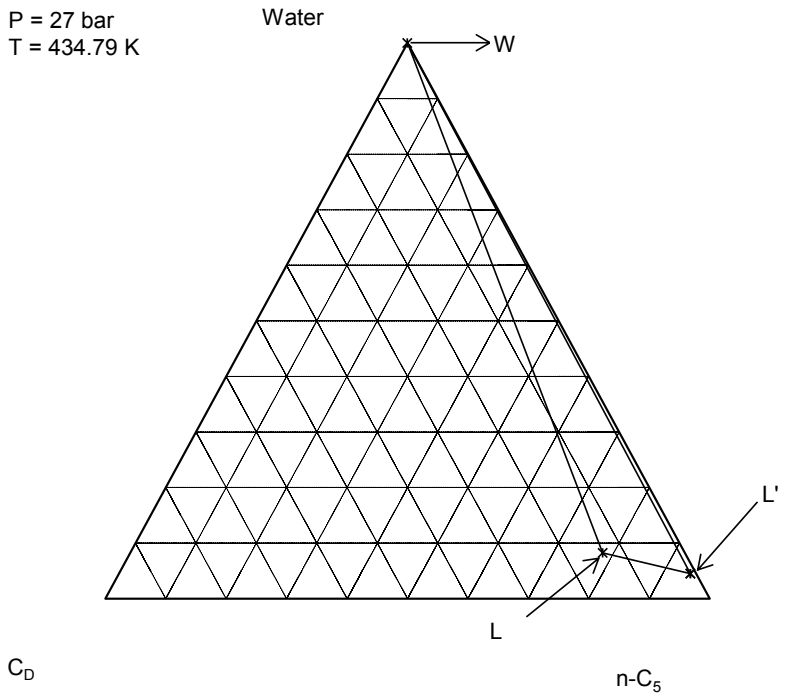

Figure 3.32g. Tie-triangle predicted using Approach 2 at 27 bars and 434.79 K. From this temperature and those lower, a solvent-rich L′ phase occurs instead of the V phase.

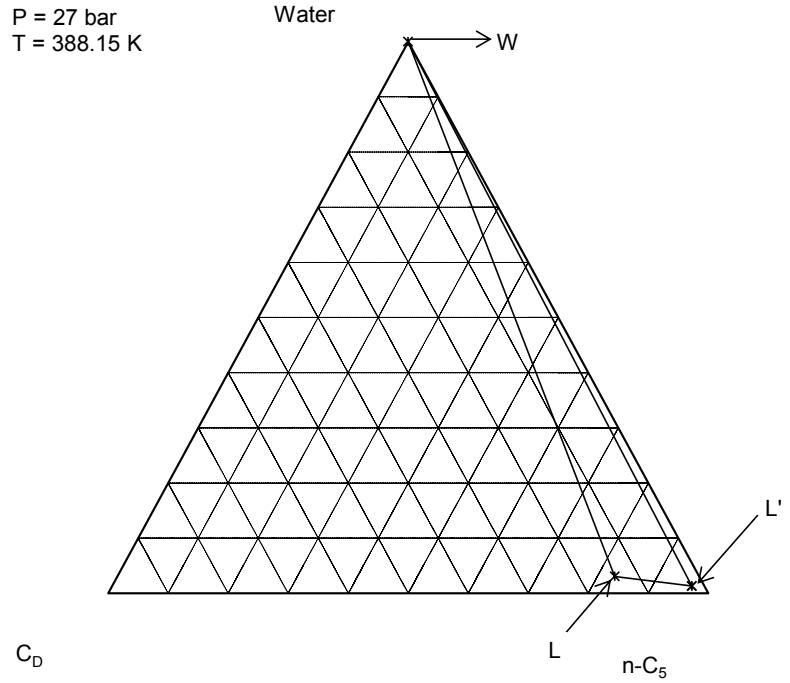

Figure 3.32h. Tie-triangle predicted using Approach 2 at 27 bars and 388.15 K.

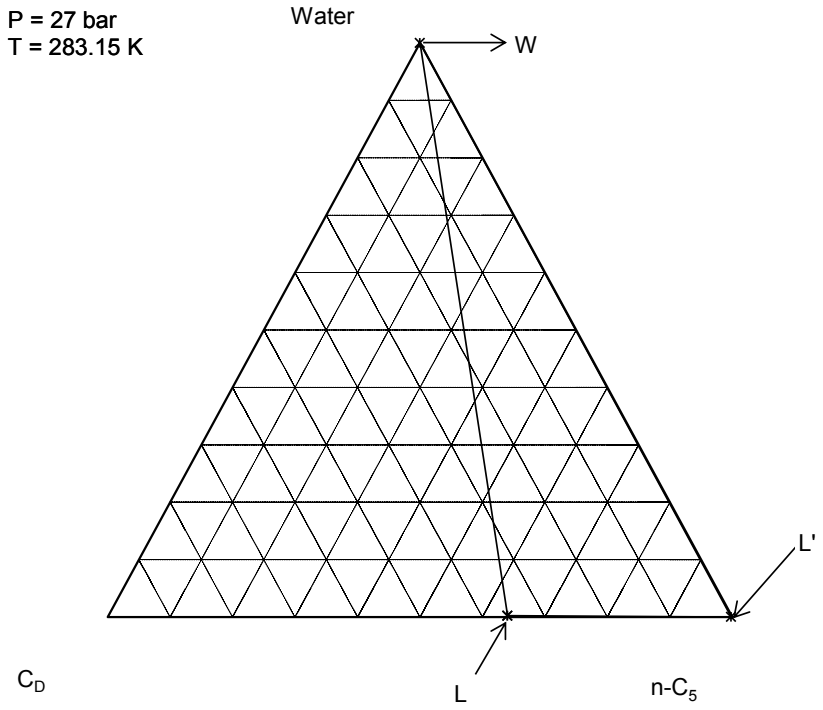

Figure 3.32i. Tie-triangle predicted using Approach 2 at 27 bars and 283.15 K.

Chapter 4. Summary, conclusions and future work

In this chapter, we summarize and conclude this research and present recommendations for future work. Chapter 1 presented the motivation behind the goal of this research – the development of a fluid model capable of accurate and efficient representation of multiphase behavior of a water-containing mixture of reservoir oil for application in steam injection processes. The key points specified in Chapter 1 are as follows:

- The commercial importance of steam injection processes and the need to improve their viability necessitate the development of a fundamental understanding of oil recovery mechanisms. A useful tool to enhance our current understanding is numerical reservoir simulation.

- Phase densities, viscosities and interfacial tension are composition-dependent properties. Inaccurate representation of these fundamental properties can potentially have a detrimental impact on oil recovery predictions through the inaccurate prediction of fractional flow of phases. Thus, reliable reservoir simulation of steam injection processes requires the accurate representation of multiphase behavior of water-containing reservoir oils.

- The efficient representation of multiphase behavior is also a priority owing to the significant computational cost associated with phase equilibrium calculations in reservoir simulation. Cubic EOSs employing the classical mixing rules serve as potential candidates for fluid modeling. This is based

on their simple mathematical formulation and capability to represent both vapor and liquid states.

- A number of EOS-based reservoir simulation studies of steam injection processes have been performed by other researchers. Prior investigations seem to exhibit potentially significant shortcomings. The two attributes that render prior investigations potentially deficient are:
    - Lack of consideration of the dissolution of water in the L phase.
    - Lack of justification for the choice of numerical values for fluid-model parameters.
- Standalone phase behavior models have also been developed in the models for water/hydrocarbon mixtures. However, the applicability of these models for water-containing mixtures of reservoir oils comprising heavy pseudo-components over a wide range of temperatures is unclear. Also for this purpose, a single framework based on a cubic EOS with the classical mixing rules has not been developed thus far.

The aforementioned points served as the motivation for the development of the product of this research. The product of this research is a new framework for the accurate representation of the multiphase behavior of water/reservoir oil mixtures based on the PR EOS with the classical mixing rules.

Chapter 2 presented a new characterization framework for the accurate representation of the multiphase compositional behavior of water/reservoir oil

mixtures (Approach 1). The development of this framework first involved the development of a new correlation for the BIP between water and n-alkanes using the measured binary three-phase curves of Brunner (1990). Following this is its extension to represent the multiphase compositional behavior of water-containing reservoir oils. The conclusions of this chapter are as follows:

- The correlation developed for water/n-alkane binaries predicts Type IIIa phase behavior for n-alkanes with CNs up to n-C_{25}, and type IIIb for CNs 26 and heavier. This transition between types IIIa and IIIb is plausible.

- The correlation for the BIP between water and n-alkanes yields reasonably accurate predictions for x_{wL} for water/n-alkane mixtures with CN up to n-C_{20}, for which limited experimental data are available. The correlation also yields systematic under-predictions for x_{wL} when employed for water-containing mixtures of reservoir oils. This observation is reasonable owing to the lower affinity that n-alkanes exhibit in comparison with aromatics and naphthenes, which are generally present in reservoir oils.

- The extension of the BIP correlation to adequately represent x_{wL} measured for water-containing reservoir oils requires a systematic reduction of the BIPs developed for water and n-alkanes.

- The BIP correlation developed for water with n-alkanes reproduces the asymptotic behavior experimentally observed for three-phase curves and x_{wL} for water with heavy n-alkanes. The x_{wL} exhibits a limiting trend line with respect to temperature that is nearly independent of the n-alkane CN

for temperatures that are not in the vicinity of the UCEP. For Approach 1, a constant BIP of 0.242 is required for the reproduction of the asymptotic behavior. This limit is reached at a value of 26 for the n-alkane CN.

- The solubilities of n-alkanes in the aqueous phase (x_{hcW}) are predicted to be orders of magnitude lower than experimental data reported in the literature. Approach 1 is inappropriate for applications that require quantitative accuracy for x_{hcW}.

Chapter 3 presented an improved framework (Approach 2) to characterize water-containing reservoir oils. The basis for its development is to address shortcomings of Approach 1 in terms of predictions of densities. Thus, the advantage of Approach 2 over Approach 1 is its capability to represent both the multiphase compositional and volumetric behavior of mixtures of water/reservoir oils with reasonable accuracy. A new correlation was developed for the BIPs for water with n-alkanes, which was then extended to water-containing bitumens. For Approach 2, the methodology for the development of the BIP correlation and its extension is akin to that for Approach 1. The development of the BIP correlation is preceded by the optimization of T_C, P_C and ω for n-alkanes with CNs < 7, and water. This optimization was performed against the experimentally measured vapor pressure and liquid phase density data, employing the method of Kumar and Okuno (2012). For n-alkanes heavier than n-C_6, the optimized T_C, P_C and ω were obtained from the previous work of Kumar and Okuno (2012). A simulation study was performed in which the impact of the dissolution of water in the L

phase on the drainage of bitumen in the ES-SAGD process employing n-C_5 as the solvent was investigated. The conclusions of this chapter are as follows:

- Approach 1 yields erroneous estimates for the density of the W phase through systematic under-prediction. In contrast, the predicted L-phase density matches reasonably well the measured data. A potentially detrimental consequence of the erroneous prediction of W-phase densities is the erroneous prediction of oil recovery through incorrect estimations of fluid saturations.

- For n-alkanes with CNs six and lower, the optimized values for T_C and P_C are lower than the physical values, while those for ω are higher than the physical values. For water, the optimized T_C and P_C are significantly higher than the physical values, while the opposite true for the optimized value of ω. The trend for the former (n-alkanes) is necessary to correct for the over-prediction of L phase densities by the PR EOS. The observation for the latter (water) results from the need to correct for the systematic under-prediction of the liquid phase density by the PR EOS.

- The optimized BIPs between water and n-alkanes for Approach 2 in the CN interval [7, 25] are systematically lower than those for Approach 1, while the reverse is true in the CN interval [3, 6]. These trends are borne out of the discrepancies in the trends for T_C and P_C for the two approaches.

- Approach 2 yields three-phase curves for water/n-alkane binaries with curvature that is slightly more accurate with the measurements of Brunner

(1990). The apparent difference in phase composition predictions made using the two approaches lie within the experimental uncertainty bounds. Thus, in terms of phase compositions, there is no distinct advantage of Approach 2 over Approach 1.

- For water/bitumen mixtures, the predicted density of the L phase using Approach 2 is slightly more accurate than Approach 1. The advantage of Approach 2 over Approach 1 is most evident in the predicted density of the W-phase. The co-volume parameter plays a crucial role in the obtainment of the improved accuracy for W-phase density predictions.

- As with Approach 1, the solubilities of n-alkanes in the aqueous phase (x_{hcW}) predicted using Approach 2 are orders of magnitude lower than experimental data. So, Approach 2 is not suitable for applications that require accurate estimates for x_{hcW}.

- The consideration of x_{wL} can have a significant impact on the drainage rate of bitumen in the ES-SAGD process. The observed improvement in the local displacement efficiency stems from an increase the L-phase mobility and molar density.

We have now reached the end of this thesis. For future research, we recommend the following:

- The characterization framework presented in this research considers the mutual solubilities of water and hydrocarbons. The results of the simplistic simulations performed using the developed framework indicate that the

consideration of x_{wL} in can be of importance in steam-injection processes specifically, ES-SAGD. However, the impact of the dissolution of water in the L phase on component and heat propagation within the reservoir has not been completely elucidated. This is owing to the shortcomings associated with the manner in which the simulations were performed. These shortcomings need to be addressed to improve the reliability of the simulation study presented in this research. The obtainment of reliability is crucial to the complete discernment of recovery mechanisms.

- The framework developed in this research can accurately represent phase compositions and phase densities of water-containing reservoir oils. The modeling of phase viscosities and interfacial tension was not performed in this work. These are important physical properties, and the modeling of them is of considerable significance in reservoir engineering application.

- Earlier, we mentioned that phase equilibrium calculations in reservoir simulation are computationally intensive. The development of efficient flash calculation algorithms capable of robust computation of phase equilibria can improve the global efficiency of EOS-based reservoir simulation.

- The shortcoming of the proposed framework in terms of x_{hcW} predictions could be addressed. A new mechanism based on simple models such as Henry's law could be developed.

References

Amani, M.J., Gray, M.R. and Shaw, J.M. 2013a. Phase Behavior of Athabasca Bitumen Water Mixtures at High Temperature and Pressure. *The Journal of Supercritical Fluids* **77**: 142-152.

Amani, M.J., Gray, M.R. and Shaw, J.M. 2013b. Volume of Mixing and Solubility of Water in Athabasca Bitumen at High Temperature and Pressure. *Fluid Phase Equilibria* **358**: 203-211.

Aparicio-Martínez, S. and Hall, K.R. 2007. Phase Equilibria in Water Containing Binary Systems From Molecular Based Equations of State. *Fluid Phase Equilibria* **254**(1): 112-125.

Badamchi-Zadeh, A., Yarranton, H., Maini, B.B. and Satyro, M. 2009. Phase Behaviour and Physical Property Measurements for VAPEX Solvents: Part II. Propane, Carbon Dioxide and Athabasca Bitumen. *Journal of Canadian Petroleum Technology* **48**(3): 57-65.

Badamchi-Zadeh, A., Yarranton, H., Svrcek, W. and Maini, B. 2009. Phase Behaviour and Physical Property Measurements for VAPEX solvents: Part I. Propane and Athabasca Bitumen. *Journal of Canadian Petroleum Technology* **48**(1): 54-61.

Baker, L.E., Piece, A.C., Luks, K.D. 1982. Gibbs Energy Analysis of Phase Equilibria. *Society of Petroleum Engineers Journal* **SPE 9806**: 731-742.

Barrufet, M.A., Liu, K., Rahman, S. and Wu, C. 1996. Simultaneous Vapor-Liquid-Liquid Equilibria and Phase Molar Densities of a Quaternary System

of Propane + Pentane + Octane + Water. *Journal of Chemical and Engineering Data* **41**(4): 918-922.

Beattie, J. A., Levine, S. W., Douslin, D. R. 1951. The Vapour Pressure and Critical Constants of Normal Pentane. *Journal of American Chemical Society* **73**: 4431-4432.

Brunner, E. 1990. Fluid mixtures at high pressures IX. Phase Separation and Critical Phenomena in 23 (n-alkane + water) mixtures. *The Journal of Chemical Thermodynamics* **22**(4): 335-353.

Chawla, I.S., Barrufet, M.A., Rahman, S., Beladi, M.K., and Wu, C.H. 1995. Influence of Temperature, Pressure and Molecular Weight of Hydrocarbon Components on the Multi-Phase Equilibria of Hydrocarbon/Water Systems. Presented at the SPE Annual Technical Conference and Exhibition, Dallas, U.S.A, 22 – 25 October.

Claus, P., Kleinrahm, R., Wagner, W. 2003. Measurements of the (p, V, T) Relation of Ethylene, Ethane, and Sulphur Hexafluoride in the Temperature Range from 235K to 520K at Pressure upto 30MPa Using and Accurate Single Sinker Densimeter. *Journal of Chemical Thermodynamics* **35**: 159-175.

Constantinou, L. and Gani, R. 1994. New Group Contribution Method for Estimating Properties of Pure Compounds. *AIChE Journal* **40**(10): 1697-1710.

Constantinou, L., Gani, R. and O'Connell, J.P. 1995. Estimation of the Acentric Factor and the Liquid Molar Volume at 298 K Using a New Group Contribution Method. *Fluid Phase Equilibria* **103**(1): 11-22.

Daridon, J.L., Lagourette, B., Saint-Guirons, H. and Xans, P. 1993. A Cubic Equation of State model for Phase Equilibrium Calculation of Alkane + Carbon dioxide + Water Using a Group Contribution k_{ij}. *Fluid Phase Equilibria* **91**(1): 31-54.

Daubert, T. and Danner, R. 1997. *API Technical Data Book-Petroleum Refining*. Washington DC: American Petroleum Institute (API).

Economou, I., Heidman, J., Tsonopoulos, C. and Wilson, G. 1997. Mutual Solubilities of Hydrocarbons and Water: III. 1-Hexene, 1-Octene, C_{10}- C_{12} Hydrocarbons. *AIChE Journal* **43**(2): 535-546.

Eubank, P.T., Wu, C.H., Alvarado, J.F., Forero, A. and Beladi, M.K. 1994. Measurement and Prediction of Three-Phase Water/Hydrocarbon Equilibria. *Fluid Phase Equilibria* **102**(2): 181-203.

Ewing, M. B., Ochoa, J. C. S. 2006a.Vapour Pressure of n-Pentane Determined by Comparative Ebulliometry. *Journal of Chemical Thermodynamics* **38**: 289-295.

Ewing, M. B., Ochoa, J. C. S. 2006b. Vapour Pressures of n-Hexane Determined by Comparative Ebulliometry, Journal of Chemical Thermodynamics, 38, 283-288Funke, M., Kleinrahm, R., Wagner, W. (2002). Measurement and Correlation of the (p, V, T) Relation of Ethane II. Saturated – Liquid and

Satuarted – Vapour Densities and Vapour Pressure along the Entire Coexistence Curve. *Journal of Chemical Thermodynamics* **34**: 2017-2039.

Ferguson, A.L., Debenedetti, P.G. and Panagiotopoulos, A.Z. 2009. Solubility and Molecular Conformations of n-Alkane Chains in Water. *The Journal of Physical Chemistry B* **113**(18): 6405-6414.

Freitas, L., Platt, G., Henderson, N. 2004. Novel Approach for the Calculation of Critical Poitns of Binary Mixtures Using Global Optimization. *Fluid Phase Equilibria* **225**: 29-37.

Glandt, C.A. and Chapman, W.G. 1995. Effect of Water Dissolution on Oil Viscosity. *SPE Reservoir Engineering* **10**(1): 59-64.

Glos, S., Kleinrahm, R., Wagner, W. 2004.Measurements of the (p, V, T) Relation of Propane, Propylene, n-Butane, and Isobutane in the Temperature Range from (95 to 340) K at Pressure up to 12 MPa Using an Accurate Two Sinker Densimeter. *Journal of Chemical Thermodynamics* **36**: 1037-1059.

Griswold, J. and Kasch, J.E. 1942. Hydrocarbon-Water Solubilities at Elevated Temperatures and Pressures. *Industrial and Engineering Chemistry* **34**(7): 804-806.

Heidemann, R.A. 1974. Three-Phase Equilibria Using Equations of State. *AIChE Journal* **20**(5): 847-855.

Heidman, J.L., Tsonopoulos, C., Brady, C.J. and Wilson, G.M. 1985. High-Temperature Mutual Solubilities of Hydrocarbons and Water. Part II: Ethylbenzene, Ethylcyclohexane, and n-Octane. *AIChE Journal* **31**(3): 376-384.

Huron, M. and Vidal, J. 1979. New Mixing Rules in Simple Equations of State for Representing Vapor-Liquid Equilibria of Strongly Non-Ideal Mixtures. *Fluid Phase Equilibria* **3**(4): 255-271.

Kayukawa, Y., Hasumoto, M., Kano, Y., Watanabe, K. 2005.Liquid Phase Thermodynamic Properties for Propane (1), n-Butane (2), and Isobutane (3). Journal of Chemical & Engineering Data **50**: 556-564.

Kelso, E. A., Felsing, W. A. 1940. The Pressure – Volume –Temperature Relation of n-Hexane and of 2-Methylpentane. *Journal of American Chemical Society* **62**: 3132-3134.

Keshavarz, M., Okuno, R., and Babadagli, T. 2013. Optimal Application Conditions for Steam-Solvent Coinjection. Presented at the SPE Heavy Oil Conference, Calgary, Canada, 11 – 13 June.

Keshavarz, M., Okuno, R., Babdagli, T. 2014. Efficient oil displacement near the chamber edge in ES-SAGD. Journal of Petroleum Science and Engineering **118**: 99-13.

Keshavarz, M., Okuno, R., Babdagli, T. 2014. A Semi-Analytical Solution to Optimize Single-Component Solvent Coinjection with Steam (manuscript in preparation).

Klimeck, J., Kleinrahm, R., Wagner, W. 2001. Measurements of (p, V, T) Relation of Methane and Carbon Dioxide in the Temperature Range of 240 K to 520 K at Pressure upto 30 MPa Using a New Accurate Single Sinker Densimeter. *Journal of Chemical Thermodynamics* **33**: 251-267.

Kobayashi, R. and Katz, D. 1953. Vapor-Liquid Equilibria for Binary Hydrocarbon-Water Systems. *Industrial and Engineering Chemistry* **45**(2): 440-446.

Kontogeorgis, G.M. and Tassios, D.P. 1997. Critical Constants and Acentric Factors for Long-Chain Alkanes Suitable for Corresponding States Applications. A Critical Review. *Chemical Engineering Journal* **66**(1): 35-49.

Kumar, A., Okuno, R. 2012. Critical Parameters Optimized for Accurate Phase Behavior Modeling for Heavy n-Alkanes up to C100 using the Peng-Robinson Equation of State. *Fluid Phase Equilibria* **335**: 46-59.

Kumar, A. and Okuno, R. 2013. Characterization of Reservoir Fluids Using an EOS Based on Perturbation From n-Alkanes. *Fluid Phase Equilibria* **358**: 250-271.

Kumar, A., Okuno, R. 2014. Direct Perturbation of the Peng-Robinson Attraction and Covolume Parameters for Reservoir Fluid Characterization. Chemical Engineering Science (manuscript under review since June 5).

Lake, L.W. 1989. *Enhanced Oil Recovery*. Englewood Cliffs, New Jersey: Prentice-Hall.

Lee, A. L., Ellington, R. T. 1965. Viscosity of n-Pentane. *Journal of Chemical and Engineering Data* **10**(2): 101-103.

Li, Y. and Nghiem, L.X. 1986. Phase Equilibria of Oil, Gas and Water/Brine Mixtures From a Cubic Equation of State and Henry's law. *The Canadian Journal of Chemical Engineering* **64**(3): 486-496.

Linstrom, P.J. and Mallard, W.G. 2001. *NIST Standard Reference Database 69: Phase Change Properties*. Gaithersburg, Maryland: Standard Reference Data Program, National Institute of Standards and Technology, http://webbook.nist.gov/chemistry (accessed March 4 2014).

Luo, S. and Barrufet, M.A. 2005. Reservoir Simulation Study of Water-in-Oil Solubility Effect on Oil Recovery in Steam Injection Process. *SPE Reservoir Evaluation and Engineering* **8**(6): 528-533.

Maczynski, A., Shaw, D.G., Goral, M., et al. 2005. IUPAC-NIST Solubility Data Series. 81. Hydrocarbons With Water and Seawater-Revised and Updated. Part 4. C_6H_{14} Hydrocarbons With Water. Journal of Physical and Chemical reference data **34**(2): 709-753.

McGarry, J. 1983. Correlation and Prediction of the Vapor Pressures of Pure Liquids Over Large Pressure Ranges. *Industrial and Engineering Chemistry Process Design and Development* **22**(2): 313-322.

McKetta, J.J. and Katz, D.L. 1948. Methane–n-Butane–Water System in Two-and Three-Phase Regions. *Industrial and Engineering Chemistry* **40**(5): 853-863.

Mehra, R.K., Heidemann, R.A. and Aziz, K. 1982. Computation of Multiphase Equilibrium for Compositional Simulation. *SPE Journal* **22**(1): 61-68.

Mehrotra, A.K. and Svrcek, W.Y. 1985. Viscosity, Density and Gas Solubility Data for Oil Sand Bitumens. Part II: Peace River Bitumen Saturated with N_2, CO, CH_4, CO_2 and C_2H_6. *AOSTRA Journal of Research* **1**(4): 269-279.

Miyamoto, H., Uematsu, M. 2007. Measurements of Vapour Pressures and Saturated –Liquid Densities for n-Butane at T= (280 to 424) K, *Journal of Chemical Thermodynamics* **39**: 827-832.

Okuno, R., Johns, R.T., Sepehrnoori, K. 2010. A New Algorithm for Rachford-Rice for Multiphase Compositional Simulation. *Society of Petroleum Engineers Journal*. **SPE 117752**: 313-325.

Perry, R.H., Green, D. W. 2008. *Perry's Chemical Engineers' Handbook*, *8th Edition*. New York: The McGraw Hill Companies, Inc.

Phillips, E. M., Thodos, G. 1962. The PVT-Behavior of Ethane in the Gaseous and Liquid States, *Society of Petroleum Engineers Journal* **SPE 1632-G:** 83-86.

Mohebbinia, S., Sepehrnoori, K. and Johns, R.T. 2013. Four-Phase Equilibrium Calculations of Carbon Dioxide/Hydrocarbon/Water Systems With a Reduced Method. *SPE Journal* **18**(5): 943-951.

Nasrifar, K. and Moshfeghian, M. 2002. Liquid–Liquid Equilibria of Water–Hydrocarbon Systems From Cubic Equations of State. *Fluid Phase Equilibria* **193**(1): 261-275.

Nikitin, E.D., Pavlov, P.A. and Popov, A.P. 1997. Vapour-Liquid Critical Temperatures and Pressures of Normal Alkanes with From 19 to 36 Carbon Atoms, Naphthalene and m-Terphenyl Determined by the Pulse-Heating Technique. *Fluid Phase Equilibria* **141**(1): 155-164.

Olds, R.H., Sage, B.H. and Lacey, W.N. 1942. Phase Equilibria in Hydrocarbon Systems. Composition of the Dew-Point gas of the Methane-Water System. *Industrial and Engineering Chemistry* **34**(10): 1223-1227.

Peneloux, A., Rauzy, E. 1982. A Consistent Correction for Redlich-Kwong-Soave Volumes. *Fluid Phase Equilibria* **8**: 7 – 23.

Peng, D. and Robinson, D.B. 1976. Two and Three Phase Equilibrium Calculations for Systems Containing Water. *The Canadian Journal of Chemical Engineering* **54**(5): 595-599.

Prats, M. 1982. *Thermal Recovery*: New York: HL Doherty Memorial Fund of AIME, SPE.

Reamer, H.H, Olds, R.H., Sage, B.H. and Lacey, W.N. 1943. Phase Equilibria in Hydrocarbon systems. Composition of Dew-Point gas in Ethane-Water System. *Industrial and Engineering Chemistry* **35**(7): 790-793.

Reamer, H.H., Olds, R.H., Sage, B.H., and Lacey, W.N. 1944. Phase Equilibria in Hydrocarbon Systems. n-Butane–Water System in Three-Phase Region. *Industrial and Engineering Chemistry* **36**(4): 381-383.

Reis, J. C. 1992. A Steam-Assisted Gravity Drainage Model for Tar Sands: Linear Geometry. *The Journal of Canadian Petroleum Technology.* **31** (10): 14-20.

Rowlinson, J.S., Swinton, F.L. 1982. *Liquids and Liquid Mixtures*. Great Britain: Butterworth Scientific.

Sage, B. H., Lacey, W. N. 1942. Thermodynamic Properties of n-Pentane. *Industrial and Engineering Chemistry* **34**(6): 730-737.

Satyro, M.A., Shaw, J.M. and Yarranton, H.W. 2013. A Practical Method for the Estimation of Oil and Water Mutual Solubilities. *Fluid Phase Equilibria* **355**: 12-25.

Scheffer, F.E.C. 1913. On the System Hexane-Water. *Koninklijke Nederlandse Akademie van Weteschappen Proceedings* **16**(1): 404-418.

Scheffer, F.E.C 1914. On Unmixing in a Binary System for Which the Three-Phase Pressure is Greater Than the sum of the Vapour Tension of the two Components. *Koninklijke Nederlandse Akademie Van Weteschappen Proceedings Series B Physical Sciences* **17**: 834-839.

Shaw, D.G., Maczynski, A., Goral, M., et al. 2005. IUPAC-NIST Solubility Data Series. 81. Hydrocarbons With Water and Seawater- Revised and Updated. Part 7. C_8H_{12}–C_8H_{18} Hydrocarbons With Water. *Journal of Physical and Chemical Reference Data* **34**(4): 2261-2298.

Shaw, D.G., Maczynski, A., Goral, M., et al. 2006a. IUPAC-NIST Solubility Data Series. 81. Hydrocarbons With Water and Seawater-Revised and Updated. Part 9. C_{10} Hydrocarbons with Water. *Journal of Physical and Chemical Reference Data* **35**(1): 93-151.

Shaw, D.G., Maczynski, A., Goral, M., et al. 2006b. IUPAC-NIST Solubility Data Series. 81. Hydrocarbons With Water and Seawater-Revised and Updated. Part 11. C_{13}–C_{36} Hydrocarbons with Water. *Journal of Physical and Chemical Reference Data* **35**(2): 687-784.

Shinta, A.A. and Firoozabadi, A. 1997. Predicting Phase Behavior of Water/Reservoir-Crude Systems With the Association Concept. *SPE Reservoir Engineering* **12**(2): 131-137.

Skripka, V.G. 1979. Solubility of Water in Normal Alkanes at Elevated Temperatures and Pressures. *Chemistry and Technology of Fuels and Oils* **15**(2): 88-90.

Søreide, I. 1989. Improved Phase Behavior Predictions of Petroleum Reservoir Fluids from a Cubic Equation of State. *Ph.D. dissertation*. Trondheim, Norway: Norwegian University of Science and Technology.

Søreide, I. and Whitson, C.H. 1992. Peng-Robinson Predictions for Hydrocarbons, CO_2, N_2, and H_2S With Pure Water and NaCl Brine. *Fluid Phase Equilibria* **77**: 217-240.

Thomas, S. 2008. Enhanced Oil Recovery- An Overview. *Oil and Gas Science and Technology* **63**: 9-19.

Tsonopoulos, C. and Heidman, J.L. 1986. High-Pressure Vapor-Liquid Equilibria With Cubic Equations of state. *Fluid Phase Equilibria* **29**: 391-414.

Tsonopoulos, C. 1999. Thermodynamic Analysis of the Mutual Solubilities of Normal Alkanes and Water. *Fluid Phase Equilibria* **156**(1): 21-33.

Tsonopoulos, C. and Wilson, G.M. 1983. High-Temperature Mutual Solubilities of Hydrocarbons and Water. Part I: Benzene, Cyclohexane and n-Hexane. *AIChE Journal* **29**(6): 990-999.

Valderrama, J.O. The State of Cubic Equations of State. 2003. *Industrial and Engineering Chemistry* **42**: 1603-1618.

Van Konynenburg, P.H. and Scott, R.L. 1980. Critical Lines and Phase Equilibria in Binary van der Waals Mixtures. *Philosophical Transactions of the Royal Society of London.Series A, Mathematical and Physical Sciences* **298**(1442): 495-540.

Varavei, A., Sepehrnoori, K. 2009. An EOS-Based Compositional Thermal Reservoir Simulator. Presented at the SPE Reservoir Simulation Symposium, Woodlands, Texas, USA, 2 – 4 February.

Wang, P. and Pope, G.A. 2001. Proper Use of Equations of State for Compositional Reservoir Simulation. *Journal of Petroleum Technology* **53**: 74-81.

Wagner, W. and Pruß, A. 2002. The IAPWS Formulation 1995 for the Thermodynamic Properties of Ordinary Water Substance for General and Scientific use. *Journal of Physical and Chemical Reference Data* **31**(2): 387-535.

Appendix A. Peng-Robinson EOS with classical mixing rules

The Peng-Robinson EOS (Peng and Robinson, 1976) for a pure component is presented equations A-1 to A-8.

$$P = \frac{RT}{\underline{V}-b} - \frac{a(T)}{\left(\underline{V}^2+2\underline{V}b-b^2\right)} \quad \text{(A-1)}$$

where a is the attraction parameter, b is the co-volume parameter, R is the universal gas constant, and $\underline{V}$ is the molar volume.

$$a = 0.45724\frac{R^2{T_c}^2}{P_c}\alpha(T) \quad \text{(A-2)}$$

α is the temperature dependence factor for the attraction parameter

$$\alpha(T) = \left(1.0 + m(1-\sqrt{T_r})\right)^2 \quad \text{(A-3)}$$

$$m = 0.37464 + 1.54226\omega - 0.26992\omega;\ \omega \leq 0.49 \quad \text{(A-4)}$$

$$m = 0.379642 + 1.48503\omega - 0.1664423\omega^2 + 0.01666\omega^3;\ \omega > 0.49 \quad \text{(A-5)}$$

$$b = 0.0778\frac{RT_c}{P_c} \quad \text{(A-6)}$$

The PR EOS can be extended to mixtures using mixing rules for the attraction and co-volume parameters. The van der Waals mixing rule for an N_C component mixture is presented in equations A-7 and A-8.

$$a = \sum_{i=1}^{N_c}\sum_{i=1}^{N_c} x_i x_j\sqrt{a_i a_j}(1.0 - BIP) \quad \text{(A-7)}$$

$$b = \sum_{i=1}^{N_c} x_i b_i \quad \text{(A-8)}$$

All BIPs are considered to be symmetric, and the value of the BIP for interactions between the same chemical species is set to be zero.

Appendix B. Computational methods for three-phase curves of water/n-alkane binaries

This appendix presents the mathematical methods employed in this research for the computation of three-phase curves of water/n-alkane binaries. In Appendix B-1, the procedure for the estimation of the three-phase temperature for specified pressure is described. In Appendix B-2, the procedure for the estimation of the UCEP is described.

Appendix B-1. Estimation of three-phase temperature for specified pressure for binary mixtures

Overview

In this sub-section, the methodology for computing the three-phase temperature ($T_{3\varphi}$) for specified pressure is described. The information key to the development of this procedure is the number of degrees of freedom. For a system existing at non-critical conditions, the number of degrees of freedom is given by ($N_C - N_P + 2$), where N_C and N_P represent the number of components and equilibrium phases, respectively. For a binary system, this is equivalent to unity, which means that for specified pressure or temperature, the corresponding three-phase temperature or pressure is unique.

The proposed method is different from the conventional methodology for the determination of three-phase coexistence using P-T flash calculation, and the basis for this difference as hinted above, is related to the available degrees of freedom. In the conventional method, at specified pressure, temperature and overall composition (z), the stability of the homogeneous fluid phase is determined based on the Tangent Plane Distance (TPD) criterion (equation B-1),

$$\sum_{i=1}^{N_C} x_i\left(\ln x_i + \ln \hat{\varphi}_i\,(T, P, \mathbf{x}) - \ln z_i - \ln \hat{\varphi}_i\,(T, P, \mathbf{z})\right) \geq 0 \qquad \text{(B-1)}$$

If deemed unstable, a phase-split calculation is performed for two equilibrium phases. Both equilibrium phases are subject to stability tests again, using the TPD criterion. If one of the phases is found to be unstable, another phase-split calculation is performed for three-phase equilibrium. In the phase-split calculation, the Rachford-Rice equation is solved. The solution of the multiphase Rachford-Rice equation requires that the number of degrees of freedom to be at least zero ($N_C \geq N_P$) at specified T and P. Binary systems existing forming three equilibrium phases do not fulfil this condition, and this necessitates the development of an alternative methodology for the determination of three-phase coexistence.

The first order necessary condition for phase equilibrium for a closed system requires the component fugacities to be phase-invariant (Baker et al. 1982). So for specified P, at the corresponding three-phase temperature, equation B-2 must hold.

$$\hat{f}_{iV}(P, T_{3\varphi}) = \hat{f}_{iL}(P, T_{3\varphi}) = \hat{f}_{iW}(P, T_{3\varphi}) \qquad \text{(B-2)}$$

Due to the degree of freedom constraint, the three-phase temperature, and the corresponding phase compositions, for fixed pressure is determined by solving either of the two systems of equations shown in equation sets B-3 and B-4,

$$\begin{aligned} \hat{f}_{iL}\left(P, T_{3\varphi}, \mathbf{x_L}\right) - \hat{f}_{iW}\left(P, T_{3\varphi}, \mathbf{x_W}\right) &= 0 \\ \hat{f}_{iV}\left(P, T_{3\varphi}, \mathbf{x_V}\right) - \hat{f}_{iW}\left(P, T_{3\varphi}, \mathbf{x_W}\right) &= 0 \end{aligned} \tag{B-3}$$

$$\begin{aligned} \hat{f}_{iL}\left(P, T_{3\varphi}, \mathbf{x_L}\right) - \hat{f}_{i,W}\left(P, T_{3\varphi}, \mathbf{x_W}\right) &= 0 \\ \hat{f}_{iV}\left(P, T_{3\varphi}, \mathbf{x_V}\right) - \hat{f}_{iL}\left(P, T_{3\varphi}, \mathbf{x_L}\right) &= 0 \end{aligned} \tag{B-4}$$

In this work, an interval search method has been employed to determine $T_{3\varphi}$.

The solution of the equation systems shown above requires the determination of the V, L and W lobes of the Gibbs free energy change on mixing in composition space for specified T and P. These are determined through an exhaustive search in composition space, which is rendered feasible for binary systems as the composition space is one-dimensional. The determinability of all three lobes requires that for specified pressure, the temperature must be equal to the corresponding three-phase temperature or located in its neighborhood. Thus, as with most numerical algorithms, the functionality of this procedure is also contingent upon the quality of the initial estimate for $T_{3\varphi}$ around which, a search interval for the three-phase temperature is defined. For water/n-alkane binaries, a suggested guide for the initial estimate $T_{3\varphi}$ is the temperature, T, at which the pressure of interest is equivalent to the sum of the saturation pressures of the pure components as shown in equation B-5.

$$P \approx P_{hc}^{Sat}(T) + P_{w}^{Sat}(T) \tag{B-5}$$

Procedure

Step 1. Define a search interval for the three-phase temperature, for specified pressure and overall composition. Equation B-5 can be used to obtain an initial estimate for $T_{3\varphi}$ around which the search interval can be defined.

Step 2. Starting from either the upper bound or the lower bound for the defined search interval, sequentially solve equations B-6 and B-7, separately.

$$\hat{f}_{iL}(P, T, \mathbf{x_L}) - \hat{f}_{iW}(P, T, \mathbf{x_W}) = 0 \quad \text{(B-6)}$$

$$\hat{f}_{iV}(P, T, \mathbf{x_V}) - \hat{f}_{iW}(P, T, \mathbf{x_W}) = 0 \quad \text{(B-7)}$$

If the solution of equation B-7 becomes difficult, solve equation B-8 instead.

$$\hat{f}_{iV}(P, T, \mathbf{x_V}) - \hat{f}_{iL}(P, T, \mathbf{x_L}) = 0 \quad \text{(B-8)}$$

Define the term $\Delta\hat{f}_i(P, T)$ as specified in equation B-9.

$$\Delta\hat{f}_i(P, T) = \hat{f}_{iV}(P, T, \mathbf{x_V}) - \hat{f}_{iL}(P, T, \mathbf{x_L}) \quad \text{(B-9)}$$

Step 3. Identify a sub-interval within the defined search interval over which $\Delta\hat{f}_i(P, T)$ changes sign. The three-phase temperature lies within the identified sub-interval. At $T_{3\varphi}$, equation B-10 must hold.

$$\Delta\hat{f}_i\left(P, T_{3\varphi}\right) = 0 \quad \text{(B-10)}$$

Step 4. Over the ascertained sub-interval for the three-phase temperature, identify $T_{3\varphi}$ using an interval search method (e.g., Regula Falsi). The recommended stopping criterion for the interval search method is presented in equation B-11.

$$\left|\Delta\hat{f}_i\left(P, T_{3\varphi}\right)\right| \leq 10^{-8} \tag{B-11}$$

Appendix B-2. Estimation of UCEPs for water/n-alkane binaries

Theoretical development

In this sub-section, the classical criteria for the UCEPs of water/n-alkane binaries are presented. As the UCEP is a critical point, the classical criteria for criticality must hold. For a binary mixture, these criteria are presented using the Gibbs free energy specification (Rowlinson and Swinton, 1982, Freitas et al., 2004), and shown in equations B-12 to B-14.

$$\left.\frac{\partial^2 \underline{G}}{\partial {x_2}^2}\right|_{T,P} = 0 \tag{B-12}$$

$$\left.\frac{\partial^3 \underline{G}}{\partial {x_2}^3}\right|_{T,P} = 0 \tag{B-13}$$

$$\left.\frac{\partial^4 \underline{G}}{\partial {x_2}^4}\right|_{T,P} > 0 \tag{B-14}$$

In these equations, $\underline{G}$ represents the molar Gibbs free energy, while the term x_2 represents the mole fraction of component designated the index 2, which can be either of the two components.

The criticality criteria can also be expressed in terms of the molar Gibbs free energy change on mixing ($\Delta_m\underline{G}$) without the loss of generality (equations B-15 through B-17).

$$\left.\frac{\partial^2 \Delta_m \underline{G}}{\partial {x_2}^2}\right|_{T_{UCEP},P_{UCEP}} = 0 \tag{B-15}$$

$$\left.\frac{\partial^3 \Delta_m \underline{G}}{\partial {x_2}^3}\right|_{T_{UCEP},P_{UCEP}} = 0 \tag{B-16}$$

$$\left.\frac{\partial^4 \Delta_m \underline{G}}{\partial {x_2}^4}\right|_{T_{UCEP},P_{UCEP}} > 0 \tag{B-17}$$

Since at the UCEP, critical phase is in equilibrium with another phase (W for type IIIa systems, L for type IIIb systems), the first order necessary criterion for phase equilibrium must also hold (Baker et al., 1982). This is presented in equation B-18.

$$\hat{f}_i(T_{UCEP}, P_{UCEP}, \mathbf{x_{UCEP}}) = \hat{f}_i(T_{UCEP}, P_{UCEP}, \mathbf{x}) \tag{B-18}$$

Where x_{UCEP}, and x, stand for the compositions of the critical and non-critical phases, respectively. $\hat{f}_i$ stands for the fugacity of component 'i'.

The molar Gibbs free energy change on mixing for a mixture comprising N_C components is presented in equation B-19.

$$\frac{\Delta_m \underline{G}}{RT} = \sum_{i=1}^{N_c} x_i \ln\left(\frac{x_i \hat{\varphi}_i}{\varphi_i^0}\right) \tag{B-19}$$

Where, x_i represents the mole fraction of component 'i' in the mixture, while $\hat{\varphi}_i$, and φ_i^0 represent the fugacity coefficient of component 'i' in the mixed and pure states, respectively, for specified temperature and pressure.

Equations B-15 through B-17 imply that at the UCEP, the critical phase is a stable phase whose composition lies on the stability limit (spinodal locus) wherein, the curvature of $\Delta_m\underline{G}$ in composition space bounded between the intrinsic limits of stability of the merging phases vanishes (undulation). Equation 15 represents the spinodal locus of $\Delta_m\underline{G}$ in P-T-x space. Equation B-16 represents the undulation condition, while equation B-17 represents the stability criterion. In terms of the second order composition derivative function of $\Delta_m\underline{G}$ in composition space at specified T and P, at the UCEP, the composition of the critical phase must represent its minimum.

Analytical expression for second order composition derivative of $\Delta_m\underline{G}$

For a binary mixture, equation B-19 can be expanded as shown in equation B-20.

$$\frac{\Delta_m\underline{G}}{RT} = \{(1-x_2)\ln(1-x_2) + x_2 \ln x_2\} + \{(1-x_2)\ln\hat{\varphi}_1 + x_2 \ln\hat{\varphi}_2\} - \{(1-x_2)\ln\varphi_1^0 + x_2 \ln\varphi_2^0\} \quad \text{(B-20)}$$

For water/n-alkane binaries, water is assigned the index of 1, while the n-alkane is assigned the index 2. Equation B-20 has three parts: the first, second, and third representing ideal mixing, non-ideal mixing, and pure component terms, respectively.

The partial derivative of equation 2 with respect to x_2 is shown in equation B-21

$$\frac{1}{RT}\frac{\partial \Delta_m G}{\partial x_2}\Big|_{T,P} = \{\ln x_2 - \ln(1-x_2)\} +$$

$$\left\{\ln \hat{\varphi}_2 - \ln \hat{\varphi}_1 + x_2 \frac{\partial \ln \hat{\varphi}_2}{\partial x_2}\Big|_{T,P} + (1-x_2)\frac{\partial \ln \hat{\varphi}_1}{\partial x_2}\Big|_{T,P}\right\}$$

$$+\{\ln \varphi_1^0 - \ln \varphi_2^0\} \quad \text{(B-21)}$$

The Gibbs-Duhem criterion is shown in equation B-22.

$$(1-x_2)\frac{\partial \bar{G}_1}{\partial x_2}\Big|_{T,P} + x_2 \frac{\partial \bar{G}_2}{\partial x_2}\Big|_{T,P} = 0 \quad \text{(B-22)}$$

where $\bar{G}_1$and $\bar{G}_2$ represent the partial molar Gibbs free energy of components 1 and 2, respectively.

Equation B-22 can be further simplified as shown in equations B-23 through B-25

$$(1-x_2)\frac{\partial \ln(\hat{\varphi}_1(1-x_2))}{\partial x_2}\Big|_{T,P} + x_2 \frac{\partial \ln(\hat{\varphi}_2 x_2)}{\partial x_2}\Big|_{T,P} = 0 \quad \text{(B-23)}$$

$$(1-x_2)\frac{\partial \ln \hat{\varphi}_1}{\partial x_2}\Big|_{T,P} + x_2 \frac{\partial \ln \hat{\varphi}_2}{\partial x_2}\Big|_{T,P} = 0 \quad \text{(B-24)}$$

$$\frac{\partial \ln \hat{\varphi}_1}{\partial x_2}\Big|_{T,P} = -\frac{x_2}{(1-x_2)}\frac{\partial \ln \hat{\varphi}_2}{\partial x_2}\Big|_{T,P} \quad \text{(B-25)}$$

Substituting equation B-24 in equation B-21, we have equation B-26.

$$\frac{1}{RT}\frac{\partial \Delta_m G}{\partial x_2}\Big|_{T,P} = \{\ln x_2 - \ln(1-x_2)\} + \{\ln \hat{\varphi}_2 - \ln \hat{\varphi}_1\} + \{\ln \varphi_1^0 - \ln \varphi_2^0\} \quad \text{(B-26)}$$

The partial derivative of equation B-26 computed with respect to x_2 is shown in equation B-27**.**

$$\frac{1}{RT}\frac{\partial^2 \Delta \underline{G}_{mix}}{\partial {x_2}^2}\Big|_{T,P} = \left\{\frac{1}{x_2} + \frac{1}{(1-x_2)}\right\} + \left\{\frac{\partial \ln \hat{\varphi}_2}{\partial x_2}\Big|_{T,P} - \frac{\partial \ln \hat{\varphi}_1}{\partial x_2}\Big|_{T,P}\right\} \quad \text{(B-27)}$$

Substituting equation B-25 in equation B-27, we have equation B-28.

$$\frac{1}{RT}\frac{\partial^2 \Delta_m \underline{G}}{\partial {x_2}^2}\Big|_{T,P} = \left\{\frac{1}{x_2} + \frac{1}{(1-x_2)}\right\} + \left\{\frac{\partial \ln \hat{\varphi}_2}{\partial x_2}\Big|_{T,P}\left(1 + \frac{x_2}{(1-x_2)}\right)\right\} \quad \text{(B-28)}$$

Equation B-28 is further simplified to yield **equation B-29**.

$$\frac{1}{RT}\frac{\partial^2 \Delta_m \underline{G}}{\partial {x_2}^2}\Big|_{T,P} = \left\{\frac{1}{x_2} + \frac{1}{(1-x_2)}\right\} + \left\{\frac{\partial \ln \hat{\varphi}_2}{\partial x_2}\Big|_{T,P}\left(\frac{1}{(1-x_2)}\right)\right\} \quad \text{(B-29)}$$

Overview of methodology for the estimation of the UCEP for type IIIa binaries

In this sub-section, the procedure employed to compute the UCEP for water/n-alkane binaries exhibiting type IIIa phase behavior is succinctly described. For type IIIa systems, the V and L phases merge in the presence of the W phase at the UCEP. In the proposed method, the pressure, temperature and the composition of the critical phase at the UCEP are computed by solving the criticality criteria defined using the Gibbs free energy specification and first order necessary condition for phase equilibrium (equations B-15 through B-18).

A robust way to ascertain the UCEP is to adopt an approach where in, the three-phase curve is first computed up to conditions (in terms P-T) in the near-critical region. Near-criticality is determined based on the closeness of the compositions of the V and L phases at the largest P-T condition where three-

phase coexistence can be determined. For type IIIa binaries investigated thus far, it was observed that the composition of the V and L phases at the respective largest P-T condition at which three-phase can be ascertained is less than 0.06 (mole fraction). This observation is stated in equation B-30.

$$\left|x_{iV}\left(P, T_{3\varphi}\right) - x_{iL}\left(P, T_{3\varphi}\right)\right| < 0.06 \qquad \text{(B-30)}$$

where x_{iV} and x_{iL} represent the mole fractions of component 'i' in the V and L phases, respectively.

The aforementioned approach wherein the three-phase curve is systematically computed up to conditions in the near-critical region, prior to determining the UCEP has the following merits:

- It facilitates the definition of a search grid in P-T space. That is, a search grid is P-T space is defined by first creating a search interval for the UCEP temperature, and the corresponding initial estimates for the UCEP pressure are then obtained by extrapolating the three-phase curve obtained thus far.

- It facilitates the determination of an interval in composition space wherein the composition of the critical phase must lie. The compositions of the V and L phases at three-phase coexistence lie on the V-L binodal locus and their corresponding limits of stability lie on the spinodal locus. Either the binodal limit (V-L) or spinodal limit (V-L) corresponding to the highest P-T condition at which three-phase

coexistence can be ascertained, may be used to define the bounds for the composition of the critical phase. The latter is preferable as the resulting composition interval is narrower.

As the search for the UCEP is performed in P-T-x space, the best specification of the criticality criteria in terms of the thermodynamic potential is the Gibbs free energy. Equations B-15 through B-18 are solved using an exhaustive search approach, the procedure for which is furnished in the following section.

Procedure for the estimation of the UCEP for type IIIa binaries

Step 1. Identify the composition bounds within which, the composition of the critical phase must lie. This interval can be derived either from the binodal locus or the spinodal locus, although the latter is preferable.

Step 2. Define a preliminary search grid in P-T space by increasing the temperature and calculating the corresponding pressure by extrapolating the three-phase curve computed thus far. The recommended resolution of this search grid in temperature space is at least 10^{-2} K.

Step 3. For each point in the defined search grid, perform a P-T flash calculation, and identify if the grid point can potentially represent the UCEP. If for a specified grid-point, the resulting composition of the non-aqueous phase is outside the ascertained composition bounds, that P-T condition does not potentially represent the UCEP, and must be disregarded.

Step 4. For those P-T grid-points that can potentially represent the UCEP, evaluate the second order composition derivative of the molar Gibbs free energy change on mixing (equation B-29) at various compositions lying within the composition interval ascertained in step 1, for each grid-point in P-T space. A resolution of at least 200 points is recommended for the composition interval.

Step 5. Identify the global minimum of this function over the defined composition interval, at each grid point in P-T space. The global minimum of this function is the solution of the undulation criterion specified in equation B-31.

$$x(T,P) = \min\left(\frac{\partial^2 \Delta_m \underline{G}}{\partial x_2{}^2}\Big|_{T,P}\right) \tag{B-31}$$

Step 6. Identify that P-T grid-point whose solution for equation B-30 best satisfies second order necessary criterion (equation B-32). Over the defined search grid, this grid-point best represents the UCEP solely in terms of the criticality criteria (equations B-15 to B-17). The tolerance employed for equation B-32, in this work, is 10^{-3}.

$$\frac{\partial^2 \Delta_m \underline{G}}{\partial x_2{}^2}\Big|_{T,P}\big(x(T,P)\big) = 0 \tag{B-32}$$

Step 7. At the P-T grid-point identified in step 6, which is potentially representative of the UCEP, evaluate if the composition of the critical phase ascertained in steps 5 through 6 matches that of the non-aqueous

phase in equilibrium with the W phase, determined by a P-T flash calculation (equation B-33).

$$\delta_x = \left|x_i(T_{UCEP}, P_{UCEP}) - x_{iNA}{}^{flash}(T_{UCEP}, P_{UCEP})\right| \leq \epsilon_x \qquad \text{(B-33)}$$

where $x_i(T_{UCEP}, P_{UCEP})$ represents the mole fraction of component 'i' obtained in step 6, and $x_{iNA}{}^{flash}(T_{UCEP}, P_{UCEP})$ is mole fraction of component 'i' obtained by performing a P-T flash calculation at the T_{UCEP} and P_{UCEP} (potential values) ascertained in step 6.

Step 8. If the criterion specified in equation B-33 is not fulfilled at the identified P-T grid-point ($\epsilon_x \sim 10^{-4}$), then create a secondary P-T search grid around the identified grid-point and repeat steps 3 through 7. The recommended resolution for the secondary search grid is on the order of 10^{-4} in both T and P.

Method for the estimation of the UCEP for type IIIb binaries

The BIP correlation developed in this work yields a value of 0.242 for the limiting BIP, and it occurs for water/n-C_{26} binary. For water/n-alkane binaries with CN 26 and higher, type IIIb phase behavior is observed wherein the V and W phases are apparently merging.

For type IIIb systems, the estimated UCEPs represent the largest P-T condition at which three-phase coexistence can be predicted. The difference between the composition of the V and W phases expressed in terms of the mole fraction of the n-alkane is shown in equation B-34.

$$\left|x_{hcV}\left(P, T_{3\varphi}\right) - x_{hcW}\left(P, T_{3\varphi}\right)\right| < \epsilon_x \quad \text{(B-34)}$$

At the limiting BIP, the largest value for ϵ_x (0.004) is observed for water/n-C_{26} binary, and it systematically decreases with increasing CN for the n-alkane. Among the type IIIb systems investigated, the smallest value for ϵ_x (2.47E-06) is observed for water/n-C_{36} binary. Even the largest observed value for ϵ_x, 0.004, is reasonably small to justify criticality.

The classical criteria for criticality presented in equations B-15 through B-17 cannot not be solved for type IIIb systems, which is why the basis for the determination of criticality for these systems is distinct from those exhibiting type IIIa phase behavior. The explanation requires a close examination of the topology of the Gibbs energy change on mixing in composition space in the near-critical region, and is furnished in the subsequent sub-section.

Issues with the estimation of the UCEP for type IIIb systems using the classical criticality criteria

In **Figure B-1**, the molar Gibbs free energy change on mixing in composition space for water/n-C_{36} binary, at T = 646.82 K and 220 bars, for a value of 0.242 for the BIP is presented. At this P-T condition, three equilibrium phases exist with the concentration of n-alkane (mole fraction) being 6.864E-06, 0.222 and 1.524E-07 in the V, L and W phases, respectively. The compositions of the V and W phases are very similar, indicating that the specified pressure and temperature lie in the near-critical region. The discontinuity observed in Figure B-1b is the consequence of a discontinuous change in the volumetric behavior in composition

space. The volumetric behavior (in terms of the compressibility factor) in the composition domain of figure B-1b is visualized in **Figure B-2**.

Visualized in **Figure B-3** is the analytical first order composition derivative of $\Delta_m\underline{G}$. As seen in equation B-29, the first order composition derivative is composed of three terms- one that represents the derivative of the ideal mixing part, the second representing the derivative of the non-ideal mixing part, and the third involving the fugacity coefficient of the pure components. In **Figure B-4**, the behavior of these terms in composition space is visualized.

In **Figures B-5 and B-6**, the second order composition derivative of $\Delta_m\underline{G}$, presented in equation B-37, and the impact of ideal mixing and non-ideal mixing terms on its value are visualized. For both first and second derivatives of $\Delta_m\underline{G}$, as the infinite dilution limit is approached, the ideal mixing part becomes increasingly more dominant of the two terms.

For the water/n-alkane binaries investigated thus far, the predicted dissolution of the n-alkane in the aqueous phase is several orders of magnitude less than unity. As the infinite dilution limit is approached, if the second derivative of the molar Gibbs free energy change on mixing is dominated by the ideal mixing part (**equations B-29 and B-35**), from **equation B-36**, we see that it tends towards large positive values.

$$\lim_{x_2\to 0} \frac{1}{RT}\frac{\partial^2 \Delta_m \underline{G}}{\partial {x_2}^2}\Big|_{T,P} \approx \lim_{x_2\to 0}\left\{\frac{1}{x_2}+\frac{1}{(1-x_2)}\right\} \tag{B-35}$$

$$\lim_{x_2\to 0}\left\{\frac{1}{x_2}+\frac{1}{(1-x_2)}\right\} \to \infty \tag{B-36}$$

For water/n-alkane binaries, case studies indicate that near the edge corresponding to 100% water, the ideal mixing term in equation B-37 exceeds the non-ideal term by a few orders of magnitude. Thus, the computability of the UCEP for type IIIb systems is related to how well the non-ideal behavior of water-rich phases is modeled. For type IIIb systems, in the near-critical region, the V phase is also very rich in water owing to the very low volatility of the n-alkane relative to water. Also, it is well established that the PR EOS employing classical mixing rules is inadequate with regard to the prediction of the compositional behavior of the W phase, and it is mainly its computational efficiency that renders the model viable for reservoir engineering applications.

The shortcomings of the PR EOS model deters the computability of the UCEP of type IIIb systems using the rigorous criteria for criticality (equations B-15 through B-17). Nevertheless, the three-phase curve cannot extend infinitely in P-T space, which necessitates the definition of a finite upper bound in terms of P and T. Hence, it is recommended that the critical state be defined based on the compositions of the V and W phases along the three-phase curve, in the near-critical region.

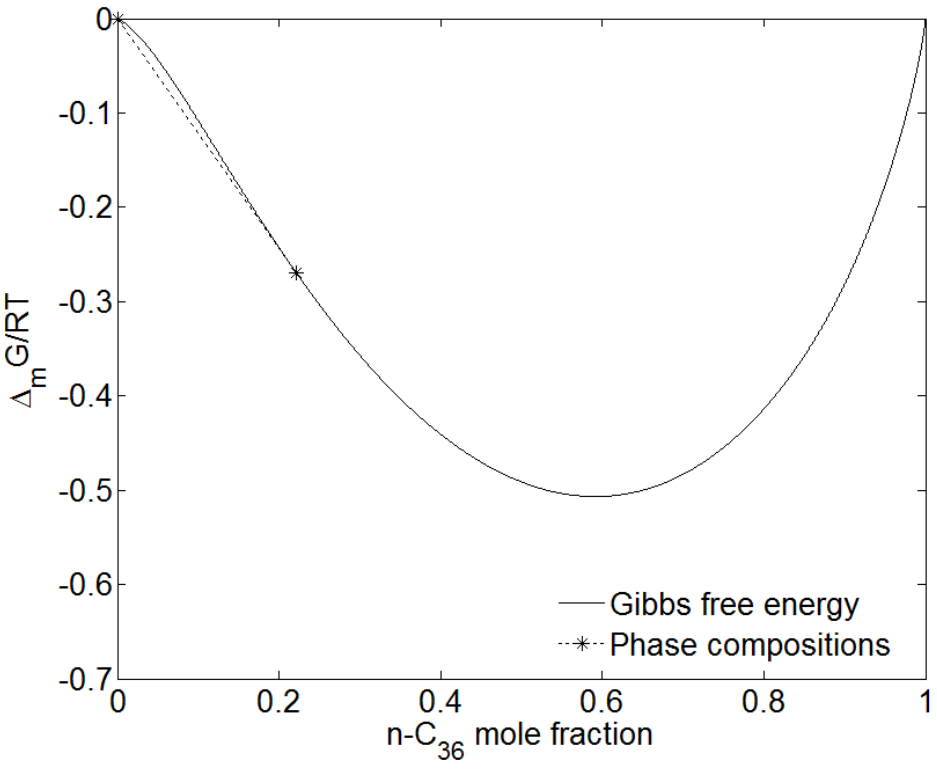

Figure B-1a. Predicted molar Gibbs free energy change on mixing in composition space for water/n-C_{36} binary at 220 bars and 646.82 K. The value for the BIP used in calculations is 0.242. At these conditions, three-phases (V, L and W) coexist at equilibrium. The mole fraction of n-C_{36} in the V, L and W phases are 6.864E-06, 0.222 and 1.524E-07, respectively.

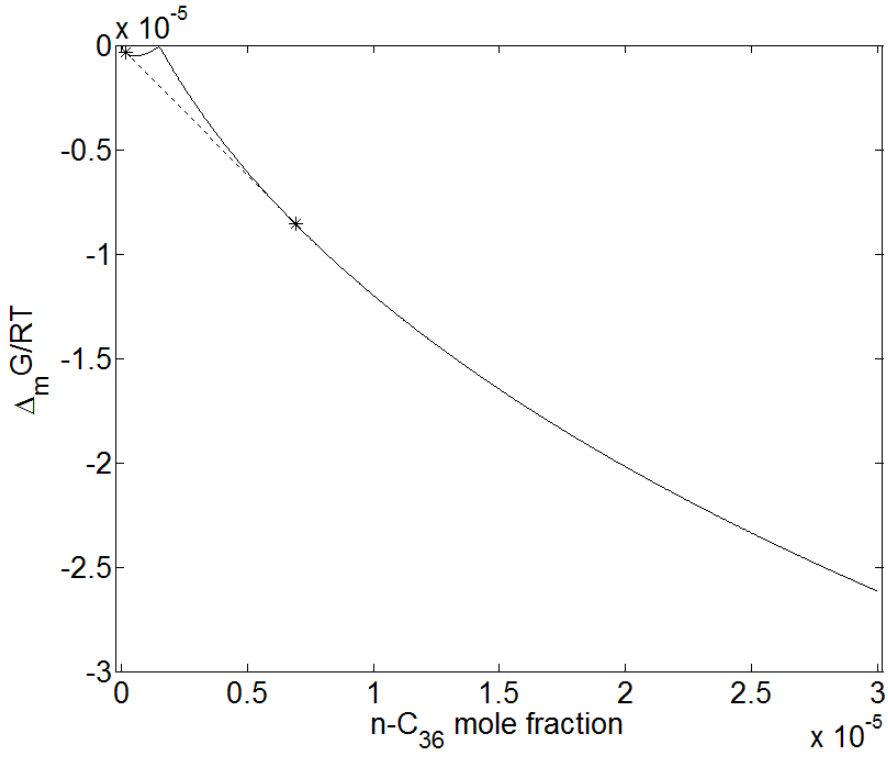

Figure B-1b. Predicted molar Gibbs free energy change on mixing in composition space for water/n-C_{36} binary at 220 bars and 646.82 K. The value for the BIP used in calculations is 0.242. This figure is a close-up snapshot of the V-W region which is not apparent in figure B-1a due to the closeness of the compositions of the two phases. The asterisks represent the equilibrium phase compositions at three-phase coexistence. The mole fraction of n-C_{36} in the V, and W phases are 6.864E-06, and 1.524E-07, respectively.

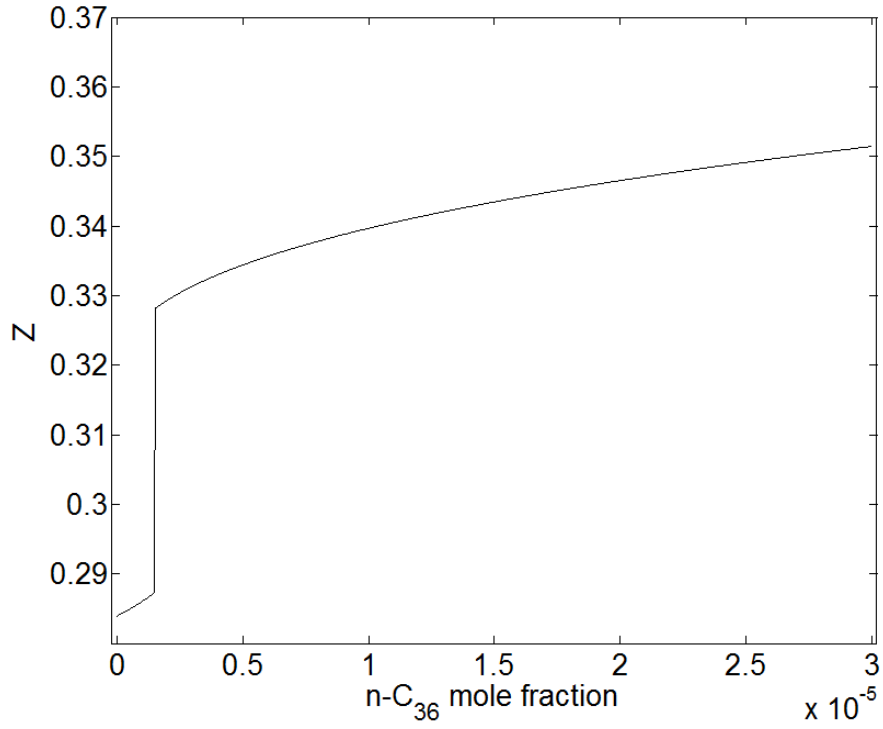

Figure B-2. Predicted compressibility factor in composition space for water/n-C_{36} at 220 bars and 646.82 K, for a value of 0.242 for the BIP. The purpose of this figure is to demonstrate that the basis for the observed discontinuity in the molar Gibbs free energy change on mixing in figure B-1b is a discontinuous change in volumetric behavior with respect to composition.

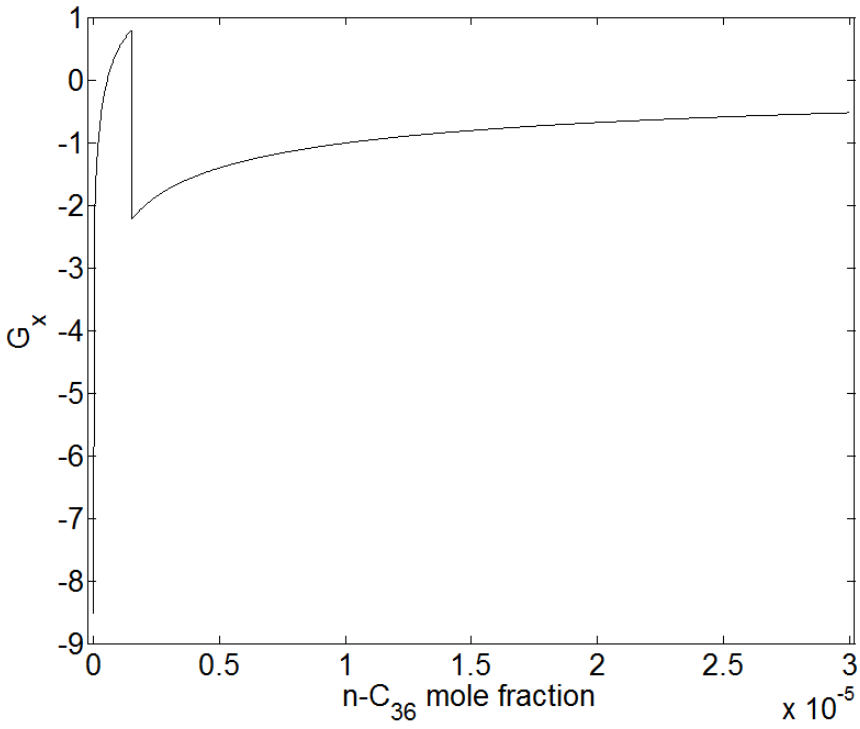

Figure B-3. First order composition derivative of predicted molar Gibbs free energy change on mixing for water/n-C_{36} binary at 220 bars and 646.82 K. Note that G_x stands for $\frac{1}{RT}\frac{\partial \Delta_m \underline{G}}{\partial x_2}\Big|_{T,P}$. At three-phase equilibrium, the mole fraction of n-C_{36} in the V and W phases is 6.864E-06, and 1.524E-07, respectively. Consequently, these two compositions have the same values for the first order composition derivative of $\Delta_m\underline{G}$. The span of the domain of the composition space in this figure is close to the composition of V phase to facilitate viewing.

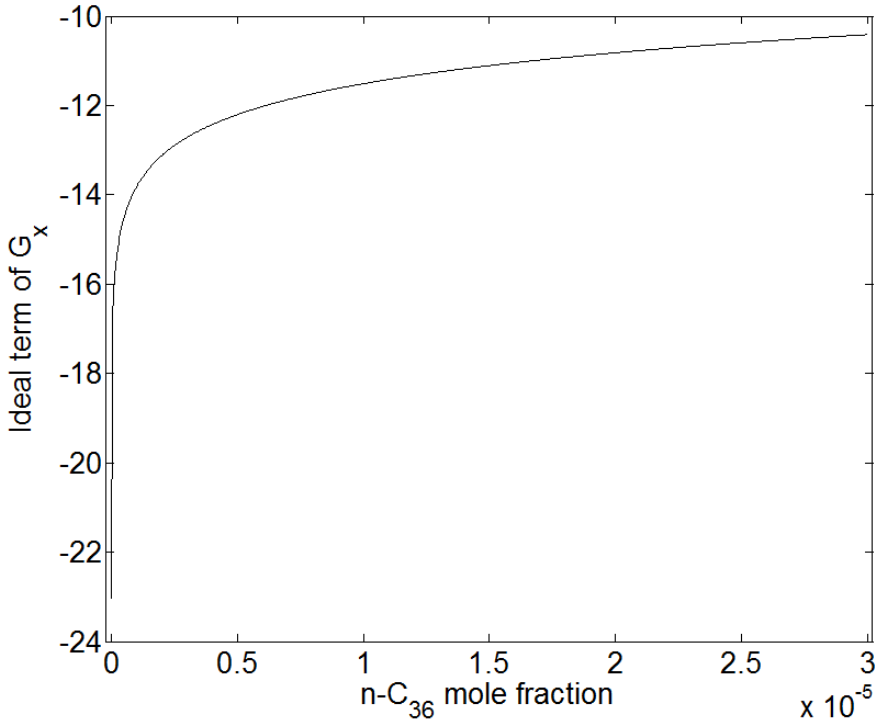

Figure B-4a. Ideal mixing part of the first order composition derivative of the molar Gibbs energy change on mixing for water/n-C_{36} binary at 220 bars and 646.82 K, for a BIP value of 0.242. The analytical expression for this term is presented in equation B-26. As the infinite dilution limit is approached, the ideal part of the first order composition derivative tends towards negative infinity. This is manifested by a steep decline in the function value.

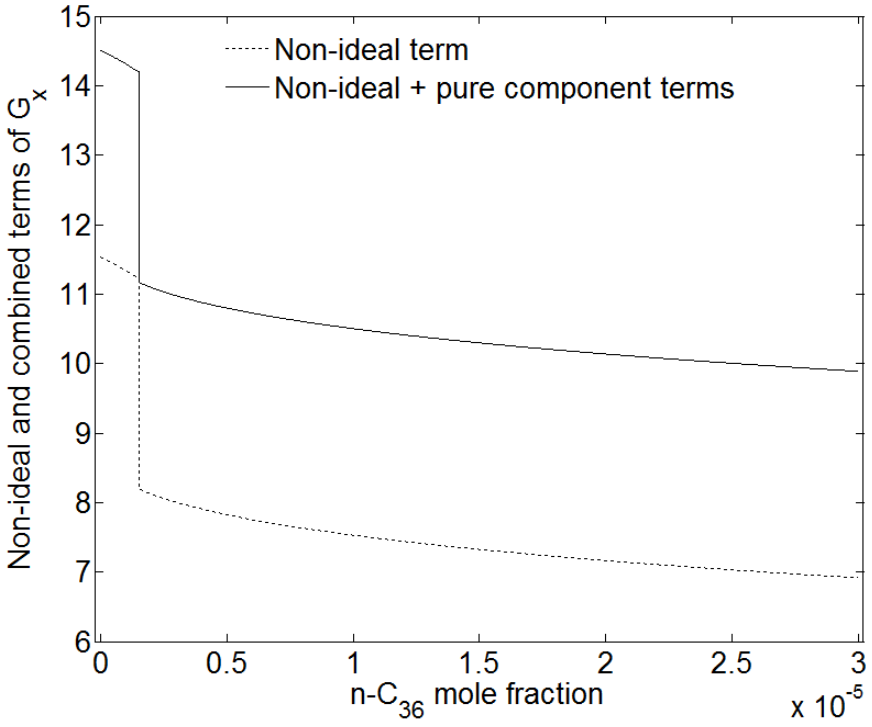

Figure B-4b. Non-ideal mixing term and its combination with the pure component term (equation B-34) for the first order composition derivative of the molar Gibbs energy change on mixing for water/n-C_{36} binary at 220 bars and 646.82 K, for a BIP value of 0.242. The analytical expressions for these terms are presented in equation B-34. From figure B-4a, we see that as the infinite dilution limit is approached, the first order composition derivative becomes increasingly dominated by the ideal part of equation B-34, which in turn tends towards negative infinity.

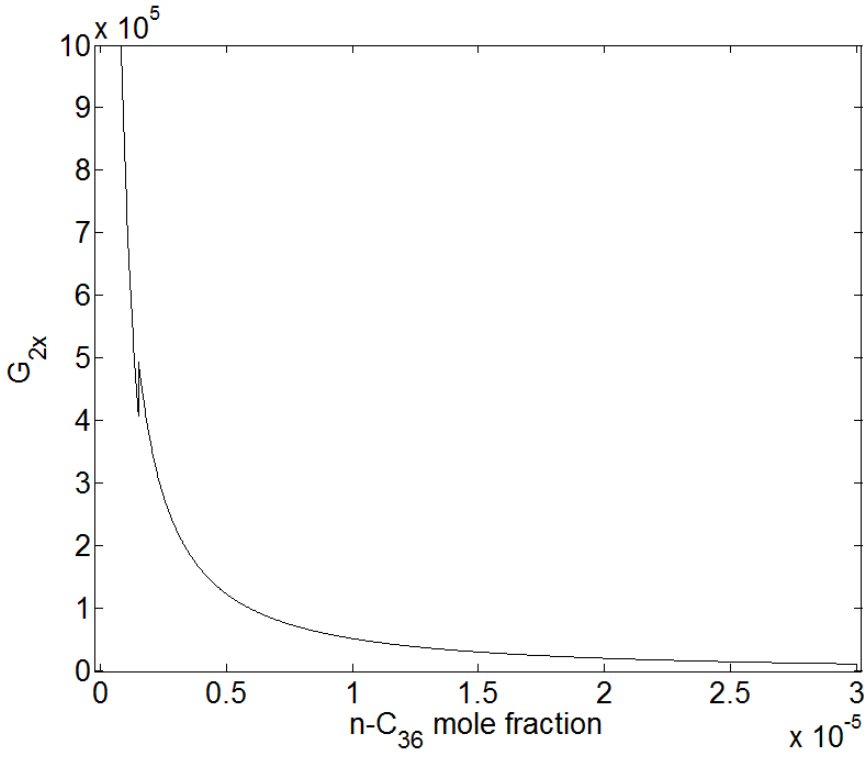

Figure B-5. Second order composition derivative of predicted molar Gibbs free energy change on mixing for water/n-C_{36} binary at 220 bars and 646.82 K, for a value of 0.242 for the BIP. Note that G_{2x} stands for $\frac{1}{RT}\frac{\partial^2 \Delta_m G}{\partial {x_2}^2}\Big|_{T,P}$. The observed discontinuity is the consequence of a discontinuous change in the volumetric behavior as shown in Figure B-2. As the infinite dilution limit is approached the function value tends to large positive values owing to the increasing dominance of the ideal mixing part (equation B-29). The effect of the ideal and non-ideal mixing parts on the function value of the second derivative is shown in figure B-6.

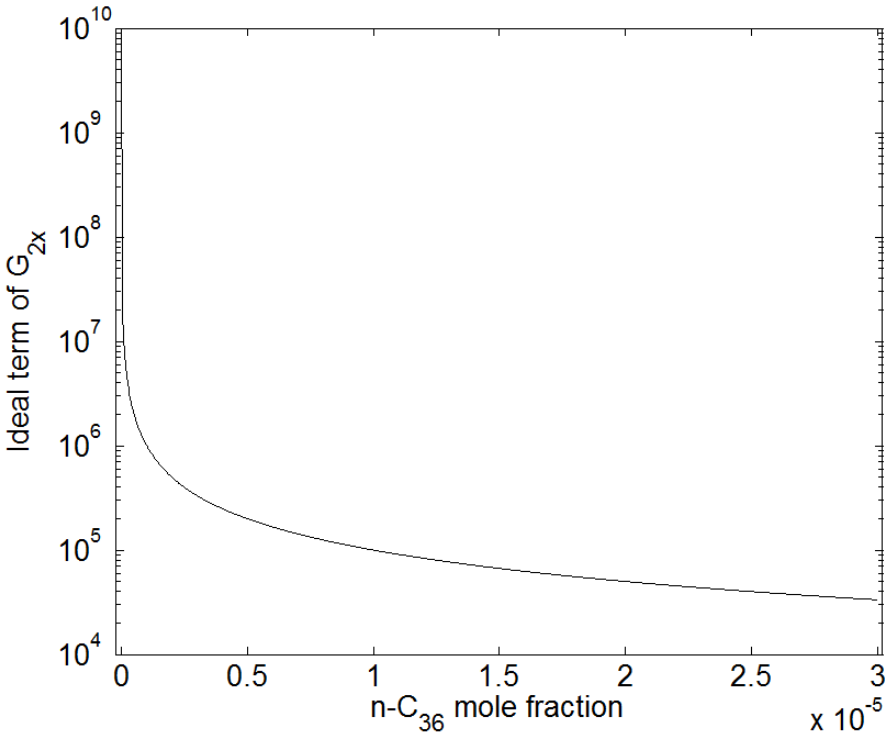

Figure B-6a. Ideal mixing part of the second order composition derivative of the molar Gibbs energy change on mixing for water/n-C_{36} binary at 220 bars and 646.82 K, for a BIP value of 0.242. The analytical expression for this term is presented in equation B-29. As the infinite dilution limit is approached, the ideal part of the first order composition derivative tends towards large positive values.

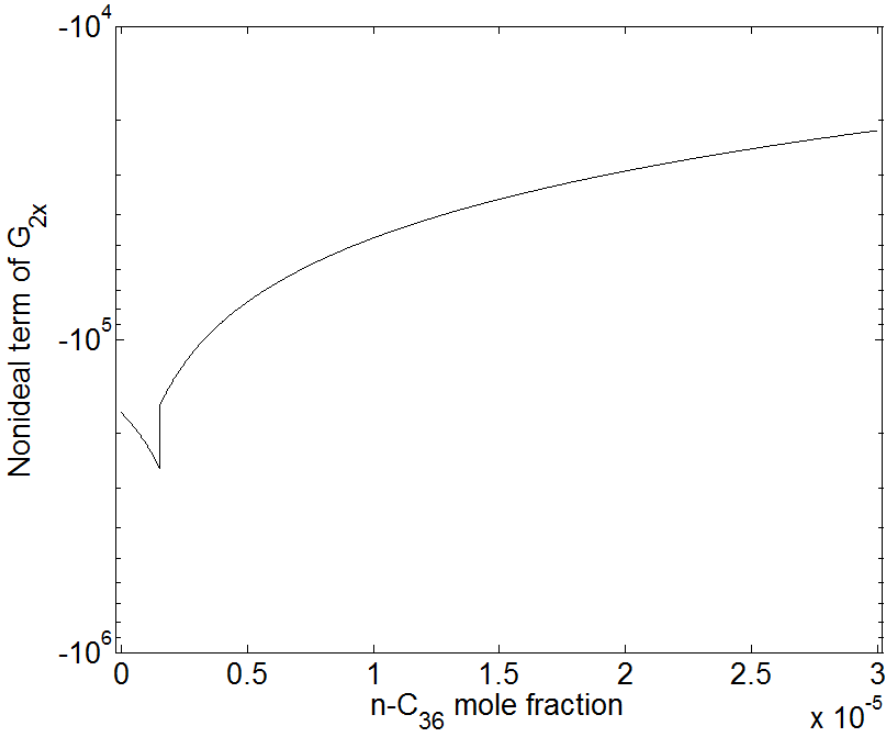

Figure B-6b. Non-ideal mixing part of the second order composition derivative of the molar Gibbs energy change on mixing for water/n-C_{36} binary at 220 bars and 646.82 K, for a BIP value of 0.242. This figure serves as a complement to figure B-5. The analytical expression for this term is presented in equation B-37. As the infinite dilution limit is approached, this term becomes less dominant of the two terms in equation B-29.

Appendix C. Critical points and acentric factors for n-alkanes

The API technical data book (Daubert and Danner, 1997) gives recommended values for T_C, P_C, and ω for n-alkanes up to n-C_{30}. Kontogeorgis and Tassios (1997) presented a critical review for various estimation methods for T_C, P_C, and ω of heavy n-alkanes. They concluded that the group-contribution method of Constantinou and Gani (1994) and Constantinou et al. (1995) is reliable for the extrapolation to extended CNs. In this research, the values from the API technical data book (1997) and from the group contribution method are integrated with smooth trends. The integration keeps the accuracy within the experimental uncertainties when measured values are available.

Table C-1 presents the integrated set of T_C, P_C, and ω for n-alkanes from C_1 to n-C_{100}. Available experimental data are also listed; the NIST Chemistry webbook (2001) is used for C_1 through n-C_4, and Nikitin et al. (1997) for n-C_5 through n-C_{36}. The T_C, P_C, and ω values given in Table A-1 are internally consistent in that Pitzer's definition of ω is satisfied when used with the PR EOS.

The values given in Table C-1 are correlated with the following equations:

$$T_C = 1410.705429[\ln(CN + 2.203385)]^{0.332560} - 1293.54872 \qquad \text{(C-1)}$$

$$P_C = 46.83909\exp\{-0.5[\ln(CN/1.47310)/1.45642]^2\} + 1.31706 \qquad \text{(C-2)}$$

$$\omega = 0.074020(CN)^{0.86699}\exp(-0.00245CN) - 0.04618 \qquad \text{(C-3)}$$

The R^2 values are 0.9995, 0.9993, and 0.9999 for T_C, P_C, and ω, respectively. Maximum absolute deviations for T_C, P_C, and ω are 8.37 K for n-C_{24}, 1.58 bars

for C_2, and 0.0120 for C_1. The standard deviation is 2.06 K for T_C, 0.206 bars for P_C, and 0.0024 for ω.

Table C-1. Critical constants and acentric factors for n-alkanes up to n-C_{100}.The integrated set is based on the API technical data book (Daubert and Danner, 1997), Constantinou and Gani (1994) and Constantinou et al. (1995). This table is spread over two pages. The uncertainty in the experimental measurement is denoted using |η|

CN	Integrated set			Experimental data			
	T_c, K	P_c, bar	ω	T_c, K	P_c, bar	|η| in T_c, K	|η| in P_c, bar
1	190.56	45.99	0.0157	190.60	46.10	0.30	0.30
2	305.32	48.72	0.0906	305.30	49.00	0.30	0.30
3	369.83	42.48	0.1543	369.82	42.50	0.20	0.10
4	425.12	37.96	0.2014	425.18	38.00	1.00	0.10
5	469.70	33.70	0.2511	469.70	33.70	0.20	0.67
6	507.60	30.25	0.3010	507.60	30.25	0.20	0.61
7	540.20	27.40	0.3505	540.20	27.40	0.30	0.55
8	568.70	24.92	0.3980	568.70	24.90	0.30	0.50
9	594.60	22.90	0.4459	594.60	22.90	0.60	0.46
10	617.70	21.10	0.4898	617.70	21.10	0.60	0.42
11	639.00	19.50	0.5306	639.00	19.80	1.00	0.40
12	658.00	18.20	0.5680	658.00	18.20	1.00	0.36
13	675.00	16.80	0.6077	675.00	16.80	1.00	0.34
14	693.00	15.70	0.6482	693.00	15.70	2.00	0.31
15	708.00	14.99	0.6896	708.00	14.80	2.00	0.30
16	723.00	14.14	0.7320	723.00	14.00	2.00	0.28
17	736.00	13.31	0.7753	736.00	13.40	2.00	0.27
18	747.00	12.51	0.8200	747.00	12.90	3.00	0.26
19	758.00	11.76	0.8634	755.00	11.60	8.00	0.23
20	768.00	11.05	0.9063	768.00	10.80	8.00	0.22
21	779.00	10.39	0.9430	778.00	10.30	8.00	0.21
22	788.00	9.77	0.9801	786.00	9.91	8.00	0.20
23	797.00	9.20	1.0168	790.00	9.15	8.00	0.18
24	806.00	8.88	1.0532	800.00	8.71	8.00	0.17
25	813.00	8.21	1.0894	—	—	—	—
26	820.23	7.79	1.1253	816.00	7.95	12.00	0.32
27	826.19	7.42	1.1609	—	—	—	—
28	831.85	7.29	1.1962	824.00	7.44	12.00	0.30
29	837.36	6.79	1.2312	—	—	—	—
30	842.67	6.52	1.2660	843.00	6.36	12.00	0.25
31	847.75	6.28	1.3004	—	—	—	—
32	852.63	6.07	1.3320	—	—	—	—
33	857.37	5.90	1.3665	—	—	—	—
34	862.01	5.75	1.4006	—	—	—	—
35	866.59	5.63	1.4344	—	—	—	—
36	871.16	5.53	1.4678	872.00	4.72	13.00	0.19
37	875.75	5.22	1.5008	—	—	—	—
38	880.38	5.07	1.5335	—	—	—	—
39	885.03	4.92	1.5659	—	—	—	—
40	889.67	4.78	1.5979	—	—	—	—
41	894.29	4.65	1.6296	—	—	—	—
42	898.90	4.53	1.6610	—	—	—	—
43	903.50	4.42	1.6921	—	—	—	—
44	907.59	4.31	1.7229	—	—	—	—
45	911.76	4.20	1.7533	—	—	—	—
46	915.83	4.11	1.7835	—	—	—	—
47	919.82	4.01	1.8134	—	—	—	—
48	923.72	3.92	1.8430	—	—	—	—
49	927.53	3.84	1.8724	—	—	—	—
50	931.27	3.76	1.9014	—	—	—	—

CN	Integrated set			Experimental data			
	T_c, K	P_c, bar	ω	T_c, K	P_c, bar	|η| in T_c, K	|η| in P_c, bar
51	934.93	3.68	1.9302	—	—	—	—
52	938.52	3.61	1.9588	—	—	—	—
53	942.04	3.54	1.9870	—	—	—	—
54	945.49	3.48	2.0151	—	—	—	—
55	948.88	3.41	2.0429	—	—	—	—
56	952.21	3.35	2.0704	—	—	—	—
57	955.47	3.30	2.0977	—	—	—	—
58	958.68	3.24	2.1248	—	—	—	—
59	961.83	3.19	2.1516	—	—	—	—
60	964.93	3.14	2.1783	—	—	—	—
61	967.98	3.09	2.2047	—	—	—	—
62	970.97	3.04	2.2309	—	—	—	—
63	973.92	3.00	2.2568	—	—	—	—
64	976.82	2.95	2.2826	—	—	—	—
65	979.68	2.91	2.3082	—	—	—	—
66	982.49	2.87	2.3335	—	—	—	—
67	985.25	2.84	2.3587	—	—	—	—
68	987.98	2.80	2.3837	—	—	—	—
69	990.66	2.76	2.4085	—	—	—	—
70	993.31	2.73	2.4330	—	—	—	—
71	995.92	2.70	2.4575	—	—	—	—
72	998.49	2.66	2.4817	—	—	—	—
73	1001.02	2.63	2.5057	—	—	—	—
74	1003.52	2.60	2.5296	—	—	—	—
75	1005.99	2.58	2.5533	—	—	—	—
76	1008.42	2.55	2.5768	—	—	—	—
77	1010.82	2.52	2.6002	—	—	—	—
78	1013.19	2.50	2.6234	—	—	—	—
79	1015.53	2.47	2.6464	—	—	—	—
80	1017.84	2.45	2.6693	—	—	—	—
81	1020.12	2.42	2.6920	—	—	—	—
82	1022.37	2.40	2.7146	—	—	—	—
83	1024.59	2.38	2.7370	—	—	—	—
84	1026.79	2.36	2.7592	—	—	—	—
85	1028.96	2.34	2.7814	—	—	—	—
86	1031.10	2.32	2.8033	—	—	—	—
87	1033.22	2.30	2.8251	—	—	—	—
88	1035.32	2.28	2.8468	—	—	—	—
89	1037.39	2.26	2.8684	—	—	—	—
90	1039.43	2.25	2.8898	—	—	—	—
91	1041.46	2.23	2.9110	—	—	—	—
92	1043.46	2.21	2.9322	—	—	—	—
93	1045.44	2.20	2.9532	—	—	—	—
94	1047.40	2.18	2.9740	—	—	—	—
95	1049.34	2.16	2.9948	—	—	—	—
96	1051.26	2.15	3.0154	—	—	—	—
97	1053.15	2.14	3.0359	—	—	—	—
98	1055.03	2.12	3.0563	—	—	—	—
99	1056.89	2.11	3.0765	—	—	—	—
100	1058.73	2.10	3.0966	—	—	—	—